UNIVERSITY COLLEGE LONDON

Tube-Forming Device Design For The Creation of Cell-Integrated Alginate Tubes

By

Garr Kooy Chau

A THESIS SUBMITTED FOR THE DEGREE
OF DOCTOR OF PHILOSOPHY AT
THE UNIVERSITY OF LONDON

DEPARTMENT OF BIOCHEMICAL ENGINEERING

LONDON, UNITED KINGDOM

AUGUST 2008

To my parents . . .

Declaration

I Garr Kooy Chau, confirm that the work presented in this thesis is my own. Where information has been derived from other sources, I confirm that this has been indicated in the thesis and referenced accordingly where credit is due.

……

Garr Kooy Chau

01 August 2008

Abstract

This thesis describes a generic system capable of forming cell-populated alginate tubes either by seeding cells within its lumen, or integrating cells within the tube walls. The applications of an alginate tube are as diverse as applications of alginate beads, and could be used with many types of cells for many different purposes – from cell therapy to tissue engineering. The aim of this work has therefore been on the ability: to reproducibly create alginate tubes with uniformly thick walls of predictable thickness; to be able to monitor and quality control said tubes and a generic cell suspension, including automating aspects of mammalian anchorage-dependent cell culture to improve reliability; and to integrate said cells into an alginate tube without compromise to wall thickness, cell viability and cellular spatial distribution within the alginate tube.

This work describes experimental verification a novel fluid dynamics model that predicts with any two fluids used in this reverse dip-coating device that the tube wall thickness will be approximately equal to $^2/_3$ the gap width as gap width becomes negligible. Robustness testing of the tube-forming device prompted two base unit designs and a protocol in order to achieve coefficient of variation (CV) values under 5% of tube length for infusion rates up to 100ml/min and alginate concentrations ranging from 0.50 – 1.00%. Tubes with wall thicknesses between 143.4 – 277.3μm can be reliably reproduced for tubes of any length. Optical coherence tomography (OCT) at ±10μm accuracy was adapted to directly monitor alginate wall thickness and rate of shrinkage in real-time through air. This was determined to be ~12 minutes for tube walls to stabilise and a high speed camera showed no spherical regulator spin as the tube is formed, indicating that monitoring at one point is sufficient to determine the overall quality of the tube wall consistency. Cell sample homogeneity monitored by particle sizer revealed two distinct single-celled populations, and smaller peak of cytoplasmic residue. Capillary cytometer was determined the best way to enumerate cell quantity reliably and consistently. Holding time above 3 hours can significantly cause aggregation, but this can be controlled

using filtration of known pore size. Kenics static mixers were used to integrate cells into alginate prior to tube formation and showed equally good control to wall thickness as pure alginate tubes at ~CV 7%. Cell viability of above 90% after processing through the static mixer and the tube-forming mark 2 device was achievable using Pronova SLG 100 pre-liquified alginate. The Kenics mixers at 12 elements showed a 49.6% improvement in CV of spatial distribution of cells across alginate, although this could be bettered by increasing number of Kenics static mixing elements, at the cost of increasing dead volume.

Acknowledgements

This thesis is dedicated to all the people whose support and assistance have made this documents completion possible.

First and foremost I must thank my main supervisor – Dr. Susana Levy, who offered guidance from conception of experiments to analysis of results. She has helped me develop from a student to a scientist, and her invaluable aid, especially during the write-up period I am truly indebted to.

My gratitude also goes out to my advisors: Prof. Gary Lye, Dr. Chris Mason, Prof. Mike Hoare and Prof. Peter Dunnill. Prof. Lye's shrewd comments have more than often provided an alternative insight into many experiments. Chris' support as a supervisor and friend has been a source of great inspiration. And Mike and Peter's experience and wisdom have been the backbone of my successful research.

I must also thank Prof. Ricky Wang, Prof. Yonghong He, Marco Bonesi of Cranfield University, Silsoe for their expertise with the OCT technology they have there. And thanks also go out to Prof. Ian Eames and Dr. Mark Landeryou at UCL for their work developing the fluid dynamics Theory.

I would also like to thank my engineering colleagues at UCL, Biochemical Engineering, especially Martin Town, Alfred Ding, Spyros Gerontas and Leda Pittarello with whom I have worked closely.

And finally I must thank my family who have constantly been a driving force – lighting my path and nurturing completion of my studies. Their love and patience have seen me through the hardest trial of the past five years.

Table of Contents

LIST OF TABLES

LIST OF FIGURES

NOMENCLATURE & ABBREVIATIONS

Symbol	Description
$\bar{u}$	Mean speed of propelling liquid in flow
Re_{δ}	Reynolds number based on the minimum gap width
v	Velocity of spherical regulator moving in x direction
δ_0	Minimum gap separation between glass cylinder and sphere surface
ρ	Density of matrix fluid
μ	Viscosity of matrix fluid
x	Vertical distance (see fig. 3.1)
V	Velocity of sphere in x direction
a	Internal cylinder radius
P	Any point around the spherical regulator
$\delta(x)$	Variable gap separation between cylinder and sphere surface at point P
r	Variable radial direction
r_0	Sphere radius
u_x	x component of predicted fluid velocity
u_r	r component of predicted fluid velocity
p	Pressure
t	Time required for sphere to break through matrix fluid
h	Vertical position of sphere
λ	Initial height of matrix fluid
d	Length of alginate tube
V	Volume of a tube
f	Circumferential flux of matrix fluid
ΔP	Pressure drop across the sphere top to bottom
S	Shear induced force per unit circumferential distance

F_x	Total force on buoyant sphere in vertical direction
V	Volume of matrix fluid
L	Length of tube formed
T_B	Predicted theoretical thickness of formed tube from lubrication analysis
T_0	Nominal tube wall thickness

Abbreviation	**Description**
TE	Tissue engineering
ECM	Extracellular matrix
SEM	Scanning electron microscope
OCT	Optical coherence tomography
USS	Ultrasound scanning
MRI	Magnetic resonance imaging
CM	Confocal microscopy
DOCT	Doppler optical coherence tomography
MIM	Maximum initial mode
QUIPS	Quantitative interactive programming system
MHRA	Medicines and healthcare products regulatory authority
FDA	Food and drugs administration
GMP	Good manufacturing practice
QC	Quality control
QA	Quality assurance
GLP	Good laboratory practice
SMC	Smooth muscle cells
CV	Coefficient of variation
HSD	Honestly significant difference
CLSM	Confocal laser scanning microscopy

1 Literature Review

1.1 SODIUM ALGINATE

Alginate is a family of polyanionic copolymers derived from brown algae. It consists of 1,4 β-D-mannuronic (M) and α-L-guluronic acid (G) residues in varying proportion, depending on the source of the alginate (fig. 1.1). These monomers are distributed sequentially in either repeating or alternating blocks. It is soluble in aqueous solutions at room temperature and forms a hydrogel when reacted with multi-valent cations such as Ca^{2+}, Ba^{2+}, Fe^{3+} or Sr^{2+} to form ionic bridges between G-block carboxyl groups of different polymer chains. By manipulating this ratio, mechanical properties and pore size can be altered (Smidsrod and Skjak-Braek 1990). These mechanical properties are subject to loss over time due to outward flux of cross-linking cations *in vitro*, but covalent linkage may be achieved using bi-functional cross-linkers, PEG or adipic hydrozide using standard carbodiimide chemistry (Drury and Mooney 2003). The ability to re-solubilise in the presence of phosphate, citrate or other chelating agents is often seen as a drawback, but may also be used as an advantage (Jork et al. 2000; Peirone et al. 1998). Over the years, alginate has gained pharmaceutical importance, due to its biocompatibility (Cohen et al. 1991; Sennerby et al. 1987), hydrophilicity and low cost, and has found many applications in medicine and dentistry gaining regulatory approval from several bodies including the Food & Drugs Administration (FDA) for use as an injectable, a wound dressing and a food additive (Godbey and Atala 2002; McIntire 2003). Controlled porosity in alginates has also been explored by forming sponges via gelation, freezing and drying by lyophilization (Shapiro and Cohen 1997).

The biggest problem with using alginates as a source of scaffold biopolymer is the inability of alginate polysaccharides or their hydrogels to promote protein adsorption for anchorage dependent mammalian cells due to its hydrophilic nature and lack of cell surface receptors to interact with cells (Smetana 1993). Encapsulation of cells within

(**a**)

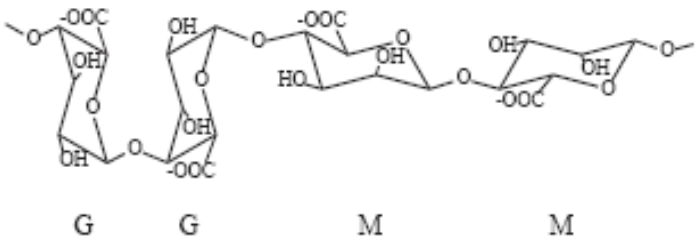

(**b**) (**c**)

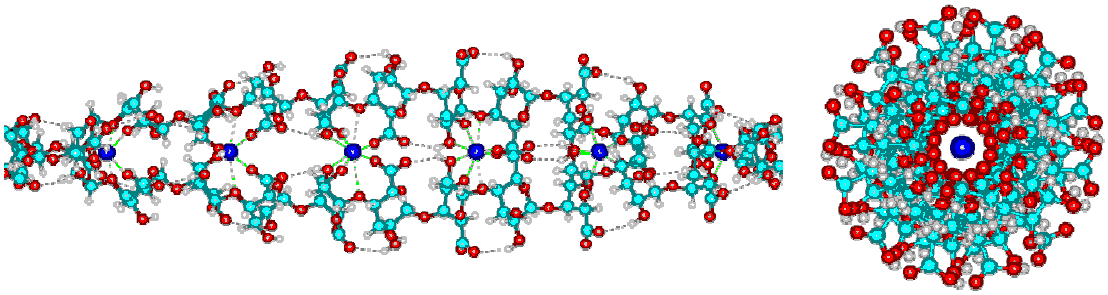

Figure 1.1 (**a**) Chemical (Drury and Mooney 2003) and (**b**)-(**c**) molecular structures (Vij et al, 2007) of naturally derived alginate polymer molecule.

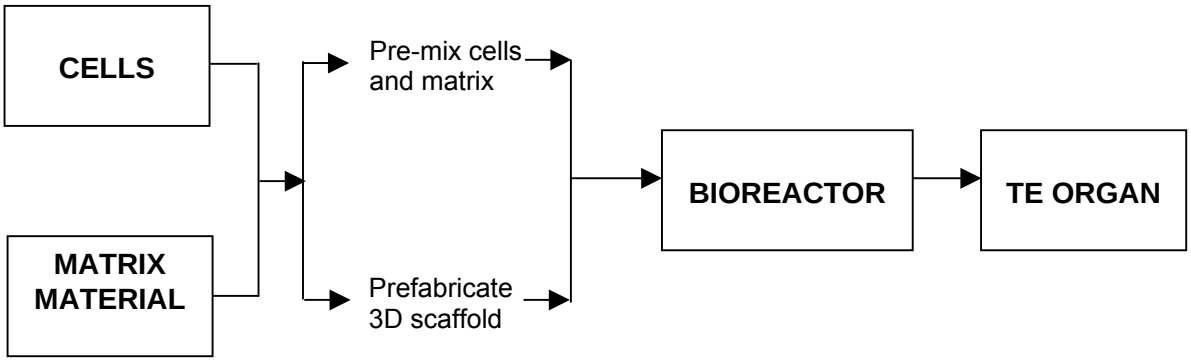

Figure 1.2 Flow diagram of generic tissue engineering. Cells and matrix material is combined via one of three methods – pre-mixing cells with matrix; simultaneous mixing of cells with matrix and formation of TE organ; or prefabricating a cell-free TE "scaffold" and populating this with cells after. This TE organ is then put into a Bioreactor, cells proliferate and the scaffold should dissolve. The resultant TE organ should consist of cells only.

beads in the past has cultured multicellular aggregates (Yagi et al. 1993). To this end, certain groups have covalently modified alginate with peptides containing RGD (Rowley and Mooney 2002). Alginate is also not resorbable (not absorbed by the body) limiting its usage to *in vitro* development if used to develop autologous transplantable organs, although this has been used to deliver protein-producing cells in allogenic and xenogenic situations (see 1.2.1).

In summary the advantages outweigh the issues. Other than those above mentioned, alginate is above all non-toxic, low cost and abundant.

1.2 USES OF ALGINATE STRUCTURES

1.2.1 Cell Encapsulation

Historically, alginate has been one of the most important proven materials involved in cell and tissue encapsulation (Leinfelder et al. 2003). Cell encapsulation falls into two main categories: micro-encapsulation, involving materials such as alginate to create cell-populated micro-beads; and macro-encapsulation, which typically involves much larger preformed thermoplastic materials in planar or hollow-fiber geometries (Uludag et al.2000).

Essentially cell encapsulation provides a permeable barrier isolating cells from, although allowing interaction with, the outside environment – which could be the homeostatic conditions of an animal host or a synthetic bioreactor – thus enabling transplantation of cells, for end uses such as cell therapy, without the need for immunosuppression. This allows control of pH, metabolic waste removal, electrolytes and nutrient exchange via diffusion. A common problem for encapsulated cells however, is variable cell viability depending on specimen thickness (Shelton 1966), which limits access to nutrients such as oxygen. Tubular constructs have been used either as an intravascular or extravascular encapsulation devices: the former with islet cells embedded in the walls of the tube acting as a surrogate pancreas in

diabetic rats (Tze et al. 1976; Chick et al. 1977; Sun et al. 1977); and the latter with the open ends of the tube heat-crimped to act as an envelope containing cells, a method able to restore growth hormone in animals for up to 3 months (Altman et al. 1981; Altman et al. 1982). In recent years mammalian cell encapsulation especially using alginate has seen great advances. Presently focus has concentrated not only on host response to the transplanted vehicle, but also interaction between the encapsulated cells and biological material.

However, despite progress, reports indicate that reproducibility of encapsulated products – both during manufacture and in pre-clinical animal studies – is lacking. Scaleup of standardised technology is also a barrier – especially with secrecy surrounding encapsulation information and protocols amongst groups. Choice of clinically proven material and final material properties remains two of many unanswered questions. An obvious material is alginate, but due to its natural source, batch on batch property consistency is lacking. Uniformity of beads (size, shape, morphology) remains a problem – but new automated devices may improve this in the future. With constant policy adjustments from regulatory authorities – cell-populated products now fall under a new category. Agencies such as the US Food and Drug Administration (FDA) have taken particular interest to protocols and procedures that demonstrate biosafety to patients (Orive et al. 2003).

Future aims of the field will include finding a method that offers more direct contact between the vehicle and the host's bloodstream in order to increase the long-term survival rate of encapsulated cells and tissues. Also greater understanding of biomaterial effects to vehicle properties and control of vehicle properties during fabrication is required to speed the transition of this technology to the real world (Uludag et al. 2000).

1.2.2 Tissue Engineering

Tissue Engineering (TE) is the combining of cells, scaffold and bio-signals (fig. 1.2) to create a transplantable human organ meant as a replacement (Bottaro et al. 2002; Chapekar 2000; Godbey and Atala 2002).

Cells can be from three main sources – autologous (own patient cells), allogenic (from another patient), or xenogenic (from an animal). An autologous source has the advantages of immune acceptance and safety from pathogens. This tissue must be obtained from a biopsy from the patient, for each patient. Because of the different types of cells needed for a tissue engineered organ, partially differentiated stem cells from a patient's bone marrow would be a likely future cell source (Faustman et al. 2002; Germain et al. 2002; Parker 2002). Historically, advances in tissue engineering have been mostly acellular due to the complexities of mammalian cells (Metzger 2002; Parenteau and Hardin-Young 2002). Biomaterial scaffolds influence cell function and response. Cellular scaffolds have also encountered physical consistency, maintenance of phenotype and host immune response problems (Sipe 2002). Cell expansion and differentiation knowledge is limited. Major problems have included monitoring cells on a scale and metabolic level (Kapur 2002). Limited success has been achieved with *in vivo* studies of cell expansion and differentiation (Sefton 2002; Taylor 2002), although *in vitro* studies have proven difficult mainly due to oxygen demands to three-dimensional constructs (Hirschi et al. 2002; Ratcliffe and Niklason 2002).

The scaffold or matrix can be comprised of many varieties of natural or synthetic materials. It serves to act as a three-dimensional guide for the proliferating cells to take a pre-designed morphology. It constitutes the temporary, surrogate extracellular matrix (ECM) that lends mechanical strength, organising and guiding cell growth and differentiation (Sipe 2002). Using this technique, one can theoretically fabricate any tissue or organ in the human body. It is important that the scaffold possesses some basic properties, including: mechanical strength; control of degradability; and, for safety reasons, compatibility with the human body – even though the level of

scaffold material should be negligible by the time of transplantation, i.e. the cells will inhabit this and eventually replaces the scaffold, which dissolves away, to form a final tissue-engineered organ. For this last point, a natural material is desirable, since residual material will often incur a foreign-body response. Usage of the final product could vary from therapeutics to cosmetics, and this implies different material properties. As a therapeutic the main desirable material properties would include: -

- Non-thrombogenic, toxic nor immunogenic upon transplantation
- Sterile
- Acceptable wound healing response without fibrosis
- Mechanical strength for ultimate use in body and handling purposes
- No propensity for creep which would lead to aneurysm (surrogate blood vessel)
- Permeable to solutes and cells
- Scalable
- Long shelf-life
- Control over degradation, either by a biological process within the body or passive hydrolytic cleavage via control of material composition, surface chemistry and topology
- Absorbable by body, via kidneys metabolism, or other means
- Control of enhanced biocompatibility depending on the end use of the product
- Free of pathogens
- High porosity and adequate pore size to accommodate cells
- Physical properties for fabrication limitations
- Compatible with anchorage-dependent cells
- Low cost
- Well characterised to better attain regulatory approval

(McIntire 2003; Tranquillo 2002)

Biomaterials can be divided into three subcategories – synthetic, naturally derived or semi-synthetic. Most materials originated from surgical procedures such as sutures, hemostatic agents and wound dressings, from a regulatory approval perspective. But as we understand more about mammalian cells, the direction tends to be more end-user orientated now. But there is the added advantage of regulatory approval for well-characterised materials (McIntire 2003).

The signals are the chemical and mechanical interfaces between the cells, and the matrix and cells in order to facilitate growth. Signals are comprised of extracellular chemical and physical inputs, and these serve to influence cellular activities such as: gene expression, cell division, migration, differentiation and apoptosis (Sipe 2002). Mechanoregulation via physical interactions are consistent and unavoidable, most notably the force of gravity, and these can drive important results such as cell morphology and tissue patterning, which in-turn affects the response to chemical stimuli (Ingber 2002). Better understanding and hierarchy of important signals is vital for future of tissue engineering. Two-dimensional culture must evolve to three-dimensional to study the signals involved (Ducy 2002).

General fabrication of TE products follows two schools of thought: seeding of cells onto a preformed matrix; and premixing cells with the matrix gel and creating the TE product afterwards (fig. 1.2) (Haverich and Graf 2002).

1.3 OTHER CELL ENCAPSULATION DEVICES

Several research groups have a well-engineered, automated approach to cell encapsulation (Lewinska et al. 2004). One such device was that at the Swiss Federal Institute of Technology (Serp et al. 2000). The Swiss group developed a highly controlled encapsulation device from a syringe pump, for creating precision beads using alginate and $CaCl_2$. The device flowed at 1-15ml/min, involving laminar jet break-up from a sinusoidal vibrating nozzle.

The device was capable of creating beads from 250 – 1000μm diameter populated with $1x10^6$ – $1x10^8$ cells/mL. The resulting beads were quality controlled using a high-speed video camera to monitor droplet size and a temperature-controlled coulter counter to count the number of beads formed. The group observed that the device was sensitive to alginate concentration, in-turn affecting viscosity. However viscous effects were physical in nature – concerning the successful formation of beads upon hitting the $CaCl_2$ bath. 1.0-2.5% shrinkage was observed to occur within 5-10 mins up to 600μm diameter beads. And re-dissolving the beads in trisodium citrate took between 20mins to several hours.

In fact, the trend for control via engineering and automation seems to be the current inclination. A group from Northwestern University have developed a device that aims to reproducibly create beads (fig. 1.3*a*-*d*) for cell encapsulation purposes (Vij et al. 2007).

Another alginate group, a joint effort consisting of Clemson University (USA) led by Dr. Phil Brown and small biotech firm – BioSurfaces, are currently working creation of <100μm thick hollow fibres (fig. 1.4*a*-*b*) lined with a layer of genetically modified endothelial cells (Wagner et al. 2006). The aim of this work is to create a lining within synthetic implanted materials to help direct wound healing by increasing the release of certain native biological factors (fig. 1.4*c*). This work is also envisaged to eventually encompass genetically modified bacteria or other cells to create commercial textiles with anti-fungal, anti-microbial or anti-soiling properties. Their process is based on a modified wet/dry spinneret system spinning degassed sodium 6% w/v alginate solutions through an air gap of 0-20cm and then dowsing in a coagulant bath of salt such as 1% calcium chloride solution (fig. 1.4*d*-*e*). Fibre morphology is fine-tuned using a mixture of salts, such as calcium and zinc, as-well-as further additives such as glycerol and ethanol. Endothelial cells are injected in the bore fluid at a rate of 1-100ml/hour. Cells were obtained commercially by ATCC and concentrations of $2x10^4$ – $2x10^5$ cells/ml were used. Cellular activity was monitored using Alamar Blue and Western Blotting. Fibre geometry was monitored using graticule/optical

(**a**) (**b**)

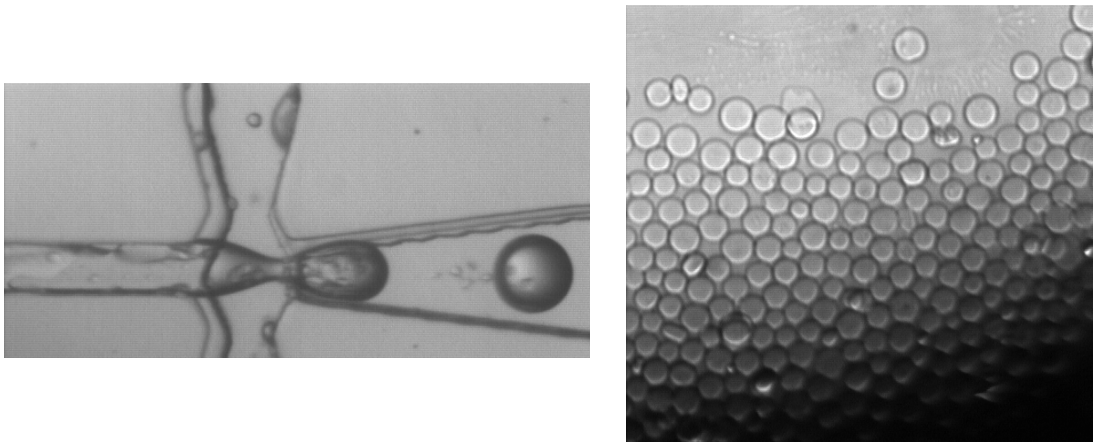

(**c**) (**d**)

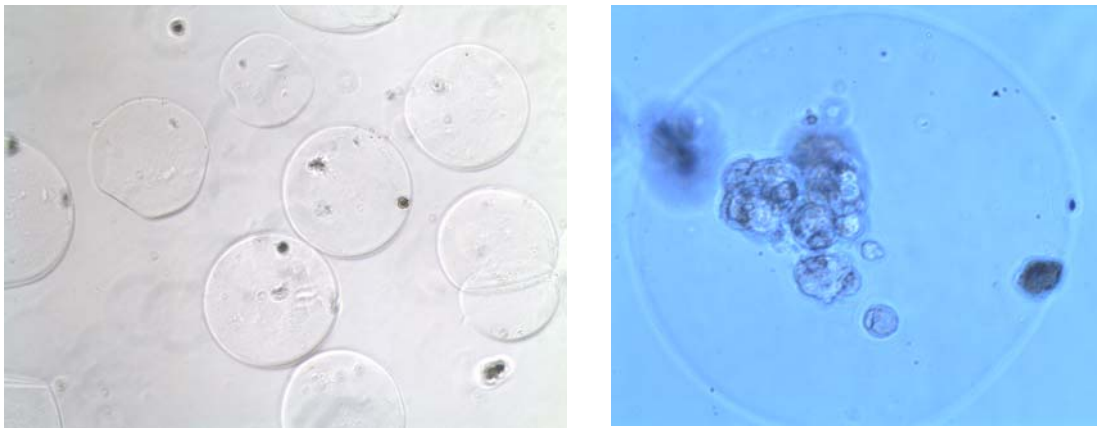

Figure 1.3 (**a**) Bead formation; (**b**) bead harvesting; (**c**) bead stability; (**d**) cell viability assessment.

(**a**)

(**b**)

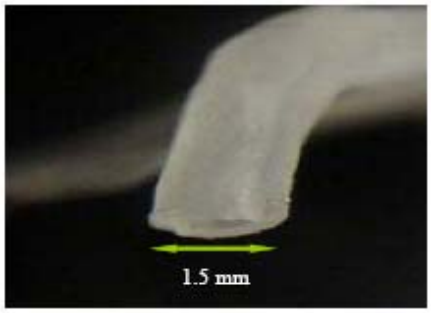

(**c**)

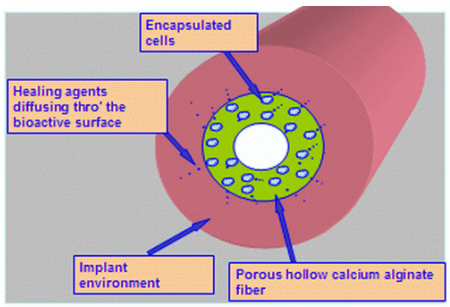

(**d**)

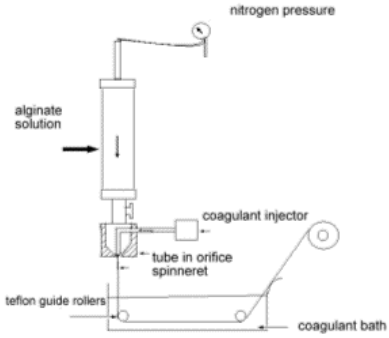

(**e**)

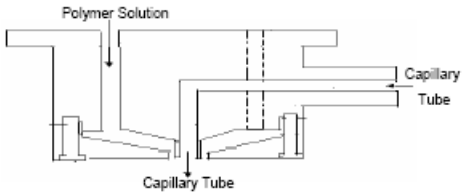

Figure 1.4 (**a**) Photograph of actual device and spinneret

(**b**) Stereomicroscopic photograph of a hollow alginate tube (Wagner et al)

(**c**) How the Clemson/BioSurfaces group aim to use the alginate/endothelial construct to line transplantable materials in order to make them more biocompatible.

(**d**) The modified spinneret system used by the Clemson/BioSurfaces group to create cell-populated hollow fibres.

(**e**) Spinneret schematic

microscope and scanning electron microscopy (SEM). The system is designed to operate in a laminar flow hood (i.e. sterile) after undergoing autoclaving.

Although it can be easy to dismiss shape-forming devices to just those that encapsulate cells, one must point out that even a tube can have many different end-uses. From bandages and membranes to envelopes for cell therapy usage (Altman et al. 1981; Altman et al. 1982).

1.4 OPTICAL COHERENCE TOMOGRAPHY (OCT)

1.4.1 Understanding OCT

Optical Coherence Tomography (OCT) is a non-invasive, newly emerging technique utilising novel imaging technology to produce high-resolution cross-sectional images of a sample in situ and in real time. First demonstrated in 1991 (Huang et al. 1991), it operates on a principle similar to conventional B-mode pulse-echo imaging of clinical ultrasound scanning (USS), except using light backscatter instead of sound backscatter, to create an image. The time for reflected light to travel, or "echo time delay", together with intensity data, is then used to create an image (Schmitt J.M. 1997).

Advantages over other medical imaging techniques such as USS, magnetic resonance imaging (MRI) and confocal microscopy (CM) are superior resolution over the former two – OCT has a resolving power of 1-15μm compared to the 100-200μm resolution of USS – and greater penetration depth over CM (Drexler et al. 2001; Kaufman et al. 2004). OCT can only however penetrate samples up to a depth of 2-3mm, whereas USS can penetrate *in vivo* up to 10cm (Fujimoto 2003).

The heart of the device is a Michelson interferometer (fig. 1.5). It is composed of a light source that is both "low-coherence", i.e. interference of light occurs over a distance of micrometers, and "broadband", i.e. light

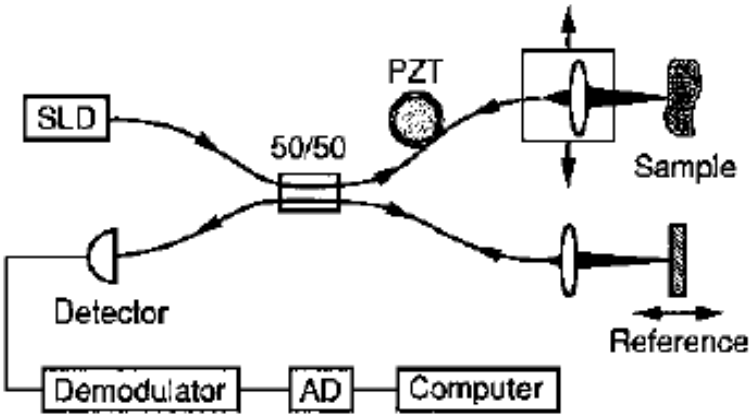

Figure 1.5 Schematic of a simple OCT scanner. The SLD output is coupled into a single mode fiber and split at 50/50 coupler into sample and reference arms. Reflections from the two arms are combined at the coupler and detected by the photo diode. Longitudinal scanning is performed by translating the reference mirror with the stepper motor stage at 1.6mm s^{-1}, generating a 3.8 kHz Doppler shift. The piezoelectric transducer (PZT) in the sample arm further provides 21.2 kHz phase modulation to the interferometric signal. Interferometric modulation of the output intensity is detected by the photodetector when the reference and sample arm delays are nearly matched. The detector output is demodulated at the sum modulation frequency of 25 kHz to produce the envelope of the interferometric signal, which is then digitised (AD) and stored on a computer. A series of longitudinal scans are performed. The lateral beam position is translated after each longitudinal scan (Huang et al. 1991).

emitting sources over a broad range of frequencies. Typical light sources would include superluminescent diodes (super bright LEDs) or femtosecond lasers, i.e. lasers capable of pulsing extremely rapidly. The light is split via a beam-splitter and channelled to two arms: a “reference arm” (usually to a mirror) of a known reference path length and time delay; and a “sample arm” (investigated item), of unknown path length. The two arms of reflected near infrared light are combined to give an interference pattern but only when they are nearly matched “in group-delay”, i.e. if the light from both arms have travelled the same optical distance. The intensity of the reflected light from the sample creates greater interference. Any light outside of the coherence length does not interfere. This “A-scan” gives information regarding spatial dimensions and structures within the sample, detected by changes in refraction index as light crosses the boundary between different materials. A-scans can be compiled to give a “B-scan” cross-sectional tomograph (Huang et al. 1991).

1.4.2 OCT and Tissue Characterisation

OCT has been used as an imaging tool in many diverse fields including clinical medicine, life science research, material science research and manufacture. In clinical medicine, the role of the pathology department is to analyse patient tissue from a biopsy, in order to diagnose and treat the patient. Other than the invasive nature of obtaining a biopsy or whole sample, this is also very labour intensive, and typically takes a few days to achieve a result, or even longer for a more complex specimen. The initial capital investment and training required for OCT is far outweighed by the cost of maintaining a histopathology department. OCT offers an alternative, non-invasive approach to achieve diagnosis in vivo and in real time. Furthermore, the use of optical fibres allows it to be used in conjunction with many medical devices such as keyhole surgery cameras, gastrointestinal tract endoscopes and coronary artery catheters (Mason et al. 2004).

OCT was first applied to Ophthalmology and imaging of the human eye (Hee et al. 1995). Figure 1.6 shows an OCT image of a human retina, measured with a device of 10μm resolution. Even at a modest resolution in OCT terms, this cross-sectional image allows differentiation of detailed structures. The retina is an almost transparent structure, but despite the low optical backscattering, OCT is sensitive enough to detect structures such as the vitreal-retinal junction, optic disc and the fovea and give an approximate retinal thickness. Such studies have contributed towards diagnosis and monitoring of retinal diseases such as glaucoma, macular edema and age related macular degeneration, as well as monitor dynamic response after retinal operations such as laser eye surgery.

Rapid advances in OCT research has utilised longer wavelengths enabling non-transparent tissues to be imaged, where optical scattering is reduced. At 1300nm wavelength, typically 2-3mm depth penetration can be achieved. Due to its optical nature to scan *in situ* and in real time, OCT is suited to cases where excisional biopsy is dangerous or impossible – such as determination of atherosclerotic plaque morphology in coronary artery disease. It is the rupture of unstable plaque formations – those with a structurally weak fibrous cap – that cause thrombosis and vessel occlusion, the most common cause of myocardial infarction. Figure 1.7 shows such a plaque formation (Brezinski et al. 1996) with corresponding histological analysis, obtained after autopsy. At a ~16μm resolution, the OCT image is able to show a small intimal layer covering a heavily calcified atherosclerotic plaque with low lipid content. As one can imagine, this analysis is only conventionally possible upon post-mortem (Fujimoto et al. 2000).

Furthermore OCT can be coupled with Doppler Flow Velocimetry to form DOCT, a method useful for capturing moving images or movies. Such techniques have been applied to monitoring liquid flow profiles (fig. 1.8) within a capillary (Proskurin et al. 2003). From this profile, one can ascertain information such as liquid viscosity and drag resistance due to the micro-vessel walls. Obviously changes such as vessel geometry will impact

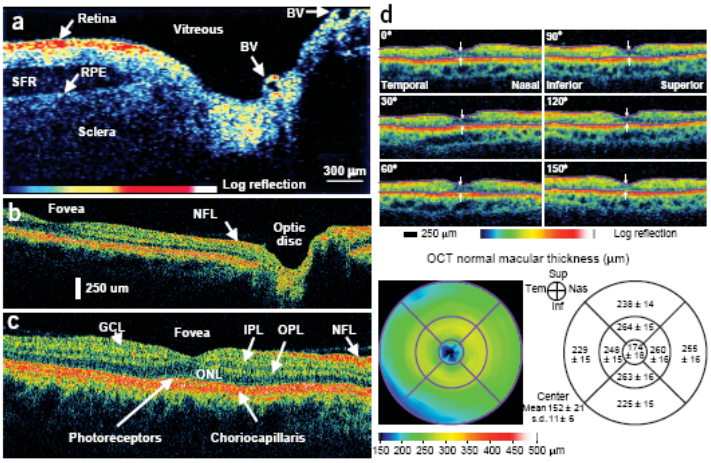

Figure 1.6 Ophthalmic OCT imaging and its development. (**a**) The first demonstration of OCT imaging showing imaging of a human retina *ex vivo* acquired at 800nm with 10-µm resolution. (**b**) Example of a current OCT clinical retinal image produced by StratusOCT instrument (Carl Zeiss Meditec) showing the papillary-macular axis of the retina between the fovea and optic disc. (**c**) Image of the fovea showing normal architectural morphology of the retina. Visible features include NFL, nerve fiber layer; GCL, ganglion cell layer; IPL, inner plexiform layer; OPL, outer plexiform layer; and INL, inner nuclear layer. (**d**) Topographic map of the macula constructed by segmenting multiple OCT images and showing thicknesses using a false colour scheme. Image processing methods such as these enable quantitative analysis of images to aid disease diagnosis (Fujimoto 2003).

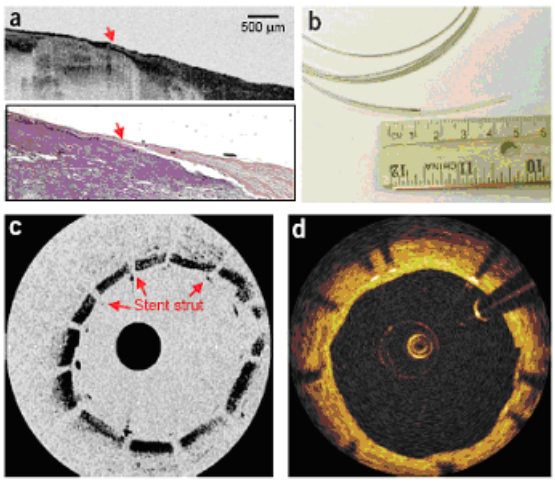

Figure 1.7 Intravascular OCT imaging and its development. (**a**) OCT image *ex vivo* and histology showing unstable plaque with a thin intimal cap layer. (**b**) Prototype fiber-optic OCT catheter consisting of a rotating fiber and

microlens assembly encased in a transparent sheath. (**c**) OCT catheter-based image of a stented rabbit aorta *in vivo*. (**d**) Clinical OCT image of right coronary artery of a human subject *in vivo*, from a follow-up study of drug-eluting stents (Fujimoto 2003).

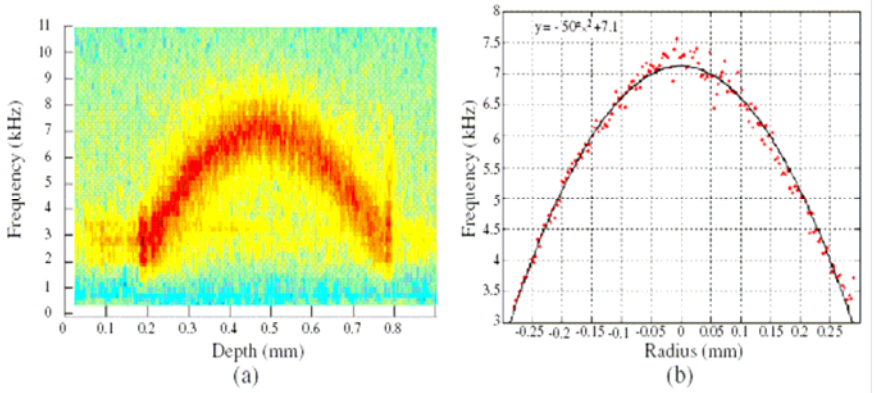

Figure 1.8 Velocity profile (**a**) obtained with an averaging over five A-scans. Least squares fitting (**b**) gives an excellent agreement with the parabola $f_D = -49.75r^2 + 7.11$ (the inset formula shows round-off values) with uncertainty $\Delta V/V \sim 2.0\%$.

dramatically on DOCT liquid velocity profiles. The suitability of the technique to measure blood flow is also discussed. It would be an excellent technique to monitor fabricated tube consistency.

1.4.3 OCT and Tube Monitoring

The characteristics of OCT make it an ideal tool for monitoring tubes created via our tube-forming device. Undoubtedly, one potential use of our alginate tubes is to create tissue-engineered products, which could contain mammalian cells. The need for a growing tissue-engineered organ is sterility and non-destructive testing at an acceptable cost. For any pharmaceutical or medical device, safety is paramount. There has as yet been no proof that low-powered near-infrared light used in OCT is harmful to tissue as opposed to high-powered near infrared, which does permanently damage cellular DNA (Boppart and Fujimoto 2002; Nishioka et al. 2002). Data remains to be generated for internal organs such as blood vessels and arteries that do not have protective melanin deposits such as those in the skin, and do not normally see any light. For years medical endoscopes have been used in the body without any documented adversity (Mason et al. 2004).

OCT has been used *in vitro* with human aorta and coronary artery sections obtained post-mortem. The high resolution allowed differentiation of different morphologies including fatty, fibrous, and water based tissue, as well as distinction between different tissues, such as adipose, skeletal muscle and tendon. The results have been compared to histological results and OCT hailed as promising new technology for high resolution “optical biopsy” (Brezinski et al. 1995).

Several features make OCT an ideal biomedical imaging tool (Fujimoto et al. 2000):

i. The resolution of OCT typically ranges from 1-15μm, compared to the 100μm resolution of USS, which has the added advantage – that scanning can be conducted through air. This resolution is more

comparative to histology, allowing architectural morphology and some cellular features to be imaged.

ii. Imaging can be performed *in situ* without specimen preparation (i.e. excision and fixing), which also minimises sampling errors involved in treating the sample.

iii. Imaging can also be performed in real time. This allows on-screen monitoring and simultaneous digital recording – an excellent surgical tool.

iv. OCT can be coupled with any existing fiber optical device, e.g. surgical probes for imaging from within the subject of study.

v. OCT is compact and portable.

1.5 MALVERN PARTICLE SIZER

1.5.1 Understanding Laser Diffraction

A particle sizer measures particle size based on the technique of laser diffraction. The principle is that particles passing through a laser will scatter the beam in different angles, and that this angle is particle size dependant. This relationship of particle size to scattering angle is logarithmic. However, intensity is inversely proportional to scattering angle – i.e. the larger the particle, the narrower the scattering angle, but at high intensity due to large surface area, and vice versa.

A typical particle sizer (fig. 1.9) consists of the following parts: a laser of fixed wavelength; a sample presentation system to ensure a homogenous stream of sample particles pass through the laser beam; and a series of detectors to measure the diffracted light at different scattering angles (www.malvern.co.uk). Range varies from device to device determined by the angular range of scattering measurement. Modern devices make measurements from 0.02 – 130.00 degrees with a logarithmic detector

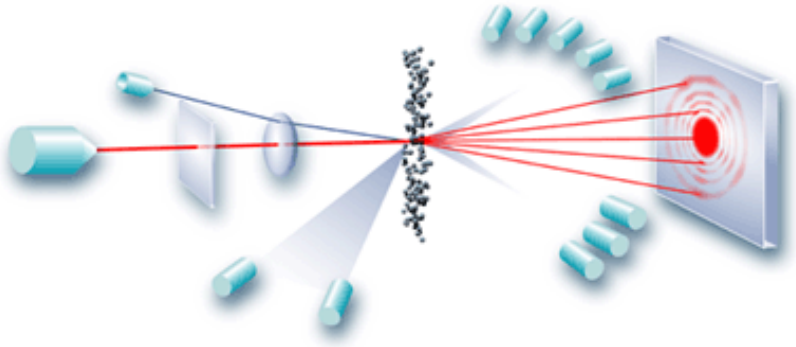

Figure 1.9 An illustration depicting the separate parts of a typical particle sizer system, which consists of laser beam, presentation system and detectors.

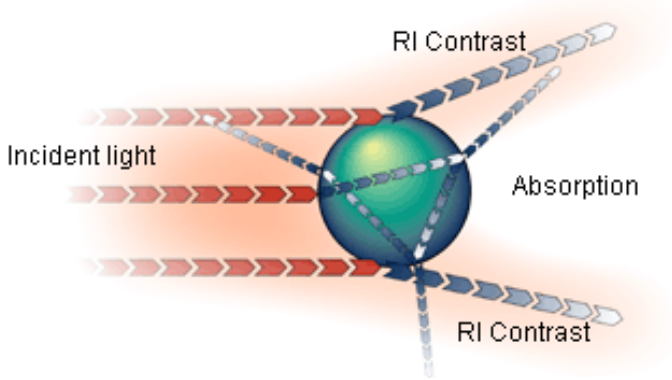

Figure. 1.10 An illustration to explain Mie Theory.

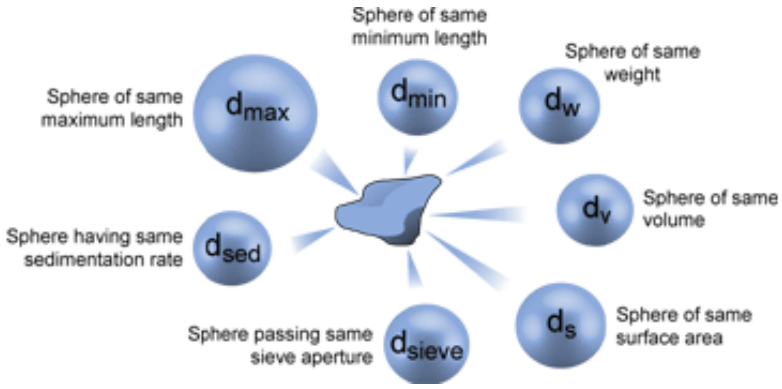

Figure 1.11 An illustration to help explain the equivalent sphere approximation on the basis of length, weight, volume, surface area, sieve aperture, sedimentation rate and maximum length.

sequence, i.e. detectors spaced increasingly far apart as the angle increases, to give optimum sensitivity.

Scattering patterns are compared to one of two mathematical models: the Fraunhofer Approximation and the Mie Theory (fig. 1.10). Mie Theory (used by Malvern particle sizers) is based on Maxwell's electromagnetic field equations. The following assumptions are used for any type of particle size and transparency: particles are assumed spherical; the suspension is dilute – i.e. light is scattered once only before detection; the optical properties of the particle and the medium is known; and finally all particles are homogeneous. The Theory predicts from the scattering data and the intensity taking into account the refractive index difference between the sample particle and medium materials. It also factors in adsorption from the sample particle – extremely important for particles below 50μm in diameter and those that are transparent (ISO13320-1, 1999).

But what is "particle size", especially for particles that are not spherical? The aim of any particle sizer is to create a single number for a particle based on the assumptions of either of the Mie Theory or the Franhofer Approximation. That is, the diameter reported is that of the equivalent spherical particle that would give the same measured variable (sample particle diameter, average cross-sectional area or volume) (fig. 1.11).

1.5.2 Using Laser Diffraction to Measure Particles

One of the most common biological tests is cell counting and classification. Classification can be quickly achieved using cell size to determine different types of cells. One such study from Jiaotong University involved using laser diffraction to analyse human: red blood cells (6-9μm diameter); white blood cells (6-20μm diameter); and blood platelets (2-3μm diameter). Of the four cell counting methods: haemocytometer (a manual counting method using a counting grid and a microscope); photoelectric nephelometric method (only used for red blood cell counting, and results in large errors); Coulter counter

or flow cytometry (which both measure a single cell flowing through a measured region, but are highly priced). Each have their advantages but none of the techniques could measure all three types of cells. This study was the first of its kind to utilise Mie Theory and apply it to quantification of blood cells. Histograms for red and white blood cells (fig. 1.12) show distinct size distributions for each population – 7.69μm mean diameter red blood cells, and a white blood cell classification of 25.1% lymphocytes, 73.5% neutrocytes and 1.4% middle sized cells (Yang 2004).

Of course laser diffraction is not limited to biological samples. A French research group looked at rubber particle coagulation kinetics, a pre-requisite for latex coagulation and the major limiting factor to yield in rubber manufacture (Kongsawadworakul 2003). The study showed that latex cell vacuoles contain proteins that cause coagulation, conversely the cytosol of latex cells also contains anti-coagulating proteins. Figure 1.13 shows a divergence from a Gaussian curve with a peak at 0.8μm denoting (maximum initial mode (MIM) prior to addition of any agents. This milky suspension remained stable and unchanged for over 3 hours prior to addition of lutoidic serum (LS). Seen here is how MIM falls from 14.89% at 0.8μm to 4.37% at 2.28μm over 20 minutes, with a maximum particle size of 7.72μm (fig. 1.13*a*). The team explored how to manipulate aggregation via breakdown of aggregates using shear via a syringe (fig. 1.13*b*). MIM was decreased partially to 0.93μm and particle range from 0.36 to 2.65μm, however this returned to previous MIM and range values when left in the LS solution. pH and buffer were also explored. Laser diffraction is suggested by this research as a way to monitor the kinetics of aggregation of any particles, organelles or cells.

1.5.3 Laser Diffraction and Cell Encapsulation

The Jiaotong study of blood cells gave many indications of the advantages of using laser diffraction over other particle classification methods (Yang 2004).

(**a**) (**b**)

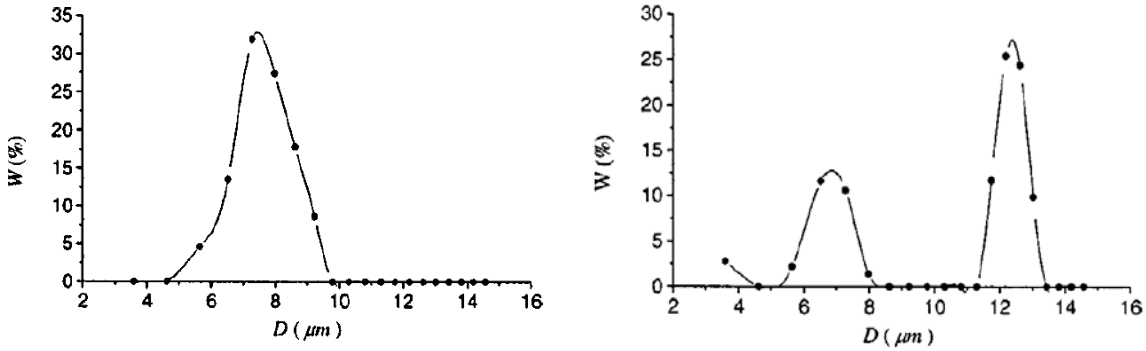

Figure 1.12 Size distribution histograms for a sample of (**a**) red blood cells and (**b**) white blood cells from a human patient.

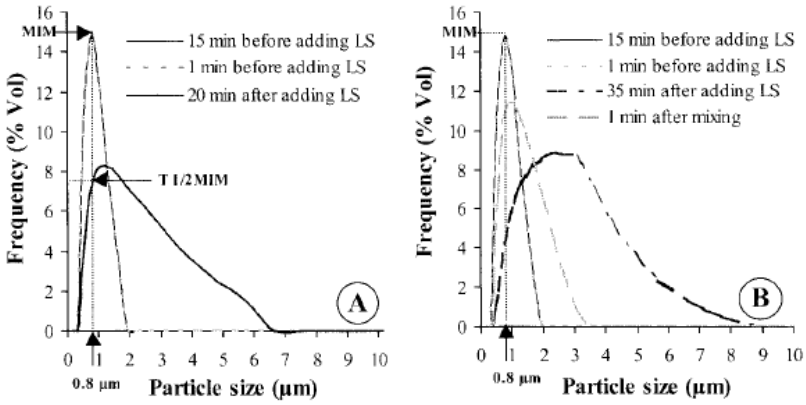

Figure 1.13 Size distribution histogram showing LS induction of rubber particle coagulation 20 minutes (**a**) and 35 minutes (**b**) after adding LS.

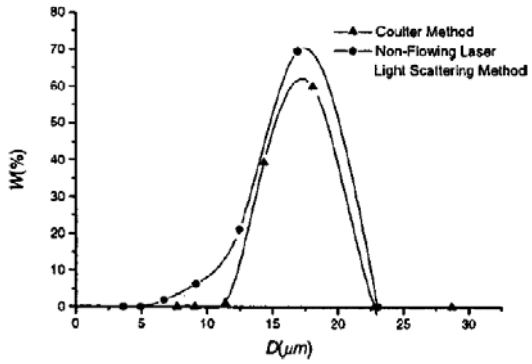

Figure 1.14 A size distribution histogram showing how a non-flowing laser diffraction method would compare for accuracy against a flowing method such as a Coulter counter or flow cytometry.

During the study, the comparison of laser diffraction with the Coulter method was compared for measurement of polystyrene latex beads in aqueous solution (fig. 1.14). One must ask the nature of particles in the system of study. A Coulter counter or flow cytometer is useful for particles in a flowing system, but non-flowing measurement approaches such as laser diffraction is more suited to study of static particles. Furthermore, Mie Theory assumes spherical particles, which is exactly the case for suspended mammalian smooth muscle, making this approach very well suited and more accurate.

1.6 THE LEICA QWIN

1.6.1 Introduction

The Leica QWin is an integrated quasi microscope/camera system that is designed to capture and quantify microscopic data. The device is composed not only of a hardware solution, but also an image analysis and processing tool compatible with Microsoft Windows. The system – comprising the sample stage, focus, lamp brightness, filter block and shutter – is completely automated and motorised, so that analysis of multiple positions of the glass slide/coverslip can be performed in a systematic fashion and customised by the user. The camera is capable of taking digital 736 x 574 pixel images at 0.83μm/pixel resolution, moving to pre-programmed fields within a sample using the motorised stage. Furthermore the Quantitative Interactive Programming System (QUIPS) software can also be setup to analyse images via a sequence of image analysis operations in a routine manner.

A diverse range of specimens maybe sampled, including: cell monolayers; plant sections and seeds; tissue sections; natural and processed food products; in-situ hybridization of stained tissue sections; protein crystals; synthetic and forensic fibres; polished and etched metals; embedded and sectioned minerals; semiconductor water defects; abrasive powders and carbon black components (fig. 1.15).

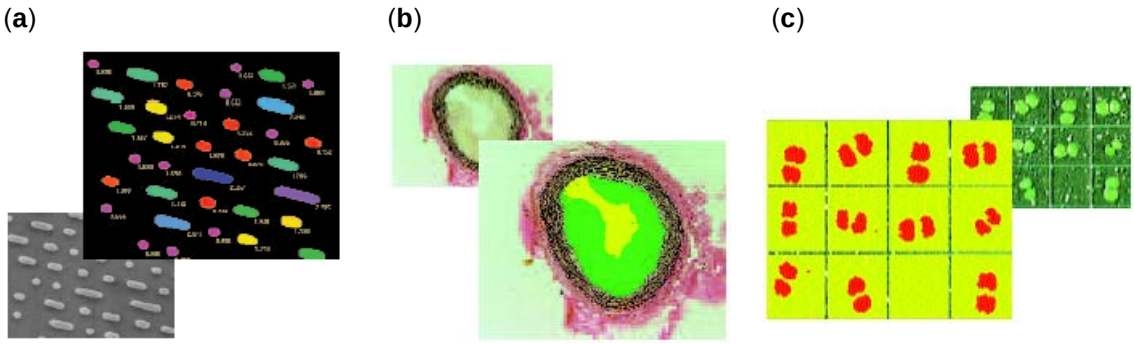

Figure 1.15 Digital images from an array of different sample materials captured on the Leica QWin system: (**a**) electronics – quality control of compact discs (CD); (**b**) artery cross-section – calculation of percentage restriction; (**c**) botany – seed germination and characteristics.

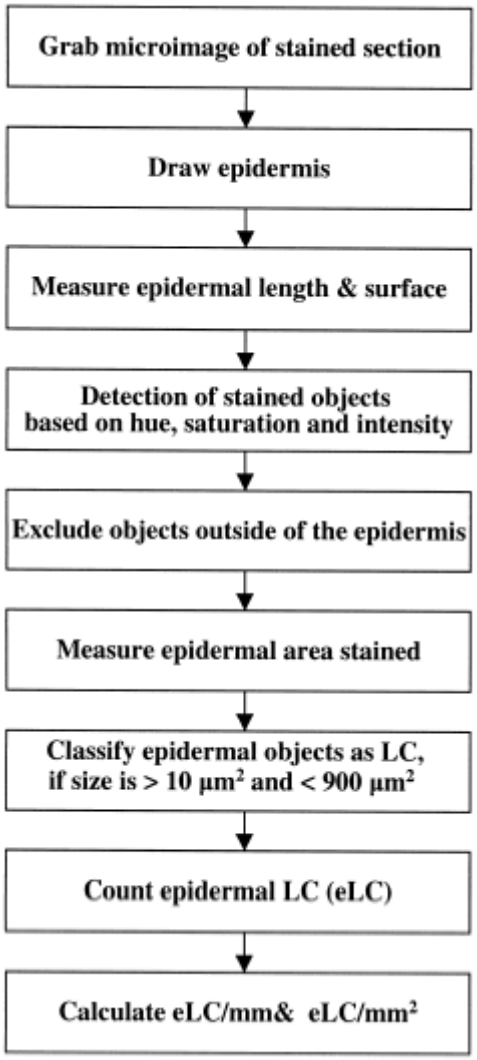

Figure 1.16 Flowsheet of Leica QWin image analysis routines

The Leica system can automatically analyse images by colour, contrast, size, number, shape, position or orientation. Selection can also be semi-automated via use of the mouse as a drawing aid. A range of illumination forms such as: incident, transmitted, polarised, Normarski, fluorescent, dark field, or interference contrast may be used. Furthermore, any digital image, imported, scanned, or negative may be taken and analysed on the Leica software making it a versatile piece of apparatus (www.leica-microsystems.com).

1.6.2 Using the Leica QWin to Measure Particles

One Dutch group has successfully utilised the Leica QWin to quantify Langerhans cells, thus reducing intra and inter-personal variations in sequential cell counts – a much-needed *in vitro* alternative to controversial vivisectional methods (Jacobs et al. 2001). Langerhans cell migration as a result of contact sensitisers is an indicator of allergic contact dermatitis – an increasing health issue in humans. When immature dendritic cells such as Langerhans cells in the epidermis come into contact with a contact allergen, they migrate to the draining lymph node and mature. Once mature, these cells stimulate the development of hapten-specific naive T-cells leading to antigen-specific sensitisation. Subsequent exposure to the allergen on the skin results in a contact dermitic response. By obtaining several human skin explants from multiple donors (n=50), staining with MGP (containing 0.5% methyl green and 0.1% pyronine) for CD1a or Lag in epidermal Langerhans cells and then analysing the 10 images using the Leica QWin (see fig. 1.16 for protocol) as-well-as manual counting (6 fields counted per biopsy) by three operators and triplicate counts for each image, a comparison between automated and manual counting was established (fig. 1.17). As can be seen, the results correlated well between methods. The study highlighted several factors of importance. Firstly, the success of manual counting was a function of staining method – aiding visualisation and contrast. The Leica QWin was

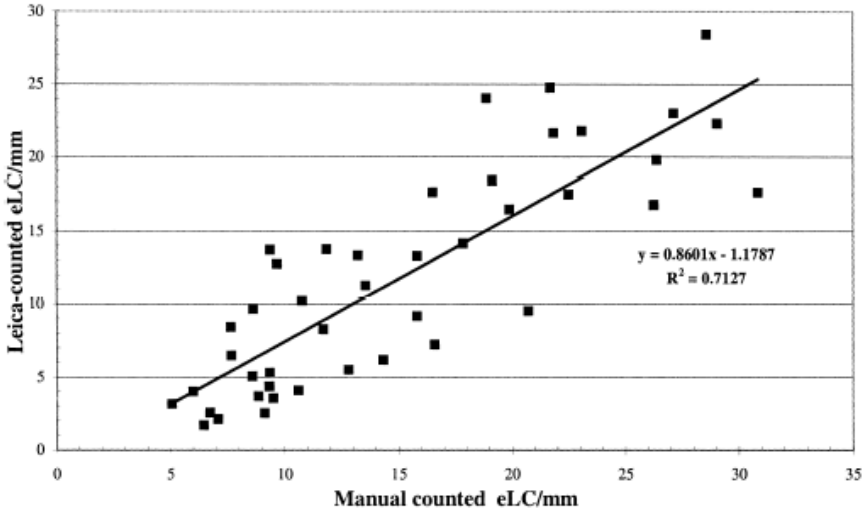

Figure 1.17 Manual vs. Leica QWin generated counts of epidermal Langerhans cells from skin explants of human donors.

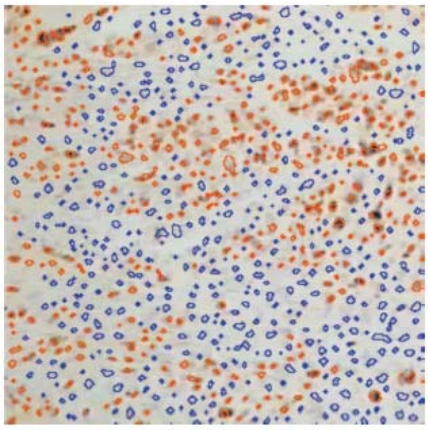

Figure 1.18 A microscopic image of histologically prepared oesophageal squamous cell carcinoma MIB-1 stained brown and then counterstained blue to show the positive and negative tumourous cells, respectively.

Table 1.1 **A comparison of quantitative (manual) versus semi-automated counting using "method A" QUIPS routine**

		Method A		
	Categories	1+	2+	3+
Quantitative counting	1+	20	1	0
	2+	4	32	0
	3+	0	6	10

reported to reduce this variability between counts and operators to a 1 and 2% variation, respectively. Secondly, distribution of Langerhans cells per biopsy and patient is not uniform and differs from field to field even from the same biopsy, i.e. the quality of the sample can influence results. Thirdly, staining intensities arising from immunohistochemistry can impact results. Even at when this effect was minimised, inter-experimental variation was 21%.

Another group have used the Leica QWin system to automate cell counting of antibody MIB-1 positively stained nuclei to aid in oesophageal cancer prognosis (Law et al. 2003). This group proved the reliability and consistency of the Leica QWin system, bringing analysis times down to 15 minutes and eliminating overlapped or missed counting by human operators. In order to achieve accurate results, counting in excess of 15,000 MIB-1 stained nuclei from a tumour sample must be carried out per case. The team histologically prepared oesophageal squamous cell carcinoma. Of the stained, 3μm thick, paraffin mounted samples brown nuclear stain was positive whereas blue nuclear stain was negative. Counting was performed in manually (by light microscope, at least 1000 nuclei counted) and semi-automated fashions (using the Leica QWin). Where operator counted brown and blue stained nuclei, the Leica QWin used RGB (red, green, blue) breakdown, primarily focusing on red and blue pigmentation to isolate and quantify positive and negative tumour cells, respectively (fig. 1.18). Manual counting was performed for 73 cases, the time for each case being approximately 30 minutes. 123 slides were analysed in total. Table 1.1 shows how the manual and Leica QWin methods compared. Both methods assessed for three categories: less than 0.40 of positive tumour cells; 0.40 to 0.70 of positive tumour cells; and over 0.70 of positive tumour cells. A strong correlation between the two methods is shown. The comparison between manual and automated counting highlighted several areas of importance. Firstly operator errors will obviously include the “inter” and “intra” variety – and for this study inter-operator error was minimised by using one operator only. Where manual counting of many nuclei are involved, there will be a degree of over and missed counting, and obviously it is very time consuming.

Also digital image capture has distinct advantages over keeping microscopic slides for future analysis – such as no need to recapture the images, no fading colour of the specimen, and therefore less errors upon re-analysing a sample.

1.6.3 The Leica QWin and Cell Encapsulation

Clearly the studies outlined in section 1.7.3 have shown that this system is compatible with biological cells and is capable of detecting and quantifying cells discriminating on colour difference. The ability to build automated routines, not just for image capture, but also image processing and analysis making the Leica QWin an invaluable tool to help automate and standardise cell quantification. However, since the technique is very much dependent on images, the quality of images i.e. staining can influence results. This point must be borne in mind when the Leica is being used.

1.7 CURRENT TISSUE ENGINEERING INDUSTRY

Tissue Engineering is a new and rapidly growing multidisciplinary industry (fig. 1.19). Its borderline status between medicines and devices has prompted the merger of the Medicines Control Agency and the Medical Devices Agency into the Medicines and Healthcare products Regulatory Agency (MHRA) in the UK in 2003. Applications include: skin patches, cartilage, bone, pancreatic, and corneal and vascular implants to date. There is as yet no procedure for market approval in many European countries including the UK. It is likely that European legislation will follow (Faulkner et al. 2003).

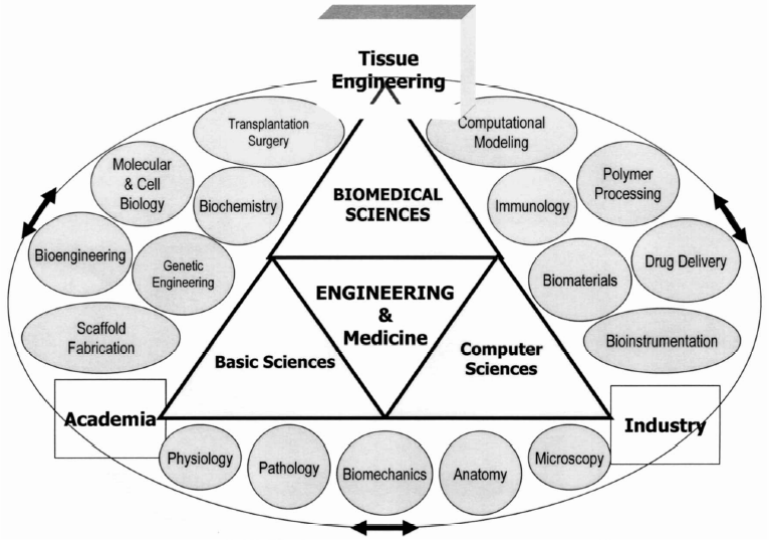

Figure 1.19 Diagram illustrating the multi-disciplinarity of tissue engineering (Pangarkar and Hutmacher 2003).

Table 1.2 Annual Organ and Tissue Deficiencies

Indication	Procedures or patients per year
Skin	4 750 000
Bone	1 340 000
Cartilage	1 150 000
Tendon and ligament repair	123 000
Blood vessels	1 360 000
Pancreas	728 000
Urological	82 000
Dental	10 000 000

(Langer and Vacanti 1993)

Table 1.3 FDA-Approved Tissue-Engineered Products

Product	*Launch*	*Description*	*2002 annual sales*
Apligraf (Organogenesis)	1998	Living skin equivalent for diabetic and venous ulcers	$23 million; 25,000 units
Carticel (Genzyme Biosurgery)	1999	Autologous chondrocytes for cartilage repair	$25 million; 2,500 units
Dermagraft (ATS)	2001	Living skin equivalent for diabetic and venous ulcers	$4.5 million 4,500 units
OrCel (Ortec)	2001	Living skin equivalent for burn patients	<$100,000

[a]*Note:* Both Organogenesis and Advanced Tissue Sciences have discontinued operations. Smith & Nephew has taken over production, marketing, and sales of Dermagraft. The future of Apligraf is unclear.

(Lysaght and Hazlehurst 2004)

Tissue Engineering is promoted by the Government, Industry and Academia and investment in this sector is heavy. It is estimated that in 2001, there were 3500 scientists in 70 companies working in this field, with a combined annual spend of $600 million (Lysaght and Reyes 2001). In 2004, accumulated investment since 1990 in Tissue Engineering exceeds $4.5 billion and investment is still growing by 22.5% annually (Langer and Vacanti 1999). This seems sound since organ replacement therapies prolong the life of 20 million patients worldwide (see table 1.2). In the US, it is estimated that 20% of people reaching 65 will receive organ-replacement therapy during their remaining life span. Worldwide, organ-replacement therapy accounts for 8% of medical spending or $350 billion annually (Lysaght and O'Loughlin 2000).

Despite the positive investment and drive from all stakeholders commercialisation of the products seems the largest barrier (Nerem 2000). Of the four pioneering Tissue Engineering firms with FDA approved products: Organogenesis has filed for bankruptcy; Advanced Tissue Sciences has been taken over by Smith and Nephew; Ortec is operating under a “going financial concern warning”; and Genzyme has downsized and been assimilated into a larger division of its parent company (table 1.3). The problem seems to be a combination of several factors: disappointing initial sales due to limited targeted market; lack of engineering and automation to produce low cost products; high regulatory costs and approval processes creating financial strain; lack of experience by start-up companies; and lack of end-user support acceptance (Bouchie 2002; Lysaght and Hazlehurst 2004). Regulatory factors cannot be controlled, but in order for a product to be successful, a well-engineered process is essential if market approval is to be achieved.

1.8 VALIDATION, QC AND GMP

Process validation is establishing documented evidence, which provides a high degree of assurance that a specific process will consistently produce a product meeting its pre-determined specifications and quality characteristics.

Under the current Good Manufacturing Practices (GMP) Regulations for Finished Pharmaceuticals, 21 CFR Parts 210 and 211 and the Good Manufacturing Practice Regulations for Medical Devices, 21 CFR Part 820, it is a legal requirement to be able to validate a process before mass producing a pharmaceutical or medical device. Our process could potentially create a tissue-engineered organ that is implanted into the human body. Although it should be classed as a medical device we must also address the stringent issues associated with an ingested pharmaceutical since it is not inert.

In order to validate our tube-forming device, we must show:

- Quality of parts and materials
- Adequate product and process design
- Control of the process
- In process and end-product testing – destructive, variations of product on safety and effectiveness

Clinical/pharmaceutical grade materials and well-documented research helps towards assurance of quality. All variables must be controllable to within a margin of error. Since there are no mass-produced blood vessels on the market, which variables will be monitored and the FDA-governed margin of acceptable error for TE products remains to be seen in the future. Certain processes of the blood vessel manufacture relies upon lab techniques, and it is essential that biochemical engineering principles are incorporated at an early stage to ensure adequate scale up/out with control of process variables. Pier reviewed research papers will contribute towards proof of principle for the device. End product testing may not be essential (although pre-clinical studies will be necessary) if we can monitor product development *in vitro* and ensure safety. That is:

- Quality, safety and effectiveness must be inbuilt in the product
- Quality cannot be inspected or tested into the finished product
- Each step must be controlled in the manufacturing process to maximise probability finished product meets all quality and design specifications

These are quality assurance (QA) steps. QA ensures products are fit for intended use. It is through careful design and validation of both the process and process controls that a manufacturer can establish a high degree of confidence that all manufactured units from successive lots will be acceptable. Successfully validating a process may reduce the dependence upon intensive in-process and finished product testing. The latter plays a huge part in QA. Where in-process or finished product testing cannot adequately measure certain attributes, process validation should be derived primarily from qualification of each system used in production and from consideration or the interaction of the various systems. Validation and end product testing are not mutually exclusive.

It is Good Laboratory Practice (GLP) to establish protocols for all procedures. These will enable rapid construction of the written validation protocol that specifies the procedures (and tests) to be conducted and the data to be collected. Data collection must be accurate with a good measure of variability between successive runs. From these should be established upper and lower limits (worst case or most appropriate challenge conditions) within which the product will not fail. Documentation should also include evidence of suitability of materials and reliability of equipment and systems.

Key process variables should be monitored and documented, including any process changes to help pinpoint process problems. Analysis of data collected from monitoring will determine variability of process parameters for individual runs and will establish whether or not the equipment and process controls are adequate to assure that product specifications are met. This may include: component specification, air and water handling systems, environmental controls, equipment functions, and process control operations (FDA 1993).

In order for an engineered vessel to satisfy requirements as a clinically useful conduit, histological, ultrastructural, biochemical, immunocytochemical, pharmacological, mechanical and *in vivo* analyses must be performed. Histological and ultrastructural analyses reveal information regarding extracellular matrix (ECM) proteins. Biochemical analyses, includes assays that quantify cellular DNA and collagen content, so that the properties of native and engineered tissues may be compared. Immunocytochemical staining for SM α-actin, calponin, and myosin will determine the differentiation state of smooth muscle cells (SMC) present. Information regarding SMC hyperplasia, by staining for proliferating cell nuclear antigen (PCNA), may also be obtained and subsequent risk to luminal occlusion upon implantation. Pharmacological testing will test SMC response to vasoconstrictive and vasodilatory agents. Endothelial cells may also be tested for platelet endothelial cell adhesion molecule (PECAM) for identity, or thrombomodulin/prostacyclin for prothrombotic state. Mechanical testing assesses the graft's ability to withstand long-term exposure to physiological pressures and forces, such as stress-strain analysis to determine the elastic modulus and compliance data and suture retention strength (Atala and Lanza 2002).

Other product variables that may require justification include sterility, purity from animal products and toxic entities, homogeneity of material, and wall thickness. It is likely that since our product is a bioactive tissue for implantation, that most validation parameters will be control of biological pathways. Sampling will play a large part in process validation, in our case, the sterile sampling of dissolved oxygen tension (DOT)/CO_2, glucose/lactate, pH and temperature levels. Protocols for sterilisation are also a key variable. However for our process, most parts will be disposable to ensure sterility is maintained.

1.9 RESEARCH QUESTIONS

The literature shows us the properties of working with an alginate system, commercially available in powdered or liquid form as sodium alginate, this can quickly be solidified into any shape using a wide array of multivalent cations, each offering a way of controlling reaction speed. Such structures have the added benefit of resolubilisation upon high concentration of monovalent ions. Alginate has a rich literature in pharmaceutical research, due to availability, price, biocompatibility and non-toxicity.

The porosity of solidified structures allows nutrient exchange as long as wall thickness/diameter of structures are controlled. The hydrophilicity of alginate means that cells will cluster together as aggregates when the two are introduced together, historically to encapsulate cells in a protective material for transplantation in a non-immunosuppressed host. This could be both beneficial or detrimental depending on the object of the structure being created. When cells aggregate, they proliferate and mature to become tissues and eventually organs. Where single cells are required, i.e. where matured cells are encapsulated to produce protein for the host, aggregation may mean cell death in the centre of large cell aggregates that have been cut off from supply of nutrients (Sen et al. 2002). In the latter case aggregation is not desirable and a homogeneous distribution of cells is more appropriate.

Clearly cell encapsulation is highly researched area due to the benefits of immuno-shielding of allogenic or xenogenic cells from a host, especially useful for cell therapy purposes when the host is unable to produce a protein, e.g. in diabetes. And this can be achieved either by lining a sheet of alginate or embedding the cells within the structure's walls. Such alginate structures could also extend to becoming a matrix or scaffold for tissue engineering purposes, rarely seen to involve alginate despite its many beneficial properties.

The research with respect to cell/alginate interaction and clinical effectiveness upon transplantation is extensive. However, it seems that despite the promise of this technology, there are few well-engineered processes able to reproducibly create structures with a degree of geometrical

control. If such a fabrication device could be developed, then scaleup or scale-out of this technology would ensure a mass production capable possibility and subsequent FDA approval for therapeutic use. Serp's work was one of many well-developed processes for the creation of beads using vibration frequency to control droplet break-up, but the other useful structure for macro-encapsulation purposes – a tube – has seen less success. No publications to date exists, the results of the two groups outlined were work in progress.

A well-engineered process would not just involve creation of a well-formed tube, but also the monitoring methods to accompany it. A technique such as OCT could firstly help qualify the quality of alginate structures produced, and secondly form an integral part of the process monitoring quality of subsequent mass-produced tubes. The non-destructive ability of OCT to analyse samples in real time through air make it an ideal tool for monitoring walls of semi-transparent macro-encapsulation structures upto a thickness of 2-3mm. Furthermore the resolution of such a device gives it the ability to capture information on a cellular level. Techniques such as laser diffraction, proven to be just as accurate yet more versatile than a Coulter Counter or flow cytometry, could be useful to qualify the types of cells used, presence of any cellular aggregates, or the size of cell-encapsulated beads formed. The use of Mie Theory based on the equivalent spherical particle makes laser diffraction all the more suited to mammalian cells, which are spherical when in suspension. Finally the Leica QWin is another tool that could be exploited to automate cell counting, eliminating inter and intra-operator error and help control cell quantification. The QUIPS software aspect makes it all the more suited to other digital image capture techniques such as OCT, and brings current technology to this well-engineered process, ensuring no loss of information when viewing past analysed samples.

Thus it is the aim of this thesis to address the engineering design involved in a creating a cell-populated tube. Clearly there are many end uses of such a tube, and therefore specifics (such as cell type and alginate properties) will be left open to future development. Cell-alginate literature is abundant, and therefore it is not the intention of this research to add to this

work. Moreover the intention here is to focus on a well-designed process that could create a tube of alginate – an alginate shape lacking publications in the current literature. It is also the intention to create a system capable of scaleup, working towards FDA approval. Such research will focus in three areas. Firstly, reproducibility of tubes formed based on geometrical control – primarily wall thickness due to the direct relationship between wall thickness and nutrient availability to encapsulated cells. Secondly, monitoring methods to qualify the quality of the system and its components, offering a means of real-time monitoring and QA of cellular components in a final working system. As part of this second focus: cells naturally aggregate in alginate structures, therefore we look at creating a homogeneously distributed single cell population to ensure even growth on cell-embedded structures, thus lending to the versatility of this research. Rat aortic mammalian smooth muscle cells will be used as a model, although characterisation of such cells are deemed unnecessary due to the adaptable end use of such tubes. We will also look at placing controls on mammalian cell control using automation methods. Thirdly and finally, we look at integrating the alginate tube forming, the monitoring methods and the homogeneous cell suspension together and look at alginate and processing impacts on biological cell viability, cellular effect to wall thickness consistency, and spatial distribution of single biological cells within the alginate walls.

To be specific, we can expand on each of these points – <u>how can we reproducibly create well-engineered cell-populated tubes?</u> – This question could be broken down into: what is the current status of the tube forming technology at UCL?; is the design of the current fabrication design the most effective?; is there any mathematical Theory that supports wall thickness?; what is the current protocol and how can it be improved?; what needs to be developed to make it work?; how can we measure wall thickness?; how can this be improved?

<u>How do we ensure quality of the system and the tubes formed?</u> When we explore this question exhaustively, one might ask: how do we monitor tubes non-destructively?; which variables should we monitor to ensure QA?;

what methods are there available to collect this information?; what controls should we use?; how can we prove we have controlled all the variables?

So how do we effectively mix cells with polymer?: what are the common ways of mixing cells?; are there more appropriate, more effective ways of mixing?; what are the important variables to consider when mixing cells?; what are the effects of mixing cells using different ways on cell viability?; can we prove that we can control or optimise conditions such that viability is not compromised?; what are the important variables of tube formation?; how do cells impact these important controlled variables during formation?; how can we control or minimise this impact?; how can we monitor it?

2 Operations, Materials And Methods

2.1 OPERATIONS

2.1.1 THE UCL TUBE-FORMING DEVICE

2.1.1.1 Evolution of the Base Unit

The experimental chapters will make references to the “mark 1” and “mark 2” tube-forming device. It is therefore important to understand the subtle differences between the two. At the heart of the device is a twin-port plastic base unit, which brings the side port for the matrix fluid, and the base port for the propelling fluid together. The difference between the two is solely a change of the base unit design – specifically the injector nozzle design. The mark 1 base unit (fig. 2.1, 2.3*a*) consists of a 6.5mm tall, cylindrical injector nozzle of 1.8mm diameter; and the mark 2 base unit (fig. 2.2) is comprised of a 2.9mm tall, flanged injector nozzle of 1.8mm diameter at the base expanding to 3.6mm at the crown. The mark 1 base unit were used in experimental sections 3.2.1, 3.2.2, and 4.1.1 only. All other experiments involving the tube-forming device were performed using design mark 2.

The reasons behind this change are: firstly because the tip of the injector nozzle doubles as a seat for the spherical regulator at the start of tube formation; and secondly we are able to reduce dead space within the device from 112μl to 89μl, which means less volume of primer is needed – a critical factor should the matrix fluid consist of expensive or scarce materials. It was observed that a tighter fit around the spherical regulator was required to prevent seepage of air bubbles into the propelling fluid during tube formation. These bubbles disrupted the successful formation of a tube, and its quality was also questionable. It was theorised that the flanged design also offered greater

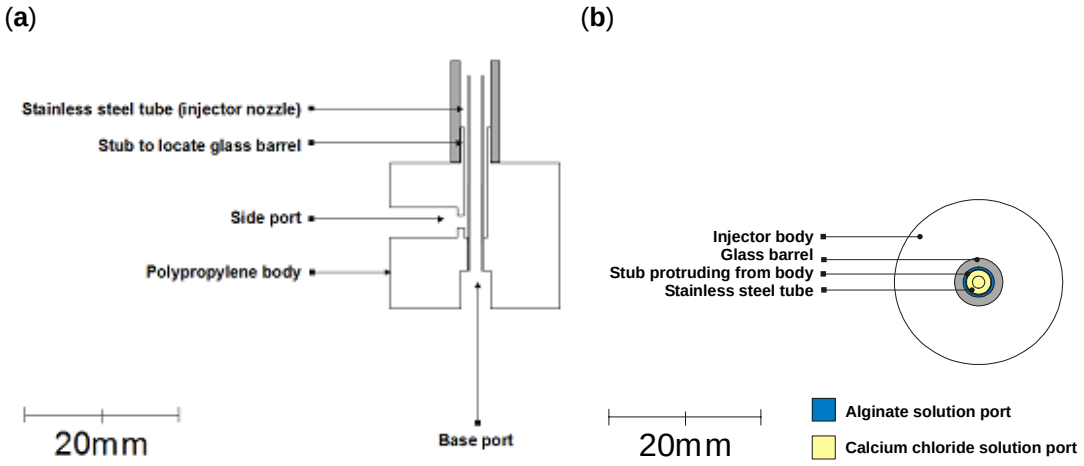

Figure 2.1 The heart of the **Mark 1** tube-forming device – the "base unit" - cross-sectioned: (**a**) longitudinally; and (**b**) laterally.

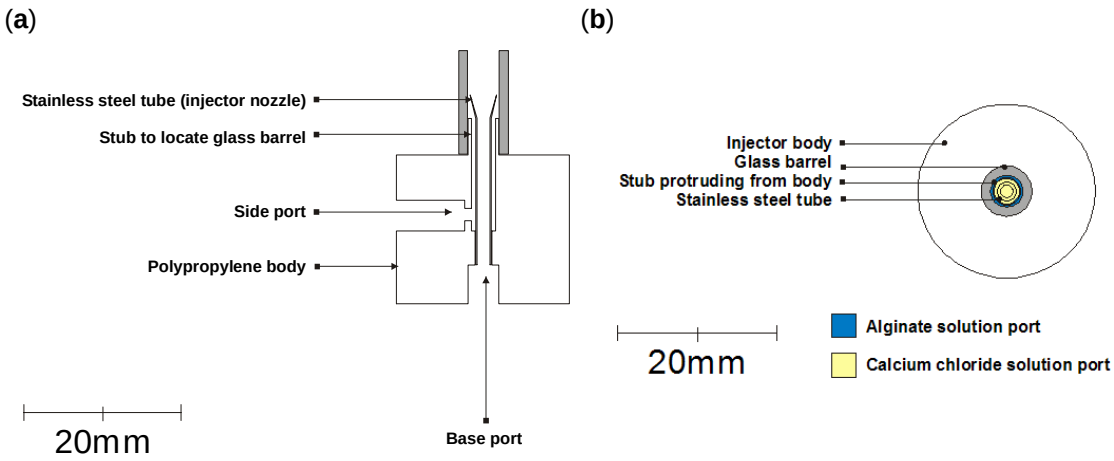

Figure 2.2 The heart of the **Mark 2** tube-forming device – the "base unit" - cross-sectioned: (**a**) longitudinally; and (**b**) laterally.

stability to the lift-off of the regulator from the injector nozzle forming a tube where the first ~7cm were of greater quality.

2.1.1.2 Tube-Forming Device Design

The basic design for the device used in this thesis has been described by Mason & Town (Mason and Town 2002). The borosilicate precision-bore glass barrel (Glass Precision Engineering, Bedfordshire, UK) is mounted on the plastic base unit, with dual injector ports (fig. 2.3*b*). A smaller cylindrical stub allows tight attachment of the glass barrel. At the base of the glass barrel and protruding from the plastic base unit sits a metal collar or injector nozzle upon which rests the plastic spherical regulator. The dual injector base unit sits on a 100ml glass syringe (Samco, CA) lubricated with silicon grease (ICI, Cheshire, UK) that is steadily driven by a modified syringe driver (Harvard Apparatus, UK). 1.825 and 2.000mm glass barrels are used in conjunction with 1.587mm and 1.700mm radii plastic spheres (table 2.1) used as regulators to extrude alginate tubes creating 3 different gap widths.

2.1.1.3 Operating the Device

Firstly the device is assembled (fig. 2.4*a*). The base unit is attached to a well-lubricated glass syringe filled with $CaCl_2$. The 1ml syringe (and later the static mixer) containing matrix fluid is attached to the side port. The spherical regulator is dropped into place on top of the injector nozzle and the dead space is primed with propelling fluid. A finite volume (300μl - 1000μl) of matrix fluid is introduced via a side port into the glass barrel, which surrounds and rests above the regulator (fig. 2.4*b*). Propelling fluid travels through the polypropylene base via the base port and is expelled via the injector nozzle into the glass barrel. A

(**a**) (**b**)

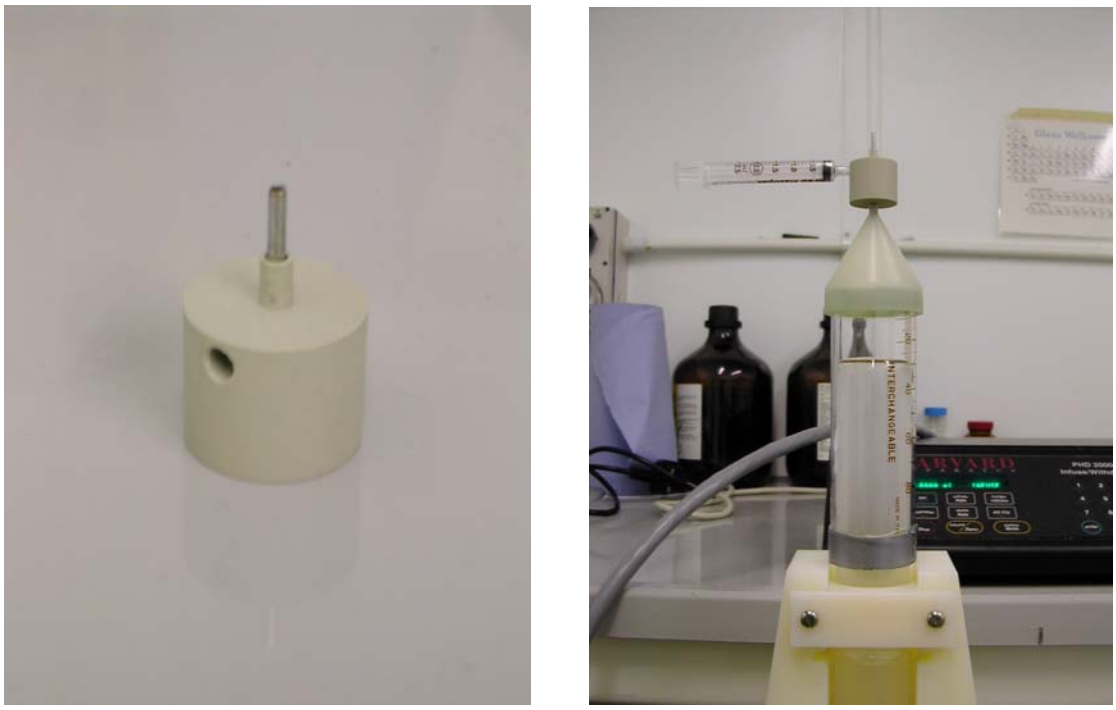

Figure 2.3 Digital photographs of (**a**) the Mark 1 design plastic twin-port base unit, and (**b**) the setup of the glass barrel fitted with the Mark 1 base unit, with a 1ml glass syringe attached to the side port (matrix fluid) and a 100ml glass syringe attached to the base port (propelling fluid).

Table 2.1 **Matrix of wall gap configurations 'δ_0', showing the wall gaps and nominal for different sized glass cylinders and spherical regulators**

Cylinder Radius, a (mm)	1.825	2.000	2.000
Regulator Sphere Radius, r_0 (mm)	1.587	1.700	1.587
Gap Width, δ_0 (μm)	238	300	413

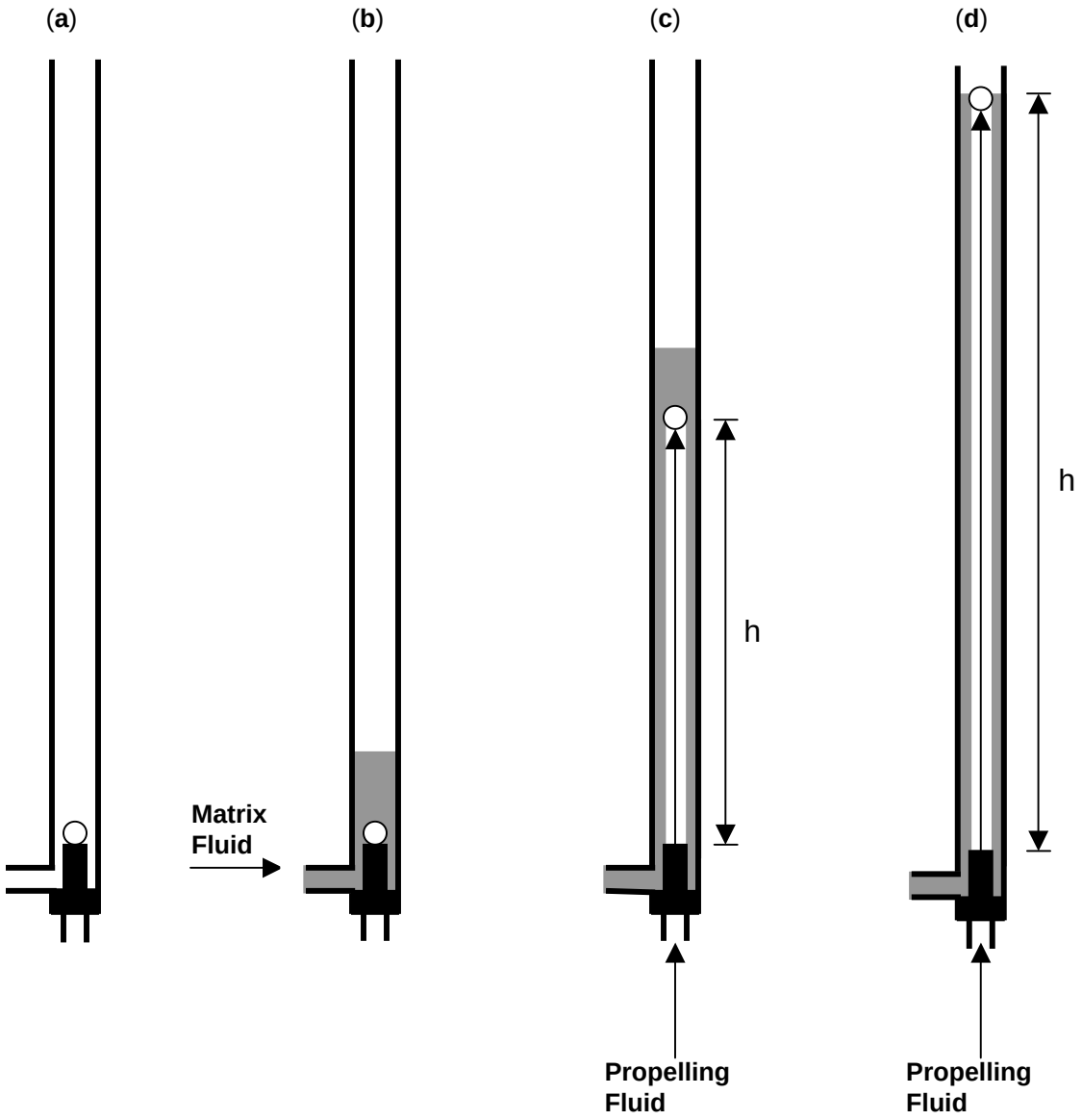

Figure 2.4 Schematic to illustrate setup procedure of the tube-forming device.

- **(a)** Device assembly.
- **(b)** The matrix fluid is loaded using the side port.
- **(c)** The propelling fluid is injected from the base port.
- **(d)** The tube length calculated as the length when the regulator sphere penetrates the meniscus of the alginate.

regulator that would sit on the injector nozzle is thus pushed up the glass barrel. This propelling fluid pushes the regulator through the matrix fluid, which drags the matrix fluid up the inner walls of the glass barrel (fig. 2.4*c*), and wall thickness is determined by the regulator and cylinder size. The syringe driver is stopped at the point the spherical regulator breaks through the meniscus of the matrix fluid.

The two fluids are then left in contact with each other. A suitable choice of fluids would cause the deposited layer to solidify. After approx. 10 mins, the deposited fluid on the wall of the cylinder would have formed a patent, cross-linked tube (fig. 2.4*d*). Cells could be premixed with the matrix fluid to produce a hydrogel tube containing embedded cells, or cells could be incubated with the tube post tube-formation to line the surface with cells.

Using sodium alginate as the matrix fluid and a propelling fluid containing divalent cations, such as $CaCl_2$, the tubular structure would cross-link and solidify. The device was specifically designed to produce patent, cross-linked alginate tubes.

High G alginates at high concentrations are required to produce viable tubes that can be easily delivered from the glass barrel. To improve visualisation, small quantities of glycerol based food colouring (Supercook Leeds, UK) were added to the alginate solution. All components must also be pre-washed in 4M sodium citrate solution and dried using compressed air prior to commencement of a study. The sodium citrate solution contains excess monovalent ions that replace the calcium ions and revert the hydrogel back to an aqueous form.

At one time the tube-forming device was manually powered, but by the time of this thesis, the device was already adapted to automated-fluid-drive, to maintain reproducible results with respect to wall thickness. Control of timing, rate and volume of cross-linking agent was essential.

Overall wall thickness is not only a result of regulator and barrel diameters, but also alginate shrinkage and swelling due to cross-linking time (Saitoh et al. 2000). Irregularities due to inconsistent regulator travel are usually

due to calcium chloride “escape” from the central stainless steel barrel to the bulk alginate fluid. Air bubbles, imperfect regulators and poor alignment are also causes.

Thorough mixing for extended periods of time using a roller bottle mixer ensured alginate homogeneity. Elimination of trapped air bubbles was achieved using sound technique i.e. good handling of the syringes used both to inject calcium chloride and alginate. Precise machining of the polypropylene base, glass barrels and regulators ensure perfect alignment. Frequent assembly/ disassembly of the cylindrical stub that secures the glass barrel causes wear and tear and hence cylinder base material is an important consideration. Rigorous cleaning of the device between runs was also absolutely essential.

The syringe driver is a Harvard Apparatus PHD2000 lead screw system. It is capable of driving two syringes in parallel (ranging from 0.5 μl to 140 ml), which can be coupled with a T-piece. Its infusion rate can be set ranging from 0.0001 μl/hr to 13.2 L/hr. Its accuracy is claimed to be ±0.1%.

Perspex and stainless steel were used for the coupling between the syringe and the device, in order to prevent wall distortion. Luer lock fittings were used throughout. Straight couplings over 2-3cm, length seemed better possibly due to turbulent/laminar regimes. The stainless steel injector was machined such that the regulator sits upon it with minimum friction.

2.1.2 The Malvern Particle Sizer

The particle sizer is a laser-based technique, which involves the beam shining through a metal block containing a sight-glass on front and back (fig. 2.5*a*). Within the block lies a small plastic impeller that is agitated via a magnetic rotor. This impeller keeps particles suspended. As particles pass through the beam, the size information is captured, and this is used to formulate a particle size distribution.

The model used was a Malvern 3600Ec. Operation is very simple: the metal sampling block must first be cleaned using saline, and then filled with 10ml of sampling fluid. For our experiments involving cells, sampling fluid would be complete medium. The impeller would then be dropped into the metal block. This would then be clamped into place within the particle sizer, slid to the end and the lever pulled to lock (fig. 2.5*b*). The laser is then adjusted to shine through the sight-glasses. Cover on the detector is removed. Then following instructions on the PC unit, the sample is first zeroed, and then the sampling can commence. The first time this experiment was carried out, the exact concentration of cells needed was not clear, therefore concentrated cell suspension was pipetted into the sampling block 200μl at a time until detection was within parameters. Range was found to lie between $1x10^5$ and $2x10^6$ cells/ml concentration. At the end of each sampling session, results must be printed.

2.1.3 The Leica QWin

The Leica QWin is a microscopic technique. It is composed of an advanced digital microscope that is connected to a computer system (fig. 2.6). The mechanised sampling base upon which the glass slide sits can be set to measure pin-pointed locations of the sample – termed “fields”. All images can be saved directly to the computer and the software package provided by Leica is a powerful tool, which can enhance images and analyse using a vast array of techniques.

The model used was the Leica Q5501W. Physical setup involved taking a glass slide and placing ~17.5μl of sample under the coverslip with or without staining to enhance the image (Trypan Blue stain was used in experiments).

(**a**) (**b**)

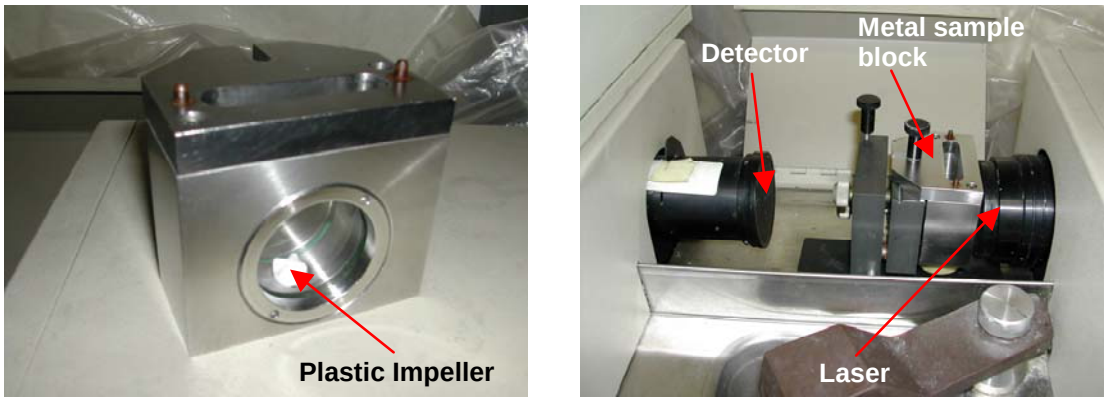

Figure 2.5 Digital photographs taken of the Malvern Particle Sizer 3600Ec. (**a**) Metal sampling block with sight-glass. (**b**) Shows the laser, detector and sampling block setup.

Figure 2.6 Digital photograph taken of the Leica QWin

Focusing was achieved at 1-1.5cm between lens and glass slide. Magnification was set at 10 x 0.30 Ph1. Stage was set to take 4 fields in a square pattern (fig. 2.7) 1cm^2 between fields.

On screen calibration of local sample (Measure → Calibration) was performed. Feature frame was set to x:0, y:0 (Measure → Frames), width = 500μm, height = 500μm, i.e. 2.5μm^2. Resolution was set to 1μm = 1 pixel. QUIPS software protocol was as follows:

1. Acquire button.
2. Image → Image Transform → Fill White → B Sharpen
3. Detect → Change band for black cells and blue background
   Check adjust (black) radio button
4. Measure Feature → Flags checkbox
5. Stage
6. Repeat x4

Results can then be saved as jpeg/gif files to a folder on the computer.

2.1.4 The NAC High Speed Camera

The NAC high speed, high-resolution camera was an additional experiment made when it was learned that the camera was in the department, on loan from the EPSRC. The model of the camera was an NAC HSV-500C3 and came complete with a digital recording unit (fig. 2.8*a*) with wired remote, a tripod, twin halogen lighting lamps, a GXMZ MonoZoom 7 microscopic lens (fig. 2.8*b*) with x0.5 and x0.75 CCD magnification (giving an overall magnification of x40), adapter/stepping rings, an additional Sony VCR SLV-SE230, a Panasonic 14” BT-H1490Y monitor, and a Viglin Genie Pentium 4 Computer with National

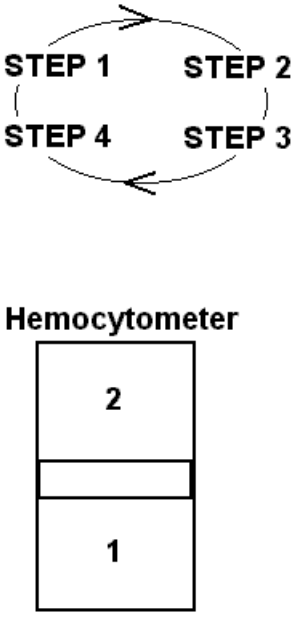

Figure 2.7 Mechanised stage setup for the Leica QWin.

(**a**) (**b**)

Figure 2.8 Digital photographs taken of (**a**) the digital recording unit, and (**b**) the NAC HSV-500C3 camera with GXMZ MonoZoom 7 microscopic lens.

Instruments LabVIEW software AVI file reader/writer and VirtualDub 1.5.2 for editing AVI files. The camera features high light sensitivity, making it ideal for low-light environments.

Operation involved firstly setting up the equipment – the Sony VCR was used as a backup source to record digital images (which could in-turn be transferred to the PC) onto VCR. Frame-rate was set to maximum of 500 frames/second (125, 250 & 500fps options). Shutter open to 1/10000 sec. The lens would be focussed manually. The experiment could then run. The wired remote could then be used to record, stop, play, FF or rewind just like any conventional recording equipment. The images could then be transferred to the PC via LabVIEW (record whilst playing back on NAC HSV-500) and edited using VirtualDub.

2.1.5 The Static Mixer

A further adaptation was made to the device during this thesis allowing the integration of cells into the tubes. Current research standard protocols for mixing cells with polymer to enable cell bead encapsulation involve hand mixing. This is irreproducible, subjective and clearly not the way to engineer a good process.

However, traditional chemical engineering methods of mixing become increasingly inefficient approaching smaller scale. At the micro-scale, mixing is generally accomplished in the industry via diffusion only. Static mixing is a viable alternative approach. The static mixer has no moving parts, and accomplished mixing via the natural flow of fluids through the mixing elements. We used one of the two types of static mixer generally available from Kenics (TAH, Northamptonshire, UK) (fig. 2.9), which contains helical shaped elements that separate, twist and folds the fluids to achieve mixing (Bertsch et al. 2001). This can achieve cellular level mixing by 10 static mixing elements (fig. 2.10).

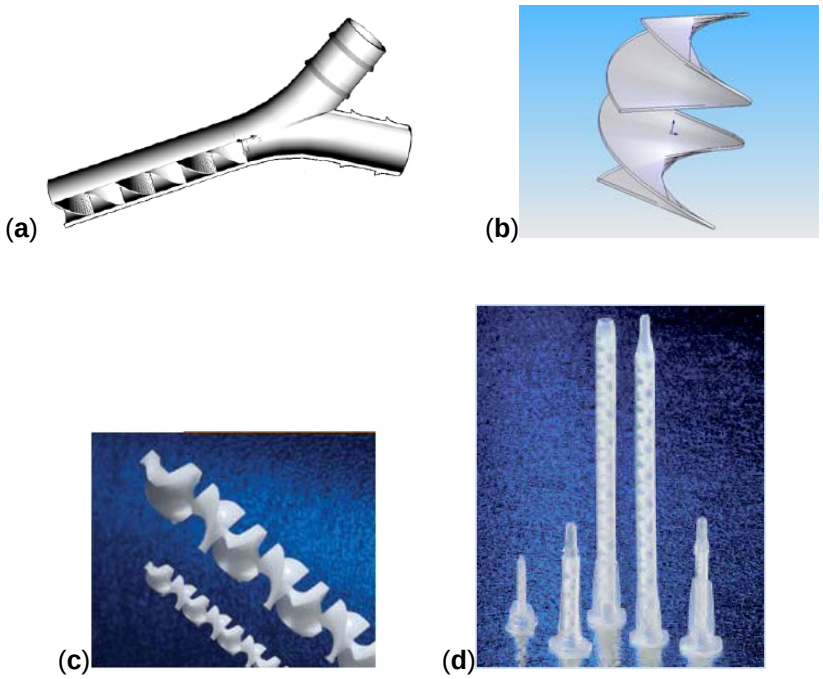

Figure 2.9 (**a**) Cut-out view of the micrometer structures/connector obtained by a CAD step with AutoCAD 2000 for a micromixer made of helical elements (Bertsch et al. 2001). (**b**) Reconstruction of Kenix design static mixing elements drawn using SolidWorks 2004. (**c**) Digital photographs taken of Kenics design static micro-mixer elements, and (**d**) the entire micro-mixer assembled (www.tah.com).

(**a**) (**b**)

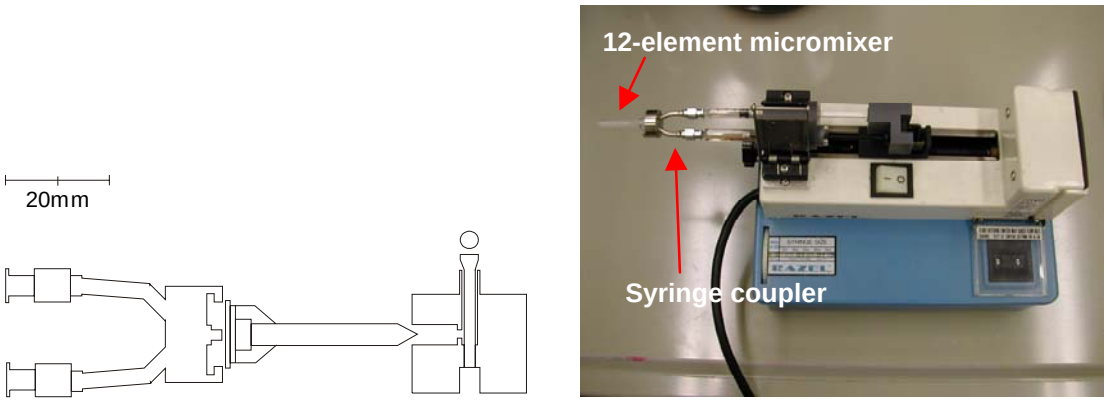

Figure 2.10 (**a**) Cross-sectional representation of static mixer setup (syringe coupler, static micro-mixer and plastic dual-port base unit), and (**b**) a digital photograph taken of the static mixer driver complete with twin syringes, syringe coupler and 12-element Kenics static micro-mixer.

Table 2.2 Series 190 Spiral Bayonet Mixer Specifications

SERIES 190 SPIRAL BAYONET MIXERS					
PART NO.	MIXING ELEMENTS	ELEMENT DIA. (INCH / MM)	ELEMENT LENGTH (INCH / CM)	HOUSING OUTLET	RETAINED VOLUME (ML)
190-208	8	0.093 / 2.36	1.1 / 2.8	Slip Luer	0.07
190-212	12	0.093 / 2.36	1.5 / 3.8	Slip Luer	0.10

There are several advantages of this technology. Firstly each static mixer is a one off disposable piece of plastic, fitting well to the aseptic requirements we require for a tissue-engineered implant. Secondly, it functions in laminar flow, so there is negligible shear damage. Thirdly the elements are cheap making it perfect for one-use applications.

Series 190 disposable spiral bayonet dental mixers were used throughout experiments. Referred throughout this thesis as 8-element (part no. 190-208) and 12-element (part no. 190-212), both came with luer-lock fittings so that they easily adapted to our process (table 2.2). These were purchased in bulk and disposed of after each use. They were adapted to a specially made syringe coupler and used in conjunction with a Razel Scientific Instruments Inc. A-99 Syringe Pump (Razel Scientific Instruments Inc., St Albans CT, USA) always set at 1.8ml/min flowrate (highest setting). This could then be coupled to the side injection port of the tube-forming device (Mason and Town 2002) to integrate cells into alginate tubes.

Operation of the static mixer assembly was as follows: fill disposable syringe with alginate and precision glass syringe with cell suspension; assemble all parts together; at 1.8 ml/min setting infuse through to prime the static micro-mixer; stop when all air bubbles are expelled; run experiment.

2.1.6 The Gauva EasyCyte Mini Capillary Cytometer

The Gauva EasyCyte GR1 is a flow cytometer equipped with a 480nm blue laser. The device can detect forward and side scatter with 3 channels for fluorescence. The package also includes a laptop PC loaded with CytoSoft 3.1.2 modular software, which acts as the control unit. As well as standard functions such as maintenance and basic operations, optional modules can be added for specific assays such as cell cycle analyses, cell tracking, mitochondrial potential and caspase activity measurements, TUNEL and Annexin V staining (www. guavatechnologies.com).

Analysis utilises 96 microwell plates, with a cell concentration range of $1x10^4$ – $5x10^5$ cells/ml giving a sampling intensity of 2000-5000 events. Gauva Viacount Flex reagent and standard protocol was used for cell enumeration and Gauva Nexin and standard protocol was followed for apoptosis studies. All other analysis stages, e.g. configuration, microwell plate mixing, etc. are automated and easy to execute on the CytoSoft system.

2.1.7 The Brookfield Viscometer

The Brookfield DV-II+ Pro is a rheometer with a speed capability of 0.01-200rpm. The device has a built-in temperature probe and by varying torque to the sample place on the spindle (via range of spindle speeds), the sample's viscosity characteristics can be measured, recorded, and printed. The rheometer was used alongside a Watson Marlow Pump 503U and Grant Y22 water bath to measure sample alginate at varying temperatures. Operating procedure was as follows:

1. Check viscometer alignment (via the sight bubble)
2. Remove and wash spindle, eliminating any trapped air
3. Turn on pump and wait for temperature to equilibrate
4. Set % torque between 10-90/100
5. Rotate bezel to lie between C840 and CP42
6. Select: Display → Set Speed → Options → Setup → Custom Speeds → (de-select unwanted speeds using "Set Speed" to select)
7. Motor Off → Options → Setup → Custom Speeds → 1.1
8. Spread sample on spindle, reattach and run device.

2.2 MATERIALS

2.2.1 Reagents

0.9% wt/vol saline was prepared from water for injection, WFI (Sigma, Dorset, UK) and NaCl (Sigma, Dorset, UK) and buffered to pH 7.3-7.4 – using NaOH 1.0N (Sigma, Dorset, UK) diluted to 0.1N. This was then used to prepare 0.50, 0.75 and 1.00% alginate solution from Manugel DB (ISP Alginates, Strathclyde, UK) on a roller mixer (Stuart Scientific, Surrey, UK). The mixture was covered using aluminium (light free) and kept at room temperature. For all alginate experiments, solutions were used same day as preparation. Alginate was sterilised by autoclaving at 121°C for 20 minutes.

0.9% wt/vol saline was used to prepare 0.09M $CaCl_2$ (Sigma, Dorset, UK), and 0.05M $BaCl_2$ (Sigma, Dorset, UK). Saline and WFI were used as infusion agents in certain experiments to look at infusing without cross-linking effects.

54% glycerol (VWR, Poole, UK) was diluted using WFI, coloured with food colouring and used as the matrix fluid to verify the Theory for a homogeneous case of Newtonian fluids. It was also used as the propelling fluid without colouring.

For visualisation enhancement purposes in all tube forming experiments except those testing cellular viability, small quantities of glycerol based food colouring (Supercook Leeds, UK) were added to the alginate solution containing cells, and 3-10µm glass beads (Polysciences Inc., PA 18976 USA) were added to model cells and provide light scatter in pure alginate solutions.

2.2.2 Infused Fluids

Alginate concentrations ranged from 0.5 – 1.0% w/v, but defaults were fixed at 1.0% with temperature controlled at 10°C by controlling lab temperature, although temperature effect was explored using lab temperature of ~20°C. Temperature and pH are said to be important factors affecting viability (Gao et al. 2005), but pH is carefully monitored when making up N-Saline and lab temperature held constant by thermostat.

Viscosities were measured using a viscometer (Brookfield Engineering Laboratories Inc., MA) and a water bath (Grant, Cambridge, UK) to vary water temperature. Alginate has a viscosity of 6.71g/cm.s and a density of 1.01g/cm^3. WFI has a viscosity of 0.0131g/cm.s and a density of 1.00g/cm^3. $CaCl_2$ and $BaCl_2$ have similar viscosities of 0.0140g/cm.s and densities of 1.04g/cm^3. Saline has a viscosity of 0.0131g/cm.s and a density 1.03g/cm^3. 55% glycerol has a viscosity of 8.19g/cm.s and a density of 1.01g/cm^3.

2.2.3 Cell Culture

A7r5 aortic rat smooth muscle cells (ATCC CRL-1444) between passage 10 and 21 were used. The cells were expanded, as described in (Mason et al. 2004), from a cell bank in T-150 tissue culture flasks (Fisher, Loughborough, UK), using Dulbecco's Modified Eagle's Medium (Cambrex, Berkshire, UK) supplemented with L-glutamine (Cambrex, Berkshire, UK), penicillin/streptomycin (Cambrex, Berkshire, UK) and fetal bovine serum 10% (Cambrex, Berkshire, UK) at 37°C temperature under a CO_2 10% environment for 96hrs. All pipette tips used were disposable (Fisher, Loughborough, UK) Trypan Blue stain (Cambrex, Berkshire, UK) was used for cell enumeration.

Centrifuge work was carried out using 15 and 50ml centrifuge tubes (Fisher, Loughborough, UK) and a tabletop centrifuge (Eppendorf AG, Hamburg, Germany).

2.3 METHODS

2.3.1 CHAPTER 3

2.3.1.1 Robustness Testing: Temperature was controlled at 15°C. A wall gap thickness of 300μm was configured, using a 3.4mm diameter regulator and a 4.0mm (inner diameter) glass capillary. Mark 1 base unit and 0.09M $CaCl_2$ was used throughout.

Variables tested were: alginate concentration and $CaCl_2$ infusion rate. As a guideline, alginate concentration was kept between 0.5-1.0% in order to stay within physiological sodium and calcium salt levels, i.e. those found within a mammalian host, and $CaCl_2$ infusion rates of 20-50ml/min were those that gave a good compromise between efficient speed and controllability. Temperature controlled conditions (15°C) were upheld, to avoid alginate breakdown and uncertainties in tube geometry due to viscosity changes.

The setup procedure shown in figure 2.4 was used for the experiment. The standard-line experiment used midrange variable conditions of 0.5% alginate solution concentration, and 30ml/min infusion rate. Different alginate volumes ranging from 300-700μl were assessed at 100μl increments and the length of tube measured using a steel rule. In order to test the effect of alginate concentration on tube length, three alginate solutions of different concentration were prepared: 0.5, 0.75 & 1.0% were used for the experiment. A total of 11 tubes were made, 5 at 0.5%, 3 at 0.75% and 3 at 1.0% alginate. Infusion rates of 20, 30, 40 and 50ml/min were also tested. Different volumes of alginate

solution were used in 100μl increments and the length of the tube formed was recorded using a steel rule, accurate to ± 0.05mm. The predicted residual volume of alginate, i.e. the dead space within the reactor, was measured from the weight of water injected up to the top of the injector nozzle of the base unit. Results obtained were plotted as length of tube formed vs. volume of sample used (μL).

2.3.1.2 Development of New Protocol: A protocol was developed for device assembly prior to tube formation:

Standard conditions:

0.9% wt/vol saline, pH 7.3-7.4

0.09M $CaCl_2$ (propelling fluid)

0.50-1.00% ISP Manugel DB (matrix fluid, unless otherwise stated)

1. Lubricate 100ml syringe using silicon gel and load using propelling fluid.
2. Fit loaded syringe into syringe driver.
3. Fit dual port base unit onto 100ml syringe.
4. Prime device using propelling fluid to the top of the injector nozzle of the plastic base unit at 1ml/min.
5. Prime 1ml luer-lock syringe (Fisher, Loughborough, UK) with desired volume (300-1000μl) of matrix fluid.
6. Fit 1ml syringe to side port of dual port base unit.
7. Remove excess propelling fluid from injector nozzle.
8. Position spherical regulator on top of injector nozzle.
9. Fit glass barrel onto stub of dual port base unit.
10. Inject entire volume of matrix fluid.
11. Infuse propelling fluid from syringe driver at 20ml/min*.
12. Leave tube to set for 10 min before removal.

Further:

1. Any run with air bubbles present, either during setup or during run, should be discarded.
2. Triplicates to be performed for each matrix fluid volume (after 3.2.3).

** N.B. Infusion speed was reduced to 20ml/min to increase control on tube formation.*

A device wall-gap configuration of 300μm was used, with 0.09M $CaCl_2$ as the propelled agent, infused at 20ml/min. Mark 1 base unit used throughout. 3 alginate concentrations were tested: 0.5, 0.75 and 1.0% on volumes ranging from 300-900μL. A total of 21 tubes were made in total, 7 per alginate concentration at 100μl increments. These were measured immediately after tube formation and the data was then plotted.

2.3.1.3 The Mark 2 Design: A matrix fluid of alginate was loaded via a disposable syringe. $CaCl_2$ was then used as the propelling fluid, and injected through the plastic base via the central metal port. Temperature was kept at 10°C by controlling lab temperature to minimise fluctuations in alginate properties. A device wall-gap configuration of 300μm and Mark 2 base unit used throughout. Volumes of ISP Manugel DB alginate at 0.5, 0.75 and 1.0%, ranging from 200-800μL was infused in 100μL increments with cross-linking medium, $CaCl_2$ at 0.09M infused at 20ml/min, and the length of the resulting alginate-calcium tube was measured from the plastic base using a precision steel rule. 19 tubes in total were made, 4 at 0.5%, 8 at 0.75% and 7 at 1.0%.

The predicted residual volume of alginate, i.e. the dead space within the reactor, was measured from the weight of water injected up to the top of the injector nozzle of the base unit.

2.3.1.4 Wall Thickness Reproducibility: Temperature was controlled at 10°C. Default settings of 1.0% alginate concentration and 300μm wall gap

device configuration were used. Mark 2 base unit used throughout. 0.09M $CaCl_2$ was infused at 20ml/min. Lab temperature was at a controlled 10°C. 21 tubes were prepared in total, with 3 replicates of each data point to examine consistency of the device. Volumes were ranged from 200-800μL varied in 100μL increments. Measurements were made with a precision steel rule immediately after tube formation.

2.3.1.5 Investigation of Wall Gap Configuration: Lab temperature was controlled at 10°C. Alginate concentration was kept constant at 1.0%. Mark 2 base unit used throughout. 0.09M $CaCl_2$ was infused at 20ml/min to maintain reasonable control. Effect of sphere reduction was explored reducing the sphere radii from 1.700mm to 1.587mm, keeping capillary radius at 2.000mm. In essence, 300μm wall gap configuration was compared with a 413μm wall gap configuration. Volumes were ranged from 200-1000μL varied in 100μL increments. 23 tubes were prepared in total, with several repeats of each data point to examine consistency of the device.

After this capillary radius effects were measured by decreasing radii of the capillary from 2.000mm to 1.825mm whilst keeping sphere radius at 1.587mm. I.e. a 413μm wall gap configuration was compared with a 238μm wall gap configuration. Volumes were ranged from 200-700μL varied in 100μL increments. Tubes were immediately measured after formation with a precision steel rule.

2.3.1.6 Effect of Altering Propelling Fluids: The experiment was temperature controlled at 10°C. Propelled liquid was infused at 20ml/min throughout conditions. Mark 2 base unit used throughout. A default wall gap configuration of 300μm for all experiments was used. Matrix fluid was 1.0% alginate in all cases. Propelling fluids tested included: 0.05M $BaCl_2$ (4 tubes made); 1.0% alginate (8 tubes made); WFI (7 tubes made); and 0.9% wt/vol saline (9 tubes made). And the trend for 1.0% alginate matrix with 0.09M $CaCl_2$

propelled fluid was included for comparison (section 3.2.4). All tubes were measured immediately after formation using a precision metal rule.

In a separate experiment, 54% glycerol was infused with 54% glycerol, and WFI infused with WFI for Theory verification purposes (data not shown). Both involved standard conditions: mark 2 base unit; 238, 300 and 413μm gap widths (4 tubes, 4 tubes, 4 tubes for glycerol; 5 tubes, 6 tubes, 7 tubes for WFI, respectively); infusion rate 20ml/min; and propelling fluids were coloured to aid visualisation. Volumes 200 to 800μm (100μm intervals) were tested for all configurations and both sets reacting and non-reacting fluids.

2.3.1.7 Alginate Viscosity Data: Alginate was made up using Manugel DMB and N-saline, and this was placed on the spindle of the viscometer (Brookfield, Massachusetts, USA). This was set up to run water from a water bath through the spindle to simulate conditions at different temperatures. Viscosities were tested for: 1.00% alginate for temperatures of: 15, 20, 25, 30 and 35°C.

2.3.2 CHAPTER 4

2.3.2.1 Primary Tube Scans: 8 tubes (4 at 0.50% alginate, 2 at 0.75% alginate, 2 at 1.0% alginate) were prepared a day in advance using the mark 1 device. All tubes made were 15cm in length, 4mm in diameter and 300μm wall gap configuration. Conditions tested were: 0.5, 0.75 and 1.0% alginate with 0.0005g/ml glass beads and 0.5% alginate with 0.005g/ml glass beads, meant to represent cells and also induce light scattering, so as to aid visualisation of OCT. Pure alginate control tubes contained glass beads at 0.14% volume fraction. All tubes were formed using 0.09M $CaCl_2$ at 20ml/min infusion rate. All tubes contained blue dye for visualisation purposes and to ensure tubes formed

were not failed tubes. Tubes were refrigerated and scanned next day using a motorised platform and real-time measurements were made using an 820nm wavelength near infrared light-source and a resolution of 10µm. 20 (300 for cross-sectional scans) A-scans at 27,680 points, averaged every 20 points were made. 6 points were scanned per tube (fig. 2.11) and one cross-sectional point. Images were then produced using Matlab (Mathworks, MA, USA) to analyse collected OCT data, which takes into account the refraction index of the borosilicate glass (Mason et al. 2004).

2.3.2.2 Mark 2 Tube Scans: 3 tubes prepared a day in advance 20cm in length, 4mm in diameter and using 238µm, 300µm and 413µm gap width. Mark 2 base unit used throughout. Conditions used throughout were: 1.0% alginate with 0.0005g/ml glass beads; and 0.09M $CaCl_2$ concentration; 20ml/min infusion rate; and 20µl/ml alginate of blue food colouring. Tubes were refrigerated and scanned next day together with the glass barrels. Tubes were horizontally mounted on a motorised platform and real-time measurements were made using a 820nm wavelength near infrared light-source and a resolution of 10µm. 20 A-scans at 30,000 points, averaged every 20 points were made. 5 points were scanned per tube (figure 2.12). Images were then produced using Matlab to analyse collected OCT data, which takes into account the refraction index of the borosilicate glass.

2.3.2.3 Shrinkage Effects: A tube containing glass beads at 0.0005g/ml approximately 4cm in diameter and 16cm in length was formed using in the device using a 300µm configuration, 0.09M $CaCl_2$ concentration at room temperature (~18°C). Mark 2 base unit used throughout. For control purposes, a pure alginate tube (at 1.0% alginate concentration) was also formed. Upon formation these tubes were sequentially OCT analysed at a fixed point using an 820nm wavelength near infrared light-source and a resolution of 10µm. 1600

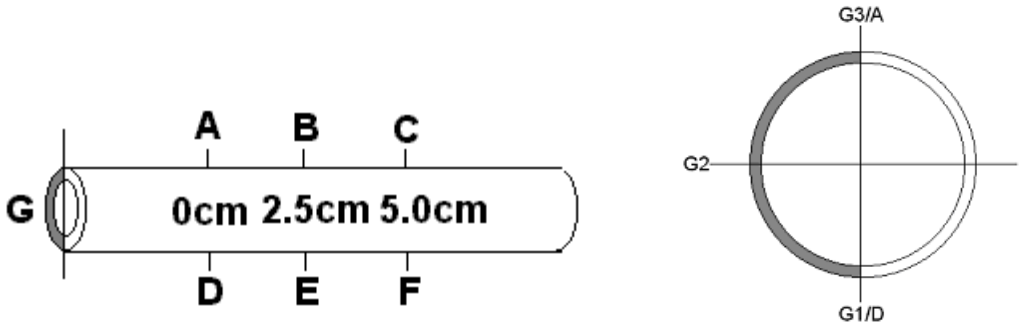

Figure 2.11 Experimental scanning setup and nomenclature used for Mark 1 primary OCT experiment. Point A is 180° from D on the opposite face of the glass capillary and so on. Points A, B and C are 2.5cm apart, point B lying in the centre of the glass capillary. Scan G was a half cross-section taken from a random point in the tube. The table was constructed using G1, 2 and 3 terminologies, taken from set points from the cross-section. G3 corresponds to point A, and G1 to point D.

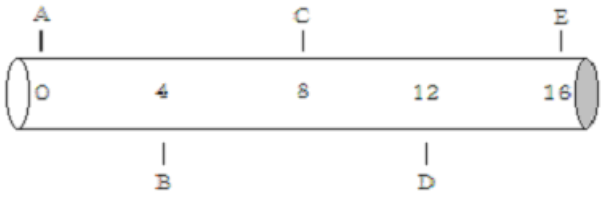

Figure 2.12 Experimental scanning setup and nomenclature used for Mark 2 OCT tube scans. Points A, C and E are 180° from B and D on the opposite face of the glass capillary. Points A to E are 4cm apart, point C lying in the centre of the glass capillary.

point-scans, averaged every 20 points were made, to give 80 points, one per 30 seconds. This data was then used to produce graphs with corresponding images using Matlab to analyse collected OCT data, which takes into account the refraction index of the borosilicate glass.

2.3.2.4 High Speed Camera Monitoring: The camera used was an NAC V-142 digital high-speed colour video camera with a multitude of lenses allowing high magnification. This camera was connected to a NAC HSV-500 compact cassette recorder which allowed transfer of data to PC, a VHS to convert all data to video cassette and a colour monitor to observe everything as it occurs. Using this setup it was possible to study tube formation at 500 frames/sec and x40 magnification to obtain video clips over a large section of tube.

5 x T150 rat SMCs were harvested, pooled then concentrated using a centrifuge and resuspended to $4X10^7$ cells/ml using 1% N-Saline. 20ml of 1% and 1.33% alginate was also prepared with 0.09M $CaCl_2$. Cells were embedded 1:3 ratio cells to alginate to make up $1X10^7$ cells/ml and 1% alginate concentration overall. Default settings (unless otherwise stated) included: 20ml/min infusion rate, 300μm device configuration, 0.09M $CaCl_2$ as infusion medium, and 1.0% alginate concentration. Mark 2 base unit used throughout. In order to improve visualisation, potassium permanganate dye was added to the infusion medium. All tubes were formed at 15°C constant room temperature. In order to eradicate glass distortion effects, a sealed Perspex box was filled with optical fluid (Cargill, Minneapolis, US) at the same refractive index as the borosilicate glass (1.473), and this housed the glass barrel that was used to make to the alginate tube. The following camera settings were used: 500 frames/second; F (full) screen size, 0.2g/ml permanganate dye in $CaCl_2$; and uncoloured alginate.

The following variables and their subsequent impact on tube formation were studied: the effect of infusion rate; the effect of gap-width configuration; the effect of setting and non-setting infusion medium; the effect of alginate

concentration; the effect of cell presence in alginate; and "lift-off" effects – i.e. tube formation at the device metal collar. This was achieved using the following variables: infusion rate 50 ml/min; gap-width configuration of 300 and 413μm; infusion medium of 0.09M $CaCl_2$ (setting) and WFI (non-setting); alginate concentration of 0.05 and 0.09M; cell concentration of 0 and $1X10^7$ cells/ml. Regulator rotation and "lift-off" effects were also explored. The conditions are summarised in table 2.3.

The tube was filmed at 2.5cm from the base unit/regulator interface to analyse "lift off" and at 10cm up from the plastic base unit to obtain a representation of the tube formation process at "full flow". For ball spin experiments, a spot was put onto a plastic regulator using permanent marker pen and all fluids were left uncoloured, so that the effect of ball spin could be clearly analysed. This data was then processed using the Leica QUIPS software, breaking down the dye colour data into red, green and blue profiles.

2.3.2.5 Particle Size Detection and Particle Enumeration: 5 x T-150 flasks of rat SMCs were expanded and harvested using standard procedures (Appendix A, protocol 2) at 20°C. The quenched cell suspensions were collected into one T-150 using a 25ml pipette tip to limit shear to cells. This suspension was <u>not</u> passed up and down the pipette in the ordinary manner to break up aggregates. A cell count was performed at this stage. The suspension was transferred into 50ml centrifuge tubes and centrifuged at 250xg for 5 min. The supernatant was decanted and the pellet resuspended via addition of 0.5ml per tube complete culture medium and vortexing to dispel clumps. 2ml was used to wash out residual cells per tube. Serial dilutions were then made to create the following final concentrations: $1X10^5$, $5X10^5$, $1X10^6$, $1.5X10^6$, and $2X10^6$ cell/ml. Replicates were then counted using a haemocytometer and Trypan Blue (fig. 2.13), and the samples were also analysed using the Leica QWin (Leica Microsystems AG, Wetzlar, Germany) and a particle sizer (Malvern Instruments Ltd, Worcester, UK). Samples analysed in the particle sizer were loaded into 15ml of complete culture medium.

Table 2.3 **Combinations of variables used to study effects upon tube formation using high-speed, high-resolution camera.**

Infusion Rate (ml/min)	WFI	$CaCl_2$	0.5% Alginate
20	X	X	X
50	X	X	X
Lift-off	X	X	X
Infusion Rate (ml/min)	413μm		
20	X		
50	X		
Lift-off	X		
Wall Gap Config.	WFI	$CaCl_2$	0.5% Alginate
413μm	X	X	X

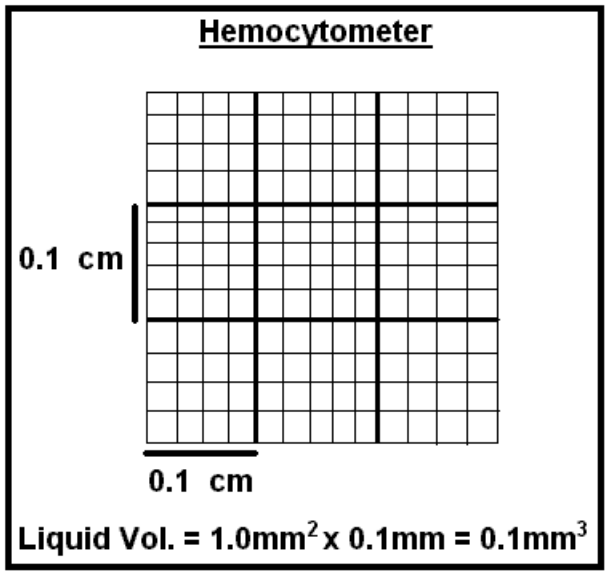

Figure 2.13 Grid setup of the haemocytometer.

Samples analysed by the Leica QWin were placed on a glass slide, with a cover slip placed over the top, and 8 x 500μm squares were snapped at 10x magnification (same as light microscope used for haemocytometer). The Leica QWin generates data by counting particles of different preset size ranges. Calibrating the number of cells with those counted using the haemocytometer an area size of 80-279 μm^2 per cell was estimated assuming perfectly round cells. This was then used to estimate the amount of cells per particle. The y-axis was also converted into % of the total number of particles counted. This information was then used to create comparative profiles (fig. 4.10) to the particle sizer data.

2.3.2.6 Enumeration Using the Capillary Cytometer: Two cell-integrated tubes were made. Both tubes were made using Kenix 12-element static mixers, 300μm wall-gap configuration, 1.0% overall alginate concentration, 0.09M $CaCl_2$ concentration, $1X10^7$ cells/ml, 20ml/min $CaCl_2$ infusion rate, and 1.87ml/min sample injection rate into the device. Mark 2 base unit used throughout. Each tube was cross-sectioned into 6 equal pieces, and each piece was weighed then re-dissolved in 1.0% sodium tricitrate (Sigma, Dorset, UK) made up in 1ml PBS (Sigma, Dorset, UK). The resultant mixture was placed on a roller mixer (Stuart Scientific, Surrey, UK) for 30 min. Then cell enumeration was performed for each section using Trypan Blue and Guava ViaCount Flex Reagent (Guava Technologies, Haywood CA, USA), a nuclear, fluorescent viability stain for cell enumeration. 200μl of cell sample was mixed with 4μl of reagent (1:50 dilution) in a well of a 90 micro-well plate (Fisher, Loughborough, UK) by pipetting up and down 3 times. Cells were incubated in foil-wrapped conditions for 5 min at room temperature. A number balance was then calculated for each tube, i.e. the number of cells per section of tube, assuming that the cells are evenly distributed throughout.

Similarly samples were prepared for apoptosis analysis adding 50μl 1X Nexin Reagent (Guava Technologies, Haywood CA, USA) to 150μl of cell sample and incubating for 20 min.

2.3.2.7 Effect of Pipetting to Breakup Cell Aggregates: 3 x T-150 flasks of rat SMCs were expanded and harvested using standard protocol. The suspensions were pooled together using a 25ml pipette to limit the shear on aggregates that maybe present and a cell count was performed. This pooled suspension was then split into 50ml centrifuge tubes and centrifuged at 100xg for 10 min. The supernatant was then decanted, and the pellets resuspended via addition of 0.5ml per tube complete culture medium and vortexing to dispel clumps. 2ml was used to wash out residual cells per tube. The timer was started at this stage. Concentrated aliquots were made and added one by one to the particle sizer to give a final cell concentration of $1X10^6$ cells/ml in 10ml of complete culture medium. 100μl micropipettes (yellow tips) were used for passes and the following passes were used to create shear on the samples: 0, 5, and 20. The time at analysis of each sample was also noted. Calibration profile used 0.001g of 3-10μm glass beads in 10ml of WFI. The particle sizer requires a minimum number of 100 counts for accuracy – for the purpose, a concentration of $1X10^5$ cells/ml was used throughout experiments.

2.3.2.8 Effect of Holding Time and Gauze Filtration on Cell Aggregation: 4 x T-150 flasks of rat SMCs were expanded and harvested using standard protocol. The suspensions were pooled together using a 25ml pipette to limit the shear on aggregates that maybe present and a cell count was performed. This pooled suspension was then split into 50ml centrifuge tubes and centrifuged at 100xg for 10 min. The supernatant was then decanted, and the pellets resuspended via addition of 0.5ml per tube complete culture medium and vortexing to dispel clumps. 2ml was used to wash out residual cells per tube. Complete culture medium was then added to make up a cell concentration of $1X10^6$cells/ml. The timer was then started and a 1ml syringe used to place 400μl of sample into the particle sizer with 10ml complete culture medium. Using a 1ml pipette with a modified adapter to house an autoclaved membrane of 20μm pore size gauze, a 400μl sample of filtered cells were then placed into

the particle sizer 10 min after the non-filtered sample was analysed, this allowed for analysis and cleaning of the particle-sizer sampling unit. This second set of repeat experiments was performed in parallel intended as a control experiment – the gauze filter would be used just prior to analysing the sample for aggregates. This process was repeated every hour for 3 hours.

2.3.2.9 Effect of Centrifugation and Passage Number on Cell Aggregation: 3 x T-150 flasks of rat SMCs were expanded, and harvested. The suspensions were then pooled together and a cell count was performed manually using Trypan Blue stain. 10ml of complete culture medium was then placed into the particle sizer and the device zeroed. 10ml of un-centrifuged sample was then placed into the particle sizer and analysed. The remaining cell suspension was subjected to 100xg and 500xg via the centrifuge in separate treatments. The supernatant was then discarded, and the pellets were resuspended in complete culture medium to make up a concentration of $1X10^6$ cells/ml. 400μl of each sample was added to 10ml of complete culture medium in the particle sizer separately and analysed.

2.3.3.1 Effect of Biological Cell Addition On Tube Wall Thickness: The cell-alginate was hand-mixed (i.e. cells were injected by micropipette, stirred and then put on the roller mixer for 30 min) using 1.0% alginate concentration and $1X10^7$ cells/ml. Mark 2 base unit used throughout. This mixture was infused into three different gap width configurations 238, 300 and 413 μm. Cell-free (pure alginate) control tubes corresponding to each tube-forming device configuration were prepared in parallel. A tube was formed per data point. A total of 20 tubes were formed using set volumes ranging from 200-800μL. The length of each tube was measured at time, t=0s (i.e. immediately after tube formation) and the relationship between the two plotted.

2.3.3.2 Static Mixers and Impact on Wall Thickness: Six tubes in total were made. Tubes were prepared a day before OCT scanning. Three conditions were used to make the tubes: a control experiment of cell-free alginate tubes (mixed with inert glass beads for visualisation); a cell-integrated tube mixed using a 12-element static mixer arrangement; and a cell-integrated tube mixed by hand. Two tubes were made per condition. Tubes were prepared a day before OCT scanning, so were fully set and all shrinkage effects had taken place (Saitoh et al. 2000; Zhang et al. 2000). All tubes were made using 300μm wall-gap configuration, 1.0% overall alginate concentration, 0.09M $CaCl_2$ concentration, $1X10^7$ cells/ml and 20ml/min $CaCl_2$ infusion rate. All statically mixed tubes were injected at 1.87ml/min max infusion rate into the Device. OCT was then used to scan each tube at 18 points per tube (fig. 2.14) in order to determine tube wall thickness. The radial repeats (A, B, C) was to ensure at least one usable image was taken at each sampling location (1 – 6). Representative cross-sectional OCT images (longitudinally through the tube) of cell-free alginate tubes (n=2) and manually mixed cell/alginate cell-integrated tubes (n=2) are shown in figure 5.4, one for each sampling location.

2.3.3.3 Effect of Processing on Viability: 20ml of 2% alginate and 0.09M $CaCl_2$ was prepared using N-saline. 40ml 0.1M sodium citrate was also prepared in PBS. Alginate was autoclaved at 121°C for 20 minutes. 7 x T-150 flasks were expanded, harvested and pooled together. A cell count was carried out. The cell suspension was then split into 50ml centrifuge tubes and centrifuged at 100xg for 5 min.

The supernatant was discarded and the pellet resuspended using complete culture medium and manually mixed with alginate via pipetting into the alginate and stirring with the pipette tip to give a final mixture of 1% alginate with $1X10^7$ cells/ml, as in Appendix A, protocol 5. Two tubes were then formed using the device. Mark 2 base unit used throughout. They were each left to set for 10

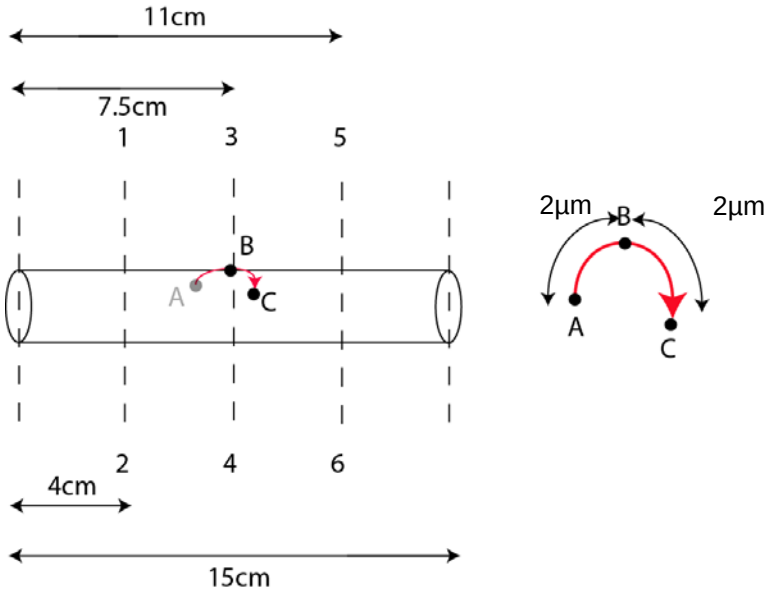

Figure 2.14 Schematic diagram (not to scale) showing experimental setup used for Optical Coherence Tomography (OCT) scanning of cell-integrated tubes. The longitudinal (numbers 1-6) and radial (letters A-C) locations correspond to images seen in figure 5.4.

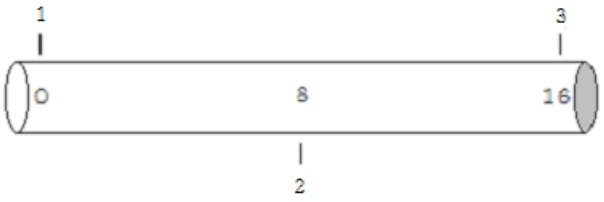

Figure 2.15 Experimental scanning setup and nomenclature used for initial cell OCT tube scans. Points 1 and 3 are 180° from 2 on the opposite face of the glass capillary. Points 1 and 3 are on either end of the tube, with point 2 lying in the centre of the glass capillary. The cross-sectional scan was taken at a random point along the tube.

min, before being dissolved in 0.1M sodium citrate to give $1X10^5$ cells/ml concentration. Cell counts were performed again at this stage. This was replicated for the second tube.

2.3.3.4 Effect of Processing on Viability Repeat: 20ml of 2% alginate and 0.09M $CaCl_2$ was prepared using N-saline. Alginate was autoclaved at 121°C for 20 minutes. 40ml 0.1M sodium citrate was also prepared in PBS. 7 x T-150 flasks were expanded, harvested and pooled together. A cell count was performed. The cell suspension was then split into 50ml centrifuge tubes and centrifuged at 100xg for 5 min. The supernatant was discarded and the pellet resuspended in 10ml volume to obtain a suspension of $4x10^7$cells/ml. This was then mixed with alginate to give a final mixture of 1% alginate with $1X10^7$ cells/ml, as in protocol 5. This mixture was rolled on a roller-mixer for 30 min for alginate to be mixed thoroughly with cells after pipetting of cell suspension into the alginate and initial stirring. A 0.4ml sample was drawn, diluted in citrate to give $1X10^5$ cells/ml concentration and a control cell count was taken. Two tubes were then formed using the device. Mark 2 base unit used throughout. They were each left to set for 20 min within the tube-forming device, before being dissolved in 0.1M sodium citrate to give $1X10^5$ cells/ml concentration. Triplicate cell counts were performed again at this stage. This was replicated for the second tube.

2.3.3.5 Effect of Concentration Steps on Viability: Rat SMCs were expanded in 27 x T150 flasks and harvested. The suspensions were pooled together. A triplicate cell count was then taken using Trypan Blue and a haemocytometer. The suspension was then centrifuged at 100xg for 5 min. This was then resuspended to: $1X10^7$, $5X10^6$, $2.5X10^6$, $1X10^6$ and $1X10^5$ cells/ml in 4ml. Each suspension was then passed through the centrifugation process and resuspended back to the original concentration using fresh medium 5 times. A triplicate cell count for each concentration was performed after each pass.

2.3.3.6 Effect of Media on Cell Viability: For this experiment 5 x T150 flasks were cultured and harvested. The suspensions from all flasks were pooled together. An initial cell count was then taken using Trypan Blue and a haemocytometer. The pooled cell suspension was then spun down using centrifugation at 100xg at 5 min, and resuspended to $1X10^5$ cells/ml in the following media: food colouring at 100μl/ml, N-Saline, complete culture media, 1.0M sodium citrate, and 0.09M $CaCl_2$. A 100μl sample was drawn from each condition every 10 min for 1 hour and triplicate cell counts were measured using Trypan Blue, light microscopy and a haemocytometer.

2.3.3.7 Effect of Liquid Alginate on Cell Viability: For this experiment 3 flasks of T-150 A5r7 rat SMCs were cultured, harvested and pooled together. An initial cell count was measured. The suspensions were then centrifuged twice at 100xg for 5min and resuspended in complete culture media. The final concentration was $4X10^7$ cells/ml. The suspension was then mixed 1:3 with several different media. Conditions tested included: 0.5% final alginate concentration, 1.0% final alginate concentration, and N-Saline control. This was kept for 3 hours and samples taken every ½ hour for triplicate cell counting. All alginate was autoclaved at 121°C for 20 minutes.

2.3.3.8 Effect of Infusion Speeds on Cell Viability: 27 x T150 flasks of A5r7 rat SMCs were cultured and harvested. All suspensions were pooled and an initial cell-count done. The suspension was then aliquoted into 50ml centrifuge tubes and centrifuged at 100xg for 5 min. This was then resuspended to 8ml with complete culture medium and centrifuged again. This was finally resuspended to $4X10^7$ cells/ml in medium and mixed 1:3 cells:1.33% alginate to give final concentrations of $1X10^7$ cells/ml and 1.0% alginate concentration. Alginate was autoclaved at 121°C for 20 minutes. This mixture was then used to form tubes using 300μm wall-gap configuration and 0.09M $CaCl_2$. In parallel (timed experiment), 1ml of the mixture was used to form beads as a control.

Beads were created manually by dripping cell-alginate mixture into a bath of 0.09M $CaCl_2$ using a 1ml disposable syringe. Mark 2 base unit used throughout. Infusion speeds of: 20, 40, 60, 80, 100ml/min were tested. After 10 min, the tubes and beads were simultaneously dissolved in 1.0M trisodium citrate. Triplicate cell counts were carried out.

2.3.3.9 Pronova SLG 100 and Static Mixer Impacts on Cell Viability: This experiment was done in two stages: through the static mixing device and through the tube-forming device. Viability experiments through the static-mixer involved passing cells through the device with no alginate present. Viability of cells through the tube-forming device involved forming cell-alginate tubes, instantly dissolving them in 1.0% sodium tricitrate, and performing triplicate cell enumeration using Trypan Blue. Alginate source was switched to SLG 100 (Pronova, Lysaker, Norway). Simultaneously cell/alginate beads were produced and dissolved in 1.0% sodium tricitrate, and cell enumeration performed in parallel as a control. Cell/alginate beads were prepared by dripping a pre-prepared cell/alginate mixture into a bath of 0.09M $CaCl_2$ via a 1ml syringe with a sterile needle tip. All tubes were made using 300μm wall-gap configuration. Beads were created manually by dripping cell-alginate mixture into a bath of 0.09M $CaCl_2$ using a 1ml disposable syringe. Mark 2 base unit was used throughout. Both tubes and beads were made at 1.0% overall alginate concentration, 0.09M $CaCl_2$ concentration, and $1X10^7$ cells/ml.

2.3.3.10 Cellular Apoptosis Analysis: Guava Nexin kit was used to study cell apoptosis. Two cell-integrated tubes were made using two cell-integration methods – hand-mixing and static mixing (12-element). Each tube was cross-sectioned into 6 equal sections, and each piece was weighed then re-dissolved in 1.0% sodium tricitrate. The analysis was carried out on central and end sections of each tube. Samples from each section were potted into wells of a 96-well plate, incubated for 20min at 20°C with Guava Nexin kit and then

analysed on the capillary cytometer. All tubes were made using 300μm wall-gap configuration, 1.0% overall alginate concentration, 0.09M $CaCl_2$ concentration, $1X10^7$ cells/ml, 20ml/min $CaCl_2$ infusion rate, and 1.87ml/min sample injection rate into the device. Mark 2 base unit used throughout. Alginate was autoclaved at 121°C for 20 minutes.

2.3.3.11 Initial Cell-Integrated Tube OCT Scans: 2 x T-150 flasks of rat SMCs were grown and harvested. The pooled mixture was then sampled for a cell count using Trypan Blue and the cell suspension was added to alginate via hand mixing to alginate using protocol 5. $1X10^7$ cells/ml final concentration was used and 1% final alginate concentration in a 1:3 part ratio, respectively. A tube approximately 4cm in diameter and 16cm in length was then formed using this mixture in the device using a 300μm configuration, 0.09M $CaCl_2$ concentration and 10°C temperature. Mark 2 base unit used throughout. This was allowed 10 min to set before the tube was bunged at either end and wrapped in foil. This was OCT analysed at Cranfield University the following morning using a 820nm wavelength near infrared light-source and a resolution of 10μm via the set-up in figure 2.15. 200 A-scans at 27,700 points, averaged every 20 points were made. 4 points were scanned in total including 1 cross-sectional scan (at 500 A-scans). Images were then produced using Matlab to analyse collected OCT data, which takes into account the refraction index of the borosilicate glass.

2.3.3.12 Effect of Static Mixers on Cellular Distribution: Cell-integrated tubes were prepared using an 8-element and 12-element static-mixers and the hand-mixed method. Alginate prepared was autoclaved at 121°C for 20 minutes. These were then each cross-sectioned into six equal pieces. Each piece was then weighed and re-dissolved in 1.0% trisodium citrate before cell counting using Trypan Blue stain and results obtained were standardised per section weight. A total of nine tubes were made. All tubes were made using mark 2 base unit, 300μm wall-gap configuration, 1.0% overall alginate

concentration, 0.09M $CaCl_2$ concentration, $1X10^7$ cells/ml, 20ml/min $CaCl_2$ infusion rate, and 1.87ml/min sample injection rate into the tube-forming device. By comparing cell counts per section of tube for cell-integration by hand-mixing, 8-element static mixer and 12-element static mixer, we were able to obtain cellular distribution data.

2.3.3.13 Visual Verification of Cell Distribution Using Light Microscopy: Rat SMCs were grown, harvested and pooled. A cell count was performed. This mixture was then centrifuged at 100xg for 5 min and resuspended in 8ml complete culture medium. This process was repeated once and resuspended to $1X10^4$ cells/ml concentration. The suspension was then integrated into 1:3 into 1.33% alginate via hand mixing and via 12-element static mixer to give a resultant mixture of 1.0% alginate concentration at $1X10^7$ cells/ml. All alginate was autoclaved at 121°C for 20 minutes prior to cell integration. These mixtures were then used to form a tube using the tube-forming device. A control tube of alginate, containing glass beads was also made. Conditions maintained throughout include: a 300μm wall-gap configuration, 0.09M $CaCl_2$, 20ml/min infusion rate and 20°C. Mark 2 base unit used throughout. A control tube of 1.0% alginate, containing $1x10^{-3}$ g/ml glass beads was also made. The tubes were then each sectioned into 6 equal pieces using a scalpel and each piece was then viewed under a light microscope at x20 magnification in the presence of a graticule. Digital photographs were then taken.

2.3.3.14 Visual Verification of Cell Distribution Using CLSM: Two tubes were made in total. Cell/alginate tubes approximately 20cm in length, 4mm in diameter and of 300μm in wall thickness were prepared on the same day of confocal analysis. Mark 2 base unit used throughout. Alginate was prepared and autoclaved at 121°C for 20 minutes. Cell-integrated tubes made via hand-mixing and 12-element static mixing were created. These were then

fluorescently stained to allow visualisation using CLSM. Fluorescent staining of nuclei was achieved using Guava ViaCount Flex Reagent (Guava Technologies, Haywood CA, USA). Tubes were washed before and after staining using buffer and thoroughly dried. The tubes were then directly analysed using liquid immersion techniques, a 558-656-emission band prism, and x40 magnification. Each tube was scanned at 3 fixed points along the tube length – top and bottom walls of the tube were simultaneously scanned. Both tubes were made using 300μm wall-gap configuration, 1.0% overall alginate concentration, 0.09M $CaCl_2$ concentration, $1X10^7$ cells/ml, 20ml/min $CaCl_2$ infusion rate, and 1.87ml/min sample injection rate into the Device. CLSM was then used to scan each tube at 3 points, through both walls of a collapsed tube to obtain cellular distribution verification data. Raw data was analysed using LCS Lite (Leica Microsystems AG, Wetzlar, Germany) to produce snapshots and profiles. The area under these profiles were then analysed using curve analysis software (Cyber Solutions, Dundee, Scotland).

3 Tube Formation

This chapter follows the progression of design of the tube-forming device, its protocols and reliability testing of the device. At the beginning of this thesis the tube-forming device was an untested prototype, perhaps capable of forming tubes, but not of high precision and not very robust, i.e. tubes could be formed but had inconsistent length with the same volumes. No standard protocol existed and there was much room for design improvements.

The aims of this chapter were therefore: to establish the tube-making ability of the device, which variables should be measured, how much variation existed and what is an acceptable error; what are the optimum settings for tube formation in order to limit variations in tube consistency and what is the protocol to do so; what improvements could be made to reduce these variations, and what is the new variance; and what other variables could influence tube formation and how do they influence tube geometry.

3.1 INTERPRETATION OF THE FLUID DYNAMICS THEORY

Although the Theory for this thesis was developed during work from this chapter, it is more logical to explain it at an early stage, in order to better grasp how tubes are formed and how the findings of the results relate to the fluid dynamics.

It is necessary firstly to point out that the Theory was developed entirely by the Department of Mechanical Engineering, UCL and no claim to its development is made by this thesis. The raw equations and non-standard derivations can be found in Appendix B. The Theory was, however, verified experimentally by results taken from this thesis, which also adds several interesting discussion points due to the cross-linking nature of the alginate-calcium system.

In this sub-section the Theory will be explained in “laymen’s terms” and although the explanation will not follow Appendix B equation by equation,

the key equations underpinning the fluid dynamics will be described, as well as some key figures.

The starting point is figure 2.4. After assembly of the tube-formation device, a finite volume of liquid alginate is injected as the matrix fluid into the system via the side injection port of the dual port base unit. The propelling fluid – $CaCl_2$ is then infused, pushing the spherical regulator upwards through the matrix fluid. The first key concept is that the matrix fluid flows upwards throughout tube formation – i.e. it is dragged upwards with the rising spherical regulator. Therefore the gap width (distance between the regulator and the glass barrel walls) is not the thickness of the alginate layer deposited – in fact the nominal wall thickness of the alginate tube is considerably thinner than the gap width, the question is how thin?

The Lubrication Theory mentioned in Appendix B can be explained with the help of figure 3.1. Basic fluid dynamics states that any moving fluid has a velocity profile. The parabolic profile on the bottom of figure 3.1 resembles a standard velocity profile for a Newtonian fluid, flowing in a laminar regime within a cylindrical pipe i.e. fluid at different points flows at different velocities much like sheets. The fluid moves with velocity zero at the wall of the glass barrel; and velocity ν at point P (any point around the wall of the spherical regulator). Next we concentrate on the Navier Stokes Equation. The equation basically states that: the forces acting on a fluid = pressure gradient + resistance due to viscous forces, or:

$$\rho^{Du}/_{Dt} = -\nabla p + \mu\nabla^2\underline{u}, \qquad (A)$$

We assume steady state conditions – therefore no acceleration occurs eliminating the left-hand part of equation (A). This gives us equation (1) from Appendix B:

$$0 = -\frac{dp}{dx} + \mu\frac{\partial^2 u_x}{\partial r^2}, \qquad (1)$$

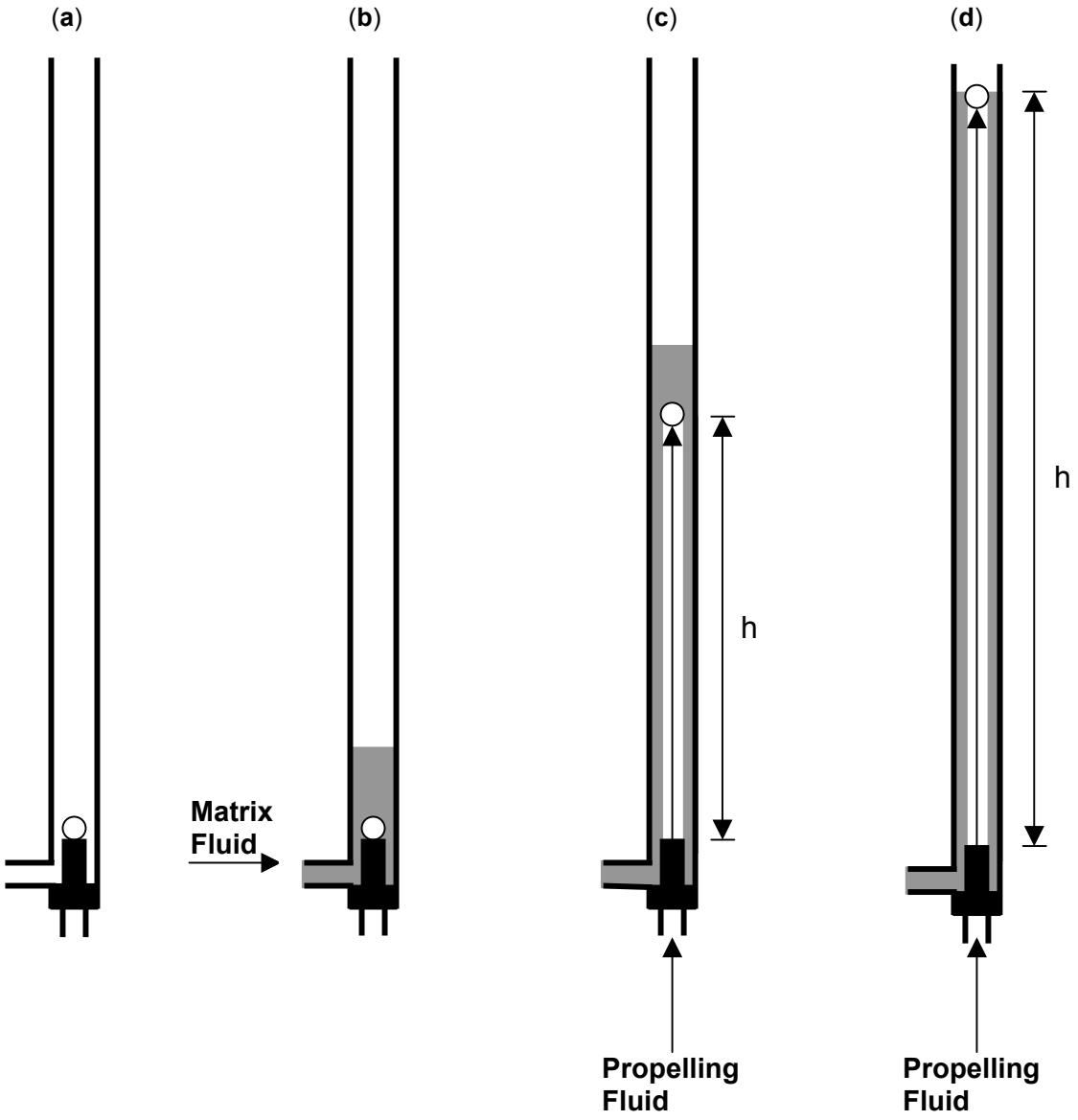

Figure 2.4 Schematic to illustrate setup procedure of the tube-forming device.

- **(a)** Device assembly.
- **(b)** The matrix fluid is loaded using the side port.
- **(c)** The propelling fluid is injected from the base port.
- **(d)** The tube length calculated as the length when the regulator sphere penetrates the meniscus of the alginate.

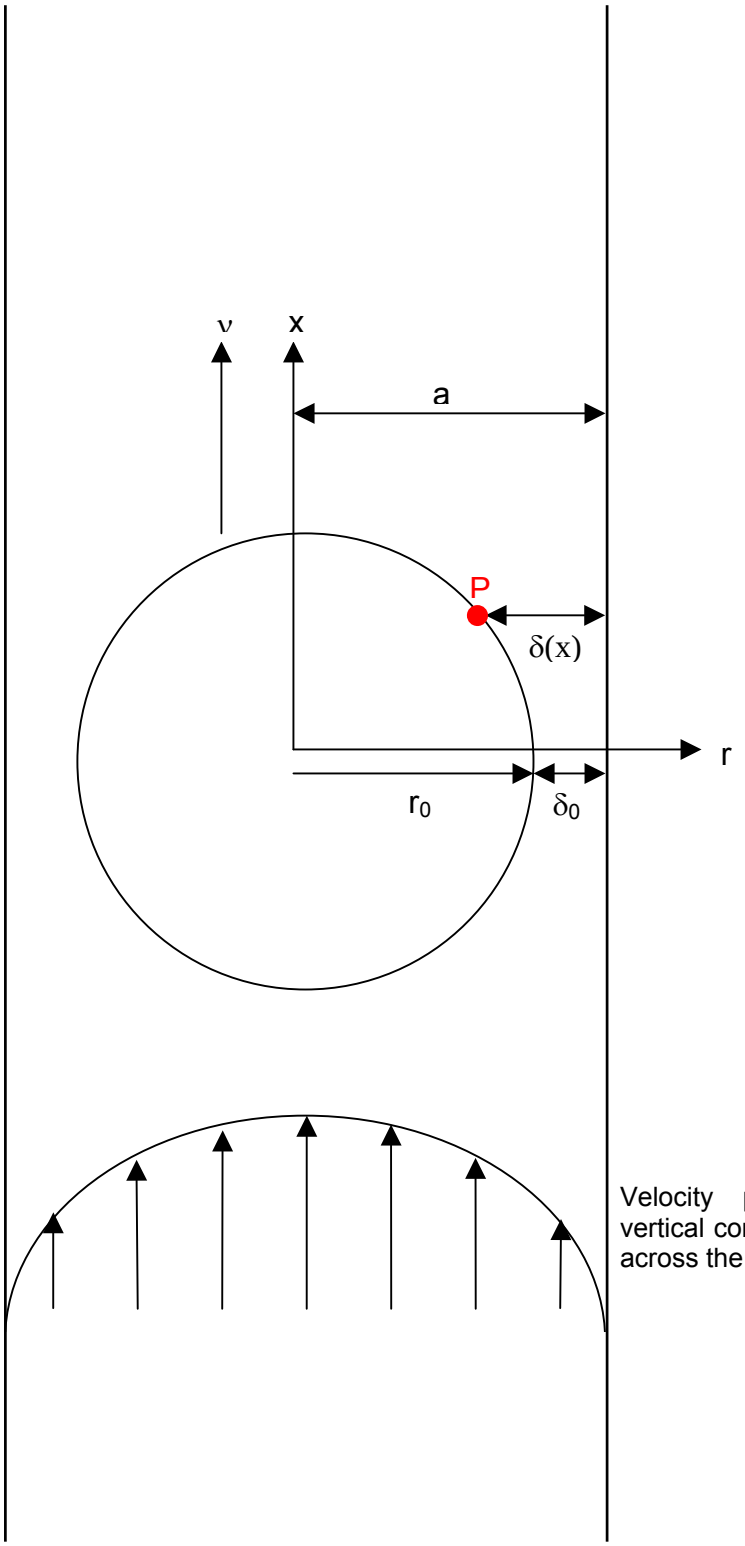

Figure 3.1 Schematic to show the arrangement of the spherical regulator in a cylinder propelled upwards by a flow at the inlet.

The pressure gradient term from equation (1) can be split into vertical and radial pressure gradients exerted on the spherical regulator during tube-formation. Because radial pressure gradients are negligible compared to vertical pressure gradients, we disregard radial pressure gradients in the Theory. Rearranging equation (1):

$$\frac{\partial^2 u_x}{\partial r^2} = \frac{1}{\mu}\frac{dp}{dx} = K\,, \qquad \text{(B)}$$

We know from this type of equation that the solution will take the format:

$$u_x = K(Ar^2 + Br + C), \qquad \text{(C)}$$

By substituting the limits previously identified:

u_x = V when r = (a - δx)

u_x = 0 when r = (a)

And solving equation (C) we obtain equation (13) from Appendix B, a solution for the Lubrication Theory, which gives us velocities ν and $\bar{u}$ during tube formation.

$$\frac{v-\bar{u}}{v} \approx \frac{4\delta_0}{3r_0}\left(\frac{1-8\delta_0/3r_0}{1-4\delta_0/3r_0}\right). \qquad (13)$$

This is however not what we want. We need an equation relating to tube wall thickness, in particular at the end of tube formation. If we look at figure 3.2, we can see that the initial height of the matrix fluid is 'λ' and after travelling with velocity '$\bar{u}$' at time 't' (at the end of tube formation) the total height of the matrix fluid is '$\bar{u}t + \lambda$'. If the spherical regulator travels with

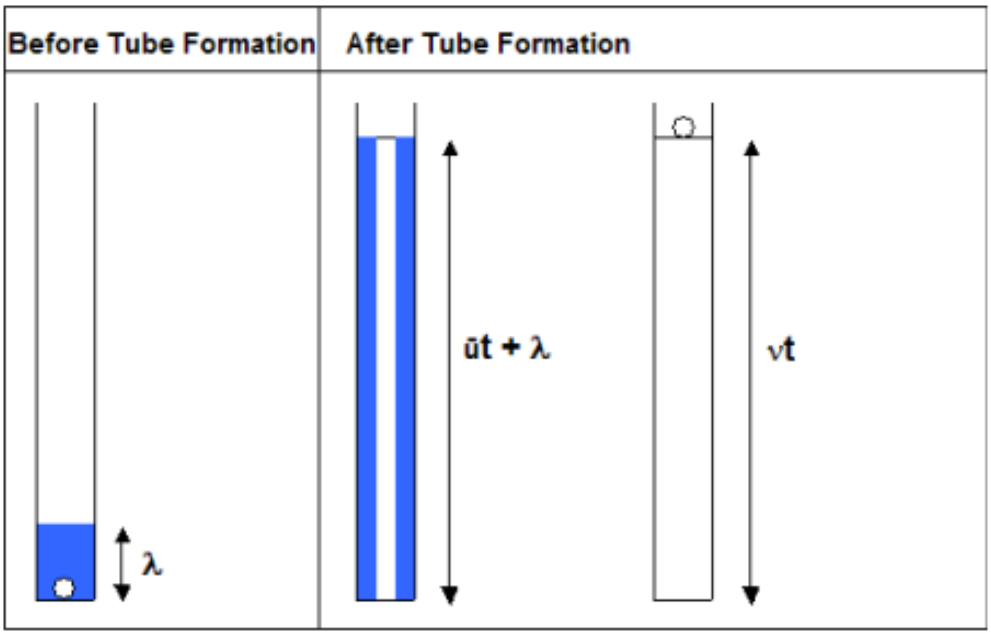

Figure 3.2 Diagram showing the distances travelled before and after tube formation by both the matrix fluid and the spherical regulator.

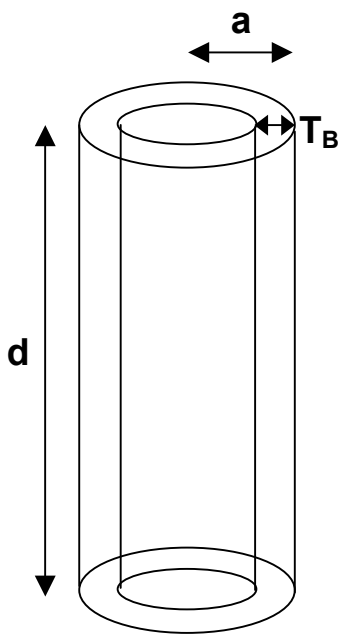

Figure 3.3 Diagram of a cylinder or hollow tube, similar to the open tubes formed using the tube-forming device.

velocity 'ν' (it will travel faster than the average speed of matrix fluid flow), and it also reaches the end of tube formation at time 't', then the distance travelled is 'νt'.

Since the distance is equal for both the spherical regulator and the matrix fluid at the end of tube formation, then:

$$\nu t = \bar{u} t + \lambda \qquad (D)$$

Rearranging we get:

$$\nu t = {}^{(V\lambda)}/_{(V-\bar{u})} \qquad (E)$$

Finally by taking equations for the volume of a tube, V (fig. 3.3):

$$V = d \times \pi[a^2 - (a - T_B)^2] \qquad (F)$$

And substituting from equation (E):

$$V = \nu t = [{}^{(\nu\lambda)}/_{(\nu-\bar{u})}]\pi[a^2 - (a - T_B)^2] \qquad (G)$$

And if we substitute equation (13) into equation (G) we finally have an equation whereby we can extract geometry information from the theoretical prediction of tube formation – equation (14).

$$\frac{T_B}{a} = 1 - \sqrt{1 - \frac{(\nu - \bar{u})}{\nu}} \approx \frac{2\delta_0}{3r_0} - \frac{2\delta_0{}^2}{9r_0{}^2}. \qquad (14)$$

This can be approximated to the right-hand side part of the equation. 'T_B' is the predicted wall thickness of the tube formed. And if 'δ_0' is the gap width between the spherical regulator and the glass barrel wall then '$\delta_0{}^2$' is an extremely small number and can be considered negligible. It therefore

follows that overall, the predicted wall thickness of the deposited layer is approximately equal to $^2/_3$ of the gap width, i.e.:

$$T_B \approx {}^2/_3\,\delta_0 \qquad \text{(H)}$$

as 'a' (glass barrel radius) approaches 'r_0' the radius of the spherical regulator.

That is to say that this $^2/_3$ rule of thumb does not always apply, but only for very small gap widths. Figure 3.4 was a joint effort between the Mechanical Engineering, UCL and Biochemical Engineering, UCL departments. The lines on the diagram represent limits predicted by CFD based on the Theory. The data points show experimental results for the alginate-$CaCl_2$ system (collated data from Chapter 3 is shown in table 3.1). We can see in figure 3.4 how the experimental results verify the $^2/_3$ Approximation that the fluid dynamics Theory predicts, by falling into the pre-defined range.

This Theory was developed not just for alginate-$CaCl_2$ systems, but any two fluids (even the same matrix and propelling fluid), reacting or non-reacting.

3.2 TUBE-FORMING DEVICE

3.2.1 Robustness Testing

Initial experiments were carried out using the mark 1 device. The aim was to evaluate the robustness of the device to generate tubes of reproducible length (for fixed volume) and hence thickness – the governing variable – as thickness directly relates to the effectiveness of nutrient exchange (Glickis et al. 2004) and therefore the viability of using the alginate tube as a macro-encapsulation structure.

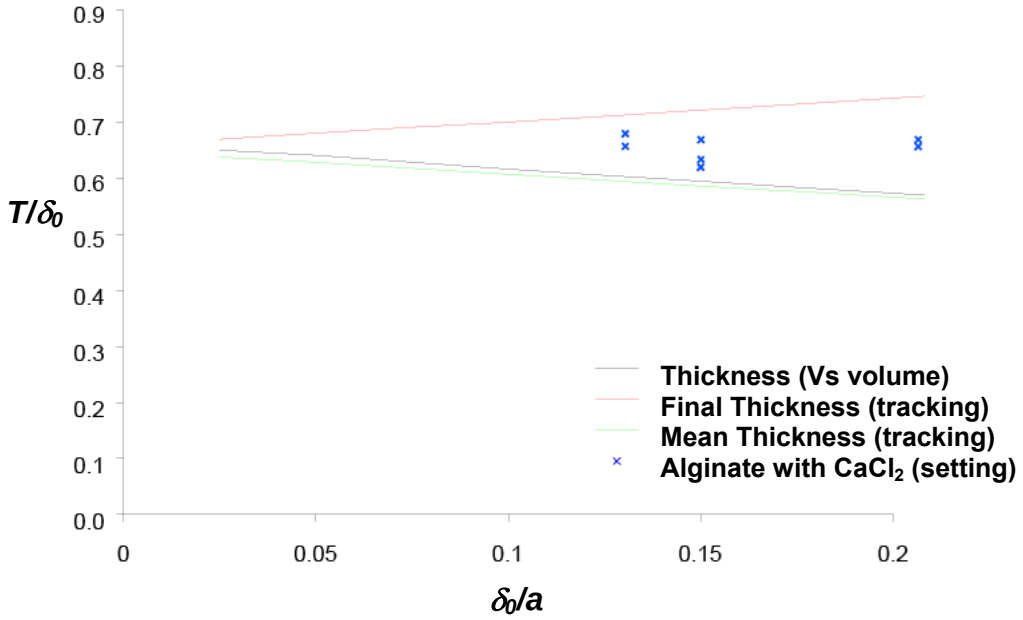

Figure 3.4 Tube wall thickness, 'T' as a fraction of gap width, 'δ_0' versus gap width as a fraction of cylinder radius 'a'. Alginate infused with $CaCl_2$ wall thickness data, T_0 is marked as (**X**). The predicted wall thickness (T_B) (14) is plotted as a green line.

Table 3.1 Summary of Raw Data For All Alginate-$CaCl_2$ Experiments

Spherical Regulator Radius, r_0 (mm)	Glass Barrel Radius, a (mm)	Slope of Graph ($^{mm}/_{mm^3}$)	Nominal Wall Thickness, T_0 (mm)	Predicted Wall Thickness, T_B (mm)	Gap Width, δ_0 (mm)	δ_0/a	T_0/δ_0
1.700	2.000	0.447	0.187	0.206	0.187	0.150	0.622
1.700	2.000	0.441	0.189	0.206	0.189	0.150	0.631
1.700	2.000	0.418	0.201	0.206	0.201	0.150	0.669
1.588	2.000	0.310	0.275	0.283	0.275	0.206	0.667
1.588	2.000	0.315	0.271	0.283	0.271	0.206	0.658
1.588	1.825	0.584	0.156	0.158	0.156	0.130	0.657
1.588	1.825	0.567	0.161	0.158	0.161	0.130	0.677

An initial standard-line experiment, using mid-range variable values for a combination of safe physiological conditions and process control was used to establish the reproducibility of the device (fig. 3.5). The dead-space, i.e. the residual alginate lost in the device was measured to be 112μl using water. Data was fitted by linear regression giving an R^2 = 0.9814 hence indicating that the relationship between the variables was linear. The coefficient of variation (CV) of 3.56% shows fluctuation across replicates.

The first variable to test was the effect of alginate concentration on tube length and hence geometry. The aim was to establish the effect of fluctuations brought about by alginate concentration. Three conditions were evaluated: 0.5, 0.75 and 1.0% alginate. The results of the lengths of tubes were plotted and compared. We can see from figure 3.6 that there seems to be a gradient of the slope from incremental increases in alginate concentration – i.e. the greater the concentration the steeper the slope. This is of concern if small changes affect trends, and hence wall thickness so greatly. However the data points do not always fit very tightly to their corresponding regression lines especially seen for 0.75% alginate concentration falling below R^2 = 0.9, perhaps due to the lack of data points to regress to a linear trend.

The analysis of infusion speeds (fig. 3.7) shows little variation between different trends. The slopes are almost inseparable and there is no pattern to the gradient of the slopes, perhaps suggesting that this variation is due to the error of data and not due to device sensitivity.

Overall the data shows highly linear trends of length of tube against volume of alginate used, as indicated by high R^2 values. When compared to other well-engineered devices, such as the bead formation device of Serp (Serp et al. 2000) – who quote a CV of 5% - then a CV of 3.56% across data points for the standard line experiment indicates a level of precision within the device. However, the range of tube lengths (and therefore tube wall thicknesses) with varying alginate concentrations indicates a very sensitive system. We know from the theoretical fluid dynamics that fluid properties play no part in determining tube wall thickness. Even though viscosity is an

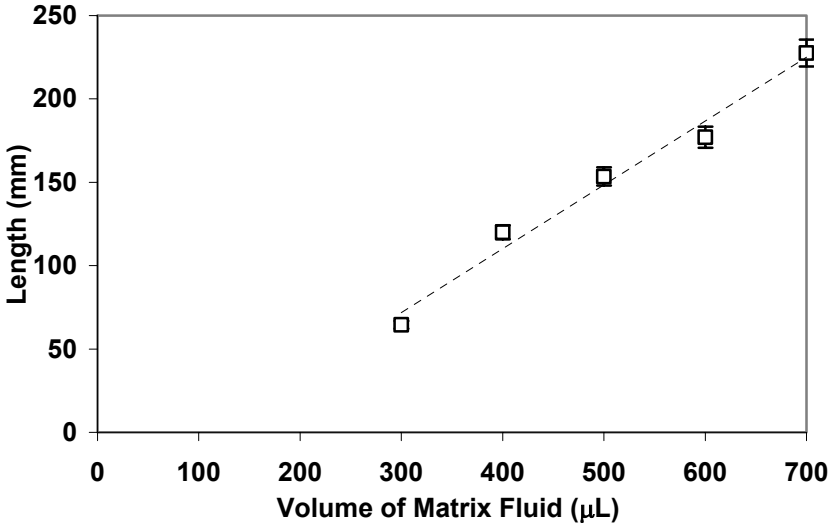

Figure 3.5 Standard-line experiment, showing relationship between volume of sample (μL) against length of tube formed. Conditions used throughout: 300μm wall gap configuration; 0.5% alginate concentration; 0.09M $CaCl_2$ concentration; 30ml/min infusion rate; and 15°C. Symbols represent the average length of n=2 replicate tubes per set volume. Dotted line represents line of best fit. Error bars represent CV across data points. R^2 = 0.9814. Mark 1 device was used.

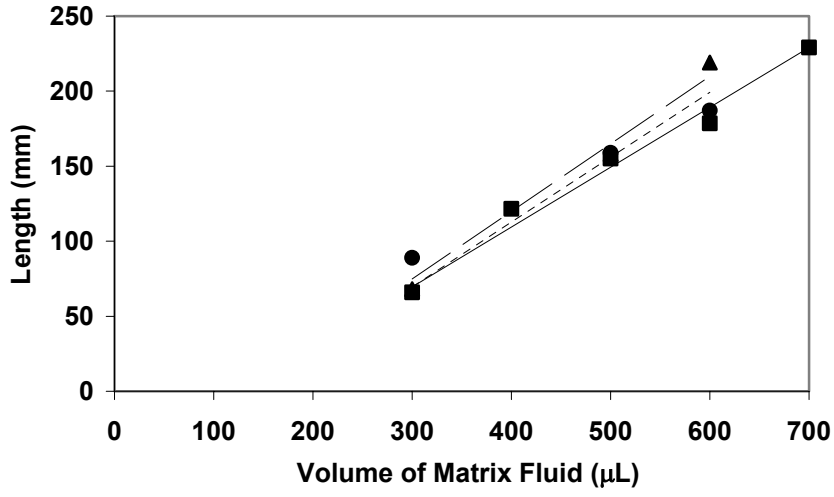

Figure 3.6 Effect of alginate concentration on tube length. Alginate concentrations of 0.5% (■); 0.75% (●); and 1.0% (▲) were tested and compared. Conditions used throughout: 300μm wall gap configuration; 0.09M $CaCl_2$ concentration; 30ml/min $CaCl_2$ infusion rate; and 15°C. Symbols represent the length of n=1 tubes per set volume. The solid, dotted and broken lines represent

average lines of best fit for 0.5%, 0.75% and 1.0% alginate, respectively. R^2 = 0.9796, 0.8952, and 0.9845, respectively. Mark 1 device was used.

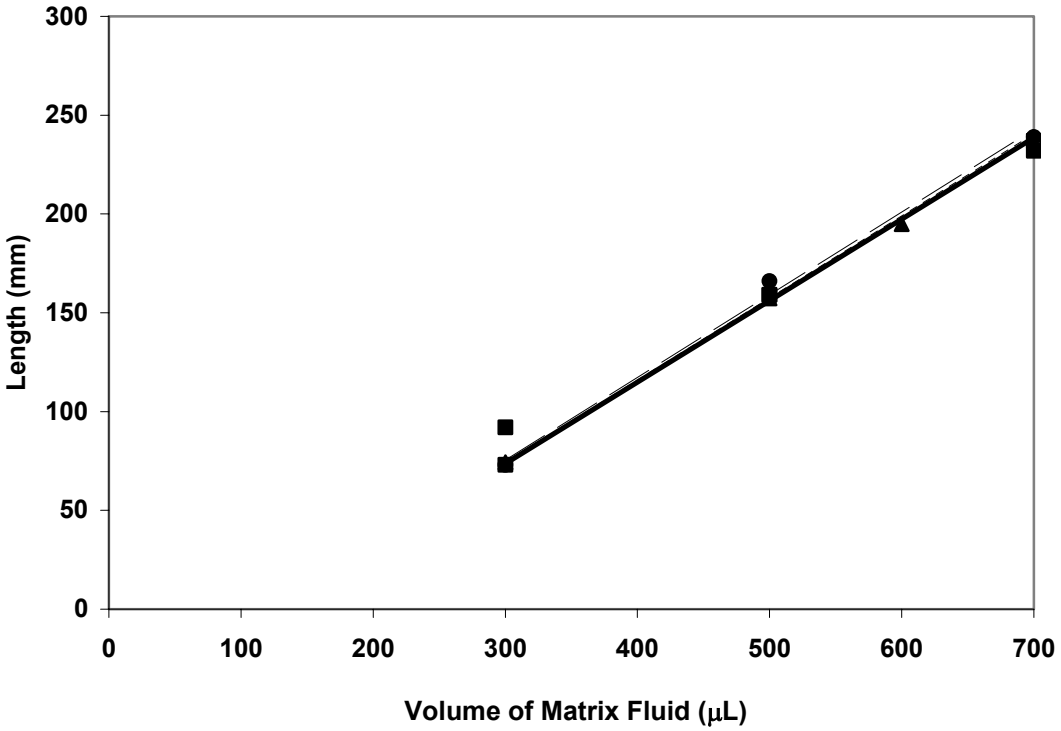

Figure 3.7 Effect of infusion speed on tube length. Infusion speeds of 20ml/min (■); 30 ml/min (▲); 40ml/min (●); and 50 ml/min (□) were tested and compared. Conditions used throughout: 300μm wall gap configuration; 15°C; 0.5% alginate concentration; and 0.09M $CaCl_2$ concentration. Symbols represent the length of n=1 tubes per set volume. The bold, solid, dotted and broken lines represent lines of best fit for 20, 30, 40 and 50ml/min, respectively. R^2 = 0.9612, 0.9990, 0.9951, and 0.9992, respectively. Mark 1 device used.

initial term in (A) and (1), it does not form part of the final equations – (14) and (H). We must therefore assume that the trends observed in figure 3.6 are down to data error. Infusion speed, V is also a term that appeared in the equations up to (14). However, despite its presence in the final equation, it appeared that infusion speed, V was a variable we could control accurately via the syringe driver within the range tested and it seemed to play no substantial part to influence tube length and therefore tube wall thickness.

3.2.2 Development of New Protocol

The previous experiment showed significant impact to tube length from small changes in alginate concentration. These data errors of the mark 1 device could have been due to either: a lack of data points, i.e. short range of sample volumes tested; or due to data collection. On a practical front, it was also noticed that during tube formation, bubbles would creep into the system during setup, and the size of the bubble would determine the disruption to the geometry of the tube. It was unclear which of the two causes was more substantial at this stage. Therefore a new protocol was devised (fig. 3.8) to counter any disruption to measurement and simultaneously more data points were measured across a wider range of volumes. Any run where a bubble had crept into the system was discarded. Furthermore, the standard infusion rate was lowered to 20ml/min to gain more control since it was learned from the previous experiment that the infusion rate did not affect the length of tube formed (and therefore thickness).

This new SOP was tested via a repeat experiment, again measuring tube length against the effect of alginate concentration. Data points over a larger range of sample volumes were taken on this experiment to ensure more precise results.

Figure 3.9 shows the effect of optimised settings on tube length. It is immediately apparent that there was a marked improvement with linear trend consistency – all R^2 values are now above 0.99 – also shown by the data

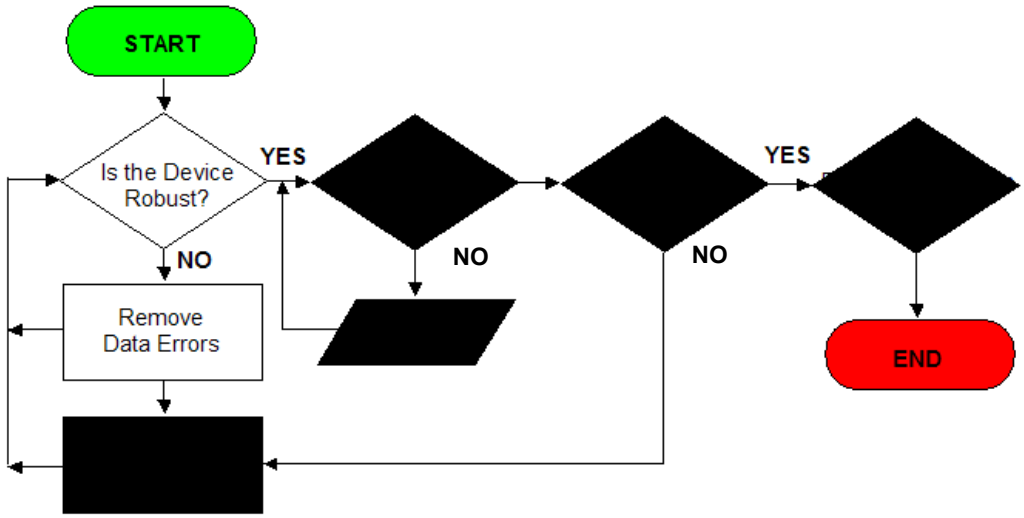

Figure 3.8 Flow diagram of experimental decisions for section 3.2.2.

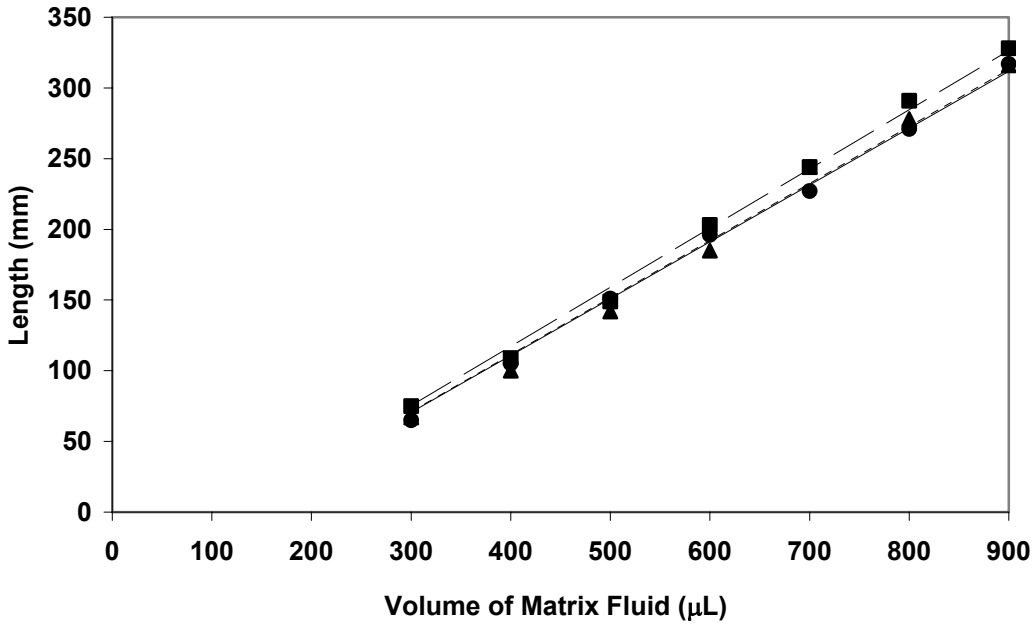

Figure 3.9 The effect of optimised device settings to tube length. Alginate concentrations of 0.5% (■); 0.75% (▲); and 1.0% (●) were tested and compared. Conditions used throughout: 300µm wall gap configuration; 20ml/min; 15°C; and 0.09M $CaCl_2$ concentration. Symbols represent the length of n=1 tubes per set volume. Broken, dotted and solid lines represent average lines of best fit for 0.5, 0.75 and 1.0% alginate concentrations, respectively. R^2 = 0.9958, 0.9912 and 0.9972, respectively. Mark 1 device used.

points being closer to the linear regression line. There are still two very different trends, but this time the 0.75 and 1.0% alginate concentration trends are overlapping.

The new protocol tightens the data errors previously found from section 3.2.1, however alginate concentration (within range of 0.50-1.00%) still plays a significant factor to tube length and tube wall thickness determination. Using optimised settings and a data points across a wider range taken reduced the variability of data points from the linear regression line. However physical limitations of the current device design may have introduced these large data variations despite improvements to protocols and techniques. From parallel OCT studies (see section 4.1.1), it was observed that the initial third of 20cm tubes (~7cm) were poor quality compared to the rest of the tube. It was therefore hypothesised that the initial lift-off of the spherical regulator may have caused poor uniformity tubes, affecting tube thickness and therefore tube length. After the initial ~7cm, the tube forming process is thought to stabilise. I.e. the variability may arise from the initial part of the tube formation process due to the design of the injector nozzle upon which the plastic spherical regulator sits.

3.2.3 The Mark 2 Design

The design of the device was altered to take into account the results from section 3.2.2 (fig. 3.10). The metal collar upon which the spherical regulator sat was modified to an 'eggcup' geometry (fig. 2.2). It was predicted that this design would enable a smoother initial lift-off from the device right from the start of tube formation, leading to more consistent tube wall thicknesses throughout, and hence more reliable tube lengths. The tight fit of the regulator sphere to the metal collar was also expected to eradicate the problems of air bubbles seeping into the process. Furthermore, the shortening of the injector nozzle reduced the dead space prior to tube formation from 112μl to 89μl. Triplicates per matrix fluid volume were also introduced to the protocol to reinforce reduction to inherent sampling errors.

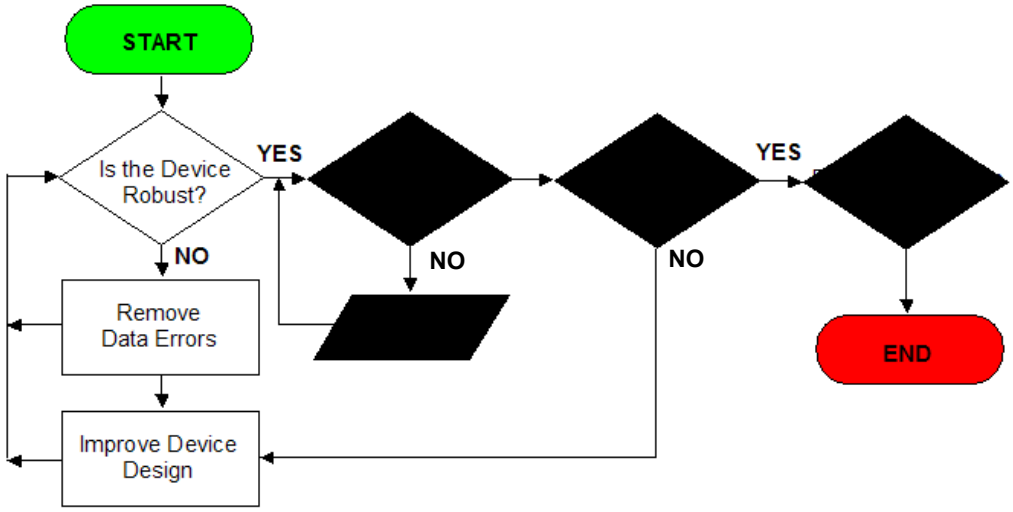

Figure 3.10 Flow diagram of experimental decisions for section 3.2.3.

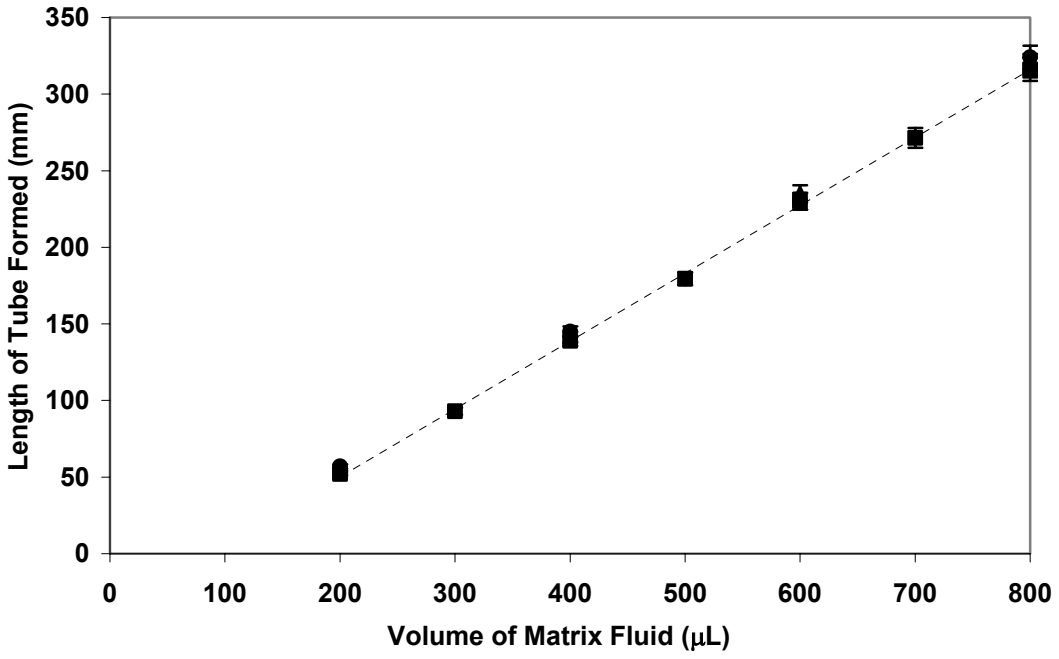

Figure 3.11 Effect of alginate concentration on tube length using the mark 2 device. Alginate concentrations of 0.5% (●); 0.75% (▲); and 1.0% (■) were tested and compared. Conditions used throughout: 300µm wall gap configuration; 20ml/min; 10°C; and 0.09M $CaCl_2$ concentration. Symbols represent the average length of replicate tubes of set volume. Number of replicates for: 0.50% (n=1), 0.75% (n=2), 1.00% (n=1). Dotted line represents line of best fit. Error bars represent CV across data points. $R^2 = 0.9995$.

With the mark 2 base unit in place, effect of alginate concentration was retested by a repeat experiment. It was hypothesised that the combination of improved protocol with the new mark 2 device would improve robustness of tube formation, manifested by a reduction in tube length CV for different alginate volumes.

Figure 3.11 shows the effect of alginate concentration with the mark 2 tube-forming device. Immediately obvious is the lack of variation between all 3 sets of data. This improvement could only be due to improvements in tube making protocol and the mark 2 base unit design – a fact verified by parallel OCT studies showing that the entire tube was now of reproducible quality including the first ~7cm (see 4.1.2). The CV remained small at an average of 2.4% throughout all 3 sets of differing alginate concentration data. An extremely important factor was the reduction in dead space within the device, mostly due to the shortening of the injector nozzle, which reduces tube "end effects" (fig. B2(ii) taken from Appendix B). This figure shows a more realistic view of tube formation for the mark 1 device. The fluid dynamics Theory assumes that the system is in steady state, but we know that the spherical regulator starts at 0 and quickly accelerates to speed, V. Alginate also flows upwards throughout tube formation, and hence thinning at the ends is inevitable. The extra material that should have formed tube wall of predicted thickness T_B is therefore applied to the rest of the tube, and therefore nominal tube thickness is T_0, which is marginally thicker than T_B. What must be noted however are the scales of the diagram – the vertical being 0-60 and the horizontal 0.8-1.0 – the vertical axis is therefore massively compressed to exaggerate the tube end effects. Due to the injection nozzle shape of the mark 2 base unit, it is theorised that these end effects are much reduced and therefore T_0 is closer to T_B than for the mark 1 device.

This experiment showed that the design of the device was finally robust enough to withstand changes to alginate concentration within the tested range.

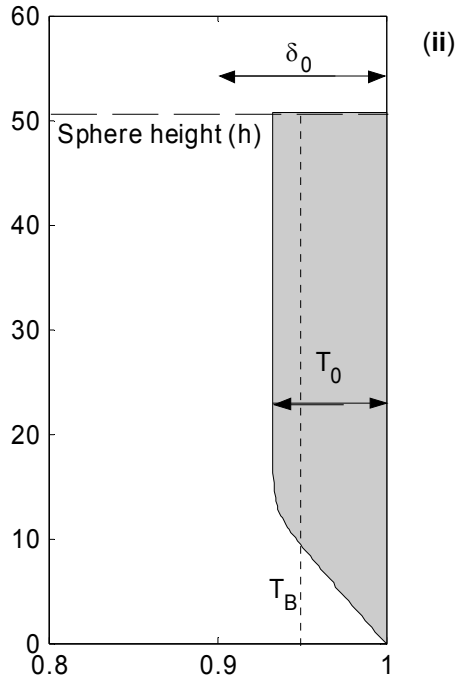

Figure B2 **(ii)** Calculated interface from tracking a number of particles distributed across the sphere-cylinder wall gap.

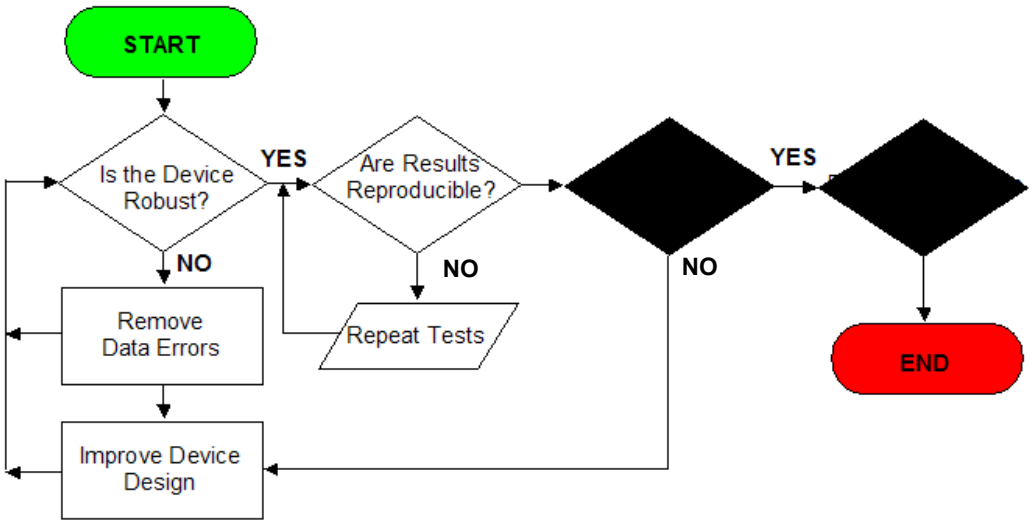

Figure 3.12 Flow diagram of experimental decisions for section 3.2.4.

3.2.4 Wall Thickness Reproducibility

The focus of this study was to demonstrate a high degree of reproducibility using only one alginate concentration (1.0%) in the tube forming process and the robustness of the experimental techniques, via repeated tube formation and measuring for any variation in tube length (fig. 3.12).

Figure 3.13 shows the reproducibility of tube formation for fixed reactor geometry. The R^2 value of 0.9995 shows the high linear correlation of volume with length of tube formed, as anticipated. This shows high "inter-tube" and "intra-tube" reproducibility – i.e. it was easy to predict the length of consistent thickness tube formed from any given volume of alginate, and this given value varies within a controlled margin of error from tube to tube. The CV from point to point on three replicates of data varied from 0.4 – 3.0% (as a % of tube length) and was 1.9% on average. At this stage, it would seem that control of tube length based on alginate volume within acceptable CV limits (Serp et al. 2000), and coupled with the high R^2 value, we could say these sets of data were highly reproducible.

With the assurance that the mark 2 device is no longer sensitive to data errors arising from fluctuations in alginate concentration, figure 3.13 shows a theoretical line (broken line) of tube lengths were there no contraction effects of fluid dynamics at play. As we can see, a ~340mm length tube would be equivalent to a 200mm tube with much thicker tube walls. As we know, such effects brought about by the drag of the spherical regulator on the matrix fluid do exist and therefore we must be able to predict tube wall thicknesses and compensate to achieve desired thickness tubes.

3.2.5 Investigation of Wall Gap Configuration

With reliable results now achievable from the mark 2 base unit design, we turn our attention back to the Theory and the end uses of the alginate tube. As we have discussed in Chapter 1, this thesis will not make

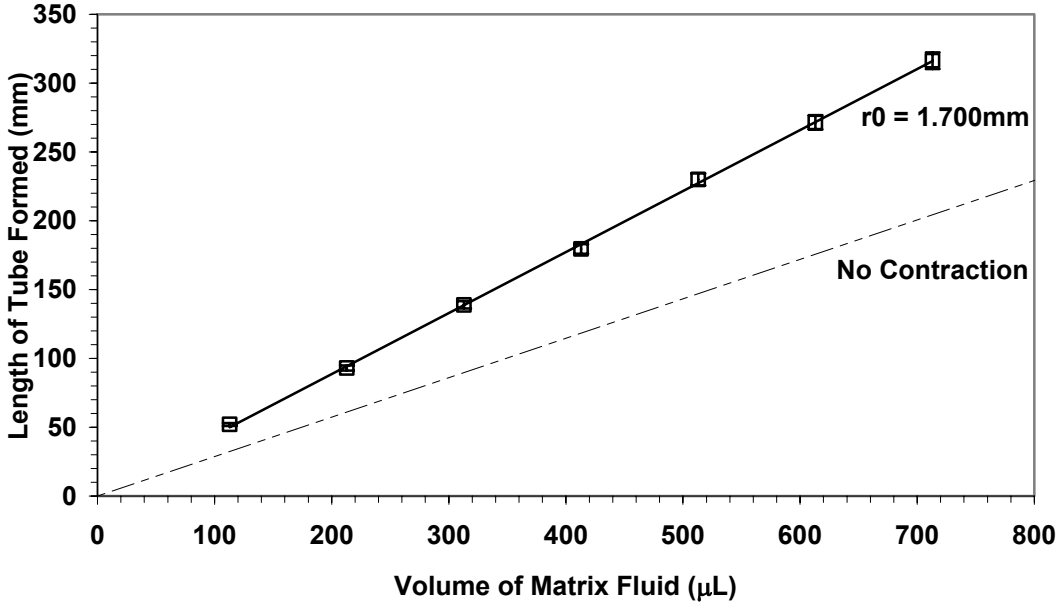

Figure 3.13 The reproducibility of tube using the Mark 2 tube formation device. Alginate volume, number of measurements and CV were: 200µl, (n=3, CV 1.9%); 300µl, (n=2, CV 3.0%); 400µl, (n=4, CV 3.0%); 500µl, (n=2, CV 0.4%); 600µl, n=4, (CV 2.6%); 700µl, (n=2, CV 1.3%); 800µl, (n=4, CV 1.1%). Line of best fit is shown (solid line), 0.443mm/µl (R^2 = 0.9995). Conditions used: capillary radius 2.0mm; sphere radius 1.7mm; wall gap thickness (per side) 0.3mm (300µm); 1% w/v alginate concentration; infusion rate 20 ml/min. 1% $CaCl_2$ infused. Symbols represent the average length of replicate tubes of set volume. Line (.._.._) is tube length assuming no contraction due to fluid flow effects.

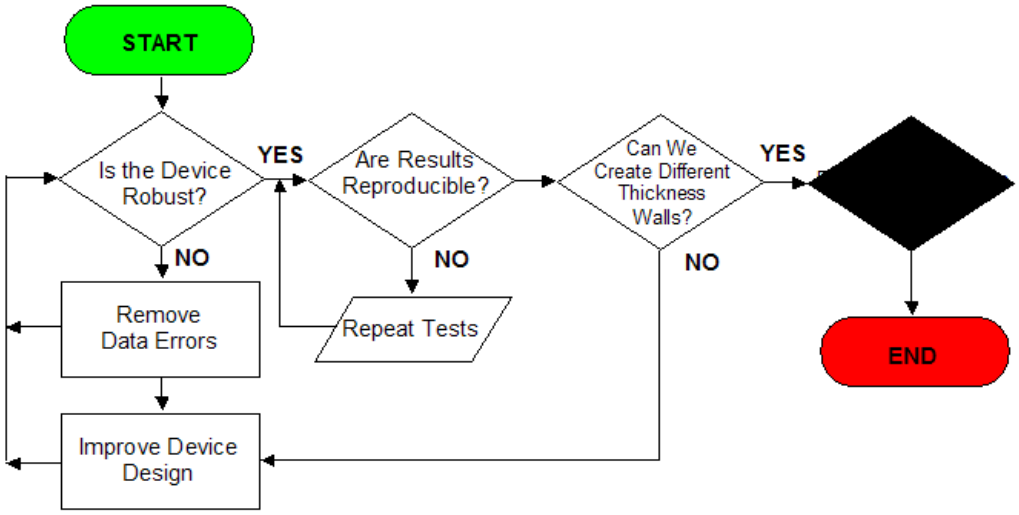

Figure 3.14 Flow diagram of experimental decisions for section 3.2.5.

prescribed end uses of the tubes created, but moreso, it will make suggestions as to the multiple uses of alginate tubes. Undoubtedly, end use will involve some type of cells integrated with the tube – either embedded in the tube walls, or lining the tube surface. With any cells, be them bacterial, mammalian or fungal, suspended or anchorage dependant, all require nutrients to survive and to grow. Nutrients such as oxygen, a food source and waste exchange is essential for any cell, and such nutrient exchange in our tubes will be proportionally limited by tube wall thickness (Glickis et al. 2004).

But how do we physically manipulate tube wall thickness? As we have described in section 3.1 regarding tube formation, the speed of the device and the ratio of gap-width (wall gap) to regulator diameter can subtly alter the tube wall thickness from a maximum thickness of $^2/_3$ gap width. However, since the deposited matrix layer is a direct result of the gap width created by the spherical regulator and the glass barrel wall, we can manipulate wall thickness by altering either glass barrel diameter, or spherical regulator diameter (or both). Therefore, we pose the question – is the system still reproducible when we alter glass barrel diameter and spherical regulator diameter (fig. 3.12)?

Tube formation robustness by the device was investigated experimentally using a combination of capillary and regulator dimensions (table 2.1). Device performance was again characterised by measurement of length of tube formed using different alginate volumes for each of the gap-width configurations studied. In all cases the alginate volumes reported were corrected for the dead volume of the system (89.0μl). The slopes of these graphs were then used to derive the tube thickness.

The 'average' thickness of the tube wall, T, was related to how the length of the tube formed varied with the volume of injected fluid:

$$T_0 = a - \sqrt{\left(a^2 - \frac{1}{\pi} \cdot \left(\frac{dL}{dV} \right)^{-1} \right)}, \qquad \text{(I)}$$

Table 2.1 **Matrix of wall gap configurations 'δ_0', showing the wall gaps for different sized glass cylinders and spherical regulators**

Cylinder Radius, a (mm)	1.825	2.000	2.000
Regulator Sphere Radius, r_0 (mm)	1.587	1.700	1.587
Gap Width, δ_0 (μm)	238	300	413

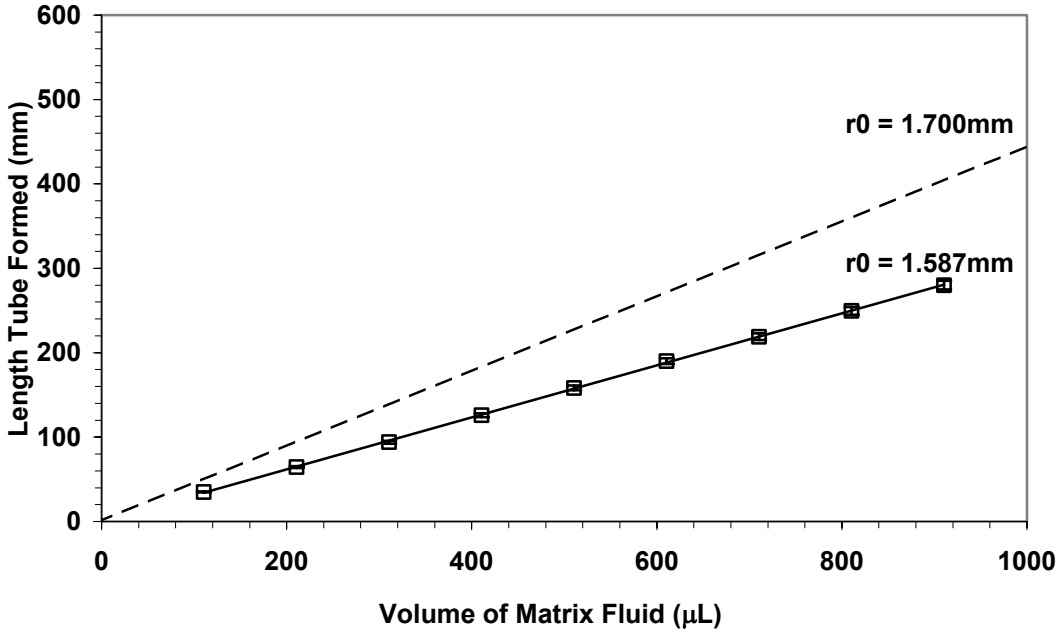

Figure 3.15 Effect of regulator sphere radius. Alginate volume, number of measurements and CV were: 200μl, (n=1); 300μl, (n=3, CV 5.5%); 400μl, (n=3, CV 4.9%); 500μl, (n=3, CV 0.8%); 600μl, (n=3, CV 1.6%); 700μl, (n=3, CV 1.1%); 800μl, (n=3, CV 2.4%); 900μl, (n=2, CV 0.3%); 1000μl, (n=2, CV 0%). Line of best fit is plotted as a solid line, slope 0.308mm/μl (R^2 = 0.9998). Capillary radius 2.000mm; sphere radius 1.587mm; wall gap thickness (per side) 0.413mm (413μm); 1% w/v alginate concentration; 1% $CaCl_2$; infusion rate 20 ml/min. Symbols represent the average length of replicate tubes of set volume. Data for line obtained using sphere radius of 1.700mm (- - - -) see figure 3.13.

Where;

a is the capillary radius and,

$^{dL}/_{dV}$ is the experimentally measured relation between length of tube formed (*L*) and volume of alginate used.

Figure 3.15 demonstrates the effect of altering the regulator sphere radius, for a fixed glass capillary radius. The dashed line shows the data from figure 3.13 and the new data for a sphere radius of 1.587mm. The resulting gap width of 413μm was wider and hence the same volume of alginate yielded much shorter tubes. Again the R^2 value of 0.9998 was extremely high and an average CV of 1.8% showed reproducible results despite this configuration change. Tube wall thickness for gap width of 300μm was back calculated to be 188.4μm ± 3.6μm (CV) using equation (I). The ratio of nominal tube wall thickness (T_0) and gap width (δ_0), T_0/δ_0 is shown to be 0.628 (close to the $^2/_3$ rule). Wall thickness for 413μm gap width was 277.3μm ± 5.0μm, giving a T_0/δ_0 ratio of 0.671.

Similarly, figure 3.16 shows the effect of altering the glass barrel radius for a fixed sphere radius. A smaller glass barrel for the same sphere means a gap width of 238μm and hence the same volume of alginate yielded much longer tubes with thinner walls. R^2 was found to be 0.9996, and average CV was 1.4%.

Therefore for a wall thickness for 238μm gap width, the back-calculated nominal wall thickness was 143.4μm ± 2.0μm, giving a T_0/δ_0 ratio of 0.603. A summary of the configurations, back-calculated tube thicknesses and T_0/δ_0 ratios has been constructed in table 3.2 (based on table 2.1).

This set of experiments shows that by altering either the glass barrel or spherical regulator diameters we can obtain different sized tubes with different wall thicknesses. These results also show how thicknesses obtained relate with the $^2/_3$ Approximation derived from the fluid dynamics Theory. The coefficient of variation for each of the gap width configurations were within peer-acceptable limits (Serp et al. 2000) indicating reproducibility

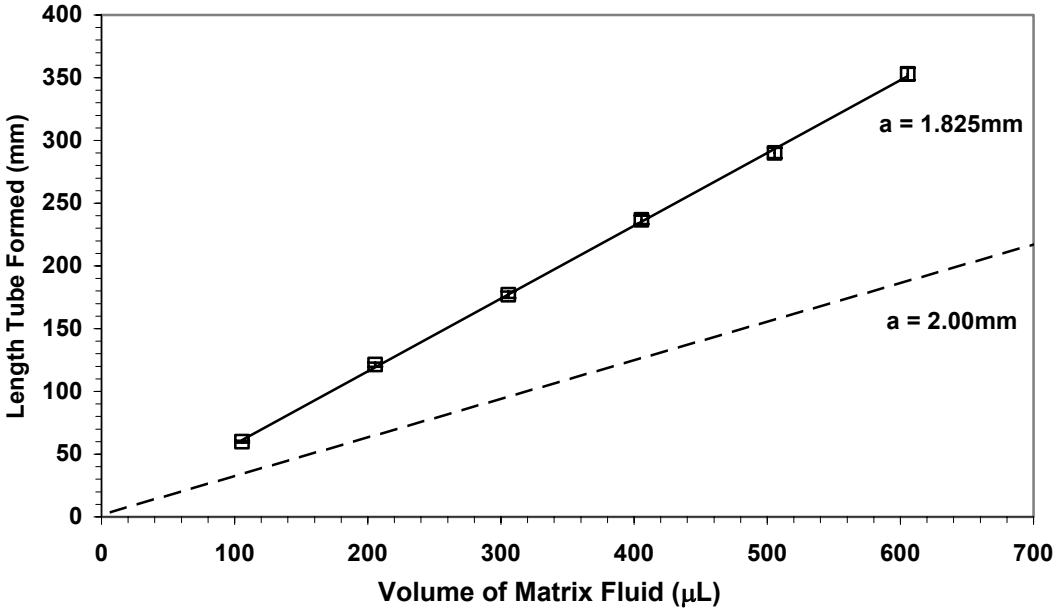

Figure 3.16 Change in capillary radius. Alginate volume, number of measurements and CV: 200μl, (n=1); 300μl, (n=3, CV 5.0%); 400μl, (n=3, CV 1.5%); 500μl, (n=3, CV 1.3%); 600μl, (n=3, CV 0.3%); 700μl, (n=1). Line of best fit is 0.580mm/μl (R^2 = 0.9996). Capillary radius 1.825mm; sphere radius 1.587mm; wall gap thickness (per side) 0.238mm; 1% w/v alginate concentration; 1% $CaCl_2$; infusion rate 20 ml/min. Symbols represent the average length of replicate tubes of set volume. Data obtained using a capillary of radius 1.825mm (- - - -) see figure 3.15.

Table 3.2 **Matrix of wall gap configurations 'δ_0', showing the wall gaps and nominal wall thicknesses 'T_0' of tubes for different sized glass cylinders and spherical regulators used in this thesis**

Cylinder Radius, a (mm)	1.825	2.000	2.000
Regulator Sphere Radius, r_0 (mm)	1.587	1.700	1.587
Gap Width, δ_0 (μm)	238	300	413
Derived Tube Thickness, T_0 (μm)	143.4	188.4	277.3
T_0 / δ_0	0.603	0.628	0.671

of the device despite changes in gap width size. This robust level of control, alongside the Theory to predict resultant wall thickness allows reliable control of tube wall thickness, and thus control of nutrient and waste exchange of any cells present in the alginate structure used as either a macro-encapsulation device or tissue engineering product.

3.2.6 Effect of Altering Propelling Fluids

As a final experiment to conclude these studies of wall thickness, robustness and how they relate back to the fluid dynamics Theory, we consider the extension of the Theory outside of the alginate-$CaCl_2$ system. Nowhere in section 3.1 is it mentioned that there are limitations to the theoretical prediction of tube wall thickness, or that even a reaction need occur and a tube needs to be formed. We therefore tested the robustness of the Theory and the system applied to different propelling fluids – both reacting and non-reacting and see how they compared to the $^2/_3$ Approximation derived from equation (14) of the Theory (fig. 3.17).

The effect of changing propelling fluids is shown in figure 3.18. The range of fluids looked at included alginate, N-saline, WFI, 0.09M $CaCl_2$ and 0.05M $BaCl_2$. Each fluid combination gave a slightly different slope, each graph's gradient equating to a different wall-thickness. The graphs appear 3 distinct groups formed – the reacting systems ($BaCl_2$ and $CaCl_2$), the non-reacting systems (WFI and N-saline), and the viscous systems (alginate). It would appear that this range of gradients showed a trend of increasing tendency to react and cross-link – the alginate giving a less steep slope, i.e. $BaCl_2$ is a stronger linking agent than $CaCl_2$, and these two reacting infusing agents had similar trends at much less-steep gradients than all other infusion materials. The other propelling fluids all had steeper slopes indicating longer tubes and thinner deposited layers (tube walls).

A further experiment involving all 3 gap width configurations using 54% glycerol matrix fluid infused with 54% glycerol propelling fluid and WFI

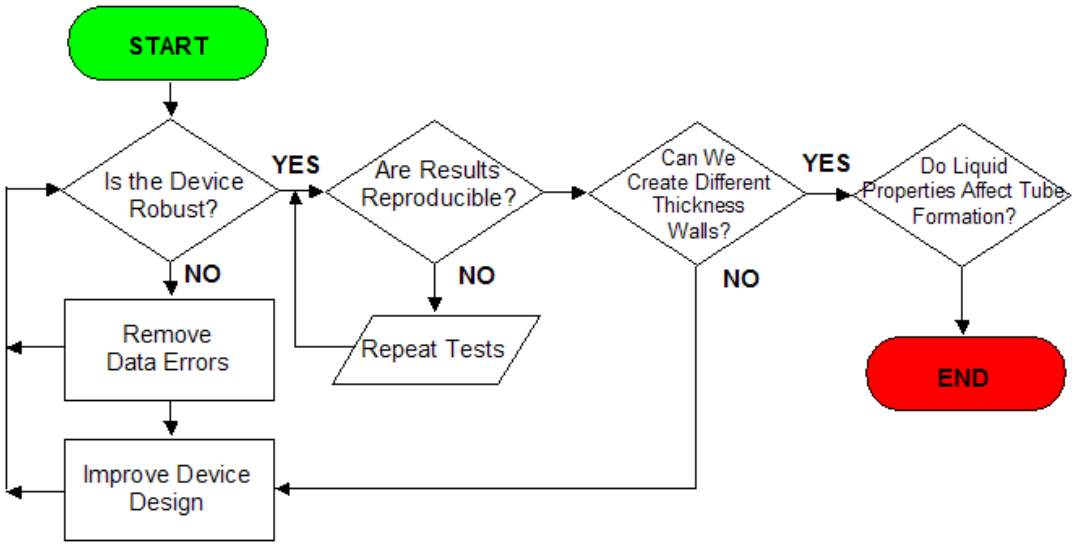

Figure 3.17 Flow diagram of experimental decisions for section 3.2.6.

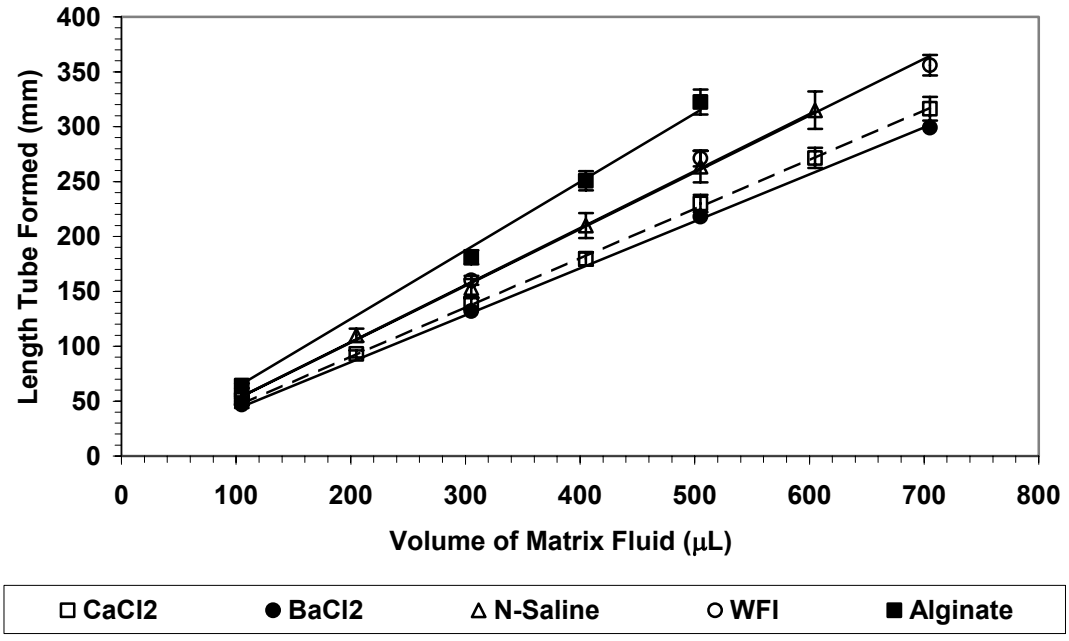

Figure 3.18 Effect of changing propelling fluids. Each data point represents the average of a number of measurements and the range of values observed. All combinations involved 1.0% alginate as a matrix fluid. Measurements using 0.09M $CaCl_2$ are denoted (- - - -) see figure 3.13. Alginate volume, number of measurements and CV of the results for:

0.05M $BaCl_2$ data was: 200μl, (n=1); 400μl, (n=1); 600μl, (n=1800μl, (n=1). Line of best fit was 0.421mm/μl (R^2 = 0.9998).

0.9% N-saline data was: 200μl, (n=2, CV 14.9%); 300μl, (n=1); 400μl, (n=2, CV 2.8%); 500μl, (n=1); 600μl, (n=2, CV 1.3%); 700μl, (n=2, CV 2.7%). Line of best fit was 0.529mm/μl (R^2 = 0.9989).

WFI data was: 200μl, (n=2, CV 0.6%); 400μl, (n=2, CV 2.7%); 600μl, (n=2, CV 7.3%); 800μl, (n=1). Line of best fit was 0.506mm/μl (R^2 = 0.9972).

1.0% w/v alginate was: 200μl, (n=2, CV 4.4%); 400μl, (n=2, CV 0.8%); 500μl, (n=2, CV 3.8%); 600μl, (n=2, CV 5.0%). Line of best-fit was 0.644mm/μl (R^2 = 0.9971).

infused with WFI was carried out to further ascertain what was occurring in the system (summary table 3.3). These results were then plugged back into figure 3.4 to see how they all compared with the Theory. Figure 3.19 shows the collated results. This time the $^2/_3$ Approximation has been added, represented by a bold green line. It is clear that there are only two groups of data, 'reacting systems' and 'non-reacting systems'. Whilst first thought that the reacting systems, having a T_0/δ_0 close to $^2/_3$ was a good indication of results falling within thicknesses theoretically predicted by equation (14) (original thin green line), it now appears that these results are in fact in error. By plotting equation (H) (bold green line) we can see that in fact the non-reacting systems are closer to the theoretical predicted wall thickness than the reacting systems. But did we not say a T_0/δ_0 of $^2/_3$ **was** the Theory? No, because it is dependent on the ratio δ_0/a, i.e. the gap width with the cylinder radius. As gap width becomes very small, we approach a maximum T_0/δ_0 of $^2/_3$. So what is happening inside the system?

What is now thought is that the reacting systems freeze the thickness of the deposited alginate layer immediately upon contact, and therefore flow contraction effects created by drag of the matrix fluid up the glass barrel walls are rendered negligable. This resulted in thicker walls of solidified alginate much closer to δ_0, hence shorter tubes and a less steep gradient in figure 3.18. We know from literature that $CaCl_2$ is a fast cross-linker and $BaCl_2$ is yet faster (Kuo and Ma 2001). The systems closest to the Theory in fact were alginate infused by WFI, alginate infused by saline and WFI infused with WFI. The other two viscous systems – glycerol infused with glycerol and alginate with alginate were thought not to form tubes due to the high viscosity of the fluids used being beyond the handling capacity of the syringe pump. Theoretically, viscosity should not affect results, but when it physically retards the formation process creating non-linear infusion rates, then this may go to explain why results did not fit. It was observed that the fluid flow for these viscous propelling fluids would continue after pressing stop on the syringe driver, due to the vaccuum of pressure formed. However, the interpretation of the findings from figure 3.19 is the subject of some debate within the department.

Table 3.3 Summary Table for All Alternate Propelling Fluid Experiments

Matrix Fluid	**1% Alginate**	**1% Alginate**	**1% Alginate**	**1% Alginate**	**1% Alginate**	**1% Alginate**	**1% Alginate**	**98% Glycerol**	**WFI**
Propelling Fluid	**1% $CaCl_2$**	**1% $CaCl_2$**	**1% $CaCl_2$**	**1% $BaCl_2$**	**(0.9% w/v) Saline**	**WFI**	**1% Alginate**	**98% Glycerol**	**WFI**
Cylinder Radius, a	1.825	2.000	2.000	2.000	2.000	2.000	2.000	2.000	2.000
Sphere Radius, r_0	1.587	1.700	1.587	1.700	1.700	1.700	1.700	1.700	1.700
Gap Width, δ_0 (μm)	**238**	**300**	**413**	**300**	**300**	**300**	**300**	**300**	**300**
Nominal Thickness, T_0 (μm)	143.4	188.4	277.3	198.9	156.6	164.0	127.7	125.6	140.2
T_0/δ_0	0.603	0.628	0.671	0.663	0.522	0.547	0.426	0.419	0.467
Bead Density (g/cm^3)	0.960	0.920	0.960	0.920	0.920	0.920	0.920	0.920	0.920
Matrix Density (g/cm^3)	1.01	1.01	1.01	1.01	1.01	1.01	1.01	1.26	1.00
Propeller Density (g/cm^3)	1.04	1.04	1.04	1.04	1.03	1.00	1.01	1.26	1.00
Matrix Viscosity (g/cm.s)	6.71	6.71	6.71	6.71	6.71	6.71	6.71	14.9	0.0131
Propeller Viscosity (g/cm.s)	0.0140	0.0140	0.0140	0.0140	0.0140	0.0131	6.71	14.9	0.0131

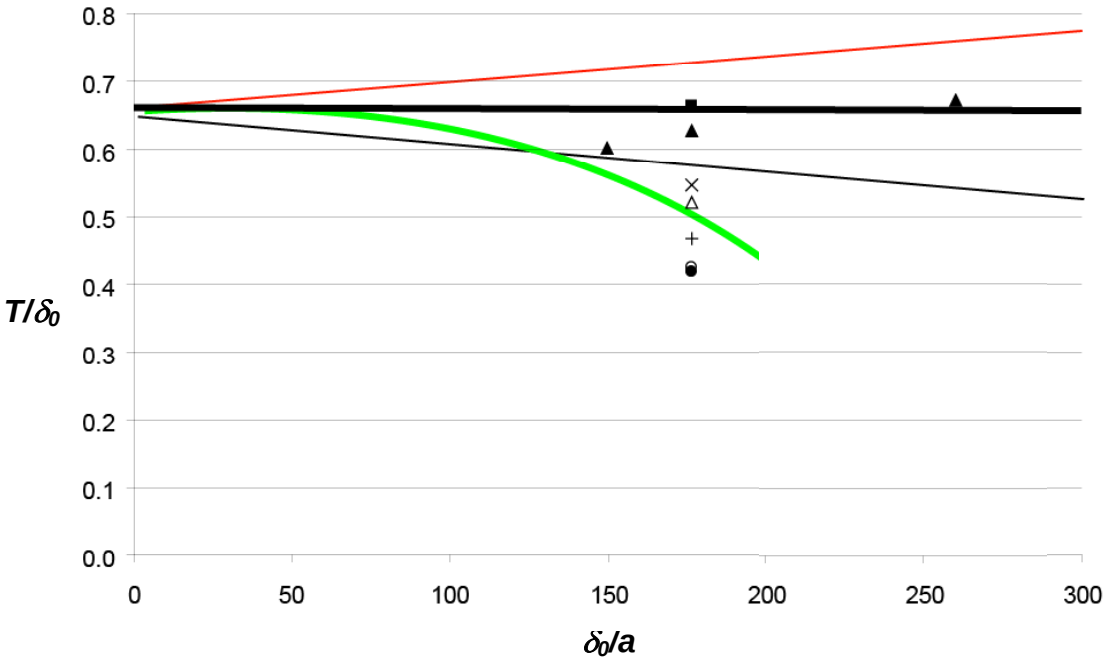

Figure 3.19 Tube wall thickness, 'T' as a fraction of gap width, 'δ_0' versus gap width as a fraction of cylinder radius 'a'. Symbols indicate: alginate infused with $CaCl_2$ (▲); alginate infused with $BaCl_2$ (■); alginate infused with N-saline (Δ); alginate infused with WFI (x); alginate infused with alginate (○); 54% glycerol infused with 54% glycerol (●); and WFI infused with WFI (+). The predicted wall thickness (T_B) based on the $^2/_3$ Approximation (H) is plotted as the bold green line, whereas the bold black line represents $T/\delta_0 = 0.66$.

In summary, we have taken a tube-forming device, created a robust protocol and redesigned the base unit to create more reproducible results. We have shown that the data is reproducible, time after time, and unaffected by fluctuations in alginate concentration within the range of 0.5-1.0%, nor by fluctuations in constant infusion speeds ranging from 20ml/min to 50ml/min. We have shown that we can create tubes of varying wall thicknesses by changing gap widths, either by using a different diameter glass barrel or a different diameter spherical regulator, and that the device is robust enough to withstand these changes to gap width configuration. Finally we have shown that the developed Theory can be applied to any system, although non-reacting systems that do form a tube successfully are best described by the $^2/_3$ Approximation. Due to the cross-linking reaction involved in any alginate-multivalent ion system, the resultant thickness of the tube walls will depend on two things: 1. the speed of the reactant (Kuo and Ma 2001) at the time of tube formation, and 2. shrinkage effects that occur over time after tube formation (Quong et al. 1998).

A final point to add is that all tube thickness were back-calculated by equation (I) only, and not measured directly – it was assumed in all cases that all sides of the tube were uniform. Indirectly measuring wall thickness via tube length is clearly not the way forward, especially as we've just discussed the thickness of alginate tube walls are subject to more factors than just the wall gap configuration of the device alone.

3.3 SUPPLEMENTARY EXPERIMENTS

3.3.1 Alginate Viscosity Data

Impact of alginate viscosity to tube length (brought about by change in alginate concentration) is a more complex variable. Alginate viscosity can be affected by large changes in temperature, autoclaving and time-degradation

– these are variables we cannot easily control. Although the Theory clearly states that viscosity does not affect the fluid mechanics of tube formation, huge shifts to viscosity beyond the physical capabilities of the pump handling capacity could affect tube formation as we have seen in section 3.2.6, and this could be reflected in the tube length. Although the Theory predicts that viscosity changes cause no change to tube wall thicknesses, it would be a good idea to gain some insight on the change of viscosity with temperature. It must also be noted that temperature was controlled at 10-15°C in all experiments. In order to collect viscosity information, a viscometer was used.

Figure 3.20 shows the impact of temperature and alginate concentration on viscosity. This graph suggests that the viscosity (cP) to alginate concentration (%) relationship become less linear with changing temperature, a well-known fact that alginate is pseudo-plastic as opposed to Newtonian (Manojlovic et al. 2006), i.e. it is a shear-thinning fluid. However, since alginate concentrations are fixed at 1.0% throughout late experiments and room temperatures are controlled, then any large changes to viscosity should be minimal. A summary of results can be seen in table 3.4.

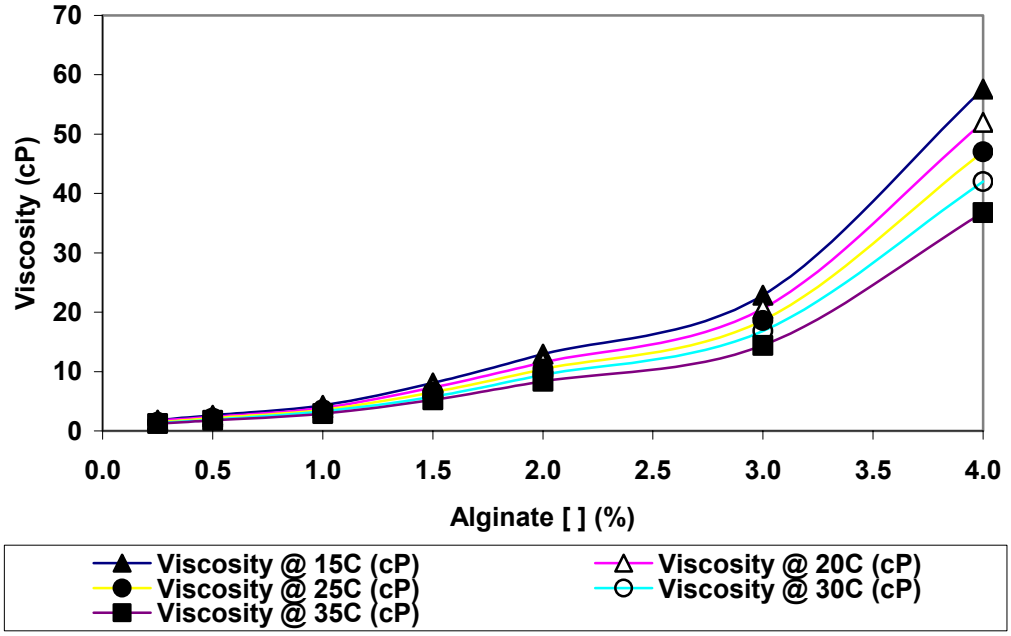

Figure 3.20 Effect of temperature and alginate concentration on alginate viscosity. Symbols represent n=1 viscosity measurements per set alginate concentrations. Solid lines represent trends through data sets. Temperatures tested were: 15°C (▲), 20°C (Δ), 25°C (•), 30°C (○) and 35°C (■). Alginate concentration tested at 1.00%. Temperature changes were manipulated using ice and a water bath, and all readings were taken using a viscometer (Brookfield, Massachusetts, USA).

Table 3.4 **Effect of varying alginate concentration, temperature and hence viscosity with respect to nominal wall thickness (T_0)**

Alginate Conc. (%)	Temp. (°C)	Nominal Wall Thickness, T_0 (μm)			Viscosity (CP)
		δ_0 = 238	δ_0 = 300	δ_0 = 413	
0.50	10.0		0.188		58.2
0.75	10.0		0.188		302.4
1.00	10.0	0.158	0.189	0.273	671.2
1.00	20.0	0.159	0.187	0.285	597.6

4 Monitoring Methods

Chapter 3 left one huge question unanswered – can we measure tube wall thickness? Although we have a seemingly robust system design and protocol, and even a mathematical model to predict tube wall thickness, we did not once verify actual tube wall thickness directly. Instead we resorted to back-calculation based on tube length and geometry of a cylinder. In this chapter we will not only look at methods to directly measure tube wall thickness at the time of tube formation, but also tube wall thickness after tube formation, that is, we will consider the added complexity of tube wall shrinkage (Kuo and Ma 2001). In addition we will look at other methods to quantify the size and number of any particle component that maybe introduced to the tubular constructs, since large particles may disrupt the wall thickness consistency of tubes made. Furthermore, we will look at introducing controls where possible to minimise variations introduced during mammalian cell culture.

Therefore the aims of this chapter were: to establish a direct method of measuring tube wall thickness immediately during and after tube formation to capture quality and shrinkage information of alginate tubes; to institute a method to capture particle size data; to find a way of improving consistency in particle quantification; to determine the impact of adding biological cells to the system; and to ascertain factors to help control cell aggregate size.

4.1 OPTICAL COHERENCE TOMOGRAPHY (OCT)

4.1.1 Primary Tube Scans

Up until this stage, tube geometry was measured as a function of tube length only. Wall thickness was back calculated using tube length and equation (I) from Chapter 3. There had been no direct way of measuring the walls of the alginate tube formed to verify the validity of the results (fig. 4.1). For this

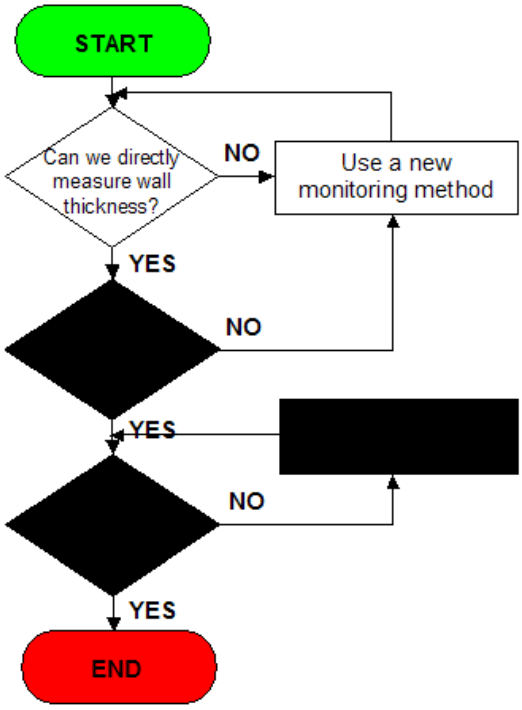

Figure 4.1 Flow diagram of experimental decisions for section 4.1.1.

task, we incorporated a technique known as Optical Coherence Tomography (OCT), which allows high-resolution, real-time imaging *in situ*. Due to section 4.1 being run parallel to Chapter 3, at the time the latest device version was the mark 1 base unit, which was used for this initial experiment.

OCT yielded the brown and orange scans shown in figure 4.2. Firstly, it must be discussed how this figure is read. Because OCT is a light source based technique, the signals used to construct these images are based on changes in refraction index as the laser beam passes from one medium to another. Therefore, although certain segments of the diagram are similar in shade of colour, this does not mean they are the same material. From knowledge of the experimental setup and taking the labelled cross-sectional scan, we know that the initial segment of all OCT scans must be part of the glass wall of the barrel. As we cross from glass to $CaCl_2$, we see the first bright orange line. Then as we cross from $CaCl_2$ back into alginate, we see a thick orange band that represents the alginate tube wall. Because this wall is embedded with glass beads, the light beam constants crosses in and out of glass-alginate boundaries, clarifying the alginate tube walls so precisely. In the centre of the alginate tube wall is $CaCl_2$ fluid.

As we can see from figure 4.2, taking 3 points along either side of the tube formed and a cross-sectional scan (greyed area on the tube schematic), the OCT image clearly shows the general uniformity of the tube formed. To aid spatial visualisation, the bottom three images have been turned 180°. From these images, table 4.1 was constructed (fig. 2.11 has been reiterated for convenience). Several key findings can be deduced from this table. It can be seen from the table, that it was characteristic of a formed tube to have walls of the same thickness on one side, i.e. taking tube 3 for example, points A, B and C on one tube face give an average wall thickness of 189μm, whilst points D, E and F on the other face give an average wall thickness of 129μm. That is, if a tube is formed with a thicker wall on one side, this trait will continue to run throughout the length of the tube (we will see this in more depth in sub-section 4.2.1). The table verifies that tubes are generally well formed, with relatively low CV ranging from 3-7%. Tube 3 however has a CV

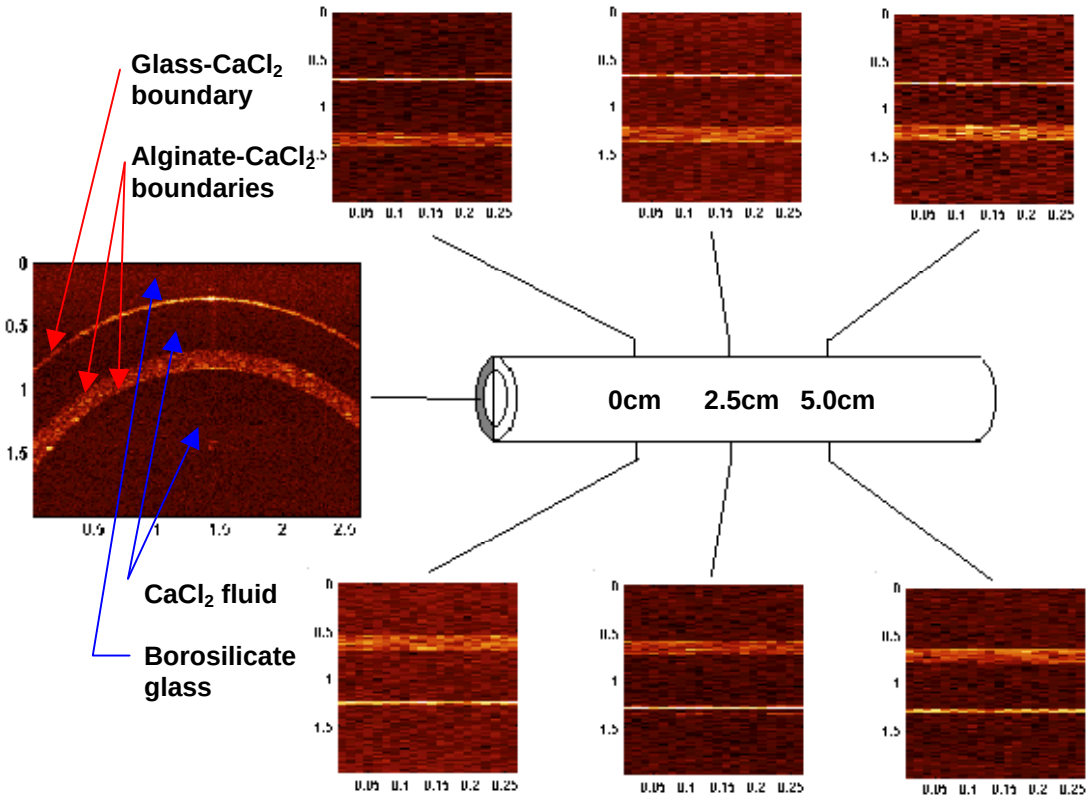

Figure 4.2 OCT tube scans of a pure alginate tube containing glass beads. Positions of images are indicated in relation to their position on the tube. Tubes were formed using base unit design mark 1.

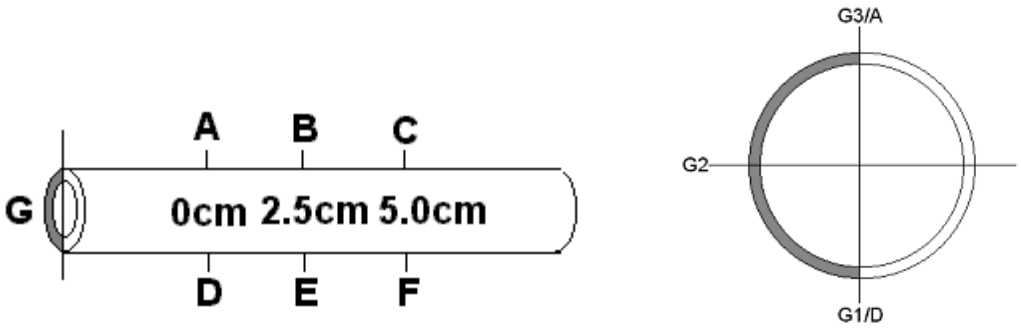

Figure 2.11 Experimental scanning setup and nomenclature used for Mark 1 primary OCT experiment. Point A is 180° from D on the opposite face of the glass capillary and so on. Points A, B and C are 2.5cm apart, point B lying in the centre of the glass capillary. Scan G was a half cross-section taken from a random point in the tube. The table was constructed using G1, 2 and 3 terminologies, taken from set points from the cross-section. G3 corresponds to point A, and G1 to point D.

Table 4.1 **Thickness measurements taken from alginate tubes with glass beads.**

% Conc.	A	B	C	D	E	F	Average	SD	CV
1.00%	157	157	157	166	157	148	157.00	5.20	3.31
0.75%	139	148	166	157	157	157	154.00	8.49	5.51
0.50%	189	189	189	123	132	132	159.00	30.15	18.96
0.50% *	170	189	189	160	160	170	173.00	12.03	6.95

Units of measurement (μm) derived from Matlab images from scan of tube (figure 4.1).

* Denotes 0.50% alginate with 0.005g/ml glass beads.

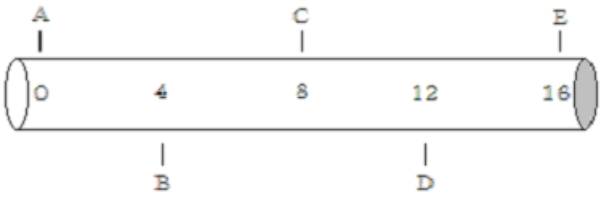

Figure 2.12 Experimental scanning setup and nomenclature used for Mark 2 OCT tube scans. Points A, C and E were 180° from B and D on the opposite face of the glass capillary. Points A to E are 4cm apart, point C lying in the centre of the glass capillary.

of over 18%. This proves OCT is a good tool, with it in place we can instantly differentiate good from bad tubes by setting a level of tolerance based on wall thickness variation – tubes were all checked visually prior to OCT scanning via blue dye and deemed sufficient quality before transporting to Cranfield for OCT analysis. Visibly, measuring tube length and assuming uniformity to back-calculate wall thickness has a blind spot that OCT cures. Interestingly, tubes 1-3 have a decreasing level of alginate concentration, and tube 3 has the lowest concentration of 0.50%. From Chapter 3, we discussed the sensitivity of the mark 1 design to alginate fluctuations that prompted the mark 2 design. Additionally, we see an average tube thickness of ~157μm for the first 3 tubes at 0.0005g/ml glass beads, yet a 173μm wall thickness for tube 4 at 0.005g/ml glass beads (x10 concentration) – clearly the concentration of the glass beads has altered the thickness of the tube formed. One also maybe wondering why the thickness of 157μm differs greatly from the 188.4μm (for gap width configuration, δ_0 of 300μm) seen from table 3.2 from Chapter 3. The explanation to both these observations is simple – final thickness of the alginate tube walls is dependent on two macro-factors: (1) the gap width configuration, δ_0 during tube formation; and (2) shrinkage (Kuo and Ma. 2001) after tube formation. In Chapter 3, we measure tube length immediately after tube formation, and here we form tubes that shrink and then set before they are scanned at a different site. A final point, perhaps not immediately obvious is that only the central third of the tube is scanned. The tube is 15cm long, yet from preliminary scans, we could see that the first third of the tube was poor quality – another point raised in section 3.2.2.

Whilst it is obvious that OCT is an excellent monitoring tool, due to the ability of the device to scan a tube non-destructively, *in situ* and through air (Fujimoto et al. 2000), we must further consider several points. The walls of the alginate tubes are in the order of 100-200μm thickness yet the resolution of the OCT scanner is 10μm (i.e. each pixel represents 10μm), meaning an accuracy of $\pm$10μm. OCT devices can reach 1μm resolution but such light sources are increasingly expensive with increasing resolution. Because OCT work is carried out in collaboration with Cranfield University, Silsoe,

shrinkage – a unique factor of alginate-$CaCl_2$ structures – must be taken into consideration when predicting tube wall thickness. Finally, this section highlighted that the most important stage of tube formation being right at the start. Any slight instability in flow would carry through the length of the tube and create a thinned wall on one side – which was the main justification for the redesign of the base unit geometry.

4.1.2 Mark 2 Tube Scans

In order to verify the efficiency of the mark 2 design, OCT was performed once again on enhanced tubes.

Results have been tabulated (table 4.2) and fig. 2.12 reiterated for convenience. At first glance, results seem disappointing considering that lower CV values were achieved for the mark 1 device. Here, we see a range of CV values from 5.9-16.3%. But it is easy to forget that the initial base unit design only produced successful tubes a fraction of the time (data not shown). Also, the previous design yielded tubes where only the central third was adequate for OCT analysis. Moreover, there appears to be no evidence of tube lopsidedness from all 3 gap-width configurations.

A gap width, δ_0 of 238μm gave a wall thickness of 115.6; a gap width, δ_0 of 300μm gave a wall thickness of 144.2; and a gap width, δ_0 of 413μm gave a final wall thickness of 205.6. In addition to fluid mechanics effects, this effect termed “shrinkage” appeared to give a final tube wall thickness in the region of ½ of gap width configuration, δ_0 for all three tubes.

4.1.3 Shrinkage Effects

Sections 4.1.1 and 4.1.2 show a discrepancy between the tube wall thicknesses during tube formation (fluid dynamics contraction effects applied) and much later after tube formation. We now know from literature that this

Table 4.2 **Table of verification OCT tube scan results. Thickness measurements were taken from alginate tubes with glass beads.**

Gap Width, δ_0	A	B	C	D	E	Average	SD	CV	% Shrinkage
238μm	107	100	100	150	121	115.6	18.8	16.3	48.6
300μm	171	129	143	114	164	144.2	21.2	14.7	48.1
413μm	186	200	214	207	221	205.6	12.1	5.9	49.8

Units of measurement are μm derived from Matlab images from scan of tube.

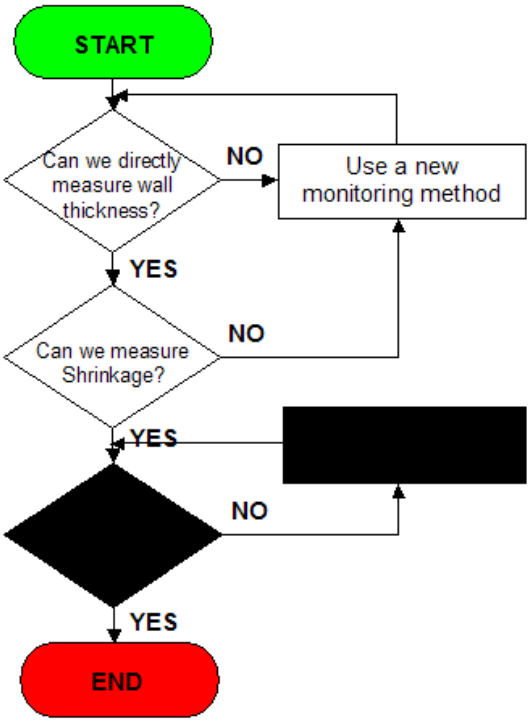

Figure 4.3 Flow diagram of experimental decisions for section 4.1.3.

discrepancy is due to shrinkage. Shrinkage is a term used to describe water loss from cross-linked alginate structures with time. When multivalent ions first come into contact with alginate, depending on the speed of gelation, structure thickness, G monomer length, and G:M ratio of the alginate involved, the reaction plane may solidify before the ions have saturated the whole structure. This results in a solid surface but varying degrees of solidity in the structure core. As these ions diffuse slowly through the structure, water molecules are lost and the remaining alginate G monomers are cross-linked resulting in further reduction of structure diameters as whole structure solidifies. This process typically lasts ~10 mins for alginate beads, but can last up to 3 days depending on alginate thickness (Martinson et al. 1989).

Many indirect methods have been used to measure the effects of shrinkage, from weight loss as water molecules are shed to tilting blocks of alginate and taking the time it no longer flows (Kuo and Ma 2001). In this section we aim to use OCT to precisely measure shrinkage effects of our alginate tubes (fig. 4.3). It is so far unknown how much shrinkage will occur as a result of formation and the time frame involved. In order to better understand the relationship between time to set and actual thickness change, OCT was used to monitor tube wall thickness in real-time, i.e. during setting, once the tube was formed. This was achieved by analysing at a set point and measuring tube wall thickness with time. A new part of the Matlab programme was developed by Cranfield University especially for this purpose, which takes into account situations where the tube is attached or not attached to the glass barrel wall.

From the scattergrams seen in figure 4.4, shrinkage can be clearly seen occurring. A rapid drop in wall thickness is followed by a plateau, roughly occurring during the initial 10-15 minutes. This time is within the range expected for the thickness of alginate specimens created (Serp et al. 2000). Section 4.1.1 experienced differing wall thickness with concentration of glass beads added. Here, we see an initial wall thickness of ~225μm falling to ~180μm within 10 mins for the pure alginate tube (fig. 4.4*a*). Conversely, we see an initial wall thickness of ~270μm dropping to ~200μm

(**a**) (**b**)

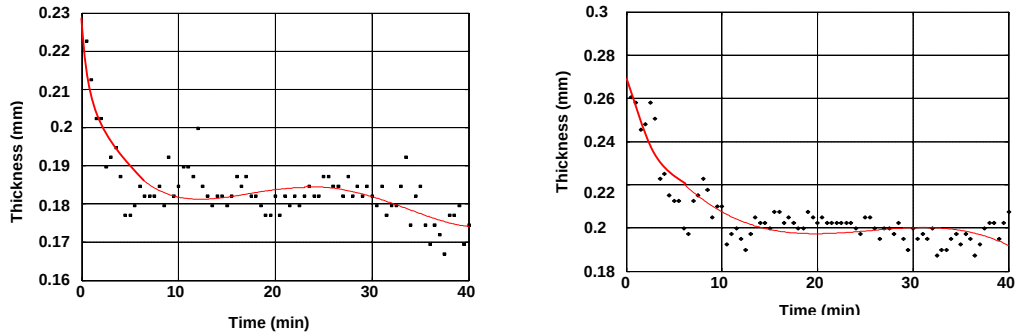

Figure 4.4 OCT scattergrams showing shrinkage of tube wall thickness with time. 2 conditions studied included: (**a**) pure alginate tube; (**b**) alginate tube containing inert glass beads at 0.0005g/ml. Red line represents line of best least squares fit, based on a polynomial approximation through all data points.

(**a**) (**b**)

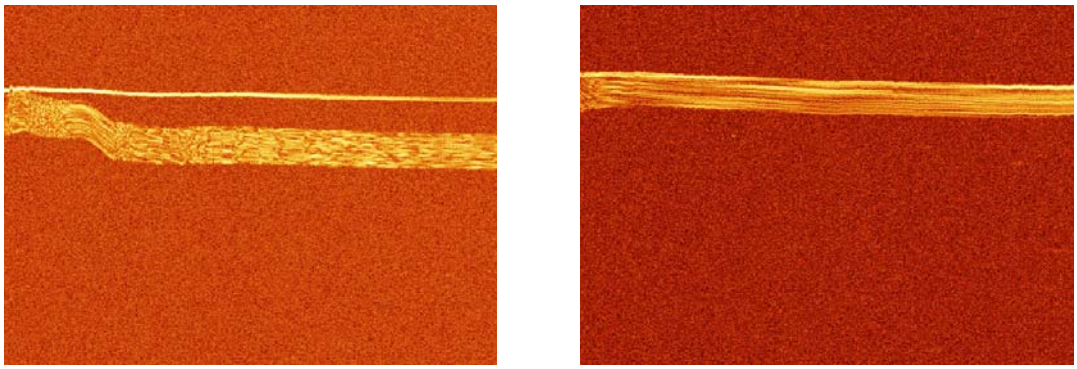

Figure 4.5 OCT images corresponding to scattergrams from figure 4.4 showing shrinkage of tube wall (y-axis) with time (x-axis). 2 conditions studied included: (**a**) pure alginate tube; (**b**) alginate tube containing inert glass beads at 0.0005g/ml. Red line represents line of best least squares fit, based on a polynomial approximation through all data points.

for the glass bead encapsulated tube (fig. 4.4*b*). This firstly confirms that solid glass beads are not a good model for biological cells, and that they do indeed affect tube thickness. The follow-on question is therefore – would biological cells affect tube wall thickness also (see Chapter 5)? However, what we expect to see is a 188μm initial thickness, falling to 150μm within 10-15 mins. This anomaly cannot be isolated, although it could be the result of a number of factors. In all previously experiments, alginate was prepared and immediately used to create tubes, which were left to set and then refrigerated for OCT analysis the following day. Here, due to the timing of the experiment, we were required to prepare alginate at UCL, and transport all materials and machinery to Cranfield University, Silsoe to carry out the experiment. During transit, temperature was not controlled, nor was it controlled in the Cranfield lab. The time difference from makeup of alginate powder to use of hydrogel could account for this difference in wall thickness. Ultimately it could either be due to concentration differences of the $CaCl_2$ beyond the range of 0.05-0.09M tested at UCL, or due to large viscosity differences due to fluctuations in temperature. Figure 4.5 shows us the corresponding images for figure 4.4. It must be pointed out that the x-axis is not length, as in previous OCT images, but time. This image is a time compilation of A-scans at a set point. We can see in figure 4.5*a* how the tube becomes detached from the glass barrel wall as the whole tube shrinks. Figure 4.5*b* shows a perfect tube. The striated pattern is due to no disruptions during the timed-experiment. Any vibration to the device during scanning would have resulted in a distorted image.

This experiment contains some anomalies with regards to previous wall thicknesses. Without UCL's own OCT team and apparatus, we cannot rule out all the factors that may have affected tube wall consistency. However, were the process to be commercialised, OCT would certainly be an integral, on-site part of it. Nevertheless, this experiment does show shrinkage visually in a precise, quantitative way that no previous groups studying shrinkage have achieved before. This highlights another potential use of the versatile OCT scanner.

4.2 HIGH SPEED CAMERA

4.2.1 High Speed Camera Monitoring

Although answers to the flow diagram (fig. 4.3) were clearly “yes”, an opportunity presented itself when it was learned that a high-speed, high-resolution camera was on loan from the EPSRC (fig. 4.6). This would allow us to observe the tube formation and further analyse how this occurs.

It is interesting to look at figure 4.7 and see tube formation during developed flow, mid-capillary. Although this figure can only give us qualitative information regarding tube formation, several important points can be discerned. The matrix fluid profiles for all but figure 4.7*f* are parabolic in shape, assumed when developing the fluid dynamics Theory. As mentioned, for lift-off conditions, i.e. when the spherical regulator first leaves the injector nozzle, this profile is not present (fig. 4.7*f)*. This second point is the best visual proof of end-effects that the Theory does not account for – resulting in a nominal tube wall thickness T_0 being slightly greater than T_B.

The 3-colour component translation of the image using Leica QUIPS software (fig. 4.8) better facilitates analysis of the effects of changing conditions. It breaks down the colour information gained by using permanganate (purple) and separates it into blue, green and red profiles. For the purpose of analysis of the tube formation, we will concentration on the blue, zigzagged line either side of the spherical regulator. Again we traverse back into wall thicknesses during tube formation, and these 3-colour profiles give us gap-width information, i.e. this can indicate the uniformity of the resultant tube formed.

It can be seen that the control experiment, figure 4.8*a*, a 20ml/min infusion rate and 1.0% alginate concentration gives a well controlled, well formed alginate tube, with both walls equal (~300μm each – estimated by pixels on x-axis) in thickness. When we reduce the alginate concentration to 0.5% (fig. 4.8*b*), we see a slight compromise in the quality of tube formed (the regulator veers off to one side, and the left-hand wall appears larger than

Figure 4.6 Experimental setup of the high-speed camera.

(**a**)

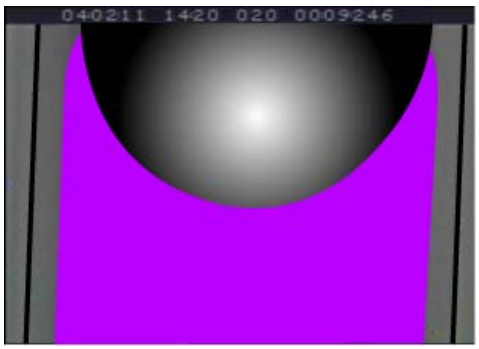

(**b**)

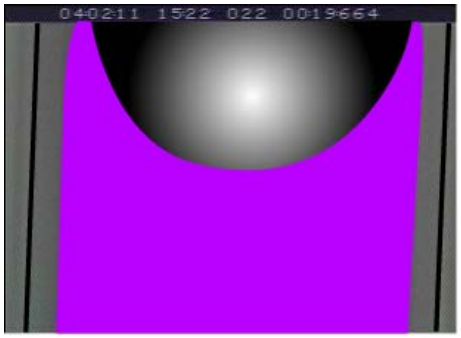

(**c**)

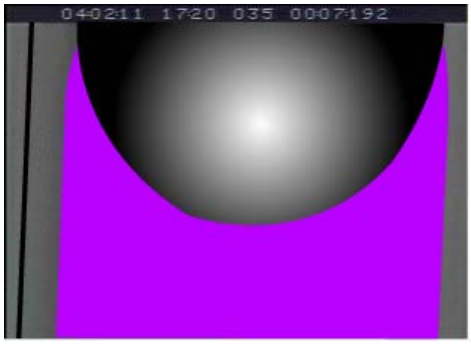

(**d**)

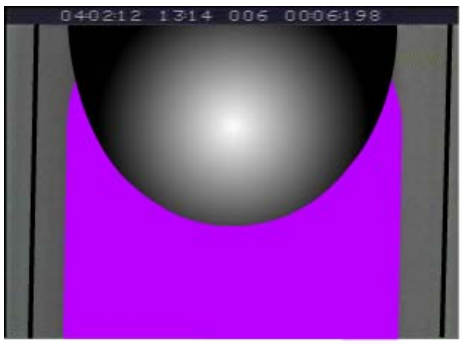

(**e**)

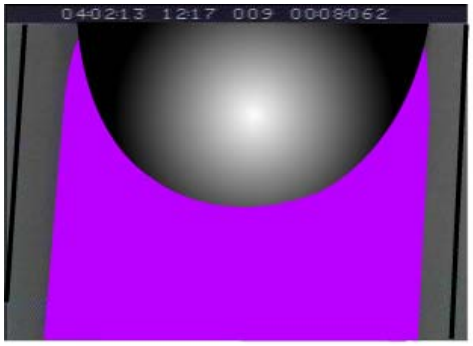

(**f**)

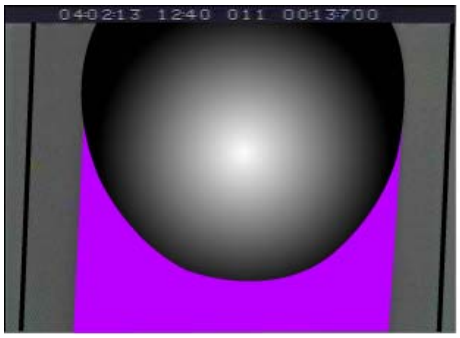

(**g**)

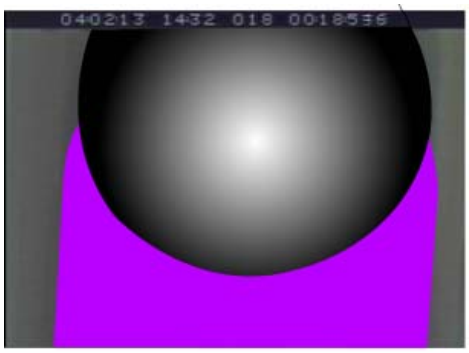

(**h**)

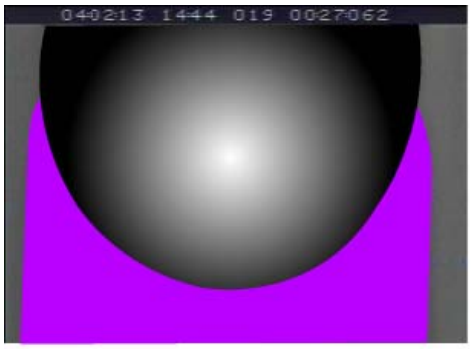

Figure 4.7 High-resolution, high-speed camera images during tube formation. Images were enhanced using Adobe Illustrator CS. The following conditions were tested: (**a**) control experiment at 20ml/min; (**b**) tube formation using uncoloured 0.50% alginate concentration; (**c**) tube formation at 50ml/min; (**d**) tube formation at 413μm wall-gap configuration; (**e**) tube formation at "lift-off"; (**f**) tube formation at "lift-off" at 413μm wall-gap configuration; (**g**) of tube formation at 413μm wall-gap configuration infused with WFI; (**h**) tube at formed at 413μm wall-gap configuration and 50ml/min with WFI.

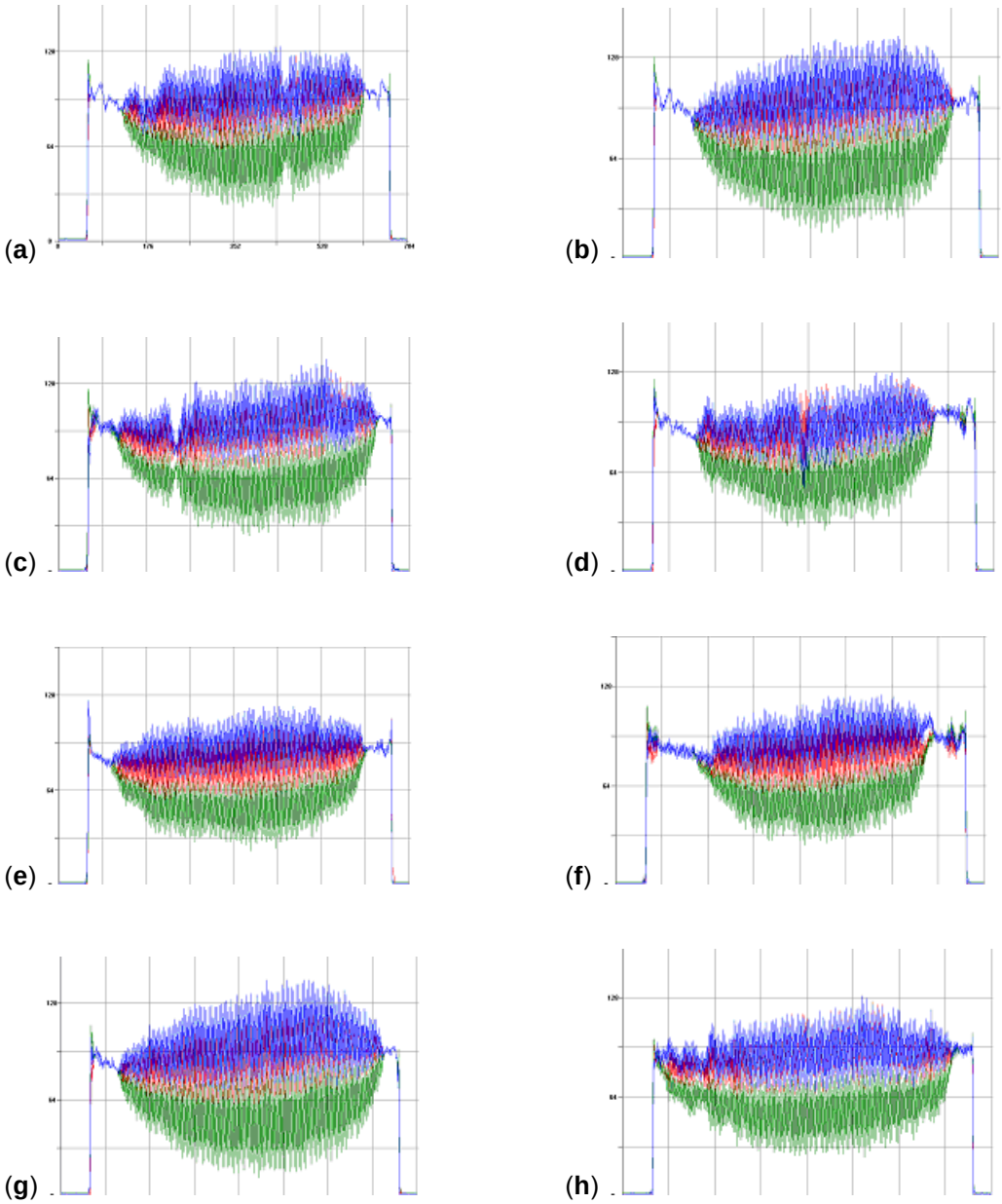

Figure 4.8 Leica 3-colour component profiles for tubes formed corresponding to images seen in figure 4.4. The graphs show grey level (y-axis) against horizontal position. The following conditions were tested: (**a**) control experiment at 20ml/min; (**b**) tube formation using uncoloured 0.50% alginate concentration; (**c**) tube formation at 50ml/min; (**d**) tube formation at 413μm wall-gap configuration; (**e**) tube formation at "lift-off"; (**f**) tube formation at "lift-off" at 413μm wall-gap configuration; (**g**) of tube formation at 413μm wall-gap configuration infused with WFI; (**h**) tube at formed at 413μm wall-gap configuration and 50ml/min with WFI.

the other by about 150μm). Increasing the infusion rate to 50ml/min in figure 4.8*c* further reduces the stability of the regulator (that lies further right). Changing the device configuration to 413μm wall-gap, 1.0% alginate and 20ml/min shows an equal spaced regulator. Figure 4.8*e-f* (300 and 413μm configurations) tells us that even at the start of the tube (un-developed flow) the gap-width is equally thick and the tube is consistent in thickness to the rest of the tube – this is an indication as to the quality of the tube overall. This further strengthens the fact that tubes are now consistent in wall thickness throughout the tube length and not just the central section, due to the efficiency of the new mark 2 design. Figures 4.8*g-h* show the effect of infusing water through the system instead of $CaCl_2$, i.e. no cross-linking. By substituting the linking agent $CaCl_2$ with WFI, there appears to be deterioration in gap-width consistency, and therefore tube wall thickness, most noticeable for the 413μm device configuration. This seemed to get increasingly substantial with increasing infusion rate (fig. 4.8*h*). This is perhaps explained by dilution effects of the permanganate dye by the WFI, and hence breakdown in the consistency of the 3-colour profile. Proof of this Theory is the blending of the 3-colour profile that indicates the spherical regulator blending into the left-hand wall of the glass barrel. It was also proven in the previous chapter that tube wall thickness for non-reacting propelling fluids ought to be closer to Theory than wall thicknesses for reacting propelling fluids. Suffice to say, the high-speed camera gives some information, but its accuracy as a monitoring tool is questionable.

Finally, figure 4.9 shows the spherical regulator at 2 positions along the tube length, a tenth of a second apart. A marked position on the ball showed the effect of ball spin. Surprisingly the ball did not spin in any direction at all. This explains the carrying of a wall thickness throughout the length of the tube (i.e. a thinned wall on one side would be seen throughout the tube length) since no ball spin indicated no ball position correction. This is an important finding since ball spin could mean the ball ricocheting throughout the glass capillary, which would in turn affect tube wall consistency. Furthermore, if all wall characteristics are the same throughout

(**a**) (**b**)

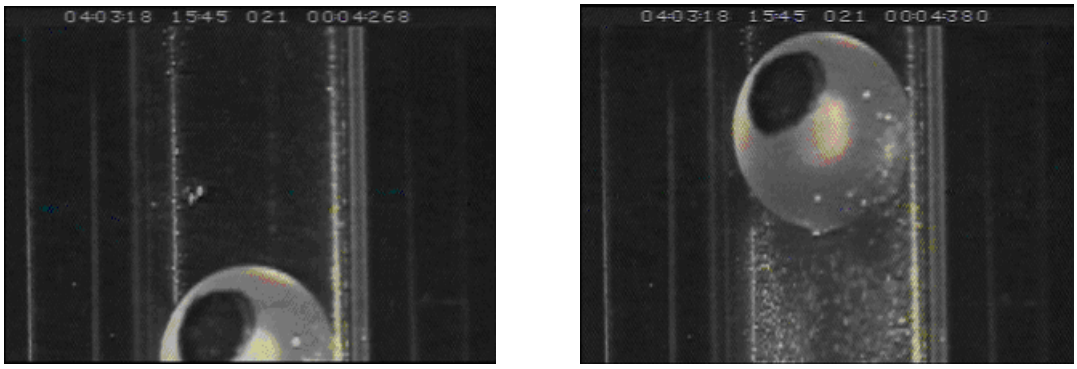

Figure 4.9 High-speed camera images of tube formation to observe ball spin in developed flow. Two time points are shown at: (**a**) t=4.268 seconds; and (**b**) t=4.380 seconds.

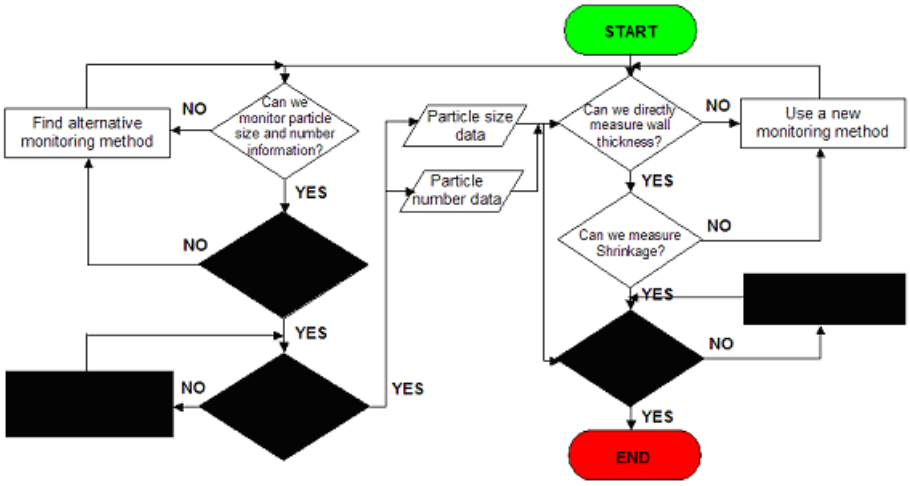

Figure 4.10 Flow diagram of experimental decisions for section 4.3.

the tube, only one point in the tube need be monitored (such as section 4.1.3) to determine tube consistency in a mass-production scenario.

4.3 MONITORING PARTICLE SIZE

4.3.1 Particle Size Detection

So far within this chapter, we have managed to find a reliable method of monitoring tube wall thickness. As we have seen from the previous sections, this wall thickness is very much dependent on the particles we embed within it. Inert solids such as glass beads will affect wall thickness as a function of concentration. Biological cell addition is left unanswered until the Chapter 5. Logic dictates that compressibility of the particles introduced is but one factor, another would be size and we have also mentioned concentration. We therefore require a monitoring method to detect particle size and also enumerate the particle concentration. If we can monitor the particle suspension prior to addition to the alginate, pre-tube formation, we gain another level of control of wall thickness. Figure 4.10 shows how this fits into the experimental decisions. To reiterate, glass beads were used as a model, but alginate structures – be it as beads or tubes – are commonly used for biological cell encapsulation. Wall thickness of our tubes would therefore determine nutrient and waste product exchange across the alginate walls. This would apply to both cells embedded within the walls (those cells furthest from the outer wall will have decreasing access to nutrients) or a lining of cells on the inner wall of an alginate tube.

Three techniques were evaluated for particle sizing and enumeration purposes: the Malvern Particle Sizer, the Leica QWin, and the Haemocytometer. For the remainder of this thesis, rat smooth muscle cells were used as a model, and particle number and size consistency across the suspension was concluded the governing variables. Particle size can be interpreted as variation in individual cell sizes or as aggregates of several

cells. The aim of this experiment was to determine a way of detecting particles and differentiating on the basis of particle size and number.

The Particle Sizer is a device used for analysing particle size and size distribution. Malvern is just one company of many, each device using different technology to obtain the required results. Such techniques can include dynamic light scattering, image analysis, laser diffraction, electrozone sensing, x-ray sedimentation, sieves methods or centrifugal particle size analyser methods. The device from Malvern uses the principle of laser diffraction, also known as low angle light scattering, which scatters a beam passing through a sample of suspended particles, which in-turn scatters onto a detector. The intensity of light is then converted via a mathematical algorithm to give a particle size distribution plot. The Leica QWin is a hardware/software solution used to quantify microscopic results. It can be used with stains and image-enhancing software to obtain absolute measurements from 2d images of cell samples under the coverslip on a glass slide. The haemocytometer has long been a laboratory standard for manual cell counting. Based on a modified glass slide with a grid, a cell sample can be injected under a cover slip and counted using a stain and a light microscope. However between users and repetitions, the same sample has been known to vary by up to 30% (Peebles et al. 1981). Although it is possible, with high magnification and a graticule, to obtain size distribution information of cells, this would be extremely time-consuming and inaccurate and large aggregates may be excluded by coverslip. Therefore, rather than for direct detection of aggregates, here the haemocytometer was used for cell enumeration, and served as a control for the other two methods.

The particle sizer was firstly calibrated against inert glass beads of known size (fig. 4.11). The particle sizer clearly demonstrates a sharp peak at 7.2μm, and the glass beads are stated to be between 3-10μm in diameter. As expected since the different concentrations of cells originated from the same sample source, a common profile was repeated throughout the 5 sets of data (fig. 4.12*a*). These profiles are further differentiated from one another by estimating the number of particles (fig. 4.12*b*), which was done on a basis

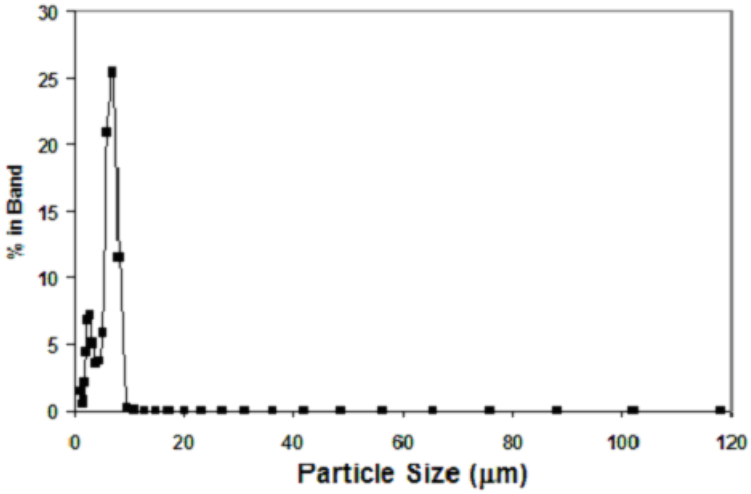

Figure 4.11 Calibration profile using the Malvern Particle Sizer. Inert, 3-10µm glass beads in WFI were used at 20°C. Dotted line is a linear interpolation between points taken. Y-axis represents a percentage based on number of beads counted.

(**a**) (**b**)

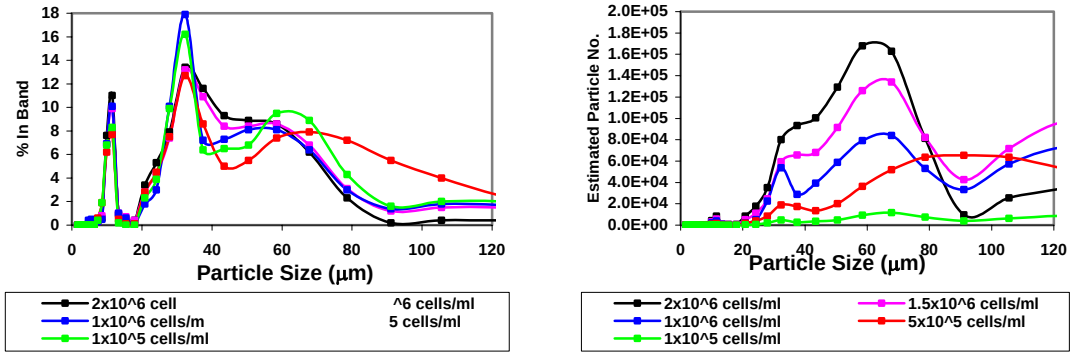

Figure 4.12 Particle size distribution plots obtained using the Malvern Particle Sizer by (**a**) % band of sample analysed and (**b**) estimated number of particles on a basis of cell area. Profiles were taken for cell concentrations of: $2X10^6$; $1.5X10^6$; $1X10^6$; $5X10^5$; and $1X10^5$ cells/ml in 15ml complete culture medium at 20°C. Coloured lines are linear interpolations between points taken. Cells were harvested at passage 19.

of area for one perfectly round cell. The area differs from experiment to experiment based on the initial one-cell peak, which is 32.4μm taken from figure 4.12*a*. The estimated particle number data used to compile figure 4.12*b* was then statistically analysed.

In order to establish whether there is any statistical difference (or similarity) between the datasets for differing cell concentration, a one-way analysis of variance (ANOVA) for a set of correlated samples was performed for the estimated particle number data in figure 4.12*b*. The t-Test is perhaps the most widely used statistical tool of all time, as it tells the user whether: two independent variables are related to one another; and secondly if we alter the level of one variable, would we alter the level of the other. This is useful for comparing two sets of data, but where multiple t-Tests are required for several sets of data, the ANOVA test is much more suitable since it removes the disjunctive probability of any two sets of data being significant at the 0.05 level purely by chance. What this means is that if we are comparing for significance of a treatment (in this case, cell concentration) and this occurs at a 0.05 level (or 5%), then if we have k=5 sets of data, that makes the likelihood of significance between any two of the sets of data 25%. The ANOVA test removes this addition of disjunctive probabilities. The samples are correlated since we compare on the basis of size of particle – in order for two graphs to be similar the % band peaks for both need to occur at the same particle sizes. Appendix C summarises the calculations. Using the df values of 4, 124, one can obtain critical F values of 2.45 at 5% and 3.48 at 1%. The F value of 10.6816 lies to the right of the 1% level meaning that the differences caused between the 5 sets of data by changing cell concentration are highly significant.

Given that this experiment was also intended to explore the robustness of the Malvern particle sizer to fluctuations in cell concentration, this statistical test is rather alarming. However, one must consider the limitations of the ANOVA test. A significant F-ratio tells you whether any of the analysed datasets are significantly different to one another, but it does not tell you which of the datasets are significantly different and by how much. This is where the TUKEY HSD (honestly significant difference) test can

enrich the information that the ANOVA does not provide. Appendix C tells us how dataset 4 ($5x10^5$ cells/ml) differs to the 5% level and dataset 5 ($1x10^5$ cells/ml) is significantly different to the 1% level. This is apparent when looking at figure 4.12. Figure 4.12*a* shows a slightly different shape for the red profile ($5x10^5$ cells/ml) and this is exaggerated when using estimated particle number data in figure 4.12*b*. The abnormal level of large aggregates is detected in the red profile. The green profile however, for $1x10^5$ cells/ml in fig. 4.12*b* is relatively flat compared to the other concentration samples. There are simply not enough cells in this sample to form any similarities with the other concentration profiles. From preliminary statistical tests (data not shown), % band information would not be satisfactory to discriminate between any of the 5 profiles, and therefore estimated particle number data was necessary. As previously stated, we will continue to used % band information to establish the one-cell peak and then use this to calculate the estimated particle number, and this will differ from experiment to experiment. Other than robustness, the analysis also requires sufficient sensitivity to detect significant changes to the profile, and this is where estimated particle number data is essential for the remainder of the particle size analysis experiments.

The figure further establishes the working range of particles needed to obtain a signal. The overall profile however did not form the shape anticipated for a rat aortic smooth muscle cell. All 5 sets of data show an initial peak at 10μm followed by a normal distribution at 30μm, and another at 60μm. From observing a rat smooth muscle cell under a light microscope at x40 magnification using a graticule, and from literature we know that average cell size ought to be ~20μm diameter (Alberts et al. 2002). At this stage, it was that believed that the 30μm peak represented a population of single smooth muscle cells. It was unknown at this stage what the 10μm or the 60μm peaks were.

The same cell sample was then analysed using the Leica QWin. Comparative cell size profiles can be seen in figure 4.13. It is instantly apparent that the level of particle size information gained from the Leica

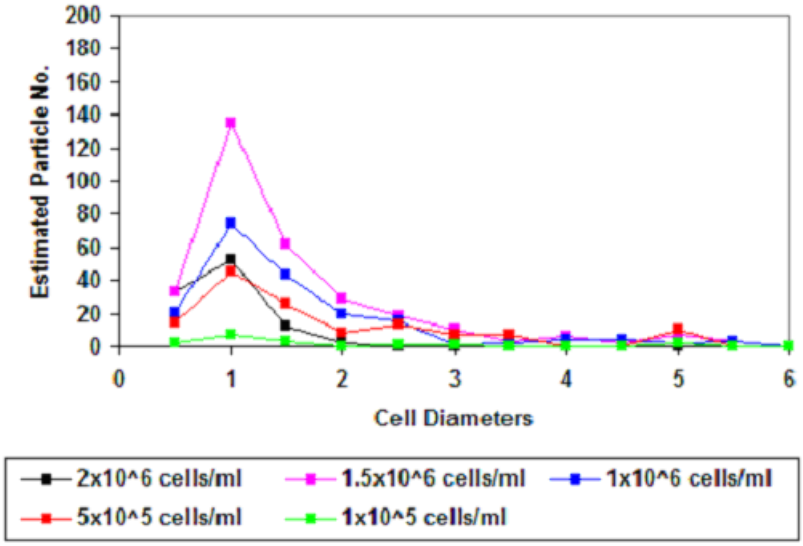

Figure 4.13 Comparative size distribution plots created from Leica QWin data. Profiles correspond to cell concentrations of: $2X10^6$; $1.5X10^6$; $1X10^6$; $5X10^5$; and $1X10^5$ cells/ml in complete culture medium at 20°C. Coloured lines are linear interpolations between points taken. Cells were harvested at passage 19.

Table 4.3 Summary table of the techniques tested for use in tissue engineering and the conclusions as to their suitability.

Technique	Features	Conclusion
Particle sizer	Measures particles 0-120 μm, operates on the principle of particles crossing the path of a beam in a sampling cell, 10ml of sample required. Minimum number of particle counts – 1X105cells/ml.	Only gives % of cells counted and does not actually count cells, but generally easy to use and generate data provided concentration of sample is already known. Hence suitable for screening of cell suspensions prior to use in tissue engineering applications.
Leica QWin	Measures particles at multiple points, range depends on magnification, obtains results via manipulation of a 2D image from a sample under a coverslip, 1ml sample volume required. Minimum number of 20 cell counts per grid.	Needs calibration with haemocytometer for cell counting. Preset particle areas, making heavy data manipulation necessary. Poor level of detail for cell size distributions created. Not suitable for tissue engineering screening.
Haemocytometer	Measures particles via staining and light microscopy, range dependent on magnification, data must be obtained manually, 1ml of sample required. Minimum number of 10 cell counts per grid.	Suitable for tissue engineering but a slow technique with much inherent error from the operator.

QWin is not as detailed as the particle size graphs obtained using the Malvern particle sizer. The same ANOVA test was run for the raw data used to compile figure 4.13 and the tabulated results can be seen in Appendix C. Critical 5% and 1% values were 2.82 and 4.26, respectively and the F result was 3.319, meaning that the 5 sets of data are not identical but there are statistical similarities. The TUKEY HSD test shows that datasets 2 ($1.5x10^6$ cells/ml) and 5 ($1x10^5$ cells/ml) are statistically different to the 5% level, which accounts for the slightly significant F ratio difference seen in the ANOVA. Due to the restricted information gleaned from the Leica QWin, all profiles show a peak at 1 cell diameter (~20μm), and there is also a population at 2-3 cell diameters – which corresponds to the 60μm peak observed using the Malvern. It can be seen that the 1 cell diameter peak for the pink $1.5x10^6$ cells/ml profile is abnormally high, given the y-axis is estimated particle number. Due to the sensitivity of the Leica, the 10μm peak is not detected. A hypothesis that the two techniques show the same data was tested statistically. A comparison of the $2x10^6$ cell/ml concentration data for both the Malvern and the Leica was analysed by ANOVA. The 5% and 1% critical F values were 7.71 and 21.20, respectively. An F-value result of 9.4263 means that the differences between the two methods are not strongly connected, yet they are not too dissimilar – a result we expect given the datasets are from two different devices. Essentially both monitoring methods show two main peaks, now thought to consist of a population of single cells at 30μm and a second population of 2-3 cell aggregates creating a 60μm peak. From this we can gather two important points. Firstly both devices are capable of detecting particle presence, and measure particle size. Secondly, the both techniques are not sensitive to fluctuations in particle concentration, and the limitations of concentration range – i.e. comparing samples with large concentration differences.

However, it must be noted that the detail of information from the Malvern particle sizer was much more useful than the data obtained from the Leica QWin, with much less effort. The Leica QWin required a lot of data manipulation per image, which was then used to create a size distribution plot and the low level of resulting information after analysis was based on

much fewer cells (due to the area physically analysed by the Leica). The particle sizer can tell us the degree of homogeneity of the particle sample. If there were a large number of aggregates, the analysis would show this in the form of a peak on the size distribution profile. It was deemed that the information gathered from the particle sizer was much more valuable and convenient than that obtained from the Leica QWin. A summary can be seen in table 4.3.

4.3.2 Particle Enumeration

In this experiment we compared the effectiveness of the haemocytometer and the Leica QWin for particle enumeration. The particle sizer is only capable of giving results as a percentage and not a total count of the particles, therefore for enumeration purposes the Malvern was omitted.
Figure 4.14 shows cell images taken by the Leica QWin microscope. The image at x40 (fig. 4.14*a*) was used in preliminary scans for experimental setup purposes. The image clearly shows cells at two different diameters. The central cell appears to be two times larger in diameter than the other two cells. Figure 4.14*b* shows a cell scan at x10 magnification. Such an image was then used to compile graphs such as figure 4.13. This cell image shows cells at two different sizes as the previous cell scan, but also two-cell and multi-cell aggregates. These images show how the peaks at 30μm and 60μm could have resulted – from two cell diameters and cell aggregates.

In figure 4.15, it can be seen how the two techniques compare. The haemocytometer gives an accurate representation of cell concentration up until $1.0X10^6$ cells/ml, but the last two data points (1.5 and $2.0X10^6$ cells/ml) seem to stray away from the perfect fit line. At these higher concentrations the data from the Leica QWin fits the perfect-fit line better than the hemocytometer. But overall the haemocytometer gives less variable data due to a smaller CV (error bars). On this last point, it can be summarised that the haemocytometer is more reliable than the Leica QWin for cell

(**a**) (**b**)

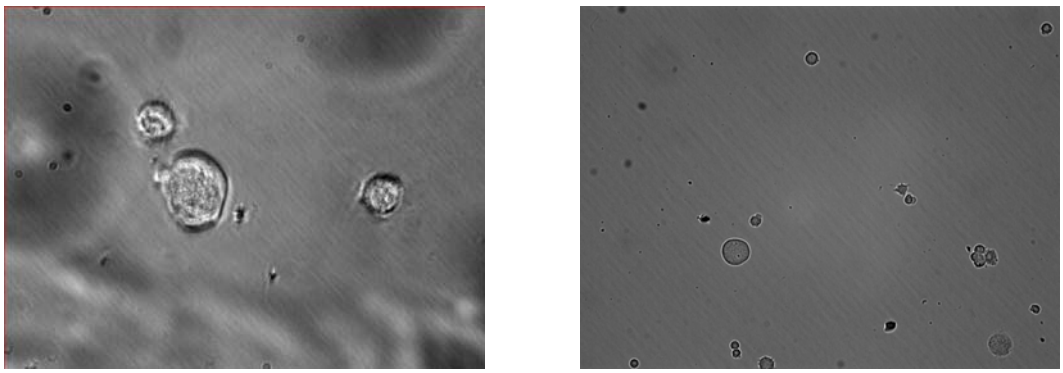

Figure 4.14 Leica images of rat aortic smooth muscle cells at (**a**) x40 and (**b**) x10 magnification.

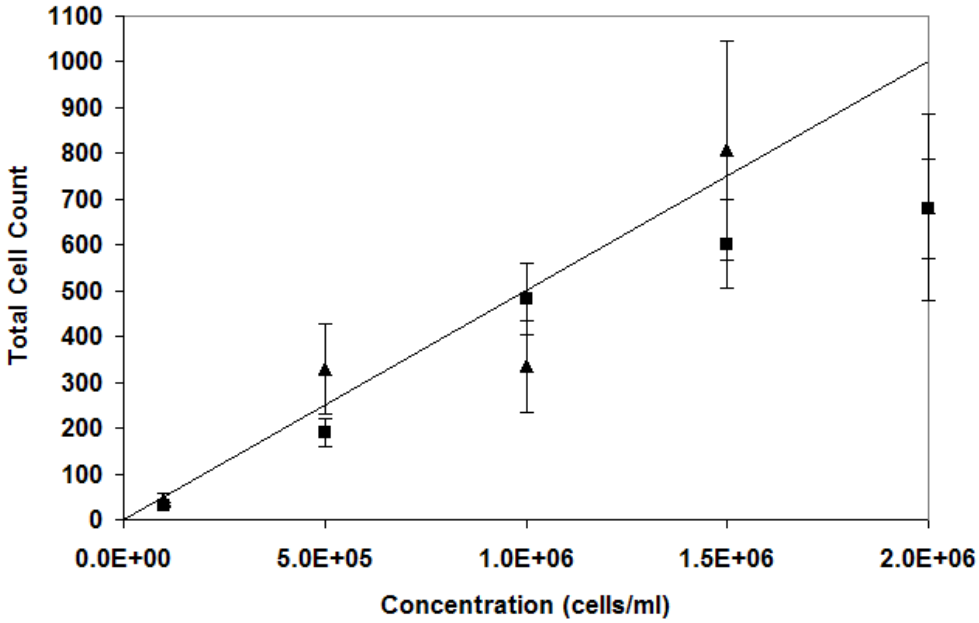

Figure 4.15 Trend showing cell enumeration against corresponding cell concentration. Comparison of cell counts using Trypan Blue and the haemocytometer (■) with those from the Leica QWin (▲). Cell concentrations of: $2X10^6$, $1.5X10^6$, $1X10^6$, $5X10^5$ and $1X10^5$ cells/ml were tested. The cell count corresponds to the number of cells counted in a $10mm^2$ area. All cells in complete culture medium and 20°C. The solid line is the perfect fit line, i.e. the actual cell count for any given concentration of cells.

counting up to $1.0X10^6$ cells/ml. Above this concentration, dilution would usually be done, since the count would be too time consuming. The lack of good fit of data to the perfect fit line could be due to large aggregates not being able to fit under the coverslip – which applies to both methods.

The particle sizer is an excellent tool sensitive enough to detect changes in the distribution of particle sizes, however it is not a tool for cell counting. The Leica QWin can analyse a small number of cells of preset size ranges, making data manipulation difficult and long-winded. The sampling is also only that of a microscopic slide, making data slightly unreliable. So both techniques have their limitations.

At this stage it was decided not to pursue the Leica QWin as a form of analysis. Granted the Leica QWin is not a particle sizer and the data manipulation required in order to achieve particle size information was also very time-consuming. It also didn't perform very well as a cell enumeration method. The number of cells counted per area was an estimate that required the haemocytometer for calibration in the first place. Also the physical area analysed was ~ a fifth of the area analysed by the haemocytometer making the errors substantial. In summary, despite the many strengths of the Leica QWin found by other groups, particularly for automotive cell enumeration (Jacobs et al. 2001; Law et al. 2003), the technique was found unsuitable for particle enumeration for our process.

4.3.3 Enumeration Using The Capillary Cytometer

Going back to the experimental thought process (fig. 4.10) we have failed to find a monitoring method for cell enumeration. Section 4.3.2 established that manual counting via the haemocytometer remains the best method of enumeration due to the inconvenience of data manipulation required and the assumptions made (for cell area) for the Leica QWin. Biological research has conventionally used haemocytometer measurement and staining with Trypan Blue as a technique for cell enumeration. Although this is widely accepted as the standard, it is well known that variability due to different

operators can result in errors of up to 30% (Peebles et al. 1981). We therefore require another method to enumerate particles – in our experiments these particles were rat aortic smooth muscle cells. Continuing with the theme of reproducibility and automation, we evaluated the use of a capillary cytometer combined with a fluorescence staining with Guava ViaCount Flex reagent. The Guava EasyCyte is a bench top capillary cytometer that can automatically count 100 cells per second from a standard 96-microwell plate.

Figure 4.16 shows how two cell-encapsulated tubes compared when enumerated using both haemocytometer and Gauva capillary cytometer. Both cell enumeration methods pivot about the number balance line, with the Trypan Blue and Guava ViaCount Flex giving inter-tubular (fig. 4.16*a*) cell counts with CVs of 29.8 and 17.6%, and intra-tubular CVs of 37.3 and 44.8%, respectively. One could comment that the Gauva flow cytometer is similarly effective at cell enumeration. Due to the lack of experiment datasets and points, statistical analysis could not be performed. However, this experiment does show that capillary cytometry can offer an attractive automated alternative to conventional manual cell counting methods. The device will be further explored in the next chapter.

4.4 CONTROL OF MAMMALIAN CELL CULTURE

4.4.1 Effect of Pipetting to Breakup Cell Aggregates

Having now established the data gathering tools required for both particle size and enumeration, we turn to control of cell culture processing (fig. 4.17). As we have already discussed, it is likely that a successful process for manufacture of alginate tubes could be used for macro-encapsulation of biological cells or will contain biological cells for the production of tissue-engineered products. From a purely generic perspective, it is favourable in the majority of cases to have a homogeneous suspension of biological cells of known size, so as not to disrupt wall thickness upon integration into an

(**a**)

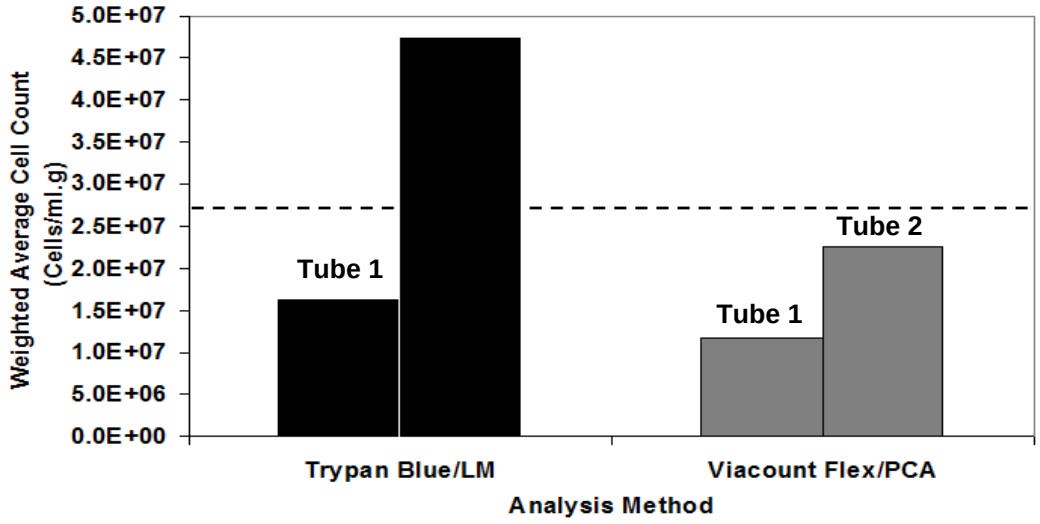

(**b**)

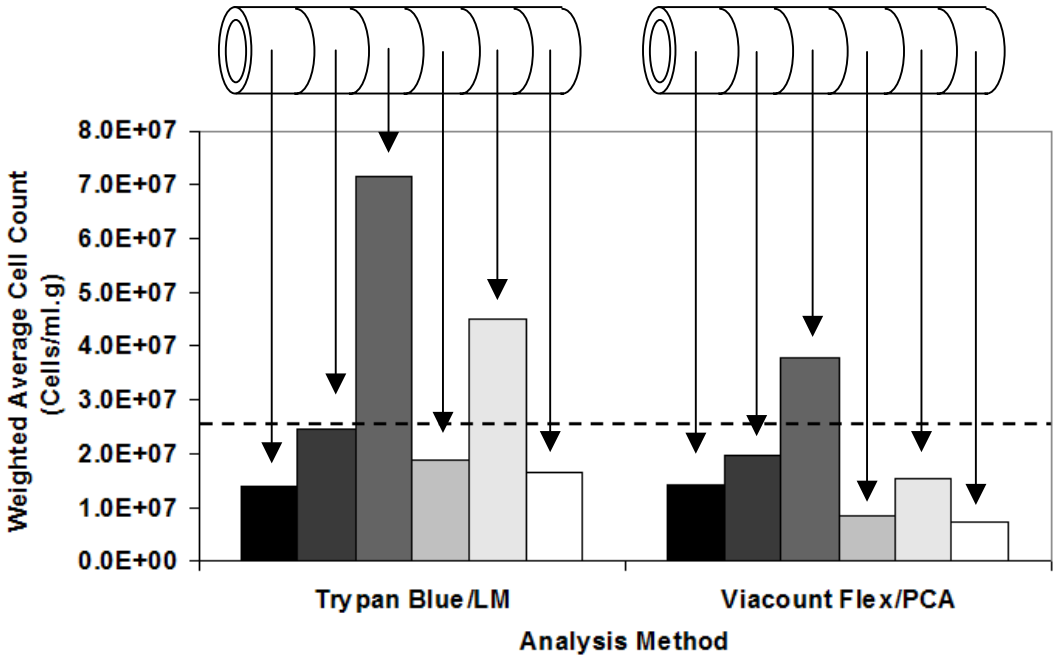

Figure 4.16 Cell quantification analysis by light microscopy and capillary cytometry. Weighted-average total cell counts for (**a**) inter and (**b**) intra-tube cell enumeration comparing Trypan Blue cell counting with Guava ViaCount Flex reagent. Dashed line represents weighted average cell count expected via a calculated number balance. All tubes were made as described in section 5.3.1.

alginate-cell tube, since cell wall thickness will determine the ease of flux of nutrients and waste products across the tube walls and ultimately the viability of the cells dwelling within. Large cell aggregates will also mean necrosis within the aggregate centres that have little access to nutritional sources (Sen et al. 2002).

In mammalian cell culture, there are three non-controlled variables whereby the particle size could be influenced – the first of these is the degree of pipetting. We have previously found a statistically sensitive method of detecting changes to particle size profiles. It is therefore the aim of this sub-section to see whether controlled pipetting induces changes to the "normal" distribution of cell sizes previously found and whether the Malvern can detect these changes. The experimental thought process is summarised in figure 4.17.

Pipetting is a commonly used mammalian cell laboratory technique used to breakup cell pellets after centrifugation. It is well known that breakup of aggregates is due to shear stress (Serra et al. 1997; Serra et al. 2007; Colomer et al. 2005). In essence pipetting is a method used to achieve a more homogeneous cell suspension. However the degree of pipetting is not controlled in manual cell culture. Therefore in this study, it was decided to look at the effect of passes using an autopipette. This experiment was calibrated against time to keep all variables constant and controlled. Any effect of time on aggregation (and the profile of the particle size distribution histogram) was assumed negligible at time zero – i.e. at time of resuspension of pelleted cells – due to the lack of any new aggregates formed with time.

The results can be seen in figure 4.18. An ANOVA statistical analysis on the estimated particle number data gives a F-ratio of 1.6264. 5% and 1% critical values of 2.45 and 3.48 mean that the differences amongst the profiles are not significant, i.e. the treatment of pipette passes to create shear to cell aggregates is not effective. This negative result can mean one of several possibilities: either (1) the shears generated by the autopipette tip is not sufficient to breakup any cell aggregates present in the cell suspension; (2) breakup does occur, but the Malvern is not sensitive enough to detect it; or

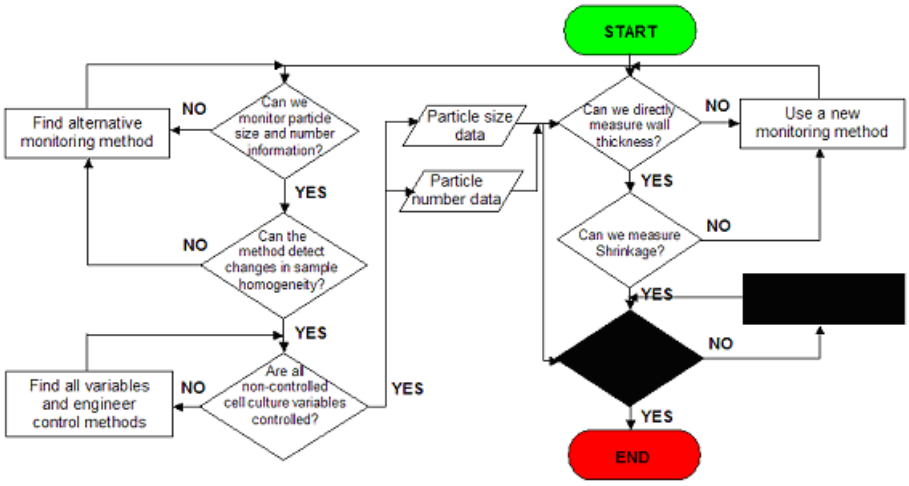

Figure 4.17 Flow diagram of experimental decisions for section 4.4.

(**a**) (**b**)

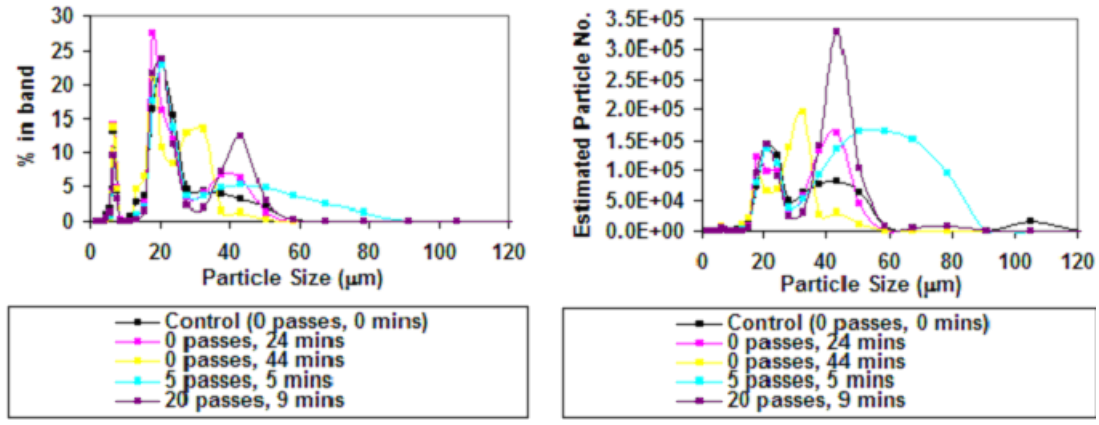

Figure 4.18 Particle size distribution plots obtained using the Malvern Particle Sizer by (**a**) % band of sample analysed and (**b**) estimated number of particles on a basis of cell area. 5 conditions (passes through a pipette) were tested and each experiment was timed: 0 passes at time, t=0; 0 passes at time, t=24min; 0 passes at time, t=44min; 5 passes at time, t=5min; and 20 passes at time, t=9min. Coloured lines are linear interpolations between points taken. Cells were harvested at passage 28.

(3) no aggregates are actually present. The 30μm and 60μm peaks seen in figure 4.12*a* correspond to the 20μm and 40μm peaks seen in figure 4.18*a* as a matter of coincidence and these peaks are 2 distinct populations of single cells – a Theory supported by images seen in figure 4.14. This result can be interpreted in a positive way – since degree of micro-pipetting does not influence aggregation of cells significantly, it is not a factor we need to control in a well-engineered generic process for creation of cell-integrated alginate tubes.

4.4.2 Effect of Holding Time and Gauze Filtration on Cell Aggregation

The next non-controlled cell culture variable we will investigate is holding time. Holding time is the time a cell spends in suspension, after harvesting but prior to processing – and this can be considerably different between batches. The Smoluchowski Theory describes aggregation of suspended colloidal particles due to Brownian diffusion via collision and formation of intercellular bonds (Longmire and Frojmovic 1990). This can be extended to include move of cells on the tissue culture surface (Neelamegham et al. 1997), although in both cases state of aggregate formation is dependent on holding time. Hence the object of this set of experiments is to study the effect of holding time and measure the effect on aggregate formation using the particle sizer.

Holding times up to 3 hours were tested. As an aggregate free control experiment, the cell solution was also passed through an autoclaved filter of a 20μm diameter sieve/gauze, intended to reduce the cell suspension to a population of single cells only.

Figure 4.19 shows the effect of holding time on particle size distribution at hourly intervals. Figure 4.19*a* does not show any large difference between profiles, but figure 4.19*b* does. The profiles at 2 hours (yellow) and 3 hours (blue) clearly are markedly different from early profiles. ANOVA analysis gives an F-ratio at 3.1977 with critical 5% and 1% values at

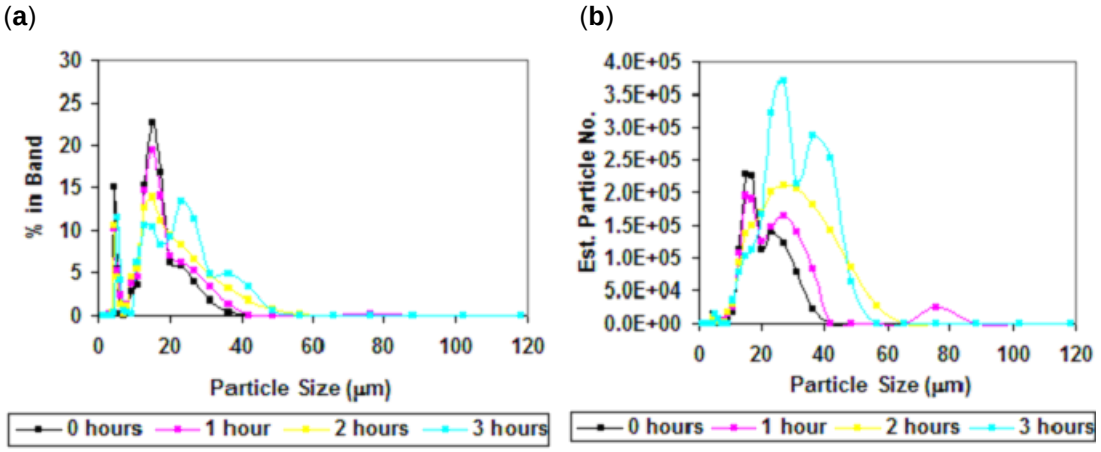

Figure 4.19 Effect of holding time on unfiltered cell size distributions using the Malvern Particle Sizer by (**a**) % band of sample analysed and (**b**) estimated number of particles on a basis of cell area. Conditions were: 0 hours; 1 hour; 2 hours; and 3 hours. Holding times were calculated from the moment cells were resuspended after centrifugation and vortexed to dispel all aggregates formed. Cell concentration throughout was $1X10^6$ cells/ml in 10ml complete culture medium at 20°C. Coloured lines are linear interpolations between points taken. Cells were harvested at passage 14.

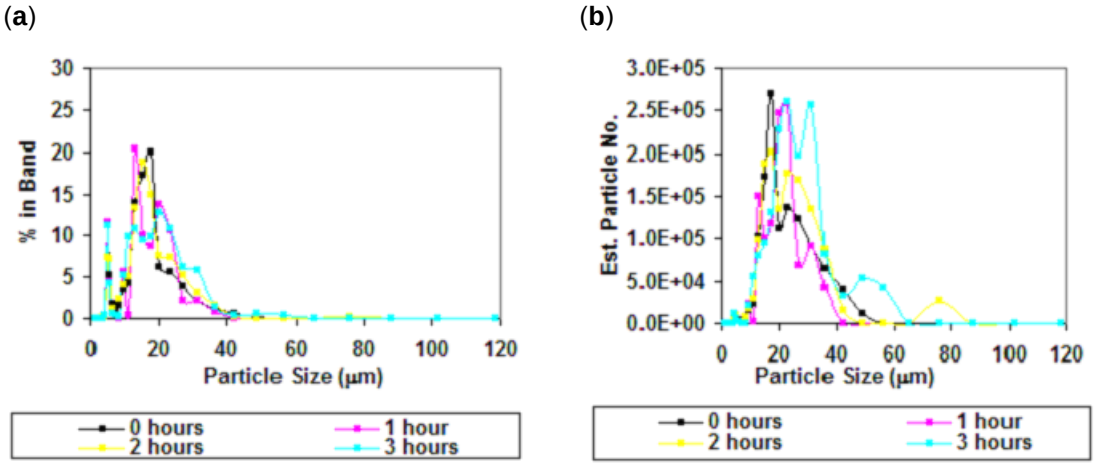

Figure 4.20 Effect of holding time on filtered cell size distributions using the Malvern Particle Sizer by (**a**) % band of sample analysed and (**b**) estimated number of particles on a basis of cell area. Conditions were: 0 hours; 1 hour; 2 hours; and 3 hours. Holding times were calculated from the moment cells were resuspended after centrifugation and vortexed to dispel all aggregates formed. Size filtration was performed using a syringe with a 20µm pore gauze membrane. Cell concentration throughout was $1X10^6$ cells/ml in 10ml complete culture medium at 20°C. Coloured lines are linear interpolations between points taken. Cells were harvested at passage 14.

2.70 and 4.00 indicating significance at the 5% level. A TUKEY HSD test reveals there to be a significant difference between profiles at 0 hours and 3 hours. This shift of the peaks towards the right is an indication of cell aggregation. As time increases, the likelihood of two particles colliding increases and aggregate formation results. 3 hours appears to be a statistically significant time upon which aggregation effects are noteworthy. Figure 4.20 shows the same cell sample processed through the 20μm gauze membrane. With an ANOVA result of F at 1.1933 and the same critical values, this time the profiles are statistical similar. This means that although there might be presence of aggregates, especially significant after 3 hours, the gauze filters out presence of particles, be it cells or aggregates of cells, any larger than 20μm. The 3-hour (blue) particle size distribution shows a peak at 30μm, but certainly no significant peaks any larger than this. This would be a good process control measure for cell size homogeneity.

4.4.3 Effect of Centrifugation and Passage Number on Cell Aggregation

This final study concentrates on the effect of centrifugation on cell size distribution. Because centrifugation is a concentration step commonly used in any cell culture process, yet the protocols involved (i.e. centrifugation steps and speed) will differ from lab to lab. As explained in the previous sub-section, aggregation is an outcome from collisions of particle and intracellular bond formation (Longmire and Frojmovic 1990). Centrifugation speed, which hastens cell settlement (Furukawa et al. 2003), and time (see above) will impact on cell aggregation. And the intracellular bond strength will determine the size of the aggregates after resuspension.

Figure 4.21 shows the results of the experiment. Visibly the graphs for % in band and estimated particle number do not show any large differences between groups for centrifugation within the range of 0 – 500g. This range reflects a realistic centrifugation range that maybe used in cell culture. The

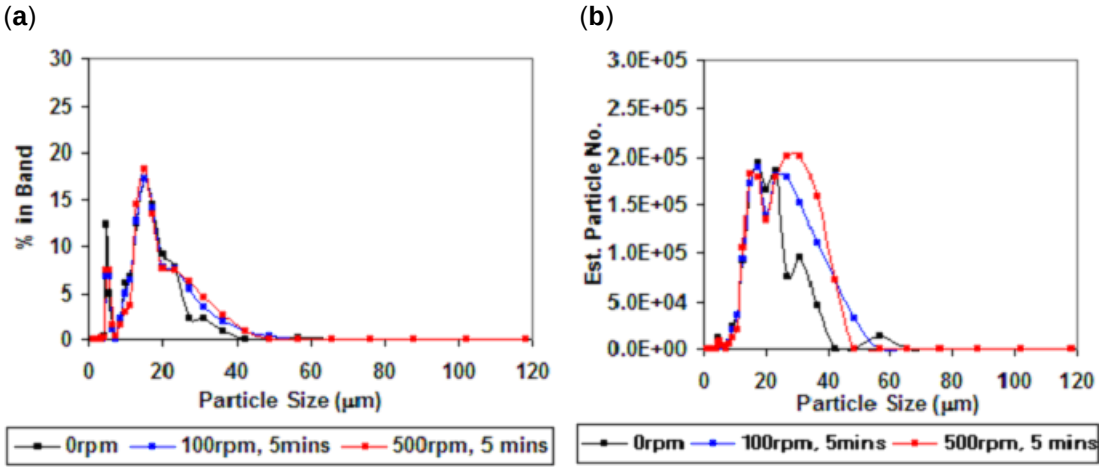

Figure 4.21 Effect of centrifugation on cell size distributions using the Malvern Particle Sizer by (**a**) % band of sample analysed and (**b**) estimated number of particles on a basis of cell area. Conditions tested were: uncentrifuged cells; cells centrifuged at 100xg for 5 min; and cells centrifuged at 500xg for 5 min. Rat SMCs cells, cell concentration of $1X10^6$ cells/ml, 10ml complete culture medium and 20°C were maintained constant throughout. Coloured lines are linear interpolations between points taken. All cells harvested at passage number 13.

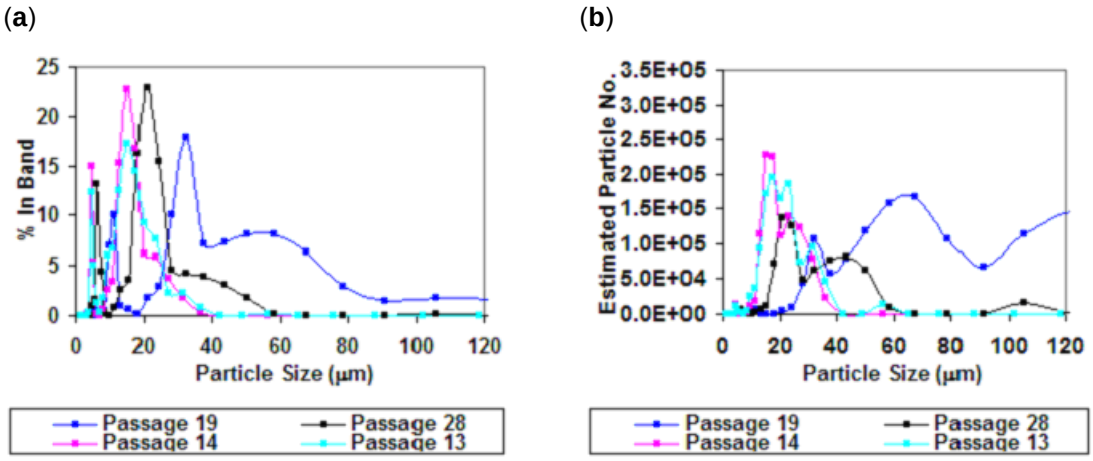

Figure 4.22 Effect of passage number on cell size distributions using the Malvern Particle Sizer by (**a**) % band of sample analysed and (**b**) estimated number of particles on a basis of cell area. Cell concentration throughout was $1X10^6$ cells/ml in 10ml complete culture medium at 20°C. Coloured lines are linear interpolations between points taken. Cells were harvested at passage 19,28, 14 and 13.

three sets of data were compared using ANOVA tests. The F result of 2.5722 falls to the left of the 5 and 1% critical values of 3.15 and 4.96, meaning that the treatment had no significant impact on the size distribution profile. This result indicates that within the range tested, increased centrifugation speed only served to speed the formation of the cell pellet, rather than cause any significant cell aggregation, which would be reflected by a shift of the 15μm peak to the right. In essence, centrifugation is not a variable that will cause batch-to-batch variability in particle size homogeneity between cell suspensions.

At this stage we have cell size distributions for cells at passage 19, 28, 14 and now 13. These were plotted and compared in figure 4.22. In each case, the profile generally remains the same, an initial peak (to date unidentified), a population of single cells and a second population of two cell diameter particles, possibly made up from larger cells or multiple cell aggregates. What does seem to change however is the size of the populations in each of these peaks. It was hypothesised that this could be a result of cell passage number (generation number of the cell), due to adaptation of cells to the culture media over several generations (Conlon and Raff 2003). Despite there being no sort of pattern emerging from figure 4.22, the profiles for $1x10^6$ cells/ml at passage 19, 0 passes at passage 28 and 0 hours unfiltered at passage 14 were statistically compared. An ANOVA F-ratio of 0.7423 falls far to the left of the 5 and 1% critical values at 2.70 and 4.00 respectively, indicating no statistically significant difference between the profiles. If there is any difference in average cell size, resulting in a shift of the cell size distribution to the right (increasing cell diameter and resulting aggregate sizes) then this is not noticeable in the 4 datasets at different passage numbers.

5 Impact of Cellular Integration

This final chapter brings all elements of the cell-integrated tube together – the alginate tube, monitoring methods and the biological cells – and looks at the system in its entirety. What happens when we integrate cells into the alginate tube walls? How does this impact on the fluid mechanics? We have already witnessed the effects of addition of inert glass beads, and discovered that they influence wall thickness as a function of concentration. However, we left the question of impact of cellular addition unanswered in Chapter 4 (fig. 5.1), as it seemed more appropriate to answer it in this final chapter.

As we have discussed, it is likely that the end use of an alginate tube would be either a macro-encapsulation envelope or perhaps it could be developed into a tissue-engineered product. Either way, biological cells will be either lined on the inner tube walls, or integrated within the walls. Since the latter option is more complex, we decided to develop this aspect in this thesis. Despite the fact that the tube can be used with any biological cells, rat aortic smooth muscle cells were used as a model, therefore other than simple mechanical aspects such as viability, no other cell identification steps were performed. As we know, cells are not rigid objects, and mammalian cells in particular are fragile and prone to lysis by process factors such as shear (Serra et al. 1997; Serra et al. 2007; Colomer et al. 2005). In concentrations such as those required to create a cell-integrated tube, percentage of cell viability could influence viscosity (due to cytosol leakage), which subsequently impacts on cell aggregation (Sen et al. 2002), which in turn impacts on wall thickness. Alginate wall thickness will control the level of oxygen tension and availability to embedded cells, which will cyclically influence cell viability (Schneider et al. 2004).

The aims of this chapter are therefore: to control the impact of cell addition to tube wall thickness; to introduce reproducible cell-alginate mixing method; to monitor biological cell viability as a result of process shears through the tube-forming process and as a result of integration with all media; and to control and quantify particle spatial distribution in alginate hydrogel.

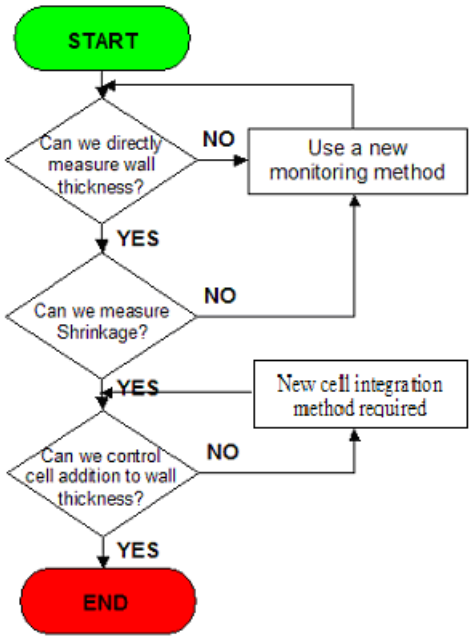

Figure 5.1 Flow diagram of experimental decisions for Chapter 5 derived from figure 4.1.

5.1 CELL IMPACT TO WALL THICKNESS

5.1.1 Effect of Biological Cell Addition On Tube Wall Thickness

This first experiment aimed to introduce biological cells to the alginate tube and measure impact on tube wall thickness as a result (fig. 5.1). Chapter 3 demonstrated the reproducibility and consistency of the tube-forming device described in (Mason and Town 2002) to produce alginate tubes of pre-defined length and wall thickness from well-mixed liquid alginate. As described previously – by measuring length of the tube with a known fixed volume (and density) of alginate, one can use the relationship between the two to back-calculate an average wall thickness, assuming that the tube walls were formed evenly on all sides. This method gave results with CV of ~1.0%. Although this measurement technique relies on the said assumptions, it remains one of the easiest methods to determine tube quality at time of formation. These results were then followed by a full cell-integrated tube OCT scan, post tube-shrinkage, at Cranfield University (5.1.2).

By comparing the trends of cell-integrated tubes with cell-free alginate tubes at identical concentrations, figure 5.2 demonstrates that the cell-integrated alginate tubes also share high correlation to linear trends, ranging from R^2 0.9972 – 0.9998, indicating good tube quality control. There is also an obvious decrease in gradient of the slopes with an addition of mammalian cells. This means that the cell-integrated tubes are shorter with thicker walls at the same volume of sample used. This result corresponds with that seen in table 4.1 from section 4.1.1. A possible theoretical explanation for this phenomenon maybe due to the solidity of the matrix fluid – as we embed solid particles into the alginate, it's ability to flow is impeded, and therefore the contraction or thinning effects of the spherical regulator dragging the matrix fluid upwards. This results in a thickness much closer to the experimental maximum $T_B \approx {}^2/_3 \times \delta_0$. With gap widths of 238, 300 and 413μm, these values would be 159, 200 and 275μm. By back calculating we can crosscheck this

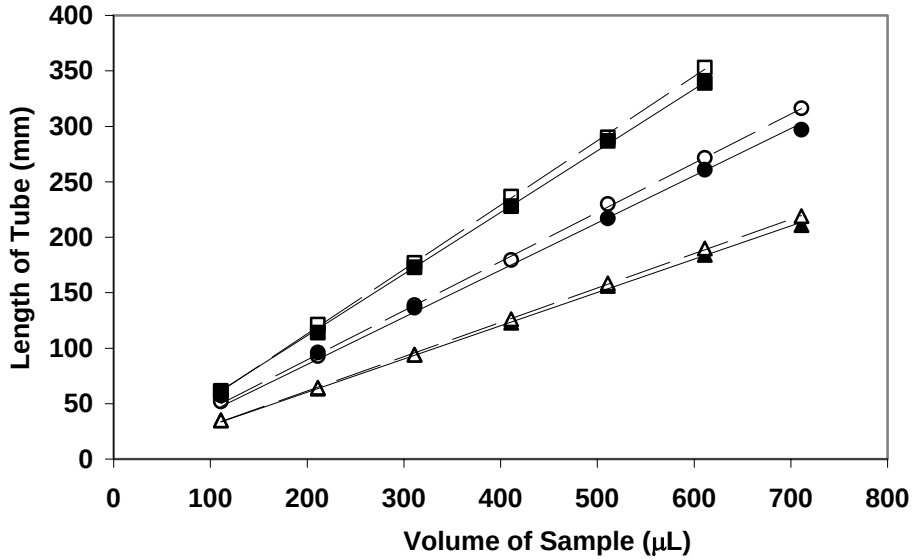

Figure 5.2 Length of tube formed as a function of injected volume of sample in the presence (cell-integrated, solid symbols) or absence (cell-free alginate tubes, hollow symbols) of SMCs at $1x10^7$ cells/ml concentration. Wall gaps (space between glass capillary and plastic regulator) were (■) 238μm, (●) 300μm and (▲) 413μm giving calculated tube wall thicknesses of 164.2μm ± 6.4μm, 196.6μm ± 8.8μm, and 285.3μm ± 9.2μm as calculated from cell-free tube data. Symbols represent single lengths of tube formed measured with a precision steel rule (see Materials and Methods). Solid lines represent linear regression fittings of the data for each cell-integrated tube whilst dashed lines represent linear regression fittings for cell-free alginate tubes under the same conditions. R^2 values for cell-integrated tubes were 0.9998, 0.9973 and 0.9996, respectively. Conditions used throughout: 1% w/v alginate concentration, $CaCl_2$ infusion rate 20 ml/min, mark 2 device.

Table 5.1 Tabulated wall thicknesses derived from figure 5.2.

Gap Width (μm)	Barrel Radius (mm)	Cell-Integrated Graph Slope (mm/μl)	Nominal Wall Thickness, T_0 (μm)	Pure Tube Graph Slope (mm/μl)	Nominal Wall Thickness, T_0 (μm)	CV (%)
238	1.83	0.556	0.164	0.577	0.158	3.91
300	2.00	0.426	0.197	0.444	0.188	4.48
413	2.00	0.300	0.285	0.309	0.276	3.25

hypothesis based on the assumption that the tube walls are uniform. Table 5.1 gives a summary of results. Indeed cell-integrated tubes are closer to T_B than pure alginate tubes.

Since manual cell-integration provides no way to control distribution of cells and clumping, this makes the reproducibility of these results questionable. CV of lengths of tubes formed using the mark 2 tube-forming device generally does not exceed 5%, and we can see that the difference between the gradients of the cell-free and cell-integrated alginate tubes comes close to this figure. Therefore, cellular additions up to $1x10^7$ cells/ml concentration may substantially affect average tube wall thickness under worse manual mixing conditions, and hence may compromise tube mechanical uniformity and therefore structural integrity, if the cells are not introduced in a controlled manner.

5.1.2 Static Mixers and Impact on Wall Thickness

In sub-section 5.1.1 we measured tube length to back-calculate tube wall-thickness. This next experiment directly measures wall thickness of cell-integrated tubes using OCT. But first we must introduce a new method of controlling cell integration with liquid alginate, which figure 5.2 showed in the last sub-section is inadequate via manual integration. The aim here was therefore to show the uniformity in wall thickness of a control cell-free alginate tube, and then to integrate cells into alginate, via hand-mixing and static mixing and compare the differences in uniformity.

We have already seen that cells will affect wall thickness, and the lack of homogeneity of cell distribution in the previous experiment. It is envisaged that the cell integration method will better control this aspect. This method should not just evenly distribute cells within liquid alginate, but also limit the amount of shear damage to the cells. Although hand mixing is usually acceptable in laboratory protocols, an automated method would be required in

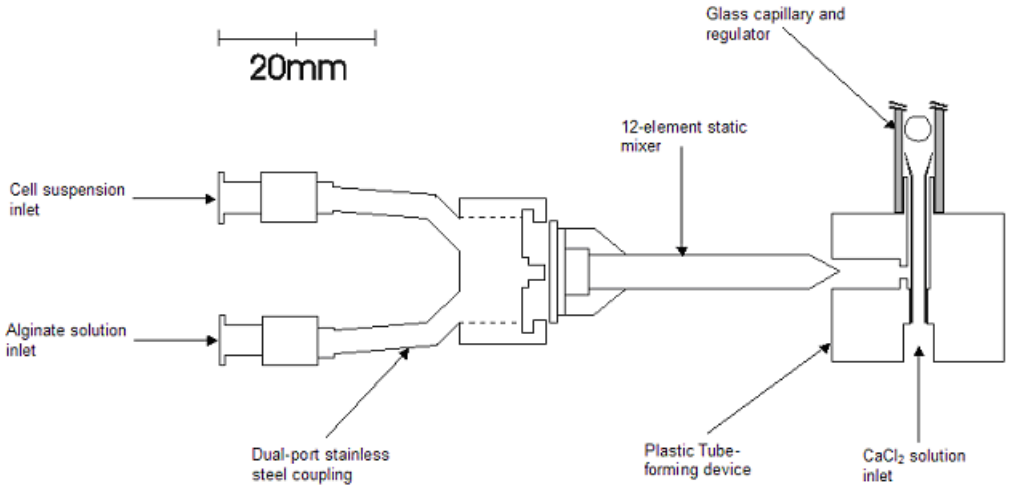

Figure 5.3 A scale diagram showing the experimental setup. The tube-forming device was modified by addition of a dual-port stainless steel coupling and an 8 to 12 element static mixer. Diagram shows components aligned but not coupled. Dead volumes within the entire static mixer arrangement and tube-forming device are ~0.31µl and 89µl, respectively.

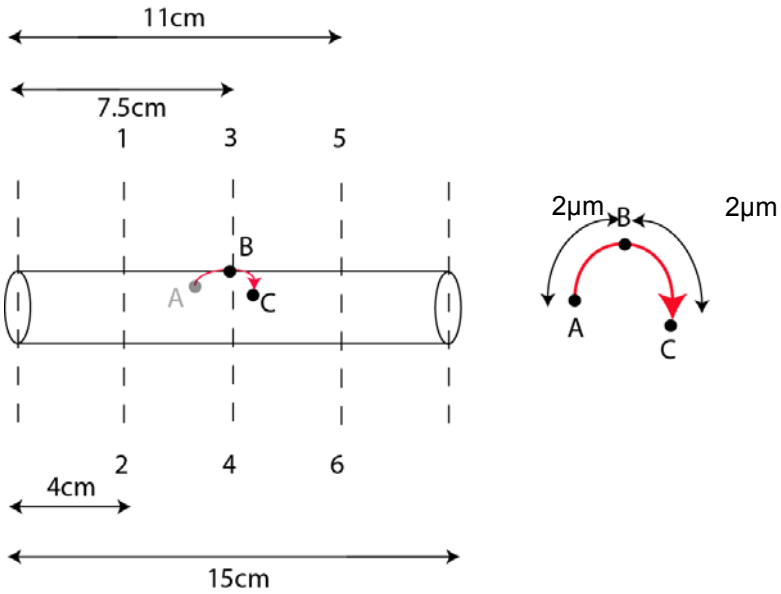

Figure 2.14 Schematic diagram (not to scale) showing experimental setup used for Optical Coherence Tomography (OCT) scanning of cell-integrated tubes. The longitudinal (numbers 1-6) and radial (letters A-C) locations correspond to images seen in figure 5.5.

an industrial process. Popular automated methods of mixing cells include roller mixing, impeller mixing and static mixing. Roller mixing requires long periods of time to achieve homogeneity while impeller mixing is known to generate large shear forces and reduce viability of mammalian cells (Abu-Reesh and Kargi 1991). Kenics design static mixers offered a cheap, negligible shear (Bertsch et al. 2001), and disposable (hence sterile) option. Figure 5.3 demonstrates a schematic of how a static mixer was used to integrate concentrated cell suspension with liquid alginate to give a resultant cell-alginate mixture of $1x10^7$ cells/ml and 1.0% alginate concentration, and how this setup was incorporated with the tube-forming device.

The experimental setup is shown in figure 2.14. Figure 5.4 shows the OCT scans for tubes of all 3 conditions. Again, since the tube was analysed within the glass barrel, we see two lines, the first thin line represents the glass to $CaCl_2$ liquid interface, the second represents the liquid to alginate wall interface and the third the alginate to liquid interface. Here we see a representation of the results obtained for each of the conditions and each of the 6 points along the tube, however there are 18 scans per tube and 2 tubes per condition and all results were used to compile figure 5.5. The variation in wall thickness along the length of the tube was quantified by calculating the coefficient variation (CV) of the wall thickness values obtained (n=18) for each tube.

The OCT scans reveal mean wall thicknesses to be 157.2±12.1μm and 134.3±8.2μm for the pure alginate tubes; 160.4±68.3μm and 349.5±150.5μm for hand-mixed cell-integrated tubes; and 160.6 ±10.1μm and 135.6±14.1μm for 12-element statically mixed cell-integrated tubes. Clearly the manually integrated cell-tubes were less uniform than pure alginate or static-mixer integrated cell tubes. Figure 5.5 shows CV data compiled from these OCT scans. Wall thickness of cell-free alginate tubes had an average CV of 7% along the length of the tube while hand-mixed cell-integrated tubes had a CV of 43%. It is hypothesised that the variation in wall thickness observed in cell integrated tubes was caused both by heterogeneous mixture of the cells with

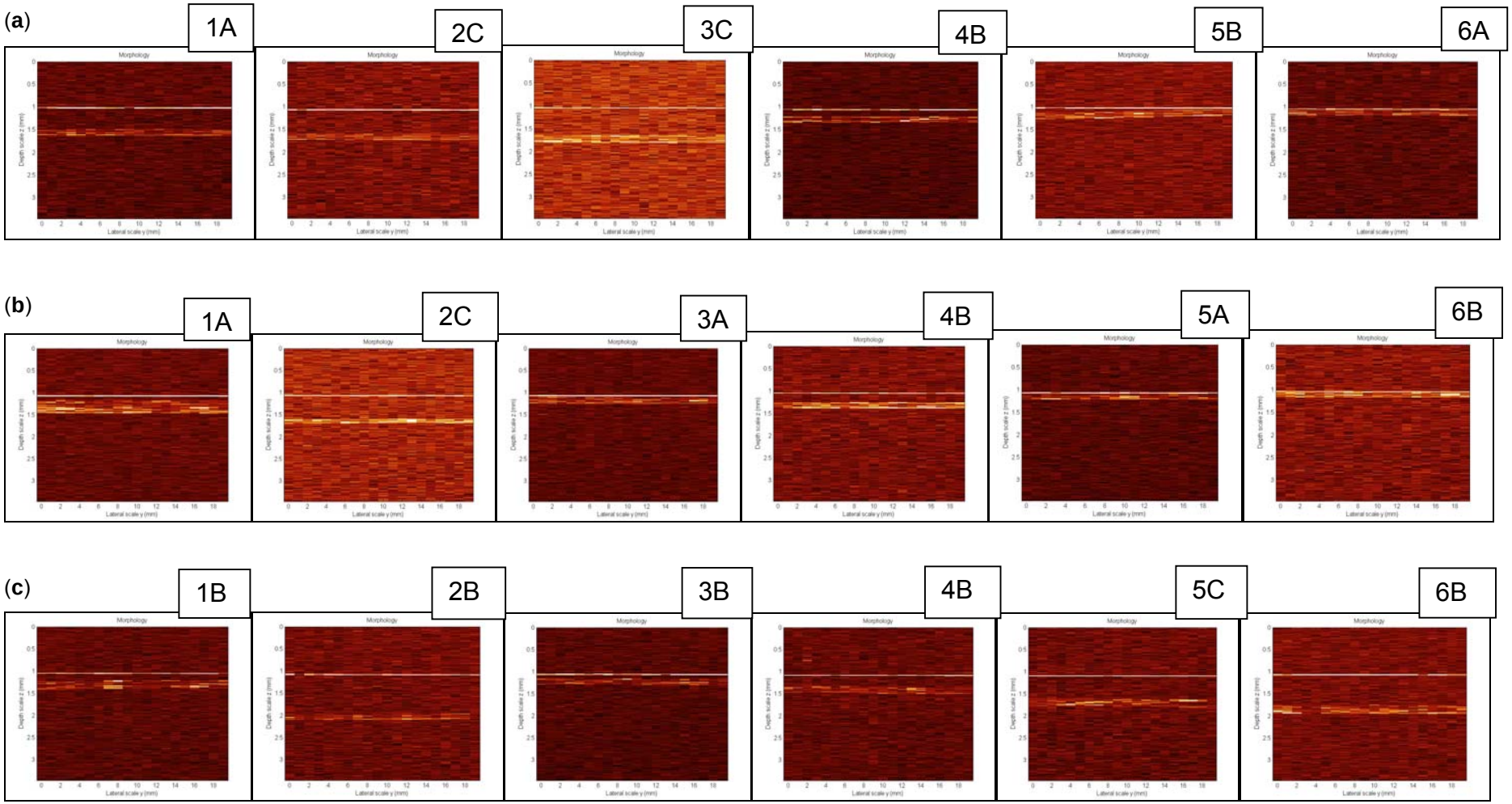

Figure 5.4 Tube wall thicknesses by real-time OCT scanning. Three types of tubes were evaluated: (**a**) a control tube: cell-free alginate with inert glass beads (to aid visualisation); (**b**) a hand-mixed cell-integrated tube; (**c**) a cell-integrated tube formed using the 12-element static-mixer in place. Images were taken at selected points along the length of tube as shown in Figure 3, the top line in each image represents the glass interface while the lower line represents the wall of the tube, respectively.

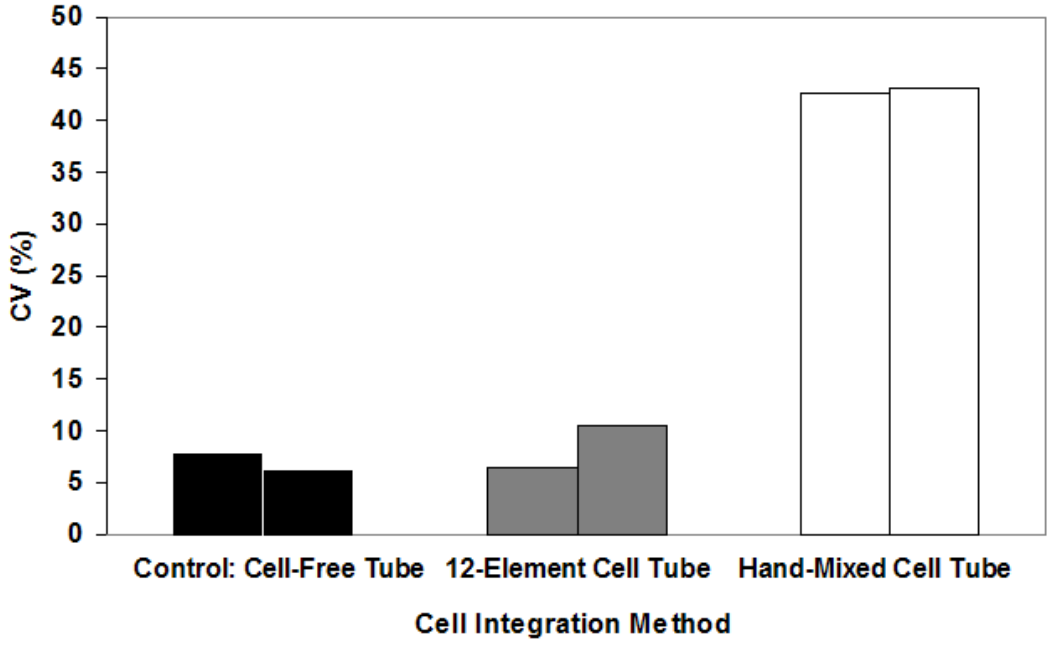

Figure 5.5 Uniformity of tube wall thickness by OCT. Three types of constructs were tested in duplicate: control tubes formed with 0.7µm glass beads integrated via roller mixer, 12-element statically mixed cell-integrated tubes and hand-mixed cell-integrated tubes. Wall thickness was measured at 18 points (as shown in figure 5.4) and coefficient variation (CV) was calculated. Mean wall thickness, (n=18) ± SD was 157.2±12.1µm and 134.3±8.2µm for control tubes; 160.6 ±10.1µm and 135.6±14.1µm for 12-element statically mixed cell-integrated tubes and 160.4±68.3µm and 349.5±150.5µm for hand-mixed cell-integrated tubes. All tubes were made using: Mark 2 device, 300µm wall gap tube-forming device configuration, 1.0% alginate concentration, 1.87ml/min sample injection rate, 20ml/min calcium chloride infusion rate at 0.09M concentration. Tubes with cells contained cells at $1x10^7$ cells/ml.

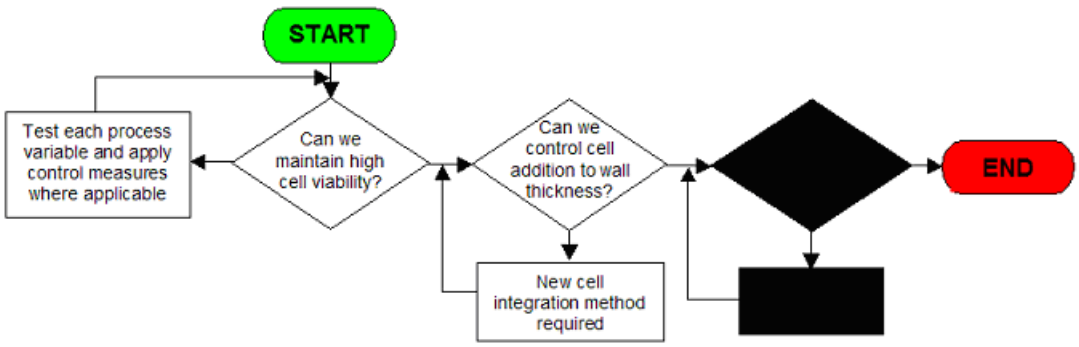

Figure 5.6 Flow diagram of experimental decisions for section 5.2.

the alginate and variation inherent to manual methods. In order to test this hypothesis 12-element static mixers were connected upstream the tube-forming device as shown in figure 5.3. OCT scanning indicated that wall thickness of cell-integrated tubes processed using a 12-element static mixer was more uniform than manual mixing with CVs similar to the ones obtained with cell-free alginate tubes (~7%). This result shows that the 12-element static mixer can help ensure effective mixing, resulting in cell-integrated alginate tubes with greater uniformity of wall thickness.

5.2 CELL VIABILITY STUDIES

5.2.1 Effect of Processing on Viability

In this section we investigated the effect of the process on cell viability (fig. 5.6). Viability is important due to its direct effect to viscosity of mixtures that are used produce the cell-alginate tubes – i.e. badly managed shear conditions could increase cell death, and poorly mixed systems have poor tube wall thickness consistency. Other groups have conducted similar viability testing to their processes (Sakai et al. 2004; Takei et al. 2006). In biochemical/pharmaceutical industries, it is conventional to agitate fluids/solids using impeller systems. Whilst this is normally acceptable for suspension cultures, here impeller mixing is undesirable due to the scale of the volumes used and need for high cell viability. Mammalian cells are large in size and hence more prone to shear forces than bacterial cells, produced by such mixing systems. The main advantage of static mixing is the negligible shear during processing. This is vital for biological cell integration.

In this first experiment, the effect of passing smooth muscle cells (SMCs) through the process and the impact on the viability of these cells was examined. Cells were counted before after harvesting, used in an alginate

mixture to form a tube, which was immediately resolubilised using citrate (Orive et al. 2003; Markusen et al. 2006), and the cells were recounted.

Results revealed a cell viability count of 93.1% just after harvesting. After processing however, averaged viability dropped to 67.7% ± 6.0. Given the CV in counting low cell numbers, this is a substantial drop in viability. It is critical to understand which factors have affected viability. The factors must be isolated and controlled. Factors that could have affected viability included: contact of cells with alginate, $CaCl_2$, sodium citrate, food colouring, or any component used to make up these fluids; damage due to centrifugation; shear via processing using the static mixer (magnitude of shear ~0.0003N/m^2 from static mixer); and shear via processing within the tube device (magnitude of shear ~0.0017N/m^2 from tube-forming device) and/or a combination of some or all. Previous studies have shown that cellular viability should only fall between shears of 0.75-10N/m^2 (Mardikar and Niranjan 2000).

5.2.2 Effect of Processing on Viability Repeat

The previous experiment showed a 25.4% drop in viability as a result of processing cells in order to create a cell-alginate tube. However, the lack of automation and consistency prompted a repeat experiment to verify the reproducibility of the viability drop before beginning a series of experiments to identify the underlying causes.

Initial cell viability counts yielded 97.7% ± 4.6 viability after harvesting. C cell counts taken after mixing cells with alginate, prior to processing within the tube-formation tube-forming device gave only 25.8% ± 3.7 viability. And final averaged cell counts were 16.5% ± 3.7 and 26.3% ± 7.2. This indicated a 73.6% drop in viability over the 60 min period required to prepare the sample and form the tubes. These results show that the largest drop in viability occurs during mixing of cells in alginate. Given this huge drop in viability any further effects from processing within the tube-forming device appeared negligible. It was concluded that the stage of mixing with alginate was highly detrimental to

the viability of the cells introduced to it. There was a mechanism that was actively destroying the cells. This could have been due to toxic effect of alginate, $CaCl_2$, redisolution step with sodium citrate, or pH. The exact cause was yet to be established. A series of experiments were therefore devised to isolate which variables were affecting viability.

5.2.3 Effect of Concentration Steps on Viability

In order to better understand the drastic drop in viability during processing, it was decided to run a series of exhaustive tests in order to isolate the main causes of this decrease. Conditions tested were all those that might affect cell viability throughout normal cell processing (see Appendix A). The first condition tested was concentration via centrifugation and resuspension. It was hypothesised that the forces exerted within the centrifugation device might impact negatively on cell viability within certain limits. Other groups have reported affects of centrifugal force on human oral cell carcinoma (Chien et al. 2006) and mouse sperm (Katkov and Mazur 1999).

Figure 5.7 shows the effects of five consecutive concentration cycles at 100xg on five different cell concentrations. A horizontal line of best least squares fit indicates that there is no cumulative effect to cell viability of up to five passes of centrifugation and resuspension steps. Although this is not a large centrifugal force applied to the cells, this experiment discounts the possible negative effects of cumulative concentration steps at 100xg to viability of this type of mammalian cell. Concentration steps would not usually exceed 3 cycles however.

5.2.4 Effect of Media on Cell Viability

The next tested condition was possible toxic effect of prolonged exposure to

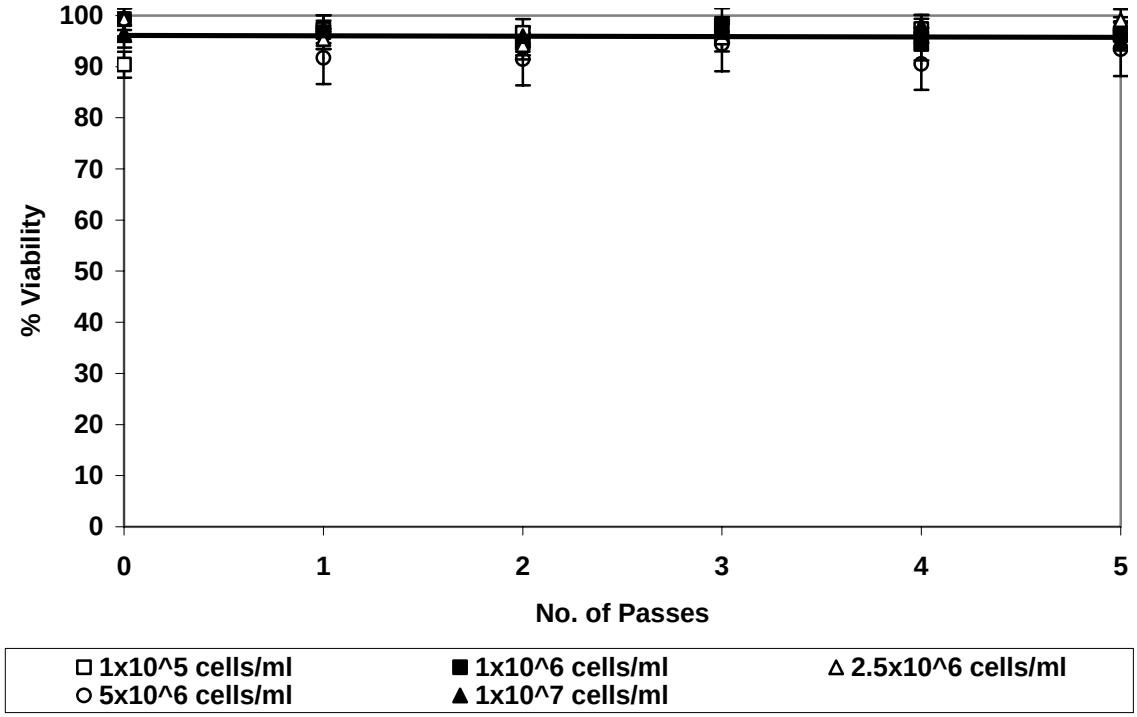

Figure 5.7 Viability as a function of number of passes through centrifugation and resuspension steps. Cell concentrations: $1x10^7$, $5 x10^6$, $2.5 x10^6$, $1x10^6$ and $1x10^5$ cells/ml were tested. Conditions used throughout were: centrifugal speeds of 100xg at 5 min, rat aortic SMCs, and 20°C. Cell counts were conducted using Trypan Blue and a haemocytometer. "No. of passes" represents concentration cycles of centrifugation followed by resuspension using complete culture medium. Symbols represent averaged triplicate cell viability counts using Trypan Blue and a haemocytometer. Solid line represents line of best least squares fit through all data points. Error bars represent CV across data points.

any of the media used during the processing of the mammalian cells. The solutions that come into contact with the cells include: complete culture medium, sodium citrate, 0.09M $CaCl_2$, food colouring and N-Saline. Each solution was tested in turn to establish any decreasing effect on viability.

It can be seen from figure 5.8 that for all 6 conditions, none of the tested media cause significant cell viability reduction within 1 hour testing time. Certain conditions (i.e. culture medium, food colouring in buffer and N-Saline) appear to give more stable trends and others ($CaCl_2$ and sodium citrate) appear to fluctuate greatly. This highlights the fact that cell counting using the haemocytometer can cause errors up to 30% (Uyeda et al. 1962). Given this point, the fluctuations seen by the $CaCl_2$ and sodium citrate trends are well within error margins. All viabilities stay above a threshold value of 80% – suggesting that these conditions do not affect cell viability of cells being processed up to periods of 60 min. It must be noted that figure 5.8 is compiled from cell data taken on different days. This impacted on the initial cell viability.

5.2.5 Effect of Liquid Alginate on Cell Viability

The next tested condition was the impact of exposure to liquid alginate on cell viability. Since there is no literature to suggest alginate should impact on cell viability, it was hypothesised that alginate should have no negative impact (Domm et al. 2004).

Figure 5.9 suggests a significant fall of cell viability with time over a fixed period of 3 hours. A typical experiment to produce 3-5 tubes can easily result in cells suspended in alginate for up to this amount of time. The trends suggest a particular pattern of falling viability associated with increasing alginate concentration from 0.5 to 1.0%. A one-way ANOVA and TUKEY HSD tests reveal that there is a significant difference between the trends with an F-value at 6.8265 and critical 5% and 1% values at 3.89 and 6.93, respectively. The TUKEY test shows that the trend for 1.0% alginate is significantly different

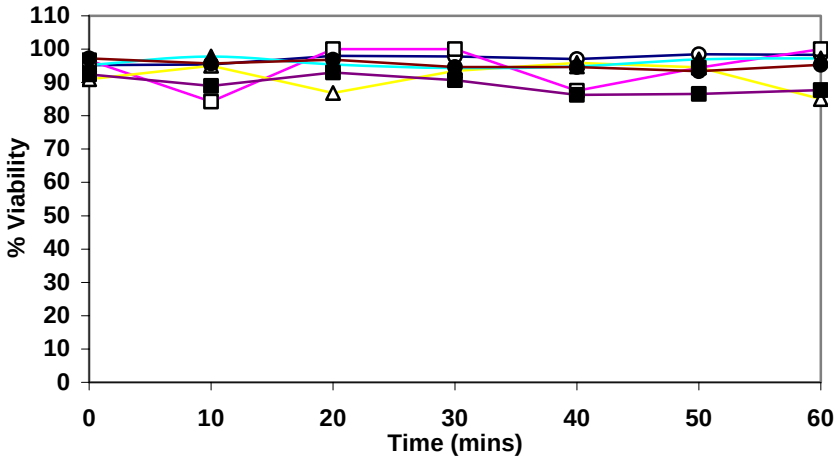

Figure 5.8 Effect of holding time on cellular viability. Following resuspension solutions were used to test impact on viability: complete culture medium (○), 0.1M trisodium citrate (□), 0.09M $CaCl_2$ (Δ), 10μl/ml food colouring in NaCl buffer (●), N-Saline (■), and complete culture medium (▲). All experiments were carried out at 20°C unless otherwise stated. A5r7 rat SMCs were used at $1x10^5$ cells/ml concentration and kept stationary over the holding time period tested. Results were obtained using Trypan Blue and haemocytometer. Symbols represent averaged cell viability. Coloured lines joins data points to help visualise trend rises and falls.

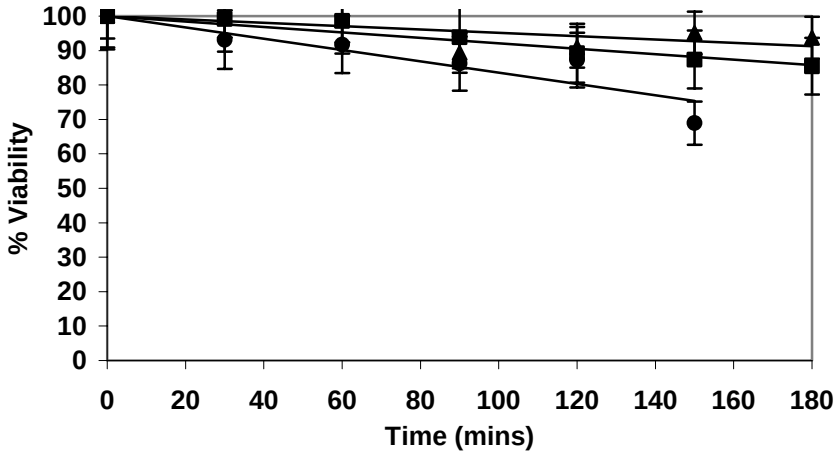

Figure 5.9 Effect of exposure time in liquid alginate (Manugel DMB). The following alginate concentrations were tested: N-Saline (■), 0.5% alginate (▲), and 1.0% alginate (●). Rat A5r7 SMCs at $1x10^7$ cells/ml final concentration was used throughout, and experiment was carried out at 20°C. All cell counts were obtained using Trypan Blue and haemocytometer. Symbols represent average cell viability. Solid lines represent lines of best least squares fit through each data set. R^2 = 0.9224, 0.4148, and 0.8238, respectively. Error bars represent CV across triplicate cell counts.

from the other two trends almost to the 1% level. The control experiment (N-Saline) also shows a drop with cell viability. This may be a further verification of holding time impacts on cell viability, regardless of the media, as well as toxic effects of alginate. The weak correlation of the 0.5% alginate trend (R^2 = 0.4148) could help explaining the lack of significant difference between this trend and that of the control. The 1.0% alginate trend (R^2 = 0.8238) is more reliable, showing a strong correlation between time and viability. The final point to note is that cell death rate does not appear to be predictable. Section 5.2.1 showed a 25.4% drop in viability, section 5.2.2 showed a 73.6% drop within 60 min, and in this experiment we see a 30% drop within 3 hours.

5.2.6 Effect of Infusion Speeds on Cell Viability

In this study we tested the final condition – effect of infusion rate to viability (normalised against an initial cell count from freshly harvested cells). Infusion speeds of $CaCl_2$ that drives the regulator ball through the alginate could create shears of up to 0.0017N/m^2. Although other research groups have reported that shears of 0.75-10N/m^2 is necessary to begin damaging cells (Mardikar and Niranjan 2000), this nonetheless needed verification testing in order to be thorough.

Analysing the results in figure 5.10, it can be seen that there are two parallel lines of best least squares fit, representing a constant difference in cell viability between manually created cell-embedded beads and cell-alginate tubes. At first glance, it would be logical to assume a consistent 5% drop in viability throughout infusion rates due to processing through the tube-forming device. This would be an obvious indication of shear damage. Upon closer inspection there is one major fault with the results – all of the results are in the region of 50-70%, indicating a drop in viability whether processed (tubes) or unprocessed (beads). This finding is in agreement to previous results, i.e. there seems to be a large drop in viability before any processing has begun.

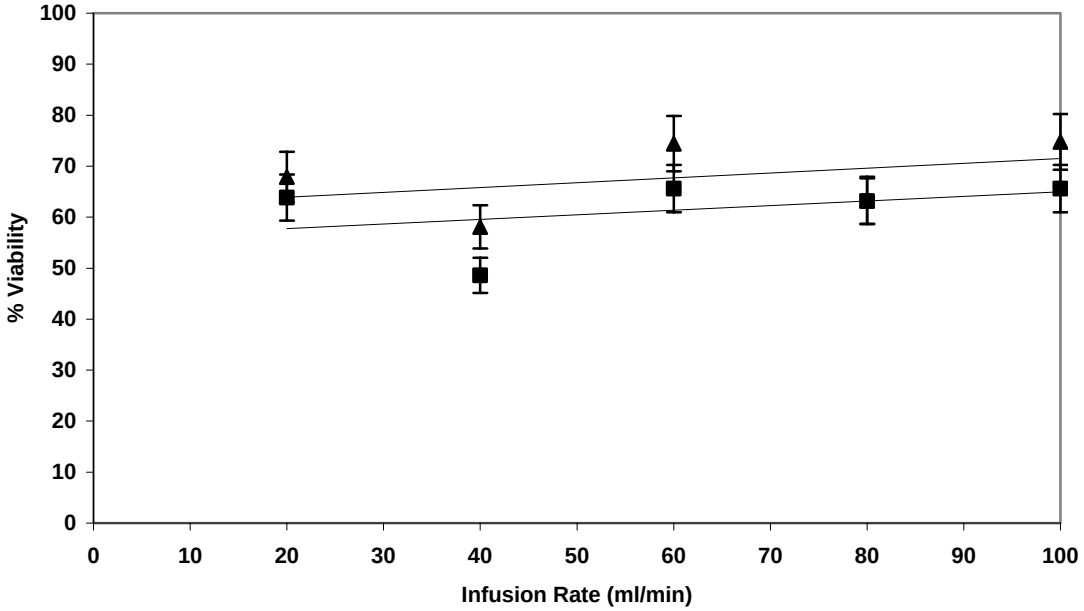

Figure 5.10 Study of viability as a function of infusion rate through the main tube-forming device. Solid lines represent lines of best fit for unprocessed cells (beads) (▲) and processed cells (tubes) (■), which correspond to the upper and lower lines, respectively. All tubes and beads were made using: (300μm wall-gap configuration), 1.0% alginate, rat A5r7 SMCs at $1x10^7$ cells/ml, 20°C and 0.09M $CaCl_2$. All were dissolved in 1.0M trisodium citrate. Cell counts were performed using Trypan Blue and haemocytometer. Symbols represent averaged triplicate cell viability. Error bars represent CV across triplicate cell counts.

Table 5.2 Summarised results from sections 6.1.1 – 6.1.5 showing affect of holding time in Manugel DMB on cell viability.

Section	Cell Passage No.	Time of Exposure (mins)	Initial Viability (%)	Resultant Viability (%)
5.2.1	18	Unknown	93.1	67.7
5.2.2	13	60	97.7	29.7
5.2.5	13	180	100.0	~ 70.0
5.2.6	19	60	100.0	~ 59.0

This time the fall in viability is ~40% over an hour used to prepare the cell-alginate mixture, form tubes and beads, and then re-dissolve them using sodium citrate.

Table 5.2 shows a summary of all holding time experiments and affect of Manugel DMB on cell viability. These experiments highlight an inherent problem with this type of alginate on rat aortic SMCs (as established statistically in section 5.2.5). Other groups have worked with Manugel DMB but have not appeared to have encountered any issues regarding viability (Domm et al. 2004). Despite this being a pharmaceutical grade product that was also autoclaved, one cannot dismiss the possibility of contamination either in the alginate itself, or the N-Saline used to makeup the alginate affecting the viability of the smooth muscle cells used in this study. The latter of the two explanations would explain the downward sloping trend seen with N-Saline in figure 5.9. This coincided with a group study into spore contamination of the lab during the time (data not shown). In that investigation, all sterilisation steps were tested and the root cause isolated to the Manugel DMB.

5.2.7 Pronova SLG 100 and Static Mixer Impacts on Cell Viability

As per figure 5.6 indicates – a control measure is necessary to manage cell death as a result of exposure to alginate. Furthermore, where the cell integration was un-automated there were many areas (harvesting, mixing cells and alginate, cell counting, etc.) where variability between experiments/batches could arise. Therefore cell viability impacts of the static mixer were also tested in this experiment. In order to attain more accurate viability results for the main tube-forming device, two people simultaneously did the cell counting to minimise operator errors. Alginate source was also replaced with sterile, liquefied alginate – Pronova SLG 100.

Viability testing through the static-mixer involved passing cells through the device with no alginate present. Viability of cells through the tube-forming device involved forming cell-alginate tubes, instantly resolubilising them in

tricitrate in parallel with cell/alginate beads, and cell enumeration performed. Shear is calculated via the shear-rate equation:

$$\tau = -\mu \cdot \frac{dv}{dy}$$

Where: τ = shear stress (N/m^2)

μ = viscosity ($N.s/m^2$)

dv = change in flowrate over area (m/s)

dy = change pipe/tube diameter (m)

Previous studies have shown that cellular viability begins to fall between the 0.75-10N/m^2 region depending on the method of measurement (Ludwig et al. 1992; Ma et al. 2002). In the tube-forming device used in the present study, at maximum practical speeds of 100ml/min, only then do shear rates approach 0.0083N/m^2, although normal operation dictates speeds of 20ml/min (0.0017N/m^2) for maximum control. Static mixers are purposely designed for low shear (Bertsch et al. 2001) and they can be operated at low flowrates without compromising mixing efficiency. In our design we use a maximum flowrate of 1.87ml/min, which generates a calculated shear rate 0.00031N/m^2.

A series of experiments were performed in order to verify experimentally whether processing through the static mixer or the tube-forming device could affect cell viability. Viability testing through the static-mixer involved passing cells through the device with no alginate present in order to expose cells to a worst-case scenario (since alginate offers lubricating protection). Viability of cells through the tube-forming device involved forming cell-alginate tubes in the tube-forming device, instantly re-dissolving them in 1.0% sodium tricitrate, with cell/alginate beads produced and dissolved, and cell enumeration (Trypan Blue) performed in parallel as a timed control. Alginate beads are a widely used research standard and are becoming increasingly popular for expansion of mammalian cells for use in tissue

engineering (Eiselt et al. 2000), and offered a relatively shear-free comparison (compared to cells passed through the shear a processing device).

Figure 5.11*a* demonstrates the viability of the cells passed through a 12-element static mixer at varying infusion rates. As expected the static-mixer had no significant effect on cell viability. Normal operation would use the top speed of the device at 1.87ml/min. Figure 5.11*b* shows viability of cells passed through the tube-forming device to form a tube, at varying infusion rates. Results obtained indicated a slight trend of decreasing viability with increasing infusion rates, but with Pronova SLG-100 overall viability remains over 90% unlike figure 5.10, which used Manugel DMB. This strengthens the previous hypothesis that the Manugel DMB was the source of the large drops in viability. Here we see a viability drop ~5% with infusion speeds of 100ml/min. This result also discounts any significant negative effects of process shear to cell viability, both through the static mixer or the tube-forming device within the shear rates tested. However, normal operating speeds of 20ml/min show a minimum fall in viability, as would be expected. This set of experiments shows that viability remains high for cells processed through the static mixer and tube-forming device in worst-case conditions, although it is customary to operate at much lower shear levels in the tube-forming device.

5.2.8 Cellular Apoptosis Analysis

As a final viability experiment, the Gauva capillary cytometer was used to analyse apoptosis. In this experiment, we wanted to investigate whether processing could trigger an apoptosis response, shown to be the case with excessive mechanical force (Kainulainen et al. 2002; Wernig and Xu 2002). This would verify or discount earlier shear experiments, which showed that there were little viability effects of processing rat smooth muscle cells through both the static mixer and the tube-forming device.

(**a**)

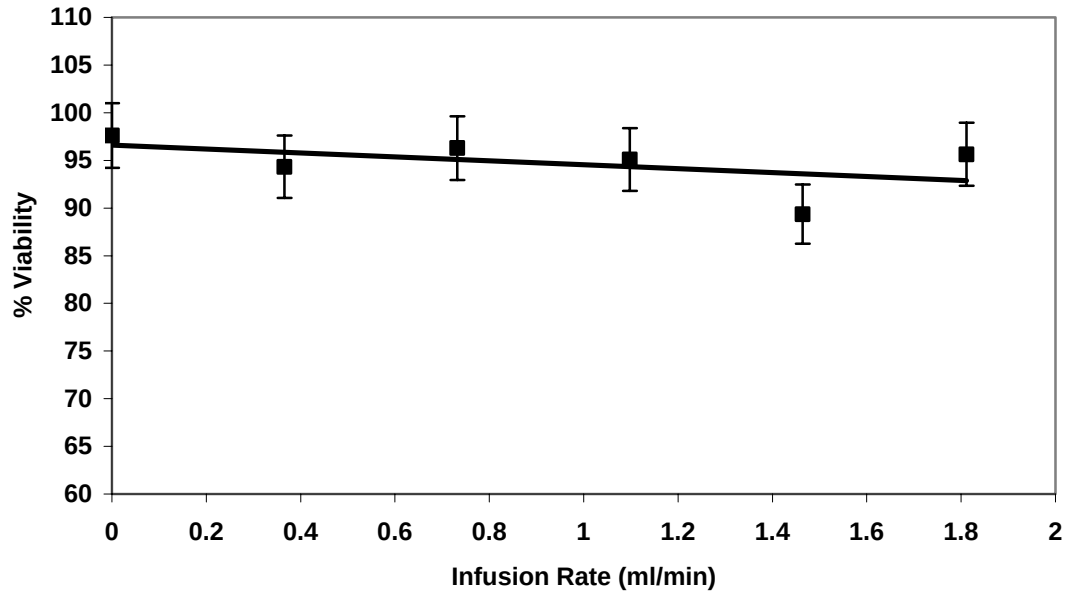

(**b**)

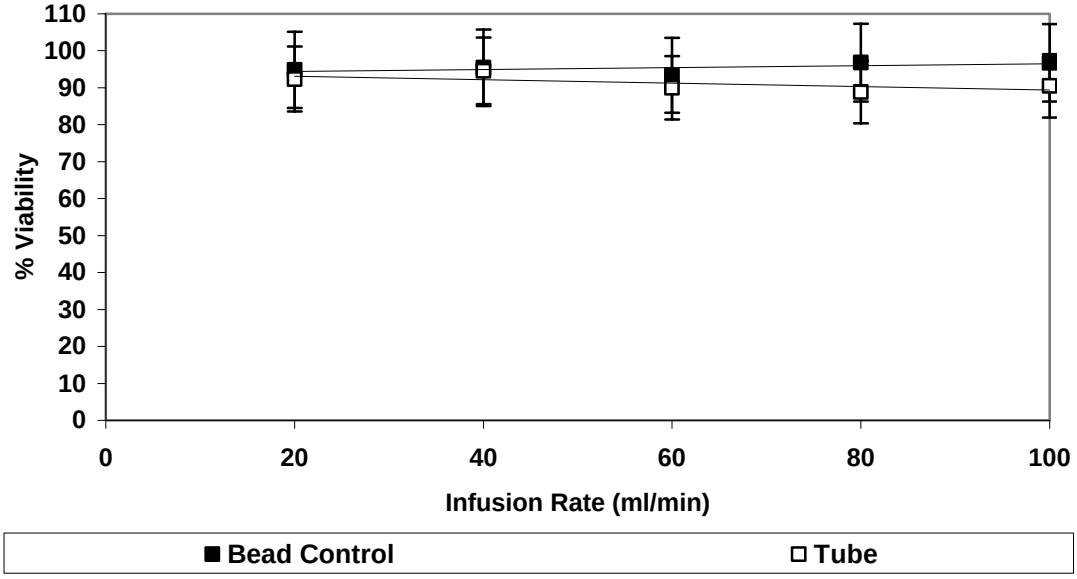

Figure 5.11 Viability as a function of infusion rate for cells processed through (**a**) a 12-element static mixer with no alginate (maximum shear); and (**b**) cells extruded into an alginate tube via the main tube-forming device. Symbols represent averaged triplicate cell viability. Solid lines represent best-fit linear trends through data points. Error bars represent CV across triplicate cell counts. For (**b**) cells encapsulated in alginate beads with negligible shear were used as controls to calculate viability values at parallel cell-counting times. R^2 = 0.2414 and 0.7494, respectively.

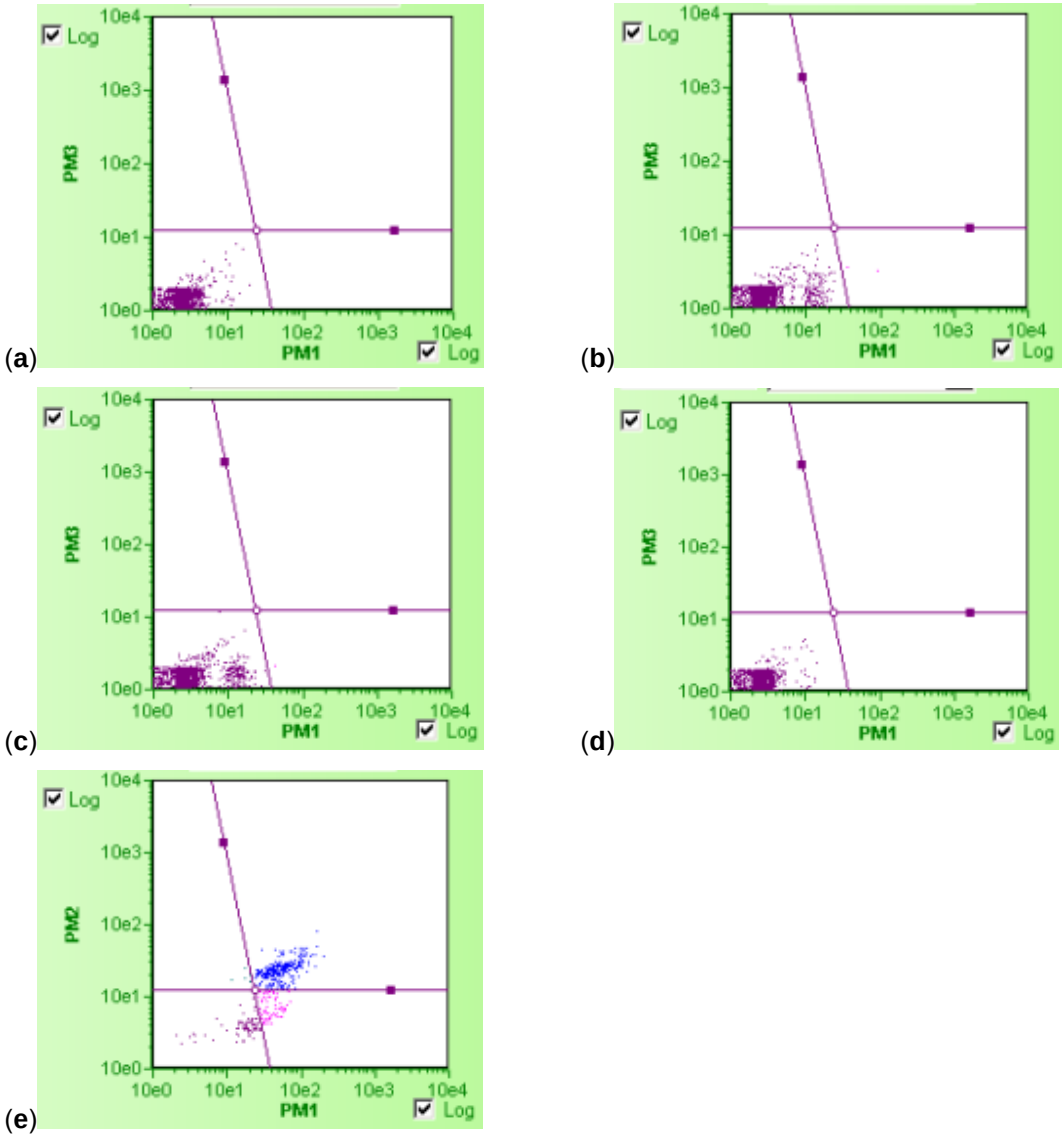

Figure 5.12 Apoptosis analysis by capillary cytometry. One end section (**a**) and middle section (**b**) from a hand-mixed cell integrated tube were analysed for apoptosis. Corresponding sections (**c**) and (**d**) were analysed for a 12-element statically mixed tube. (**e**) Shows a sample consisting of a mixture of apoptotic and non-apoptotic cells. The lower left quadrant shows viable cells, not undergoing detectable apoptosis. The lower right quadrant demonstrates cells in the early stages of apoptosis. Upper right quadrant shows cells in the late stages of apoptosis or dead cells. And upper left quadrant demonstrates cellular debris. % of cells in each quadrant lower left, lower right, upper left and upper right were: (**a**) 100, 0, 0, 0%, (**b**) 99.86, 0.14, 0, 0%, (**c**) 99.86, 0.14, 0, 0%, and (**d**) 100, 0, 0, 0% respectively. Analysis was carried out using Guava Nexin kit and Guava EasyCyte GR1 device. All tubes were analysed within 3h.

For this purpose, cells were stained with Annexin V a calcium-dependent phospholipids binding dye that binds to phosphatidylserine (PS), a molecule that is expressed on the surface of cells in the early stages of apoptosis and that of dead cells. A second component then binds to PS to emit fluorescence.

Figure 5.12 demonstrates 4 separate analyses from the end and central sections of cell-integrated tubes formed by hand-mixing 5.12*a* and 5.12*b*, and by static mixing 5.12*c* and 5.12*d*, respectively. A control sample had approximately 0.14% apoptotic cells in the lower right quadrant. Results showed that 94-99% of cells are non-apoptotic having undergone processing. These results show that sample injection at 1.87ml/min through a 12-element static mixer, 20ml/min infusion rate through the tube-forming device and contact for prolonged periods (up to 10 hours) with sodium alginate does not trigger apoptosis nor substantial cell death. This backs up earlier shear cell viability studies.

5.3 CELLULAR SPATIAL DISTRIBUTION STUDIES

5.3.1 Initial Cell-Integrated Tube OCT Scans

In order to assess the optical clarity of images obtained by OCT for alginate tubes containing biological cells instead of glass beads, a series of preliminary scans were carried out. As an added bonus, any insight into homogeneity of cells spread in the solidified alginate wall would be advantageous.

The aims of this experiment were for qualitative reasons only, namely to determine whether the quality of OCT scans would be sufficient for analysis. Figure 2.11 is reiterated for convenience. The results (fig. 5.13) show that cells offer a great enough backscatter of light for OCT images to be of sufficient clarity (i.e. backscatter is necessary to illuminate the walls of the

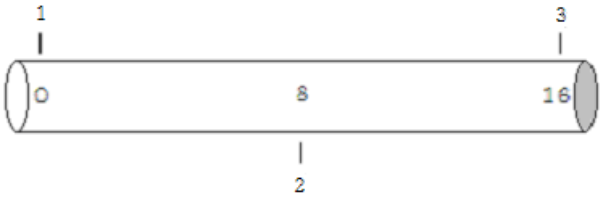

Figure 2.11 Experimental scanning setup and nomenclature used for Mark 1 primary OCT experiment. Points 1 and 3 are 180° from 2 on the opposite face of the glass capillary. Points 1 and 3 are on either end of the tube, with point 2 lying in the centre of the glass capillary. The cross-sectional scan was taken at a random point along the tube.

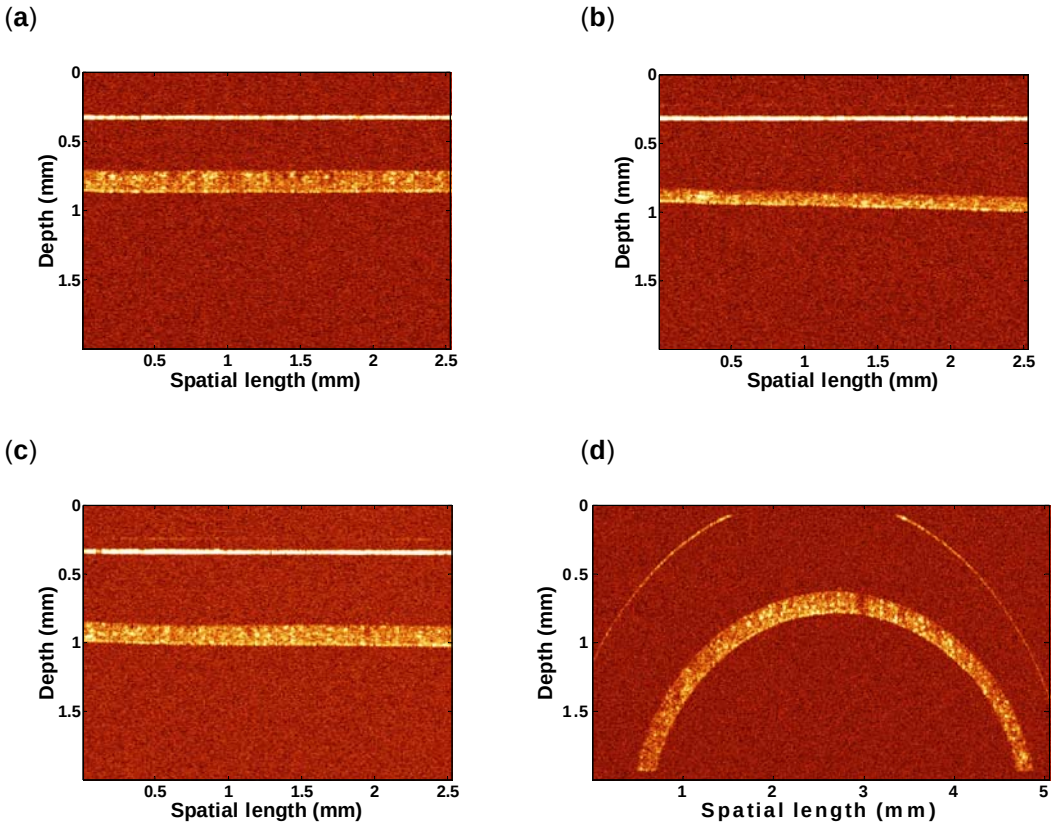

Figure 5.13 OCT images of cell tube: (**a**) at position 1; (**b**) at position 2; (**c**) at position 3; (**d**) cross-sectional OCT image. First line represent glass to air interface, second thicker line represents the cell-integrated alginate tube. Image also shows quantitatively the spread of cells within the tube. Tube was made using: 300μm gap width configuration; 1% final alginate concentration; 0.09M $CaCl_2$ concentration; $1x10^7$ cells/ml final cellular concentration; at 10°C.

tube, due to the transparency of alginate hydrogel). Results also back how hand-mixed cell-integrated tubes are not sufficient – the walls to this cell-integrated tube are obviously not the same thickness. Furthermore, some qualitative data for distribution of cells within the solidified alginate could be obtained. The bright points indicate clusters of cells reflecting light. In cell-free (pure) alginate, bright points would only be attributed to clusters of inert glass beads. It can quite easily be seen that cells in this tube were not homogeneously distributed. This is most apparent with figure 5.13*d* that shows dark patches, i.e. areas of alginate containing lower concentration of cells.

This experiment brings to light that although the suspension of cells maybe homogeneous, i.e. free from aggregates and well mixed within itself, its introduction to alginate and the mixing of the cells with the alginate requires a new engineering method to ensure consistently high cell viability with homogenous distribution of cells within liquid/solidified alginate.

5.3.2 Effect of Static Mixers on Cellular Distribution

The next important parameter to investigate was the spatial distribution of cells within the alginate hydrogel (fig. 5.14). This is important since growing cells require a homogeneous distribution to proliferate evenly throughout the alginate tube in order to form a uniform tissue – an important parameter regardless of the end use of the cell-integrated tube. To reinforce this point, Dar carried out work that looked exclusively at optimising seeding and distribution of cardiomyocetes in a porous 3D alginate matrix (Dar et al. 2002). Evidently, the long-term success of any cell-populated scaffold will depend on a uniform distribution of cells and ECM (Heywood et al. 2004). From a certain perspective, embedding cells within the alginate maybe more efficient than post-seeding cells onto a porous alginate scaffold. Whilst it may be argued that aggregation is required to form a tissue, there is always a degree of cell

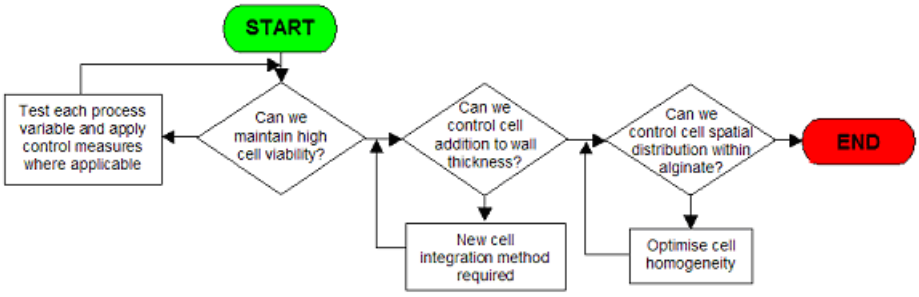

Figure 5.14 Flow diagram of experimental decisions for section 5.3.

migration, plus an extreme case would mean a cell-alginate tube with pure alginate sections and pure cell sections (i.e. un-uniform tube walls). This is clearly undesirable, as a tube would not be formed. As we have already discussed, tube wall thickness is essential for cell viability of encapsulated cells. If cells are in-homogeneously distributed in the alginate mixture, we could have a resultant tube with non-uniformly thick walls, and large percentages of non-viable cells.

The uniformity of cell distribution was quantified by calculating the inter- and intra-tubular CV of the cell counts obtained (figure 5.15). Figure 5.15*a* shows data grouped per tube, showing inter-tube variation averaged over corresponding sections, whereas 5.15*b* shows intra-tube variation averaged over 3 tubes per cell-integration method.

Figure 5.15*a* shows that cell-integration via hand mixing and 8-element static mixing yields no substantial difference in CV. However upon increasing the size of the Kenics mixers from 8 to 12 elements, average CV falls to 27.8% for 12-element static mixing indicating a more uniform cell distribution pattern. A similar pattern is observed when the intra tube variation is evaluated, with average CVs for hand-mixed, 8-element and 12-element cell-integration of 64.2, 52.4 and 19.2%, respectively (fig. 5.15*b*). Notably, the ends of the tube seem to generate much higher variations in cell numbers, and this is consistent for all three cell-integration methods. Overall, the data undeniably suggests that there is a marked improvement with static mixing over hand-mixing techniques and with increasing the number of Kenics elements within the static mixer. Obviously mixing improves with greater number of static mixer elements, but this means a larger static mixer is required and greater amount of dead-space (i.e. lost material in the system) results. Commercially, suitable static mixer elements come in 8 and 12 element sizes only, but we envisage custom made mixers to suit our requirements on demand being a possibility.

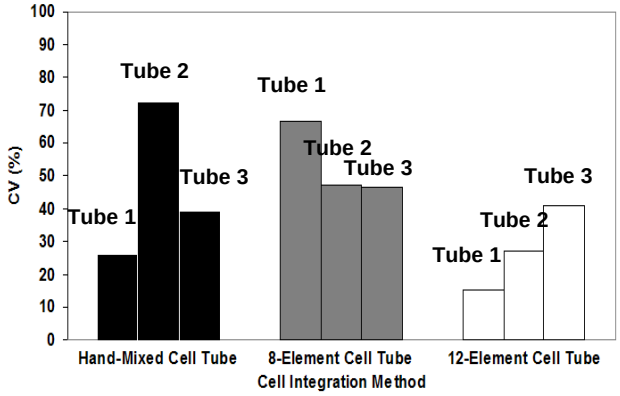

(**a**)

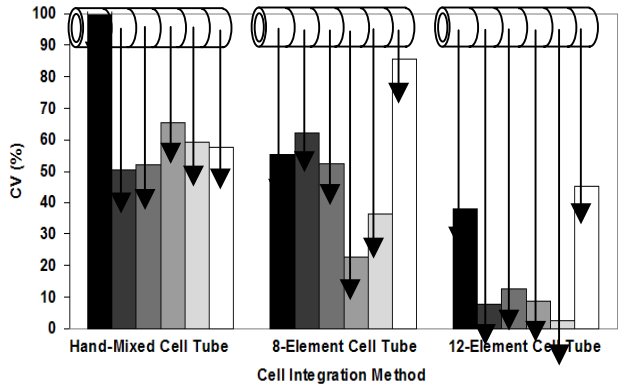

(**b**)

Figure 5.15 Cell distribution analysis by light microscopy. Inter (**a**) and intra (**b**) tube cellular distribution along the length of the tube for constructs formed by 3 cell-integration methods: hand-mixed cell tubes or in automated fashion using 8 or 12 element static mixers. 3 tubes were made per cell integration method. Tube weight/section was 0.3g/ ± 0.02g. All cell counts were normalised by section weight. CV was determined per tube and across sections. In (**b**) results are shown in section order from top to bottom. All tubes were made using: 300µm wall gap tube-forming device configuration, 1.0% alginate concentration, 1.87ml/min sample injection rate, 20ml/min calcium chloride infusion rate at 0.09M concentration and $1x10^7$ cells/ml concentration.

5.3.3 Visual Verification of Cell Distribution Using Light Microscopy

As with wall thickness, a visual verification of cellular spatial distribution was required. The aim was to attain a qualitative verification of the cellular spatial distribution through the alginate via use of a light microscope.

Images taken are shown in figure 5.16. It can be seen the difference between a pure alginate tube to one containing cells. However due to the inability to show cells in layers, the images show one superimposed image of cells within a 3D alginate gel. Both figure 5.16*b* and 5.16*c* look alike. One cannot distinguish a well-mixed, homogeneous tube to one that is mixed poorly. Although these images show us the difference between pure alginate and cell-integrated alginate, it did not provide a definitive qualitative conclusion of the benefits of using a static mixer over irreproducible hand-mixing techniques.

5.3.4 Visual Verification of Cell Distribution Using CLSM

In order to obtain a more distinctive, quantitative verification of cell distribution in-situ, confocal laser scanning microscopy (CLSM) was used. CLSM offers fast, non-destructive, cross-sectional, multipoint scanning. It allows a great range of magnification from macro to micro precision and produces high-resolution images of slices through a sample – hence constructing a digital 3D representation ready for analysis. Because the magnification can be adjusted, it was more suitable than OCT, offering a larger sample size.

Figure 5.17*a* shows the experimental setup for tube scanning locations and data manipulation in order to quantify results. From the cross-sectional scans 5.17*b*, a diagonal tangent was drawn across all images. Along the tangent, intensity profiles could be constructed (fig. 5.17*c*) and by measuring the area under these curves, we were able to quantify number of cells per volume of construct.

(**a**)

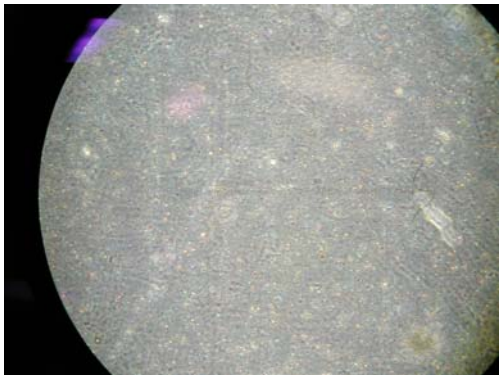

(**b**)

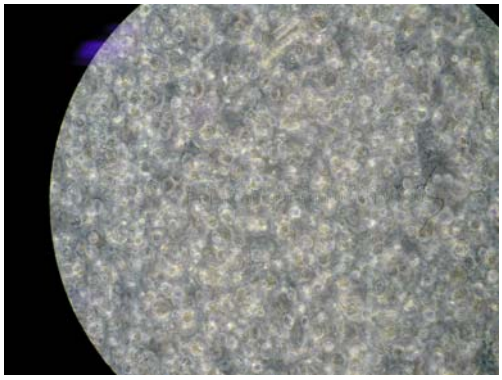

(**c**)

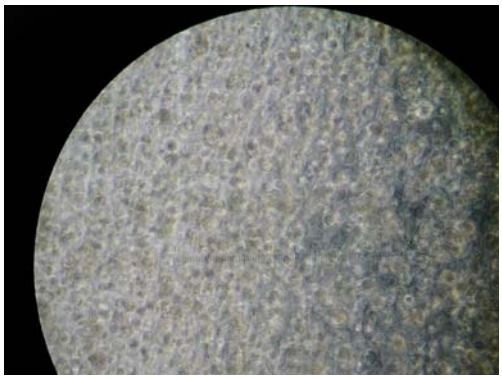

Figure 5.16 Light microscopy analysis of tubes: control tube containing glass beads (**a**); cell-integrated tube using 12-element static mixer (**b**); and cell integrated tube using hand-mixing technique (**c**). All images taken at X20 magnification using a light microscope, haemocytometer and standard coverslip. All tubes formed using: 300μm wall-gap configuration, 1.0% overall alginate concentration, $1x10^{7}$ cells/ml overall cellular concentration (where used), 0.09M $CaCl_2$ concentration, 20ml/min infusion rate, and 20°C. Glass beads were added at $1x10^{-3}$ g/ml to alginate.

Figure 5.17*d* shows the results extracted from this experiment. It can clearly be seen that the profile for the tube processed via a 12-element static mixer was more uniform than the hand-mixed control tube with a CV of 28.9% compared to 78.5%, respectively. The hand-mixed cell-alginate tube was had 3 sections with low area readings, indicating little presence of cells along the tangent. This was not the case with the statically mixed tube. Although variance appears high, a healthy concentration of cells is present in each section. In agreement with OCT and light microscopy data the CLSM results indicated that the presence of a 12-element static mixer improved cell distribution within the alginate matrix. Despite the crude results and experimental design, this is none-the-less a quantitative result for otherwise qualitative data. This experiment provides conclusive evidence, backing up previous figures, that by using a 12-element static mixer, cellular spatial distribution is improved within solidified cell-integrated alginate tubes.

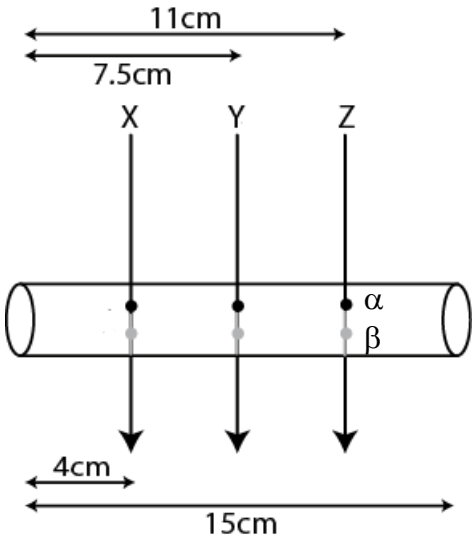

(**a**)

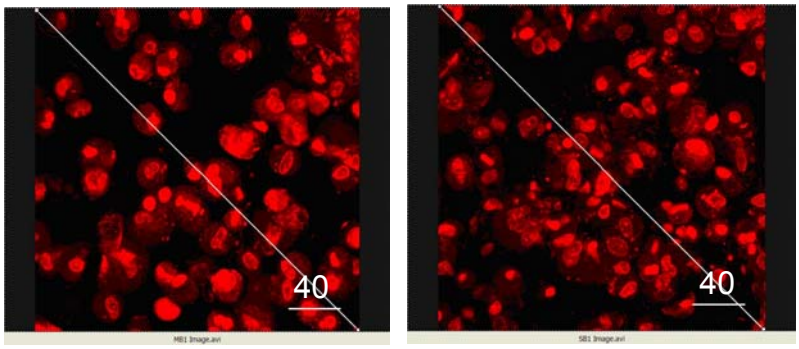

(**b**)

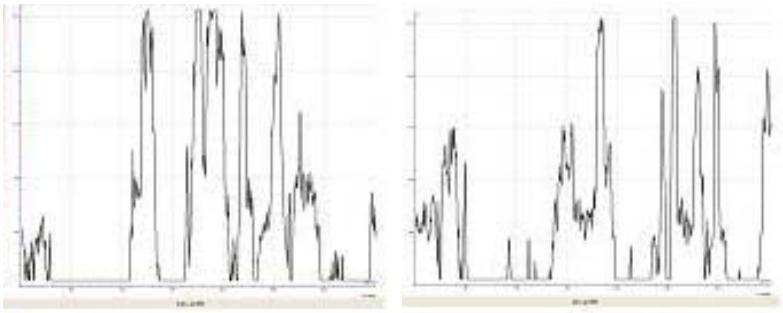

(**c**)

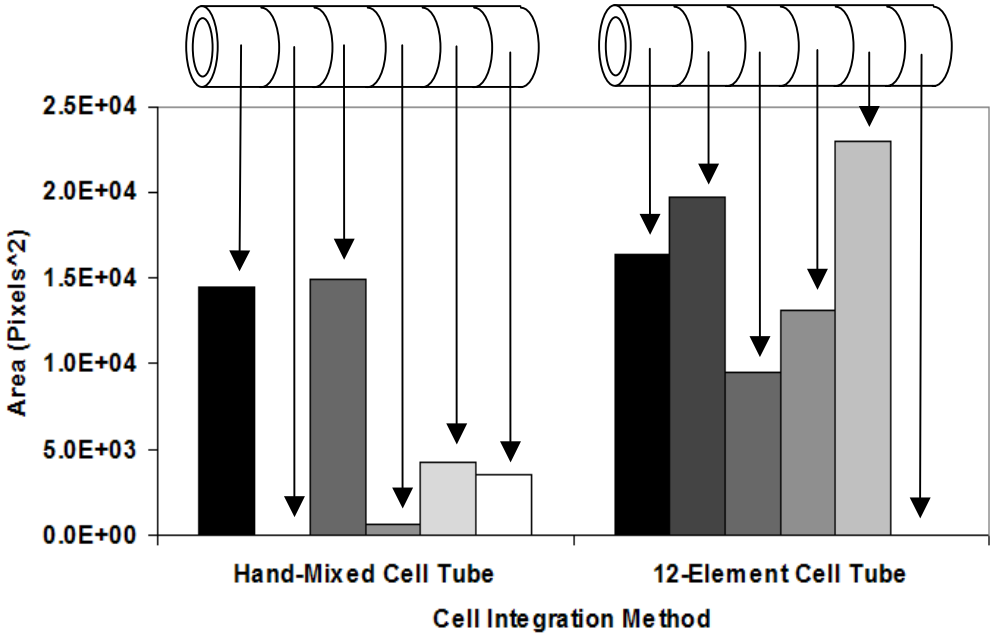

(**d**)

Figure 5.17 Cell distribution analysis by Confocal Laser Scanning Microscopy (CLSM). (**a**) Schematic diagram (not to scale) demonstrates the longitudinal (X, Y, Z) and vertical (α, β) positions used for CLSM analysis. (**b**) Representative images of hand-mixed (left) and statically mixed (right) tubes at position Yα. A scale bar is shown against 40μm. A diagonal line approximately 352µm was drawn through the sample and intensity data along this tangent was used to compile fluorescence intensity profiles shown in (**c**) from hand-mixed (left) and statically mixed (right) tubes at position Yα. (**d**) Total area under the fluorescence intensity profiles for positions: Xα, Xβ, Yα, Yβ, Zα, Zβ respectively. Area was calculated using raw confocal data and trend analysis software. One tube per cell-integration method was produced and analysed, CV across positions (n=6) was 78.5 and 28.9%, for hand-mixed and statically mixed tubes respectively. Tubes were stained as described in Chapter 2 and analysed within 6h.

6 Discussion

6.1 AIMS OF THIS THESIS

Reviewing Chapter 1, this thesis concentrated on the fundamental engineering aspects of the UCL tube-forming device. The device would provide an alternative tubular geometry to alginate structures, which could have end uses as a macro-encapsulation envelope or even provide a scaffold for tissue-engineered products. The three experimental chapters concentrated on three engineering aspects of said device: tube formation; monitoring methods; and cell integration.

How do we form alginate tubes? This was the most important question of all – without a means of forming the tube in the first place, the process would be a failed design. The patented UCL method existed, but at the start of this research had no protocols, was untried and untested, and had not been optimised or reconciled against any theoretical predictions. Goals were therefore: to develop a Theory modelling tube thickness; to then test the current state of the device; to modify and optimise its design to control process variability of this key parameter; and finally to find ways to manipulate wall thickness.

How can we monitor process efficiency? Another important part of any well-engineered process is the ability to directly monitor efficiency and engineer inherent consistency in the process. Monitoring methods to detect tube wall thickness, particle size, and particle number were required. Furthermore, quality control methods were needed to ensure that remaining operator-dependant processes such as cell culture had minimum impact on particle suspension consistency.

How do we effectively mix cells with polymer? This third and final question brings together the tube formation, monitoring methods and biological cell integration. This section would look at how cell encapsulation affects tube wall thickness, and how cell-integration impacts on cell viability. Finally the section should consider spatial distribution of cells within the

alginate tube since a basic requirement of any cell-integrated tube is to ensure that all parts of the tube contain an equal amount of cells.

6.2 RESEARCH PLAN

To achieve the research aims set out in section 1.9, the first question to tackle was whether or not we could form tubes using the UCL tube-forming device. This question was tackled in a two-pronged fashion. With the help of Prof. Ian Eames (Mechanical Engineering, UCL) and Dr. Mark Landeryou (Medical Physics, UCL), a Theory was developed based on Reynolds Laws of Lubrication, to see whether tube formation with the tube-forming device was theoretically possible, and the calculated tube wall thickness was determined. This was validated by experimentation firstly via pure alginate. Furthermore, a protocol for the device was developed to ensure consistency with human operator variables, and the device was tested for any inconsistencies and these would be rectified.

Next the monitoring methods were investigated. Chapter 4 concentrated on tube wall thickness, using Optical Coherence Tomography (OCT) as a means of directly monitoring this. This wall thickness could be compromised by aggregates of cells, plus large aggregates maybe contain necrotic centres hence by utilising several possible techniques at UCL – a Malvern Particle Sizer, a Leica QWin automated microscope, and a haemocytometer/Trypan Blue – a reliable method was found to consistently monitor cell aggregation and enumeration. Furthermore a high resolution, high-speed camera was used to directly analyse the tube formation process. Finally, we looked at developing controls to limit impact of laboratory techniques on cell homogeneity.

Chapter 5 brought together the tube formation, monitoring methods and biological cell aspects. After possible effects to tube wall thickness, the next variable to control was cell viability – if the cell viability was low at the start of the process, or heavily reduced as a result of processing this would

be inefficient. Chapter 5 concentrated on how to mix cells with alginate without compromising either the cell viability or the tube wall consistency. This was achieved using a technology from industries outside of conventional (bio)-chemical engineering – i.e. Kenics static mixers. This small plastic tip contained many elements that split, fold and recombine fluids to create mixtures. The economics of such mixers meant that they could be used once and disposed of, maintaining system sterility, and the negligible shear of the mechanics made them ideal for mixing cells with alginate. A syringe driver was modified for this technology and this was tested for impact on cell viability and also wall thickness consistency of tubes formed using these mixtures. The Kenics mixer was also tested on impact to cell spatial distribution within alginate, and CLSM used to quantify this distribution.

6.3 DISCUSSION

6.3.1 Tube Formation

In Chapter 3, a Theory to predict tube geometry was developed by solving a lubrication analysis based on the tube-forming device. This Theory is universal to any system of two liquids at the time of tube formation, however, when applied to reacting systems such as alginate-$CaCl_2$ it is only valid at the time of tube formation. After tube formation, other factors such as alginate shrinkage occur to tube wall thickness (Zhang et al. 2000). This Theory resulted in the $^2/_3$ Approximation, relevent as gap width becomes increasingly small, i.e. the predicted tube wall thickness is approximately equal to $^2/_3$ of the gap width. Due to the lack of fluid property terms in the final equations, i.e. fluid viscosity or density, the tube wall thickness is therefore independent of such properties. This is useful since it is undesirable for small fluctuations (e.g. viscosity changes due to cell lysis within alginate) to affect final tube wall thickness. The Theory goes on to describe how matrix fluid flows upwards, dragged by the spherical regulator, and due to end effects, results

in a slightly thicker tube wall thickness than that predicted. The experimental verification (fig. 3.4) shows data points falling within a preset range determined by computational fluid dynamics and the Theory.

At this early stage tube wall thickness was identified as the key geometry variable to control. This variable was decided upon consultation of existing literature. Glickis et al. outlined how oxygen and nutrient supply depends on mass diffusion (Glickis et al. 2004). Diffusional gradients are formed in large aggregates, often leading to a necrotic centre. The group found that hepatocyte spheroids any larger than 100μm in diameter began to have detrimental effects of oxygen limitation (fig. 6.1*a*). This means that a wall of mammalian cells cannot be any thicker than 50μm without a vascular network to supply nutrients. However, the oxygen limitations depends on other factors such as reactor agitation, immobilisation method and cell concentration (Khattak et al. 2007). Viability was consistently high for hepatocytes encapsulated in alginate beads (fig. 6.1*b*). In our alginate tubes, the possibility of nutrient flow on the outside and lumen of the tube, plus the inherent porosity of alginate should mean no oxygen limitations for wall thicknesses several hundreds of micrometers thick. In addition, cell-integrated alginate tubes will not initially contain cells at such a great concentration – with less demand of oxygen, less supply is necessary and walls can be thicker still. Another consideration is that, depending on the end use of the tube wall thickness will also determine its mechanical strength. But before mechanical strength can be tested in future work, we first concentrated on the ability to produce a tube with uniformly thick walls.

The robustness testing of the tube-forming device then began. Initial experiments showed fluctuations of tube length with alginate concentrations ranging from 0.5% to 1.0%. Correlation of data points to the line of best least squares fit had a R^2 value of less than 0.9 although a consistent CV under 5% indicated a level of precision within the tube-forming device, comparable to other well engineered cell-alginate encapsulating devices (Serp et al. 2000). R^2 values and robustness to alginate concentration changes between

(**a**) (**b**)

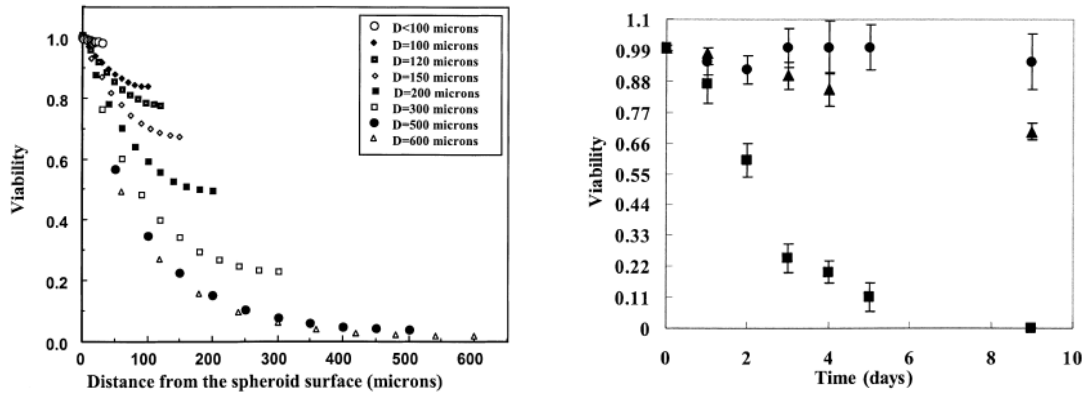

Figure 6.1 (**a**) Distribution profiles of viable cells in spheroids with a diameter ranging from 30-600μm. (**b**) Fraction of hepatocytes as a function of time in (●) alginate scaffolds, (■) spinners, and (▲) rotating t-flasks. The fraction of viable cells was calculated by dividing the number of viable cells according to MTT assay by the total number of cells according to DNA quantification assay. The error bars indicate the standard deviation around the mean value of the data point (n = 3) (Glickis et al. 2004).

0.5 and 1.0% was improved with a new protocol. However sensitivity to slight changes in alginate concentration still significantly affects tube length and therefore the design of the tube-forming device was reconsidered.

The heart of the tube-forming device consists of the dual port base unit and the spherical regulator. The mark 1 device has a narrow metal injector nozzle upon which the spherical regulator sits. When propelling fluid is expelled via this cylindrical nozzle the spherical regulator is pushed upwards. With the mark 1 design, the regulator travels upwards with little directional control, like a rocket sitting on a pad. The idea behind the mark 2 device design was to offer greater directional control, much like a barrel of a firearm and a bullet. The spherical regulator sits tightly within the eggcup-like design of the mark 2 device, offering less lateral movement on lift-off from the injector nozzle.

Tube length/back-calculated thickness consistency improved with the new design. R^2 averaged across all three trends was 0.9995, and all three alginate concentration trends now overlapped, showing impact of alginate concentrations from 0.5-1.0% was no longer significant. This was verified by a repeat experiment. The improvements from this new design was largely noticeable from the quality of tubes across its entire length in parallel OCT scans on mark 2 design, compared to mark 1 design tubes (where the initial ~7cm was not consistent in tube wall thickness). Furthermore the dead space within the base unit was reduced from 112μl to 89μl (21% reduction), saving materials that could potentially be scarce or valuable. Perhaps more subtle is the improvements of nominal wall thickness (T_0) to more closely match predicted tube wall thickness (T_B), as a result of the injector nozzle diameter more closely matching alginate tube lumen diameter, which in turn reduces end effects of matrix fluid flow.

Attention was then turned to manipulating wall thickness by altering glass barrel and spherical regulator radii and subsequent repercussions on wall thickness consistency. When spherical regulator radius was decreased from 1.700 to 1.587mm to give a resultant gap width change from 300 to 413μm, the R^2 value of the best-fit trend remained high at 0.9998 and average CV of 1.8%. Likewise, glass barrel radii was altered from 2.000 to

1.825mm decreasing the gap width from 300 to 238μm, yet still R^2 remained at 0.9996 and average CV was 1.4%. Gap widths of 238, 300 and 413μm yielded back-calculated tube wall thicknesses of 143.4, 188.4 and 277.3μm, almost exactly matching the $^2/_3$ Approximation. This was somewhat of a oddity of a result, since this approximation only applies as the gap width becomes very small. At gap widths of this magnitude, nominal wall thicknesses ought to be ~136, 150 and 41.3μm, respectively. By testing the Theory with reacting and non-reacting fluids, we were able to ascertain the cross-linking nature of the $CaCl_2$-alginate system was freezing the initial thickness of the deposited alginate layer, neutralising contraction effects caused by drag created by the upwards flowing motion of the spherical regulator. The systems that more closely resembled the Theory were in fact non-reacting fluids. This result could be useful in a practical sense – to be able to consistently manufacture alginate tubes with a wall thickness $^2/_3$ the size of the gap width. To summarise, the wall thickness of the alginate tube will depend on several factors:

- Contraction effects as a result of spherical regulator drag (affects non-reacting fluid systems only)
- End effects as a result of base unit design
- Radii of the glass barrel and spherical regulator
- Reacting or non-reacting fluid system
- Shrinkage after tube formation

The final point we have not yet seen at this point in the research. The prior points are all effective at the time of tube formation, whereas the final point happens sometime after the alginate structure has been formed. Shrinkage is a direct result of multivalent ions such as Ca^{2+} ionically bonding strands of guluronic acid together. As this occurs, water molecules are shed and the alginate structure shrinks as a result. Therefore, degree of gelation has been established by wet/dry ratio of slices in larger alginate structures in the past (Martinsen et al. 1989). Unfortunately, this makes the reproducibility of alginate structures somewhat lacking. The degree of shrinkage can be better

controlled using much slower internal gelation as opposed to external gelation methods such as $CaCl_2$ (Quong et al. 1998). Figure 6.2 shows how shrinkage can cause a relative size difference from 20 to 50% depending on alginate concentration and gelation technique.

6.3.2 Monitoring Methods

It is these shrunk alginate tubes that were scanned using OCT. So far, we have assumed that both sides of the alginate tube are equal in thickness, and have back-calculated wall thickness based on the length of the tube. OCT provided a direct way to visualise wall thickness consistency. The scans of the mark 1 tubes showed that some of the tubes did not in fact have walls of equal thickness. Glass beads were incorporated for light scatter purposes, but increasing concentration caused a much thicker tube. They therefore made a poor model for cells. It must be reiterated that we cannot refer to the Theory at this point, since the effects of shrinkage after tube formation have occurred and wall thicknesses are between 20-50% less than nominal tube wall thicknesses. Only the central third of all alginate tubes were uniform enough to scan using OCT. The most important observation was that the wall thickness at the start of the tube was repeated along its entire length, meaning that the directional control at the start of tube formation is integral to the consistency of the entire tube. This prompted the mark 2 device design.

The scans were repeated for shrunk mark 2 alginate tubes. Glass beads were again used, but at a low 0.0005g/ml concentration. Results showed that when the walls are equal in size the wall thickness ought to be ½ of gap width. CV deteriorated from the mark 1 tubes, although the entire tube length could be scanned, and percentage of failed tubes drastically decreased with the new base unit design.

OCT was then adapted to try to measure the rate of shrinkage. By monitoring a fixed point on a freshly formed alginate tube, and taking an A-scan at split-second intervals, we formed a graph of alginate tube wall

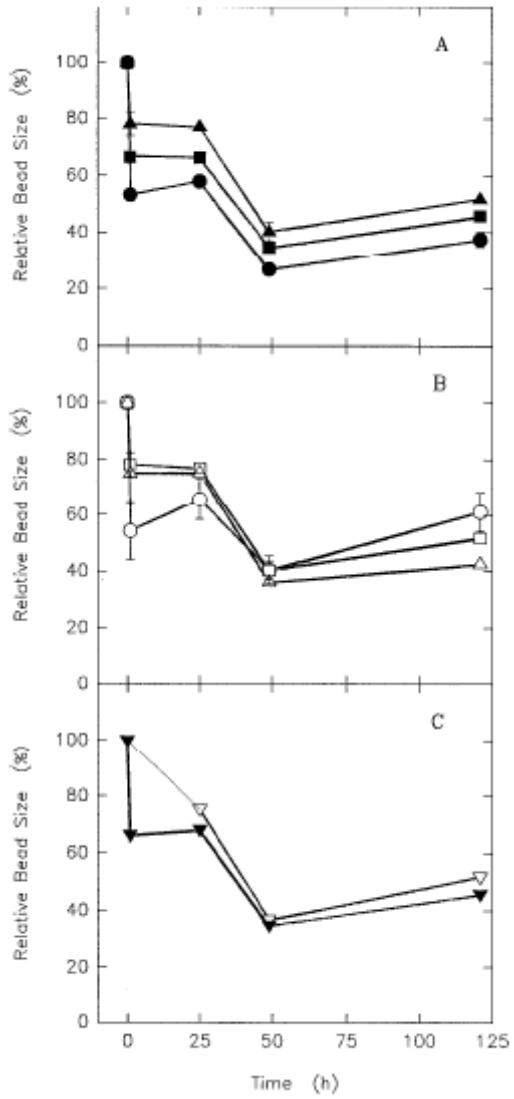

Figure 6.2 Bead mass reduction during gelification for 1 hour, followed by storage in water for 24 hours, simulated GI incubation for 24 h at pH 1.2, followed by 72 hours of incubation at pH 7.0. (**a**) Percent relative bead size for 1 (●), 2 (■) and 3% (▲) medium guluronic alginate. (**b**) Percent relative bead size for low (O) medium (□) and high (△) guluronic alginate at 3% concentration. (**c**) Percent relative bead size for 2% (w/v) medium G alginate beads formed using the external (▼) and internal (▽) gelation techniques. Error bars represent standard deviations of three replicates about the mean (Quong et al. 1998).

shrinkage. Compared to other groups that have used wet/dry ratio of alginate slices (Martinsen et al. 1989), or time taken before alginate no longer runs (Kuo and Ma. 2001), this novel approach is much more accurate and quantifiable. The results show an exponentially shaped graph, stabilising at ~12 minutes. Wall thicknesses of ~225μm fall to 180μm, rather than the expected 188 to 150μm for a gap width of 300μm. It was thought this error was either caused by the addition of glass beads, which we know can increase expected final wall thickness, or the spoiling of fresh alginate, due to transportation from London to Cranfield.

In all, OCT presented itself to be a very useful and versatile tool. As well as portability, and the ability to scan in real time through air, the OCT scanner could also be altered to measure sample thickness up to 3mm (Fujimoto et al. 2000), moving fluids within a capillary using Doppler velocimetry (Mason et al. 2004) and now shrinkage by measuring a set point in the tube, by simply altering the associated Matlab programme.

The high-speed camera also elaborated several points. Firstly, that the velocity profile of the matrix fluid is parabolic about the spherical regulator. Secondly that the spherical regulator does not spin during tube formation. This explains why a lopsided tube will have the same thickness repeated throughout its length. Since the eggcup shaped design of the mark 2 device was meant to increase stability, analogous to a firearm and a projectile, it is interesting that bullets are stabilised in air by spin (fig. 6.3). The spinning is created in rifles by the rotating band engaging grooves cut into the barrel of the firearm. At a muzzle velocity of 2800 ft/s the spin rate would equate to 250 rev/s (USAFAS 1999). In our tube-forming system however, spherical regulator spin does not occur. Propelling fluid and also buoyancy of the material used projects the spherical regulator. It may be that in fluid systems at low velocities, stability is unnecessary. Perhaps by inducing spin, we may correct tube lopsided-ness. In any case, regulator spin would be a further development to the fluid dynamics Theory. With this current system however, only one point per tube need be monitored to gain a geometrical understanding of the rest of the tube.

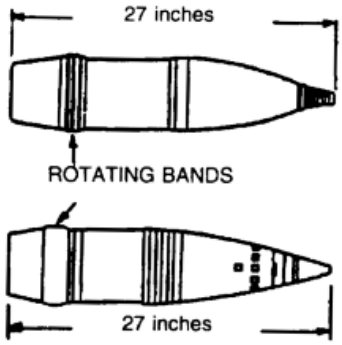

Spin-stabilized projectiles.

Figure 6.3 Spin stabilised projectiles (www.fas.org).

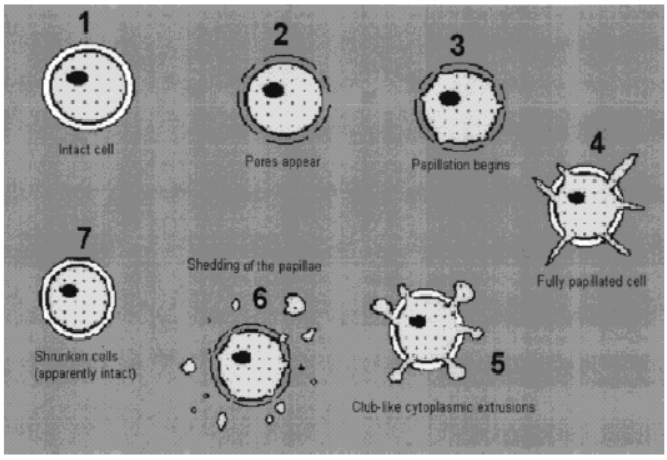

Figure 6.4 A schematic representation of the proposed mechanism of cell damage occurring at low shears (Mardikar and Niranjan 2000).

As well as monitoring overall alginate tube geometry, we must also control the particles that may be integrated within the tube such as biological cells. If left unchecked these may impact on alginate tube wall thickness, as we have shown by varying glass bead concentration and OCT. Therefore the next phase of experiments looked at particle size detection and enumeration. The aim of initial experiments was to find monitoring methods that could give a representation of size distribution of the particles (i.e. single and aggregates of cells) and methods that could enumerate the concentration of particles in a suspension. The particle sizer shows size distribution profiles for differing cell concentrations from $1x10^6$ – $2x10^6$ cells/ml. Combined with one-way ANOVA tests and TUKEY HSD analysis, this monitoring method was also sensitive enough to detect abnormally high aggregates in the $5x10^5$ cells/ml concentration sample and differentiate this from the other sample concentrations. The $1x10^5$ cells/ml concentration was too dilute to show any statistical similarities with the other sample. This only means that we cannot compare concentrations in the order of $2x10^6$ with $1x10^5$ cells/ml. Also the profile shape was not the expected bell-shaped curve with a peak at 20μm (Alberts et al. 2002), but instead a tri-peaked profile with peaks at 10, 30 and 60μm. The 30μm peak was decided the single cell peak. The other two peaks were to be further investigated. The Leica QWin system could only give limited size distribution information with peaks of 1 and 2 cell diameters (pre-determined to be ~30μm for a single cell by graticule). ANOVA and TUKEY showed a slight statistical difference between $1x10^5$ and $1.5x10^5$ cells/ml concentration samples, namely the $1.5x10^5$ cells/ml profile contained an abnormally high level of estimated cells. The same statistical tests were applied between Malvern and Leica data and showed that they were not highly significantly different, yet not statistically similar, a result expected given the two monitoring methods used. From this initial comparison test, it was acknowledged that the Malvern particle sizer was more useful for giving size distribution information.

Micrographs taken from the Leica show how cell size differs largely in a single sample. The resultant peaks of 10, 30 and 60μm may infact be a result of three distinct cell size populations in a single sample. Such size

differences have been explained by other groups to arise from adjustments over several passages in mammalian cells as a result of nutrient availability (Conlon and Raff 2003). The 10μm peak could be the result of papilation of cytoplasm (fig. 6.4) as a result of shear damage and healing of cells (Mardikar and Niranjan 2000).

For quantifying cell numbers, the experiment proved inconclusive. At concentrations up to $1x10^6$ cells/ml the standard haemocytometer and Trypan Blue were more accurate, and above this concentration the Leica QWin was more favourable. Ultimately both methods rely on a similar principle of glass slide and coverslip, which gives way for errors as a result of aggregates too large to fit underneath. Yet the area of the sample analysed by the Leica QWin is a fraction of that counted manually, making the accuracy of the data questionable. Since dilution would normally be used to enumerate using the haemocytometer, this was decided the better of the two methods for our system. This result does not help improve inter-operator errors (Peebles et al. 1981) that are associated with manual counting.

Therefore the Guava EasyCyte capillary cytometer was trialled as a cell enumeration method. Results were promising when compared with the haemocytometer giving better inter-tubular (CVs of 29.8 and 17.6%, Trypan Blue vs. Viacount Flex) and comparable intra-tubular (CVs of 37.3 and 44.8%, Trypan Blue vs. Viacount Flex) cell counts for sectioned cell-integrated alginate tubes. With further optimisation the Guava EasyCyte could make a realistic alternative to manual counting.

Now that the monitoring methods are in place, we turn to implementing control measures for the tube-forming process. Unavoidably, part of the process still involves much manual work, particularly the cell culture aspects. Therefore it was aimed to minimise variability by part-automating these processes and then monitoring them using the methods established. In particular, we aimed to create a suspension of single cells. From a perspective of organ development, cell aggregation is desirable – hepatocyte spheroids exhibit greater cell-cell interactions than monolayer cells and morphology more closely mimics the native liver lobule. Furthermore Glickis and her team found such spheroids to exhibit improved

liver-specific functions and differentiation (Glickis et al. 2000). However from a mass transfer angle, cell aggregation can have a detrimental effect to cell viability if aggregate diameter is not duly controlled (Glickis et al. 2004; Sen et al. 2002). We have seen how glass bead concentration can impact on wall-thickness, large aggregates may also cause wall distortions, and therefore this aspect ought to be controlled. Since the aims of this research extend not only to tissue-engineered organs but also cell-encapsulated solutions, we will focus on single cells of high viability and abundant nutrient availability. After analysing the protocols for cell culture (Appendix A), the following cell culture processes were studied for impact on aggregate formation:

1. Effect of micro-pipetting.
2. Holding time.
3. Centrifugation speed and duration.
4. Cell passage/generation number.

Despite the different shaped profiles formed from the different number passes through a micro-pipette, ANOVA analysis showed no significant statistical difference between the size distribution profiles. The profile did show two main peaks at 20 and 40μm, as well as a mini peak at 5μm. Firstly, since we know that mammalian cells are between 11-22μm (Alberts et al. 2002) in diameter that this initial 5μm peak cannot represent a whole cell. This result also meant that the degree of micro-pipetting up to 20 passes has no significant shear affect: neither further damaging cells and increasing the mini-peak of cytoplasm/cell debris; nor disengaging the larger 40μm peak into single 20μm cells. This profile is also oddly comparable to the 30 and 60μm peaks seen in initial visualisation experiments. This could mean that the pipetting method is an ineffective means of disassociating small cell aggregates, or that the 40μm peak is indeed a single cell population as supported by Leica micrographs. Since pipetting is a commonly used method to disassociate cell aggregates (Serra et al. 1997; Serra et al. 2007; Colomer et al. 2005), the latter explanation is more likely.

Similar research was suggested by Bongrand & Golstein (Bongrand and Golstein 1983) who looked at calibrated shear to dissociate lymphocyte aggregates. However it was found that the magnitude of the shear was not important as the cell-to-cell bonds were highly variable.

Holding time is the next important variable. The aggregation of suspended cells can be described by Smoluchowski's Theory, which is based on Brownian motion (Longmire and Frojmovic 1990). When two cells collide they may form intercellular bonds. This is also possible in a non-suspended culture by settlement and movement of cells on a culture surface (Neelamegham et al. 1997). It stands to reason that the longer the time given for such instances to occur, the more occurrences there will be. For cell-integrated alginate tube formation, this can typically extend up to 3 hours, and therefore this timeframe was chosen. Results reveal a significant impact of holding time upon cell size distribution. ANOVA and TUKEY analysis reveals that upon 3 hours the profile is statistically different to the 5% confidence level. As a control, an autoclaved gauze filter was used to process the same cell sample at the same time intervals. The cell size distribution profile at the corresponding control at 3 hours revealed no statistical difference indicating a positive effect of holding time. It is therefore logical to conclude that filtration could be a control measure, and holding times minimised to under 2 hours during cell-integrated tube manufacture.

A team in Japan experimented on rotational culture based on the principles of centrifugation in order to induce chondrocyte aggregation (Furukawa et al. 2003). The aim of their work was to control differentiation into fibroblasts associated with monolayer culture. Since a centrifuge only gives a single pellet, rotational culture was used to form a 3 dimensional layer of chondrocytes that may be developed in tissue-engineered cartilage. Similarly shaking a suspended chondrocyte culture at 80rpm was sufficient to speed aggregation of cells by enhancing cell-cell collisions and interactions. To tailor conditions to those realistically used for generic mammalian cell culture, centrifugal speeds up to 500rpm and durations up to 5 mins were tested. Upon resuspension, the cell size distribution profiles and statistical

analyses revealed no significance of centrifugal speed treatment to cellular aggregation.

From combined and collated data over several experiments, we could now also look for cell aggregation and cell size distribution traits associated with cell passage/generation number. Cell banks were able to provide rat aortic smooth muscle cells, as a model for any potential cell type, at passage 10 and typically the age of this type of cell would not be used beyond passage 21 despite them being immortalised lines. Beyond this amount of cell generations, cells were observed to be much larger in size and much more prone to form aggregates (data not shown), an observation in line with the work of Conlon and Raff describing the gradual adaptation of mammalian cells over time with environmental changes such as media (Conlon and Raff 2003). Despite all this literature, the cell size distribution profiles show no apparent pattern with passage number, and statistical analyses reveals no significant difference between cell samples.

6.3.3 Impact of Cellular Integration

We have seen in the Chapter 3 that we can reliably form alginate tubes, and in Chapter 4 that we can monitor both the geometry of the tubes formed, and the size distribution profile of the cellular suspension separately. But the end result aims to integrate cells within the alginate tube. The two separate aspects must be brought together and considered as a whole, using the monitoring methods to measure change to consistency. Therefore Chapter 5 explored the impacts of cell integration to tube geometry consistency, effects of alginate on cell viability and cellular spatial distribution within the alginate tube. The importance of particle concentration on tube wall thickness has been seen by glass bead additions in Chapter 3, and we have discussed how alginate concentration could be altered by cell cytosol leakage and therefore affect tube wall thickness (Sen et al. 2002). Cell seeding efficiency and maintenance of viability are key considerations at the early stages of construct manufacture. Low seeding efficiency and high viability of

embedded cells is usually associated with approaches that rely on cell seeding onto a pre-formed matrix. In approaches that rely on entrapment of cells into a liquid matrix, cell-seeding efficiency is inherently high but there is a concern that non-viable cells could potentially be entrapped in the construct. Shear forces generated by manipulation and processing even at a small scale can be sufficiently high to damage mammalian cells. Issues such as cellular distribution and viability have also been the focus of other work involving cardiac tissue engineering within an alginate structure (Dar et al. 2002). Cellular spatial distribution allows for greater loading of cells within alginate without impacting bead consistency. It also impinges on cell viability due to less competition for nutrients (Schneider et al. 2004) and results in more even ECM formation (Heywood et al. 2004).

An initial experiment comparing pure alginate tubes with cell-integrated alginate tubes of comparable alginate concentration revealed consistently high R^2 trend correlation indicators, which further strengthens the previous studies on tube wall thickness robustness of the mark 2 tube-forming device. However an increase in the gradient of the slopes for hand-mixed cell-integrated equivalents showed that resultant tubes were on average 4% thicker and shorter than pure alginate controls. The explanation of this is hypothesised due to the ability or inability of the matrix fluid to flow upward along the glass barrel with spherical regulator drag. As solid particles such as glass beads and cells are imbedded this ability to flow is impeded and results in a thicker deposited layer. Despite wall thickness variations not exceeding 5%, acceptable compared with other well-engineered processes (Serp et al. 2000), hand-mixing cells into alginate is not desirable for a well-controlled system.

In order to establish greater confidence in the cell-integration process we turned our experiments towards static mixers. Other automated methods of cell integration were considered. But roller mixing would take too long, and as we have seen in the from section 6.3.2 holding time is a significant variable to cell viability. Impeller mixing or vortexing is associated with high shears, which are known to reduce cell viability in mammalian cells (Abu-Reesh and Kargi 1991). Kenics mixers are disposable (and therefore sterile),

plastic (and therefore autoclavable) and negligible shear (Bertsch et al. 2001) solution. The results show how pure alginate control tubes are comparable in wall thickness consistency compared with 12-element statically mixed cell-integrated tubes. Hand-mixed tubes fared poorly against the other two sets of tubes.

Previously we have seen the mechanism of cell damage with low shears (fig. 6.5) (Mardikar and Niranjan 2000). This leads us to ask the question of whether cell damage indeed occurs at a significant level within our process. The importance of impact of process on cell viability is echoed throughout other cell-integrated alginate processes (Sakai et al. 2004; Takei et al. 2006). In our system viability could be important due to the scarcity of the cells involved. Poor viability is not a good indication of a well-designed process. Also large amounts of cell lysis may impact on alginate concentration (Klokk and Melvik 2002) and ultimate wall thickness consistency. In these experiments, we integrated cells into an alginate tube, re-dissolved this and then counted cells using Trypan Blue. Despite concerns that re-solubilisation using citrate may subsequently affect viability of the cells, this is a pier reviewed and accepted method established in literature (Orive et al. 2003; Markusen et al. 2006; Jiang et al. 1995). Initial counts comparing after cell harvesting and full tube formation and re-solubilisation yielded a 25.4% fall in viability. Factors suspected to have reduced viability included: toxicity of media used with cells, centrifugation, shear via pipetting, shear via processing both using the static mixer assembly or the mark 2 tube-forming device.

A repeat experiment was conducted viability counting of cells at harvesting, prior to tube formation and after tube formation. The largest drop (73.6% drop in viability) was found to be prior to tube formation, ushering a round of investigatory experiments on centrifugation and all the media that comes into direct contact with cells.

Centrifugal affects have been reported by other groups (Chien et al. 2006; Katkov and Mazur 1999) but results of up to 5 consecutive concentration cycles (at 100xg) of centrifugation and resuspension gave no evidence of noticeably reduced cell viability.

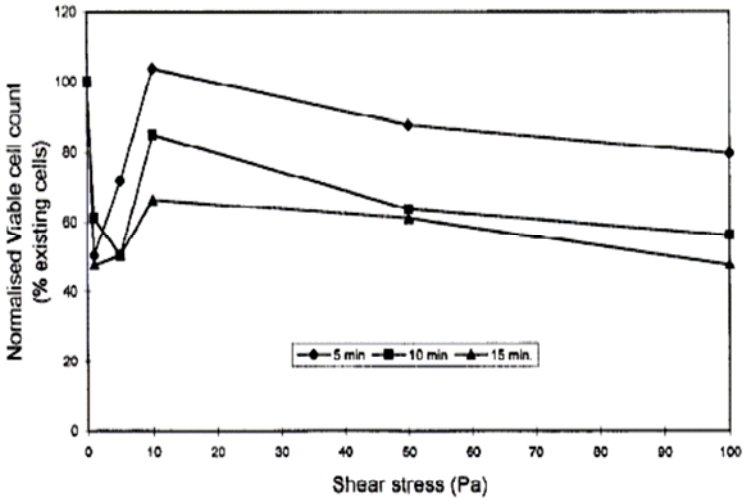

Figure 6.5 The effect of shear on the viable cell count (%) in K562 cl.6 cells (Mardikar and Niranjan 2000).

The media tests included: complete culture medium, sodium citrate, 0.09M $CaCl_2$, food colouring and N-Saline. Results showed no drop in cell viability below 80% within an exposure time of 1 hour with cells. Since alginate is consistently used with cells, it was anticipated that no toxic effects should occur with direct contact (Domm et al. 2004). However, over a 3-hour period, we see a consistent drop in viability particularly with a 1.0% alginate concentration. ANOVA and TUKEY HSD analyses show that the result is highly significant well beyond the 5% level. We also establish that we cannot control the rate of viability drop, with no apparent pattern in viability drop and time cells are exposed to alginate.

Initial tests of the effects of processing through the mark 2 tube-forming device show this impact of alginate on cell viability. This time, a fall of 40% over 1 hour strengthens the fact that there is an inherent problem with the alginate source. Despite the fact that the alginate is autoclaved, this problem seems to be due to contamination from the alginate source.

The effects of shear damage on cell viability were repeated, this time incorporating those from the static mixer assembly and those from the mark 2 tube-forming device. Alginate source was switched from Manugel DMB to Pronova SLG 100, highly sterilised alginate, pre-liquified and used throughout cell proliferation studies involving GRGDY ligand (Rowley and Mooney 2002). Both processing methods showed consistently high viabilities above 90% after processing. Only at 100ml/min in the tube-forming device do we see a 5% fall in viability, but since 20ml/min is usually used for maintaining a level of control, this should not be the case. This result is expected since the static mixer assembly and mark 2 tube forming tube-forming device give shears of $0.00031N/m^2$ and $0.0017N/m^2$, respectively. Only at low shear rates, between $0.75\text{-}10N/m^2$, is cell viability likely to be affected (Ludwig et al. 1992; Ma et al. 2002).

Although mechanical force can induce apoptosis (Kainulainen et al. 2002; Wernig and Xu 2002), the Guava EasyCyte capillary cytometer and Guava Nexin reagent showed no apoptosis resulting from processing effects. Previous studies by Reis et al have shown significant apoptotic activity in rat

medial SMCs within the hour after mechanical damage of a angioplasty guide-wire (Reis et al. 2000).

OCT was used for preliminary scans on cell-integrated tubes for qualitative analysis of spatial distribution of cells. Results showed that cells offered sufficient backscatter for OCT scans to be carried out, where previously glass beads were needed. The tube did not have uniform thickness – as the cell-integration method was via hand mixing. Finally we can see how poorly distributed the cells are in a hand mixed cell-integrated alginate tube.

Inter and intra-tubular coefficient of variance showed how spatial distribution of cells improved with increasing number of static mixer elements from hand mixing to 8-element to 12-element. However, in all cases the ends tend to have high variations in cell numbers, perhaps a result of non-optimised priming of cells with alginate prior to injection into the side port of the mark 2 base unit. Whilst we can confidently predict better results with increasing number of Kenics design static mixer elements, literature tells us that Sulzer-Koch design mixers are far superior in inefficiency and should drastically reduce the amount of dead space and hence wasted sample material (Douroumis and Fahr 2006).

A visual verification of the effectiveness of static mixing was verified using confocal laser scanning microscopy (CLSM). It is clear that by comparing a set of hand mixed cell-integrated tubes with a set of 12-element statically-integrated cell tubes that cells are more evenly distributed using the latter cell-integration method. Unfortunately, the CLSM data could not verify what other groups have seen in cell embedded alginate beads that show greater presence of cells closer to the surface of the bead than in the centre (Zohar-Perez et al. 2004). This is associated with solidification and shrinkage at the reaction plane but a liquid core and emphasised by beads many times the thickness of our tube walls.

6.4 CONCLUSIONS

This research has described a generic system capable of forming alginate tubes at high precision. A novel interpretation of fluid dynamics has been adapted into a model that has been verified by experimentation. This Theory predicts the thickness of the deposited layer of fluid (at time of tube formation) in any system of two fluids to approach $^2/_3$ the gap width as the gap width becomes very small compared to the spherical regulator diameter. The system has been optimised for robustness against infusion speed, as well as fluctuations in alginate concentration, which may arise from temperature changes or due to embedded particles such as cells. We can manipulate this tube wall thickness by altering spherical regulator radius or glass barrel radius without compromising the reliability of the system.

Tube wall thickness can be monitored using OCT, an original use of the technique. OCT was also adapted to measure tube wall shrinkage over time to establish a shrinkage time of 12 mins. High-speed video camera also elaborated there to be no regulator spin during tube formation, and hence any lop-sided tubes would have the same trait throughout its length. Cell sample homogeneity, consisting of no aggregates – a factor that impacts on cell viability and cell-integrated tube wall thickness – was measured using the Malvern particle sizer by monitoring cell size distribution plots. Three peaks observed at differing sizes were concluded to be cellular debris, and two discrete populations of cells at different diameters. Cell quantification could also be automated by methods such as the Gauva capillary cytometer, which proved to be comparable to haemocytometer. For the manual aspects of cell culture, pipetting was neither proven nor disproved for effectiveness to disassociate cell aggregates, but holding time was shown to cause aggregation after 3 hours. A control measure of gauze filtration can be used to manage particle sizes however. Centrifugation speed and rate, and passage number statistically showed to have no significant impact to cell size distribution.

These alginate tubes maybe seeded with cells or they could be embedded. Hand mixing cells into alginate was shown to influence wall

thickness up to 4%, and hence Kenics static mixers were introduced to add more consistency to such fluctuations. The results showed how 12-element statically mixed cell-integrated tubes were far superior in wall thickness variability compared to hand mixed techniques. Large falls in cell viability prior to processing cell/alginate mixture into a hydrogel tube were isolated to be caused by a contamination from the Manugel DMB used. A switch to Pronova SLG 100 showed viabilities above 90% for all aspects of cell-integrated tube production. Media toxicity was negligible up to 1 hour exposure times, as well as concentration steps and shear damage via processing through the static mixer assembly and mark 2 tube-forming device. This was confirmed by apoptosis analysis using Guava Nexin reagent. The Kenics static mixers also allowed improved spatial distribution of single cells embedded in alginate. Again the 12-element mixer was superior to 8-element mixer and hand mixing. This was verified via OCT, cell counting (haemocytometer) and confocal laser scanning microscopy.

The variables chosen to be monitored in this thesis were mechanical, i.e. wall thickness, cell dispersion, etc. The only cell related variables monitored were viability and apoptosis due to the versatility of the device to be used with any system of fluids and any type of cell. Rat aortic smooth muscle cells were used as a model, as were glass beads. The focus of this work has been on the ability: to reproducibly create alginate tubes with uniformly thick walls of predictable thickness; to be able to monitor and quality control the tubes and the cell suspension, including controlling aspects of mammalian cell culture via automation; and to integrate the cells into the tube without compromise to wall thickness, cell viability and cellular spatial distribution within the alginate tube.

References

Abu-Reesh I, Kargi F. 1991. Biological responses of hybridoma cells to hydrodynamic shear in an agitated bioreactor. Enzyme Microb Technol 13(11):913-9.

Alberts B, Johnson A, Lewis J, Raff M, Roberts K, Walter P. 2002. Molecular Biology of the Cell, 4th, Garland Science. p346-8,599-633,659-67,686-9,711-39, 39-45, 746-65.

Altman JJ, Manoux A, Callard P, Houlbert D, Desplanque N, Bruzzo F, Galletti PM. 1981. Successful pancreatic xenografts using semipermeable membrane. Artif. Organs 5:776-9.

Altman JJ, Houlbert D, Bruzzo F, Desplanque N, Manoux A, Galletti PM. 1982. Implantation of semi-permeable hollow fibers to prevent immune rejection of transplanted pancreatic islets. Islet-Pancreas Tranplantation and Artificial Pancreas 43-5.

Atala A, Lanza RP. 2002. Methods of Tissue Engineering. USA: Academic Press. p911.

Batchelor GK. 1965. An Introduction to Fluid Dynamics: Cambridge. p220.

Bertsch A, Heimgartner S, Cousseau P, Renaud P. 2001. Static micromixers based on large-scale industrial mixer geometry. Lab Chip 1(1):56-60.

Bongrand P, Golstein P. 1983. Reproducible dissociation of cellular aggregates with a wide range of calibrated shear forces: application to cytolytic lymphocyte target cell conjugates. J Immunol Methods 58(1-2):209-24.

Boppart SA, Fujimoto JG. 2002. Optical coherence tomography and developmental biology Handbook of Optical Coherence Tomography. Bouma BE, Tearney GJ, editors. New York: Decker. Chapter 19.

Bottaro DP, Liebmann-Vinson A, Heidaran MA. 2002. Molecular signaling in bioengineered tissue microenvironments. Ann N Y Acad Sci 961:143-53.

Bouchie A. 2002. Tissue engineering firms go under. Nat Biotechnol 20(12):1178-9.

Brezinski ME, Tearney G, Bouma B, Hee M, Izatt J, Swanson E, Southern JF, Fujimoto JG. 1995. High Resolution Imaging of Human Arterial Walls Via Optical Coherence Tomography. JACC 25(1).

Chapekar MS. 2000. Tissue engineering: challenges and opportunities. J Biomed Mater Res 53(6):617-20.

Chick WL, Perna JJ, Lauris V, Low D, Galletti PM, Panol G, Whittemore AD, Like AA, Colton CK, Lysaght MJ. 1977. Artificial pancreas using living beta cells: effects on glucose homeostasis in diabetic rats. Science 197(4305):780-2.

Chien CH, Chowdhury AS, Sakagami H, Kanegae H. 2006. Enhancement of sodium fluoride-induced cell death by centrifugal force. In Vivo 20(1):103-8.

Cohen S, Bernstein H, Hewes C, Chow M, Langer R. 1991. The pharmacokinetics of, and humoral responses to, antigen delivered by microencapsulated liposomes. Proc Natl Acad Sci U S A 88(23):10440-4.

Conlon I, Raff M. 2003. Differences in the way a mammalian cell and yeast cells coordinate cell growth and cell-cycle progression. J Biol 2(1):7.

Colomer J, Peters F, Marrase C. 2005. Experimental analysis of coagulation of particles under low-shear flow. Water Res 39(13):2994-3000.

Dar A, Shachar M, Leor J, Cohen S. 2002. Optimization of cardiac cell seeding and distribution in 3D porous alginate scaffolds. Biotechnol Bioeng 80(3):305-12.

Domm C, Schunke M, Steinhagen J, Freitag S, Kurz B. 2004. Influence of various alginate brands on the redifferentiation of dedifferentiated bovine articular chondrocytes in alginate bead culture under high and low oxygen tension. Tissue Eng 10(11-12):1796-805.

Douroumis D, Fahr A. 2006. Nano- and micro-particulate formulations of poorly water-soluble drugs by using a novel optimized technique. Eur J Pharm Biopharm 63(2):173-5.

Dowson D, Taylor CM, Zhu G. 1992. A transient elastohydrodynamic lubrication analysis of a cam and follower. J. Phys. D: Appl. Phys 25: 313-320.

Drexler W, Stamper D, Jesser C, Li X, Pitris C, Saunders K, Martin S, Lodge MB, Fujimoto JG, Brezinski ME. 2001. Correlation of collagen organization with polarization sensitive imaging of in vitro cartilage: implications for steoarthritis. J Rheumatol 28(6):1311-8.

Drury JL, Mooney DJ. 2003. Hydrogels for tissue engineering: scaffold design variables and applications. Biomaterials 24(24):4337-51.

Drury JL, Dennis RG, Mooney DJ. 2004. The tensile properties of alginate hydrogels. Biomaterials 25(16):3187-99.

Ducy P. 2002. Molecular signaling. Ann N Y Acad Sci 961:161.

Eiselt P, Yeh J, Latvala RK, Shea LD, Mooney DJ. 2000. Porous carriers for biomedical applications based on alginate hydrogels. Biomaterials 21(19):1921-7.

Faulkner A, Geesink I, Kent J, FitzPatrick D. 2003. Human tissue engineered products—drugs or devices? Bmj 326(7400):1159-60.

Faustman DL, Pedersen RL, Kim SK, Lemischka IR, McKay RD. 2002. Cells for repair: breakout session summary. Ann N Y Acad Sci 961:45-7.

FDA. 1993. Guideline on General Principles of Process Validation. Centre for Drug Evaluation and Research.

Fujimoto JG, Pitris C, Boppart SA, Brezinski ME. 2000. Optical Coherence Tomography: an emerging technology for biomedical imaging and optical biopsy. Neoplasia 2(1-2):9-25.

Fujimoto JG. 2003. Optical coherence tomography for ultrahigh resolution in vivo imaging. Nat Biotechnol 21(11):1361-7.

Furukawa KS, Suenaga H, Toita K, Numata A, Tanaka J, Ushida T, Sakai Y, Tateishi T. 2003. Rapid and large-scale formation of chondrocyte aggregates by rotational culture. Cell Transplant 12(5):475-9.

Kainulainen T, Pender A, D'Addario M, Feng Y, Lekic P, McCulloch CA. 2002. Cell death and mechanoprotection by filamin a in connective tissues after challenge by applied tensile forces. J Biol Chem 277(24):21998-2009.

Klokk TI, Melvik JE. 2002. Controlling the size of alginate gel beads by use of a high electrostatic potential. J Microencapsul 19(4):415-24.

Gao Y, Jiang HC, Xu J, Pan SH, Li YD. 2005. Microencapsulating hepatocytes. Transplant Proc 37(10):4589-93.

Germain L, Goulet F, Moulin V, Berthod F, Auger FA. 2002. Engineering human tissues for in vivo applications. Ann N Y Acad Sci 961:268-70.

Glicklis R, Shapiro L, Agbaria R, Merchuk JC, Cohen S. 2000. Hepatocyte behavior within three dimensional porous alginate scaffolds. Biotechnol Bioeng 67:344–353.

Glicklis R, Merchuk JC, Cohen S. 2004. Modeling mass transfer in hepatocyte spheroids via cell viability, spheroid size, and hepatocellular functions. Biotechnol Bioeng 86(6):672-80.

Godbey WT, Atala A. 2002. In vitro systems for tissue engineering. Ann N Y Acad Sci 961:10-26.

Haverich A, Graf H. 2002. Stem Cell Transplantation and Tissue Engineering. Springer, Germany. p1-13, 29-40, 73-74.

Hee MR, Puliafito CA, Wong C, Duker JS, Reichel E, Schuman JS, Swanson EA, Fujimoto JG. 1995. Optical coherence tomography of macular holes. Ophthalmology 102(5):748-56.

Heywood HK, Sembi PK, Lee DA, Bader DL. 2004. Cellular utilization determines viability and matrix distribution profiles in chondrocyte-seeded alginate constructs. Tissue Eng 10(9-10):1467-79.

Hirschi KK, Skalak TC, Peirce SM, Little CD. 2002. Vascular assembly in natural and engineered tissues. Ann N Y Acad Sci 961:223-42.

Huang D, Swanson EA, Lin CP, Schuman JS, Stinson WG, Chang W, Hee MR, Flotte T, Gregory K, Puliafito CA and others. 1991. Optical coherence tomography. Science 254(5035):1178-81.

Ingber D. 2002. Mechanical signaling. Ann N Y Acad Sci 961:162-3.

Jiang C, Wang F, Li TT. 1995. Counting total cell numbers microscopically on stained films. Lett Appl Microbiol 20(4):217-9.

Jacobs JJL, Lehe C, Cammans KDA, Yoneda K, Das PK, Elliott GR. 2001. J of Immunological Methods 247:73-82.

Jork A, Thurmer F, Cramer H, Zimmermann G, Gessner P, Hamel K, Hofmann G, Kuttler B, Hahn HJ, Josimovic-Alasevic O and others. 2000. Biocompatible alginate from freshly collected Laminaria pallida for implantation. Appl Microbiol Biotechnol 53(2):224-9.

Kapur R. 2002. Fluorescence imaging and engineered biosensors: functional and activity-based sensing using high content screening. Ann N Y Acad Sci 961:196-7.

Kainulainen T, Pender A, D'Addario M, Feng Y, Lekic P, McCulloch CA. 2002. Cell death and mechanoprotection by filmin a in connective tissues after challenge by applied tensile forces. J Biol Chem 277(24):21998-2009.

Katkov II, Mazur P. 1999. Factors affecting yield and survival of cells when suspensions are subjected to centrifugation. Influence of centrifugal acceleration, time of centrifugation, and length of the suspension column in quasi-homogeneous centrifugal fields. Cell Biochem Biophys 31(3):231-45.

Kaufman SC, Musch DC, Belin MW, Cohen EJ, Meisler DM, Reinhart WJ, Udell IJ, Van Meter WS. 2004. Confocal microscopy: a report by the American Academy of Opthalmology. Opthalmology 111(2):396-406.

Khattak SF, Chin KS, Bhatia SR, Roberts SC. 2007. Enhancing oxygen tension and cellular function in alginate cell encapsulation devices through the use of perfluorocarbons. Biotechnol Bioeng 96(1):156-66.

Kongsawadworakul P, Chrestin H. 2003. Laser diffraction: a new tool for identification studies of physiological effectors involved in aggregation-coagulation of the rubber particles from hevea latex. Plant Cell Physiol. 44(7)707-17.

Kuo CK, Ma PX. 2001. Ionically crosslinked alginate hydrogels as scaffolds for tissue engineering: part 1. Structure, gelation rate and mechanical properties. Biomaterials 22(6):511-21.

Langer R, Vacanti JP. 1993. Tissue engineering. Science 260(5110):920-6.

Langer RS, Vacanti JP. 1999. Tissue engineering: the challenges ahead. Sci Am 280(4):86-9.

Law AKW, Lam KY, Lam FK, Wong TKW, Poon JLS, Chan FHY. 2003. Image analysis system for assessment of immunohistochemically stained proliferative marker (MIB-1) in oesphageal squamous cell carcinoma. Computer Methods and Programs in Biomedicine 70:37-45.

Leinfelder U, Brunnenmeier F, Cramer H, Schiller J, Arnold K, Vasquez JA, Zimmermann U. 2003. A highly sensitive cell assay for validation of purification regimes of alginates. Biomaterials 24(23):4161-72.

Lewinska D, Rosinski S, Werynski A. 2004. Influence of process conditions during impulsed electrostatic droplet formation on size distribution of hydrogel beads. Artif Cells Blood Substit Immobil Biotechnol 32(1):41-53.

Longmire K, Frojmovic M. 1990. Long-range interactions in mammalian platelet-aggregation. I. Evidence from kinetic studies in brownian diffusion. Biophys J 58(2):299-307.

Ludwig A, Kretzmer G, Schugerl K. 1992. Determination of a “critical shear stress level” applied to adherent mammalian cells. Enzyme Microb Technol 14(3):209-13.

Lysaght MJ, Hazlehurst AL. 2004. Tissue engineering: the end of the beginning. Tissue Eng 10(1-2):309-20.

Lysaght MJ, O’Loughlin JA. 2000. Demographic scope and economic magnitude of contemporary organ replacement therapies. Asaio J 46(5):515-21.

Lysaght MJ, Reyes J. 2001. The growth of tissue engineering. Tissue Eng 7(5):485-93.

Ma N, Koelling KW, Chalmers JJ. 2002. Fabrication and use of a transient contractional flow device to quantify the sensitivity of mammalian and insect cells to hydrodynamic forces. Biotechnol Bioeng 80(4):428-37.

Manojlovic V, Djonlagic J, Obradovic B, Nedovic V, Bugarski B 2006. Immobilization of cells by electrostatic droplet generation: a model system for potential application in medicine. Int J Nanomedicine 1(2):163-71.

Mardikar SH, Niranjan K. 2000. Observations on the shear damage to different animal cells in a concentric cylinder viscometer. Biotechnol Bioeng 68(6):697-704.

Markusen JF, Mason C, Hull DA, Town MA, Tabor AB, Clements M, Boshoff CH, Dunnill P. 2006. Behaviour of adult human mesenchymal stem cells entrapped in alginate-GRGDY beads. Tissue Eng 12(4):821-30.

Martinsen A. 1989. Alginate as Immobilization Material: I. Correlation between Chemical and Physical Properties of Alginate Gel Beads. Biotechnology and Bioengineering 33:79-89.

Mason C, Markusen JF. 2004. The potential of optical coherence tomography in the engineering of living tissue. Phys Med Biol 49(7): 1097-115.

Mason C, Markusen JF, Town MA, Dunnill P, Wang RK. 2004a. Doppler optical coherence tomography for measuring flow in engineered tissue. Biosens Bioelectron 20(3):414-23.

Mason C, Town MA. 2002. Methods for forming hardened sheets and tubes. G. W. I. P. Organisation. WO02.

Matar OK, Spelt PD, Stepanek F. 2006. Collisions of liquid coated solid spherical particles in a viscous fluid. J Colloid Interface Sci. 301(2):594-606.

Udofia IJ, Jin ZM. 2003. Elastohydrodynamic lubrication analysis of metal-on-metal hip-resurfacing prostheses. J Biomech 36(4):537-44.

McIntire LV. 2003. WTEC panel report on tissue engineering. Tissue Eng 9(1):3-7.

Metzger DW. 2002. Immune responses to tissue-engineered extracellular matrix used as a bioscaffold. Ann N Y Acad Sci 961:335-6.

Neelamegham S, Munn LL, Zygourakis K. 1997. A model for the kinetics of homotypic cellular aggregation under static conditions. Biophys J 72(1):51-64.

Nerem RM. 2000. Tissue engineering: confronting the transplantation crisis. Proc Inst Mech Eng [H] 214(1):95-9.

Nishioka NS, Brand S, Bouma BE, Tearney GJ, Compton CC. 2002. Gastrointestinal applications of optical coherence tomography Handbook of Optical Coherence Tomography. Bouma BE, Tearney GJ, editors. New York: Decker. Chapter 25.

Orive G, Hernandez RM, Rodriguez Gascon A, Calafiore R, Chang T, De-Vos P, Hortelano G, Hunkeler D, Lacik I, Shapiro J, Pedraz JL. 2003. Cell Encapsulation: Promise and Progress. Nature 9(1):104-7.

Pangarkar N, Hutmacher DW. 2003. Invention and business performance in the tissue-engineering industry. Tissue Eng 9(6):1313-22.

Parenteau NL, Hardin-Young J. 2002. The use of cells in reparative medicine. Ann N Y Acad Sci 961:27-39.

Parker H. MTLF Summit. In: Foote SB, editor; 2002 April 21-22, 2002; Georgia Institute of Technology. Medical Technology Leadership Forum.

Peebles DA, Hochberg A, Clarke TD. 1981. Analysis of manual reticulocyte counting. Am J Clin Pathol 76(5):713-7.

Peirone M, Ross CJ, Hortelano G, Brash JL, Chang PL. 1998. Encapsulation of various recombinant mammalian cell types in different alginate microcapsules. J Biomed Mater Res 42(4):587-96.

Proskurin SG, Sokolova IA, Wang RK. 2003. Imaging of non-parabolic velocity profiles in converging flow with optical coherence tomography. Phys Med Biol 48(17):2907-18.

Quong D, Neufeld RJ, Skjak-Braek G, Poncelet D. 1998. External versus internal source of calcium during the gelation of alginate beads for DNA encapsulation. Biotechnol Bioeng 57(4):438-46.

Ratcliffe A, Niklason LE. 2002. Bioreactors and bioprocessing for tissue engineering. Ann N Y Acad Sci 961:210-5.

Reis ED, Roque M, Cordon-Cardo C, Drobnjak M, Fuster V, Badimon JJ. 2000. Apoptosis, proliferation, and p27 expression during vessel wall healing: time course study in a mouse model of transluminal femoral artery injury. J Vasc Surg 32(5):1022-9.

Rowley JA, Mooney DJ. 2002. Alginate type and RGD density control myoblast phenotype. J Biomed Mater Res 60(2):217-23.

Sakai S, Kawabata K, Ono T, Ijima H, Kawakami K. 2004. Preparation of mammalian cell-enclosing subsieve-sized capsules (<100 micron) in a coflowing stream. Biotech Bioeng 86(2):168-73.

Saitoh S, Araki Y, Kon R, Katsura H, Taira M. 2000. Swelling/deswelling mechanism of calcium alginate gel in aqueous solutions. Dent Mater J 19(4):396-404.

Schmitt J.M. LSL, Yung K.M. 1997. An optical coherence microscope with enhanced resolving power in thick tissue. Optics Communications(142):203-207.

Schneider N, Lejeune JP, Deby C, Deby-Dupont GP, Serteyn D. 2004. Viability of equine articular chondrocytes in alginate beads exposed to different oxygen tensions. Vet J 168(2):167-73.

Sefton MV. 2002. Functional considerations in tissue-engineering whole organs. Ann N Y Acad Sci 961:198-200.

Sen A, Kallos MS, Behie LA. 2002. Expansion of mammalian neural stem cells in bioreactors: effect of power input and medium viscosity. Brain Res Dev Brain Res 134(1-2):103-13.

Sennerby L, Rostlund T, Albrektsson B, Albrektsson T. 1987. Acute tissue reactions to potassium alginate with and without colour/flavour additives. Biomaterials 8(1):49-52.

Serra T, Colomer J, Casamitjana X. 1997. Aggregation and breakup of particles in a shear flow. J Colloid Interface Sci 187(2):466-73.

Serra T, Colomer J, Logan BE. 2008. Efficiency of different shear devices on flocculation. Water Res. In press.

Serp D, Cantana E, Heinzen C, Von Stockar U, Marison IW. 2000. Characterization of an encapsulation device for the production of monodisperse alginate beads for cell immobilization. Biotechnol Bioeng 70(1):41-53.

Shapiro L, Cohen S. 1997. Novel alginate sponges for cell culture and transplantation. Biomaterials 18(8):583-90.

Shelton E. 1966. Differentiation of mouse thymus cultured in diffusion chambers. Am J Anat 119(3):341-57.

Sipe JD. 2002. Tissue engineering and reparative medicine. Ann N Y Acad Sci 961:1-9.

Smetana K, Jr. 1993. Cell biology of hydrogels. Biomaterials 14(14):1046-50.

Smidsrod O, Skjak-Braek G. 1990. Alginate as immobilization matrix for cell. Trends Biotechnol 8(3):71-8.

Sun AM, Parasious W, Healy GM, Vacek I, Mac-morine H. 1977 The use, in diabetic rats and monkeys, of artificial capillary units containing cultured islets of Langerhans (artificial endocrine pancreas). Diabetes 26:1136–1139.

Takei T, Sakai S, Ijima H, Kawakami K. 2006. Development of mammalian cell-enclosing calcium-alginate hydrogel fibres in a co-flowing stream. Biotechnol J 1(9):1014-7.

Taylor DA. 2002. Is in vivo remodeling necessary or sufficient for cellular repair of the heart? Ann N Y Acad Sci 961:315-8.

Tranquillo RT. 2002. The tissue-engineered small-diameter artery. Ann N Y Acad Sci 961:251-4.

Tze WJ, Wong FC, Chen LM, O'Young S. 1976. Implantable artificial endocrine pancreas unit used to restore normoglycaemia in the diabetic rat. Nature 264(5585):466-7.

Udofia IJ, Jin ZM. 2003. Elastohydrodynamic lubrication analysis of metal-on-metal hip-resurfacing prosthesis. J Biomech 36(4):537-44.

Uludag H, De Vos P, Tresco P. 2000. Technology of mammalian cell encapsulation. Advanced Drug Delivery Reviews 42:29-64.

UNITED STATES ARMY FIELD ARTILLERY SCHOOL (USAFAS), FORT SILL, OKLAHOMA [LESSON PLAN LP HCXTAA] January 1999.

Uyeda M, Hara C, Shinagawa Y. 1962. [Note on the error of counting with hemocytometer.]. J Physical Soc Japan 24:215-20.

Vij A, Lee AP, Fisher JS. 2007. Biomint: Cell Encapsulation for Tissue Engineering. IM-SURE Synoposium 1-31.

Wagner AJ, Brunsen DM, Brown PJ, Burg KL. 2006. Tissue engineering applications of alginate. CAEFF 1.

Wernig F, Xu Q. 2002. Mechanical stress-induced apoptosis in the cardiovascular system. Prog Biophys Mol Biol 78(2-3):105-37.

Yagi K, Tsuda K, Serada M, Yamada C, Kondoh A, Miura Y. 1993. Rapid formation of multicellular spheroids of adult rat hepatocytes by rotation culture and their immobilization within calcium alginate. Artif Organs 17(11):929-34.

Yang Y, Yeo JH, Jiang L, Jiang D. 2004. Blood cell counting and classification by nonflowing laser light scattering method. J of Biomedical Optics 9(5):995-1001.

Zhang W, Kim JH, Franco CM, Middelberg AP. 2000. Characterisation of the shrinkage of calcium alginate gel membrane with immobilised Lactobacillus rhamnosus. Appl Microbiol Biotechnol 54(1):28-32.

Zohar-Perez C, Chet I, Nussinovitch A. 2004. Unexpected distribution of immobilized microorganisms within alginate beads. Biotechnol Bioeng 88(5):671-4.

Appendix A - Protocols

A1 Tube Forming Protocol

Standard conditions:

0.9% wt/vol saline, pH 7.3-7.4

0.09M $CaCl_2$ (propelling fluid)

0.50-1.00% Manugel DMB (matrix fluid)

1. Lubricate 100ml syringe using silicon gel and load using propelling fluid.
2. Fit loaded syringe into syringe driver.
3. Fit dual port base unit onto 100ml syringe.
4. Prime device using propelling fluid to the top of the injector nozzle of the plastic base unit at 1ml/min.
5. Prime 1ml luer-lock syringe (Fisher, Loughborough, UK) with desired volume (300-1000μl) of matrix fluid.
6. Fit 1ml syringe to side port of dual port base unit.
7. Remove excess propelling fluid from injector nozzle.
8. Position spherical regulator on top of injector nozzle.
9. Fit glass barrel onto stub of dual port base unit.
10. Inject entire volume of matrix fluid.
11. Infuse propelling fluid from syringe driver at 20ml/min*.
12. Leave tube to set for 10 min before removal.

Further:

1. Any run with air bubbles present, either during setup or during run, should be discarded.
2. Triplicates to be performed for each matrix fluid volume (after 3.2.3).

Note: Appendices A1-5 were developed by Dr. Julia Markusen, UCL and A6-7 were written by Prof. Ricky Wang, Cranfield University Silsoe.

** N.B. Infusion speed was reduced to 20ml/min to increase control on tube formation.*

A2 THAWING VIAL AND SEEDING FLASK OF CRL-1444

This protocol thaws one vial of (CRL-1444) A7r5 smooth muscle cells (SMCs) and then seeds the cells into 1 x T150 flask.

Passage 10, Date _____ (Vials were frozen at P9, so first passage is P10)

1. Pull the following medium for passaging cells:
   a) Complete medium DMEM (Cambrex, NJ 07073) supplemented with 10% FBS (Cambrex, NJ 07073), 1% (2 mM) L-glutamine (Cambrex, NJ 07073) and 1% pen/strep (Cambrex, NJ 07073) - stored at 4°C, pre-warm to room temperature
   b) Need 1 flask x 29 ml/flask = 29 ml for new flask. Complete medium formulated on _____
2. Using a 25 ml pipette, add 29 ml of complete medium to new 1 x T150 flask (Sigma-Aldrich, MO 63103)
3. Label flask with CRL-1444, passage number (P10), initials, and date.
4. Place new flask into 37°C/10% CO_2 incubator to equilibrate. (Ensure water bath is turned on and set to 37°C)
5. Remove one vial from frozen, liquid nitrogen storage. Safety note: Must wear protective gloves and face shield to protect against extreme cold temperature and possibility of vial exploding if liquid nitrogen is inside vial. Place vial into Styrofoam container with dry ice (preferred) or ice. Transfer as quickly as possible to lab.
   Time cells removed from liquid nitrogen: _____ am/pm

Note: Appendices A1-5 were developed by Dr. Julia Markusen, UCL and A6-7 were written by Prof. Ricky Wang, Cranfield University Silsoe.

6. Rapidly thaw vial in a 37°C water bath by gently swirling in the water (takes 2-3 minutes). Do not submerge vial cap under water during thaw, as water will wick up threads in cap. Safety note: Must wear face shield during thaw.

   Time start thaw of cells: _____ am/pm

   Time complete thaw of cells: _____ am/pm

7. Using 50 μl micropipette remove 10 μl of cell suspension from vial and add directly into a sample tube containing 90 μl of PBS for cell count. Using a 1 ml pipette, add entire remaining volume (ca. 0.9 to 1.0 ml) of cell suspension drop-wise to the T150 flask containing 29 ml of complete medium. Gently rock medium as drops of cells are added.

   Volume of cell suspension added to flask: _____ ml

8. Gently rock the flask so that the cells and medium mix well and are coated evenly over the growth surface. Remove 0.5 ml sample from the flask (only if you want to do metabolite analysis).

9. Time flask placed into 37°C/10% CO_2 incubator _____ am/pm

10. For samples (if needed):
    a) 1 x 0.5 ml diluted cell suspension, label with info. (e.g. JM2-01, Pxx, dil.cell, Day xx, date)
    b) Place into sample box in -70C freezer

11. Perform cell count:

    Using 100 μl sample in PBS, add 20 μl of sample to 20 μl of trypan blue dye. Perform 3 replicate counts. Count the number of live and dead cells in 10 squares:

    <u>viable/nonviable</u>

    a)

    b)

    c)

Note: Appendices A1-5 were developed by Dr. Julia Markusen, UCL and A6-7 were written by Prof. Ricky Wang, Cranfield University Silsoe.

Percent Viable = (total number viable) / (total viable + nonviable) x 100 = (expect >80%)

Total viable cells/ml = total number viable / 3 x 1000 x 20 = (expect ~ 2 x 10^6 cells/ml in vial)

(Multiply by vial volume for total viable cells/flask, and divide by 150 cm^2 for cells/cm^2)

A3 PREPARATION OF COMPLETE DMEM CULTURE MEDIUM

This protocol is used to prepare complete DMEM medium for culturing Smooth Muscle Cells [DMEM (Cambrex, NJ 07073) supplemented with 10% FBS (Cambrex, NJ 07073), 1% (2 mM) l-glutamine (Cambrex, NJ 07073) and 1% pen/strep (Cambrex, NJ 07073)]

Date _____

1. Thaw the following supplements in water bath - make sure container closures do not get submerged in the water (this is a common source of contamination).
   a) FBS (Cambrex, NJ 07073) - stored at -20°C or colder Lot number used: _____
      i) Aliquoted into ~59ml sample bottles
   b) 200 mM l-glutamine (Cambrex, NJ 07073) - stored at -20°C or colder - Lot number used: _____
      i) Aliquoted into 15 ml tubes - combined 6.5 ml of l-glutamine and 6.5 ml of pen/strep
   c) Pen/strep (Cambrex, NJ 07073) - stored at -20°C or colder - Lot number used: _____

Note: Appendices A1-5 were developed by Dr. Julia Markusen, UCL and A6-7 were written by Prof. Ricky Wang, Cranfield University Silsoe.

i) Aliquoted into 15 ml tubes - combined 6.5 ml of l-glutamine and 6.5 ml of pen/strep

2. Prepare the complete DMEM medium
   a) Remove from refrigerator the bottle(s) of DMEM (Cambrex, NJ 07073) - Lot number used: _____
   b) Place all components into laminar flow hood. Spray each bottle with 70% ethanol prior to placing in hood.
   c) Add 57 ml of FBS to the DMEM bottle
   d) Add 12 ml of the combined l-glut and pen/strep to the DMEM bottle
   e) Replace and tighten DMEM bottle cap. Mix components by inverting the DMEM bottle several times.
   f) Label DMEM bottle “complete medium, Date”.
   g) Store complete medium in refrigerator or use directly.

A4 PASSAGING CRL-1444

This protocol passages 5 x T150 flasks to 15 x T150 flasks. Any combination can be substituted, using a 1:3 split ratio (e.g. one flask becomes three new flasks).

Passage _____ , Date _____

1. Pull the following media for passaging cells
   a) Complete medium DMEM (Cambrex, NJ 07073) supplemented with 10% FBS (Cambrex, NJ 07073), 1% (2 mM) l-glutamine (Cambrex, NJ 07073) and 1% pen/strep (Cambrex, NJ 07073) - stored at 4°C, pre-warm to room temperature
      i) need 5 flasks x 18 ml/flask = 90 ml for quench

Note: Appendices A1-5 were developed by Dr. Julia Markusen, UCL and A6-7 were written by Prof. Ricky Wang, Cranfield University Silsoe.

ii) need 15 flasks x 22 ml/flask = 330 ml for new flasks
Complete medium formulated on _____

b) PBS (Cambrex, NJ 07073) - stored at room temperature

i) need 5 flasks x 30 ml/flask = 150 ml for rinse
PBS lot number _____

c) Trypsin/EDTA (Sigma-Aldrich, MO 63103) - stored frozen - thaw in 37°C water bath

i) need 5 flasks x 6 ml/flask = 30 ml
Trypsin/EDTA lot number _____

2. Add 22 ml/flask of complete medium to new 15 x T150 flasks (Corning, Cat# 430825)
3. Label flasks with CRL-1444, passage number (e.g. P14), and date.
4. Place new flasks into 37°C/10% CO_2 incubator to equilibrate.
5. Remove 5 x T150 flasks (flasks to be passaged) from 37°C/10% CO_2 incubator. Flasks are typically passaged every 3-4 days.

Indicate flasks used _____ Time cells removed from incubator: _____ am/pm

6. Observe cells under microscope and indicate % confluency, absence of microbial contamination (abnormal pH), excessive detached cells, or degeneracy of monolayer.

_____

_____

_____

_____

7. Using 25 ml pipette in BSC, remove spent medium from each flask. Pool spent medium from all 5 flasks into a sterile bottle (e.g. Nalgene 125 ml).
8. Add 30 ml/flask of PBS. Rinse PBS over the cell growth surface (to remove residual FBS proteins) and on top of flask (to remove condensation). Remove PBS from each flask and discard.

Note: Appendices A1-5 were developed by Dr. Julia Markusen, UCL and A6-7 were written by Prof. Ricky Wang, Cranfield University Silsoe.

9. Add 6 ml/flask of Trypsin/EDTA. Rinse Trypsin/EDTA over cell growth surface and let flask sit for ~ 5 minutes. (Occasionally rock flask during this time to ensure trypsin coated evenly over surface.)

Start trypsinisation: _____ am/pm

10. After 5 minutes, detach cells from growth surface by firmly tapping flask against palm of hand. (This is required to detach SMCs.) Quickly check cells are detached under microscope.
11. Add 18 ml/flask of complete medium (to quench trypsin activity). Medium should be completely washed over cell growth surface.

Time quenched: _____ am/pm (this should be less than 10 minutes total)

12. Pool cell suspension into one flask. Mix by twirling flask and remove 2 x 0.5 ml samples.
13. Add 8 ml cell suspension into each new 15 x T150 flask (pre-equilibrated). Evenly divide cell suspension over last three flasks (e.g. 7 2/3 ml/flask) due to 1ml removed for samples. Mix cell suspension and medium and remove 1 ml sample from 3 individual flasks.
14. Time last flask placed into 37°C/10% CO_2 incubator _____ am/pm
15. Take the following samples:
    a) 3 x 1 ml spent medium, label with info. (e.g. JM2-01, Pxx, spent, Day xx, date)
    b) from step 12, 1 x 0.5 ml cell suspension, label (e.g. JM2-01, Pxx, conc.cell, Day xx, date)
    c) 3 x 1 ml diluted cells suspension, label with info. (e.g. JM2-01, Pxx, dil.cell, Day xx, date)
    d) Place into sample box in -70C freezer
16. Perform cell count:

Note: Appendices A1-5 were developed by Dr. Julia Markusen, UCL and A6-7 were written by Prof. Ricky Wang, Cranfield University Silsoe.

a) Using remaining 1 x 0.5 ml sample from step 12, add 100 ul of sample to 100 μl of trypan blue dye. Perform 4 replicate counts. Count the number of live and dead cells in 10 squares:

viable/nonviable

i)

ii)

iii)

iv)

Percent Viable = (total number viable) / (total viable + nonviable) x 100 - (expect >95%)

Total viable cells/ml = total number viable / 4 x 1000 x 2 = (expect ~ 1 x 10^5 cells/ml)

A5 CELL BANKING CRL-1444

Passage _____ , Date _____

Pull the following media for passaging cells:-

a) PBS at room temperature

b) Complete medium DMEM (Cambrex, NJ 07073) supplemented with 10% FBS (Cambrex, NJ 07073), 1% (2 mM) l-glutamine (Cambrex, NJ 07073) and 1% pen/strep (Cambrex, NJ 07073) - stored at 4°C, pre-warm to room temperature

c) DMSO (Sigma-Aldrich, MO 63103) (10ml)

d) FBS (~35ml)

e) Trypsin/EDTA (Sigma-Aldrich, MO 63103) (thaw 2x100 ml in water-bath)

Note: Appendices A1-5 were developed by Dr. Julia Markusen, UCL and A6-7 were written by Prof. Ricky Wang, Cranfield University Silsoe.

Need:-

a) Complete medium (need 27 T-150 flasks x 18 ml/flask = 486 ml for quench)

Complete medium formulated on _____

2. Trypsin/EDTA (Sigma-Aldrich, MO 63103) - stored frozen - thaw in 37°C water bath (need 27 T-150 flasks x 6 ml/flask = 162 ml)

Trypsin/EDTA lot number _____

3. PBS (Cambrex, NJ 07073) - stored at room temperature (need 27 T-150 flasks x 30 ml/flask = 810 ml)

PBS lot number _____

Procedure:-

1. Remove flasks from incubator (process in groups of ~6 flasks).
4. Check confluency with microscope and make note of it.
5. Remove spent medium with a pipette.
6. Add 30 ml PBS (T150) to each flask. Rinse over cell sheet. Hold PBS on cells until next set of flasks processed.
7. Remove PBS, discard as waste.
8. Add 6 ml trypsin/EDTA (T15). Let it sit for ~5 mins, then tap flask to detach cells.
9. Add 18 ml complete medium for quench (T150) to quench trypsin activity. Rinse over growth surface to ensure cells detached & homogenous. Pool cell suspension into common flask.
10. Remove 2 x 0.5ml conc. Cell suspension samples (ensure cells well mixed by twirling flask).
11. Aliquot conc. cell suspension into 50 ml centrifuge tubes - baring in mind to keep both tubes of a pair balanced in mass.

    27 flasks x 24 ml/flask = 648 ml to centrifuge – 1ml cell sample = 647ml

Note: Appendices A1-5 were developed by Dr. Julia Markusen, UCL and A6-7 were written by Prof. Ricky Wang, Cranfield University Silsoe.

$\Rightarrow$ 12 tubes @ $\approx$ 50ml each, 2 tubes @ $\approx$ 24ml each

12. Centrifuge 50 ml tubes at 100xg (centrifuge setting of 100 RCF) for 10 minutes.
13. Concurrently (during centrifugation) perform cell counts: 100 µl sample + 100 µl trypan blue (dilution factor 2)
14. Let cells (pelleted) sit in tubes until next group of flask trypsinised.
15. Repeat steps 1-11 on second set of flasks.
16. Aliquot remaining cell-suspension into 50 ml centrifuge tubes.
17. Centrifuge set #2.
18. Concurrent 14 cell counts (set #2 flasks). Based on combined cell counts calculate the amount of viable cells/ml.
19. Calculate amount of cells to be frozen.
20. Prepare “freeze FBS medium” by adding 15 ml FBS to 50 ml complete medium.
21. Without disturbing cell pellet, remove supernatant from each 50 ml tube (~ 0.5ml residual medium in each tube after supernatant removed). Resuspend pellet by gently tapping onside with hand until pellet/cells become unclumped. Add 1ml “freeze FBS medium” to each centrifuge tube and again resuspend pellet by tapping side with hand.
22. After resuspending pellets combine all cells into one tube.
23. Rinse each tube (serially) with total of 2 ml to wash residual cells from tubes $\Rightarrow$ set # 1 volume $\approx$ 13ml
    (1.5 x 6 = 11ml + 2ml last rinse = 13ml)
24. Repeat steps 24, 25 & 26 for 2nd set of tubes.
25. Measure final resuspension of combined cells from both sets in “freeze FBS medium” as prepared in step 26 & 27 with a pipette. Add additional FBS freeze medium to get concentration to 2.2 x 10^6 cell/ml
26. Transfer into 200 ml glass bottle, place on magnetic stirrer plate inside hood and mix at 10 rpm.

Note: Appendices A1-5 were developed by Dr. Julia Markusen, UCL and A6-7 were written by Prof. Ricky Wang, Cranfield University Silsoe.

27. Add using e.g. 1 ml pipette, first 1 ml, then 0.7 ml of DMSO (1.7ml total) dropwise into mixing cell suspension (depending on cell concentration – check calculation)
28. Aliquot e.g. 35 x 1ml into 1.5ml Nalgene Cryovials, and label.
29. Place into -70°C freezer in large Styrofoam box. Transfer to liquid nitrogen within 24 hours.

Concentration Calculation

Final resuspension volume (set # 1 + 2) _____ml (e.g. ≈ 26ml)

Want to resuspend cells to $\frac{2 \times 10^6 \text{ cells/ml}}{0.90}$ = 2.2×10^6 cell/ml

(Want 10% DMSO 90% cells in FBS freeze medium)

Add additional FBS freeze medium to the 26ml to make it 2.2×10^6 cell/ml (e.g. 12.2 ml)

Then add DMSO to final conc. 10%: (0.10) x 38.2 ml = 3.8ml DMSO added dropwise

[Verify check:

3.8ml + 38.2ml = 42ml

Recall $\frac{8.411 \times 10^7 \text{ cells}}{2 \times 10^6}$ = 42ml which is what we wanted for 2×10^6 cells/ml]

E.g. cell count (average) is 1.3×10^5 cell/ml x 647 ml (centrifuged)

$\Rightarrow \frac{8.411 \times 10^7 \text{ cells}}{2.2 \times 10^6 \text{ cell/ml}}$ = 38.2 ml – 26.0 ml resuspension volume = 12.2 ml additional FBS freeze medium to be added

Note: Appendices A1-5 were developed by Dr. Julia Markusen, UCL and A6-7 were written by Prof. Ricky Wang, Cranfield University Silsoe.

A6 PREPARING CELLS FOR ADDITION TO ALGINATE TO FORM BEADS/TUBES

1. Trypsinise cells as per usual protocol. Pool the cells into one flask.
2. Dispense cell suspension into centrifuge tubes (Measure volume of cell suspension, so you can calculate the total volume).
3. Perform cell count as per usual protocol. Calculate total number of cells. Determine the cell concentration you want to have in the alginate (this is usually 1e6 to 1e7/ml). Calculate the volume of alginate + cells.

   Example: Trypsinise 4 flasks @ 3e6 cells/flask = 12e6 cells total

   Want 5e6 cells/ml, so dividing by total cells = 2.4 ml of alginate + cell solution.
4. Centrifuge cells at 100xg for 5 min., temperature can be set to 8-10C.
5. Remove supernatant without disturbing the pellets. Gently tap pellets to loosen cells.
6. Resuspend the cells with culture medium (about 2 ml), combine all of the cells into one tube. Maximise the number of cells recovered by rinsing tubes with medium and adding to the last tube with all the cells. Resuspend the cells to a total volume of 5-8ml. This step is performed to removed/dilute residual trypsin/EDTA, which will interfere with alginate cross-linking.
7. Centrifuge cells at 100xg for 5 mins, temperature can be set to 8-10C.
8. Remove supernatant without disturbing the pellet. Gently tap pellet to loosen cells.
9. Resuspend the cells with culture medium, volume as calculated below. The pellet volume must be accounted for, so the total volume includes medium + cells. Avoid excess bubbles, pipette slowly until cells + medium are homogenous.

Note: Appendices A1-5 were developed by Dr. Julia Markusen, UCL and A6-7 were written by Prof. Ricky Wang, Cranfield University Silsoe.

Example: For 1% alginate solution, a 75% alginate, 25% cells mix works well. So for 2.4 ml alginate + cells this is 0.6ml of cells, 1.8ml of alginate. It works well to put a small volume of culture medium into a separate container, so you don't have to change pipettes to get the volume accurate (and you don't lose cells with each pipette change).

10. Add the volume of alginate to a small sample tube. Flat bottom tube mixes better.
11. Add the cell suspension to the alginate, swirling the end of the pipette as you slowly add the cells (this mixes like a spoon). Do not pipette up and down. Twirling the tube or placing the on roller also works well.
12. Make beads/tubes.

A7 OCT DATA ANALYSIS MATLAB PROGRAMME

```
clear
N =27650;%////69500////104250;
nf = 0;
MN =2;
figno = 11;
ispec = 1;
specfigno = 10002;
filenam1 = sprintf('oct.TXT');%365mm 18bead 4
fid = fopen(filenam1,'r+');
shft = 2*N*nf;
status = fseek(fid, shft, 'bof');
for (kk=1:MN)
count = fix(kk/5) - kk/5;
if (count == 0) kk
```

Note: Appendices A1-5 were developed by Dr. Julia Markusen, UCL and A6-7 were written by Prof. Ricky Wang, Cranfield University Silsoe.

```
end
date = fread(fid,N, 'short');
%date(1) = date(2);
y = date*10000.0/4096.0 - 5000.0;  %Convert into voltage
clear date;
a = mean(y);     y = (y - a)/20;
if ((fix((nf+kk)/2)-((nf+kk)/2)) == 0)
y1 = flipud(y);
y=y1;
end
%  figure(11)
% plot(y)
%   [B,F,T] = specgram(y,128,20000,[],38);
%[B,F,T] = specgram(y,256,200000,100,65);
[B,F,T] = specgram(y,256,20000,100,65);
if (kk == ispec)
figure(specfigno)
imagesc(log(abs(B)));
figure(10000)
specgram(y,256,20000,140,45);
end
C=abs(B(50:75,:)); %19:46
F1 = F(50:75);
XSUM = sum(F1);
XYSUM = C'*F1;
fist(:,kk) = 20*log(XYSUM/XSUM);
%fist(:,kk) = log(max(C, [], 1)');
%   nt = max(size(T));
%   nf = max(size(F));
%   C=20*log(abs(B));
```

Note: Appendices A1-5 were developed by Dr. Julia Markusen, UCL and A6-7 were written by Prof. Ricky Wang, Cranfield University Silsoe.

```
%   for (jk = 1:nt)
%    fist(jk, kk) = max(C(26:39,jk)); %
%    end
clear C B y y1 a aver;
%shft = 2*N*2;
%status = fseek(fid, shft, 'cof');
end
fclose('all');
xx = T*240000*0.008434/1000/1.5;
yy(1:MN) = (1:MN)*12.6/1000; %1.5/60;  %spatial resolution
bb = min(min(fist));
fist = fist - bb;
A = max(max(fist));
fist = fist/A;
%fist1 = (fist.*fist);
load map_plate.m
figure(figno)
%subplot(3,2,6)
imagesc(yy,xx, fist, [0 3]);
colormap(map_plate);
%ylabel('Depth (mm)', 'fontsize', 24, 'fontweight', 'bold');
%xlabel('Spatial length (mm)', 'fontsize', 24, 'fontweight', 'bold');
%set(gca, 'fontsize', 20, 'fontweight', 'bold','Position', [0.160    0.180    0.750
0.75]);
%jpgfilename = strrep(filenam1,'TXT','jpg');
%saveas(gcf, jpgfilename);
%figfilename = strrep(filenam1,'TXT','fig');
%saveas(gcf, figfilename);
%aaa = sum(fist,2)/MN;
%figure(49)
```

Note: Appendices A1-5 were developed by Dr. Julia Markusen, UCL and A6-7 were written by Prof. Ricky Wang, Cranfield University Silsoe.

```
%hold
%plot(xx, aaa, 'b-')
%hold on
figure(1)
sm = sum(fist, 2)/size(fist,2);
bkgarray =sm(2:22);
bkg = sum(bkgarray)/size(bkgarray,1)
sm = sm - bkg;
plot(sm);%T*65/1.4,
effpixels = find(sm > 0.15);
for (ii=2:size(effpixels,1))
increament(ii)=effpixels(ii)-effpixels(ii-1);
end
[bb,idx]=max(increament);
if ( bb >= 10)
thickness = (size(effpixels,1)-idx)*(T(2)-T(1))*240000*0.008434/1000/1.4
size(effpixels,1)-idx
else
thickness = size(effpixels,1)*(T(2)-T(1))*240000*0.008434/1000/1.4
size(effpixels,1)
end
aaa= mean(mean(fist((360:390),:)))  %
fist = (fist  - aaa);
counts = find(fist > 0);
cuntnum = size(counts ,1)
clear all
```

Note: Appendices A1-5 were developed by Dr. Julia Markusen, UCL and A6-7 were written by Prof. Ricky Wang, Cranfield University Silsoe.

A8 OCT MATLAB PROGRAMME EXTENSION – THICKNESS

```
figure(1)
sm = sum(fist, 2)/size(fist,2);
bkgarray =sm(2:22);
bkg = sum(bkgarray)/size(bkgarray,1);
sm = sm - bkg - 0.08;
plot(sm);%T*65/1.4,
effpixels = find(sm>0);
for (ii=2:size(effpixels,1))
increament(ii)=effpixels(ii)-effpixels(ii-1);
end
[bb,idx]=max(increament)
if ( bb >= 10)
thickness = (size(effpixels,1)-idx)*(T(2)-T(1))*240000*0.008434/1000/1.4
else
thickness = (size(effpixels,1)-3)*(T(2)-T(1))*240000*0.008434/1000/1.4
end
clear all
```

Note: Appendices A1-5 were developed by Dr. Julia Markusen, UCL and A6-7 were written by Prof. Ricky Wang, Cranfield University Silsoe.

Appendix B: Fluid Mechanics Theory

B1 Theoretical Considerations

The aim of the theoretical analysis is to understand the physical processes responsible for the tube forming process and to provide practical estimates, testable experimentally, of the tube wall thickness. As we shall demonstrate, the tube forming process does not depend on having dissimilar charging and propelling fluids. For this reason, we first simplify our analysis by considering the case when both fluids are Newtonian and have identical physical properties. A rigid, neutrally buoyant sphere of radius r_0 being propelled along a cylinder whose inner radius is *a*, as illustrated in Figure 3.1. The cylinder is assumed to be infinitely long so that the influence of the end conditions on the flow is negligible. The sphere is propelled along the cylinder by a fluid whose mean velocity is $\bar{u}$. Both the matrix and propelling fluid are assumed to have the same properties, and the same density as the sphere. A lubrication analysis of the Newtonian flow around a tightly fitting sphere is first considered and the predictions of the thickness of a layer are tested against numerical calculations using FEMLAB. This estimation of the thickness of the deposited layer forms the new component of the study, which draws on the lubrication analysis of Dowson (Dowson et al. 1992).

B2 Lubrication Analysis

In the vicinity of the narrowest region between the sphere and cylinder, the local Reynolds number based on the minimum gap width is $\mathrm{Re}_\delta = v\delta_0\rho/\mu$, where ρ, μ are the density and viscosity of the fluid respectively and δ_0 is the minimum gap separation between the sphere and tube wall. Typically Re_δ = 0.01, so that inertial forces are weak. Therefore, the radial pressure gradient is small, and the axial flow can be described by the lubrication equation (Batchelor 1965),

---

Note: All mathematical Theory was developed by Prof. Ian Eames, (Department of Mechanical Engineering, UCL) and Dr. Mark Landeryou (Department of Medical Physics, UCL).

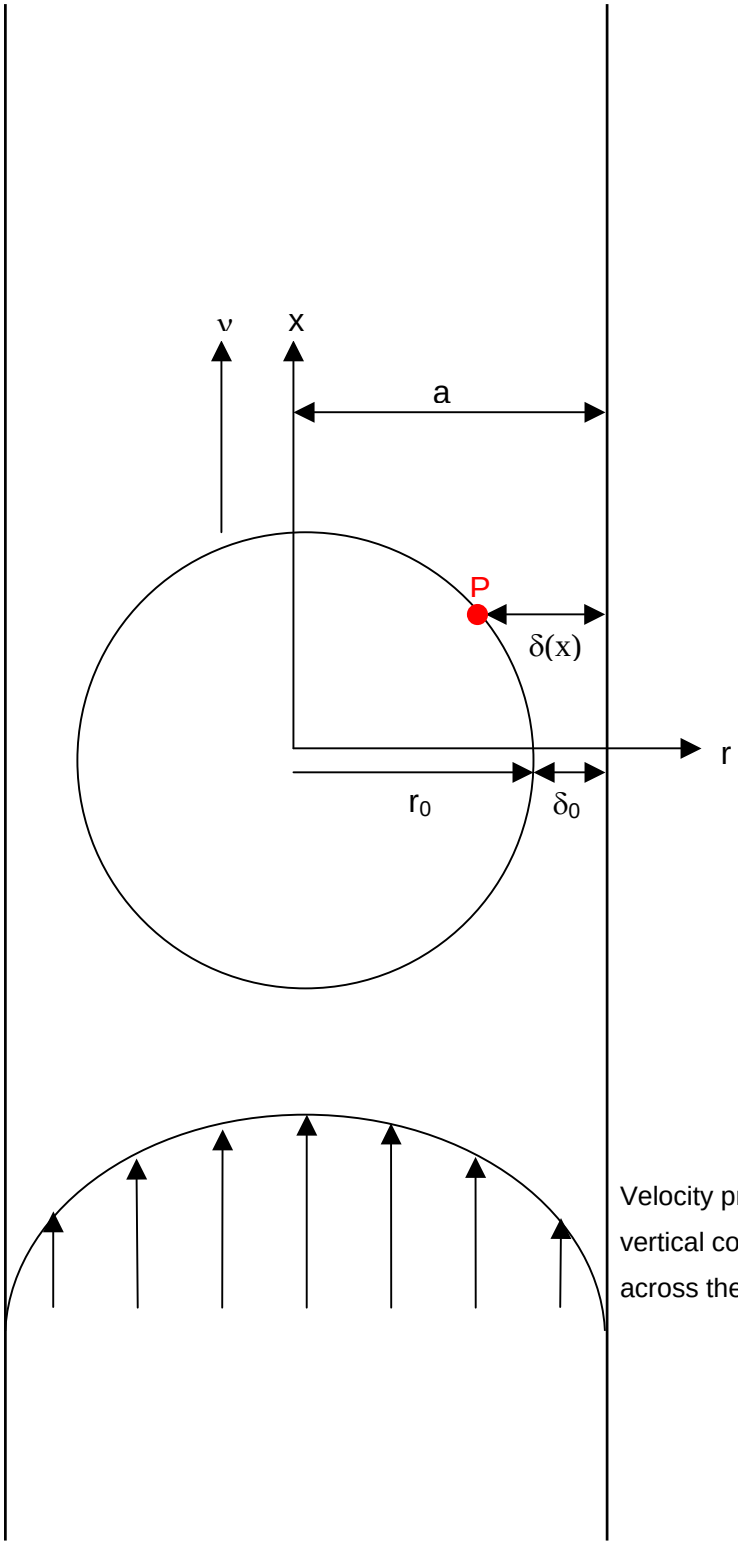

Figure 3.1 Schematic to show the arrangement of the spherical regulator in a cylinder propelled upwards by a flow at the inlet.

Note: All mathematical Theory was developed by Prof. Ian Eames, (Department of Mechanical Engineering, UCL) and Dr. Mark Landeryou (Department of Medical Physics, UCL).

$$0 = -\frac{dp}{dx} + \mu \frac{\partial^2 u_x}{\partial r^2}, \qquad (1)$$

Integrating this equation leads to a parabolic velocity profile, which after including the non-slip condition on the wall and sphere yields

$$u_x = -\frac{v(r-a)}{\delta(x)} - \frac{1}{2\mu} \cdot \frac{dp}{dx} \cdot (r-a)(r-a+\delta(x)), \qquad (2)$$

Where u_x is the vertical component of velocity and δ is the gap separation. The cylindrical coordinates (r, x) refer to the radial distance from the centreline and the vertical distance above the centre of the sphere. The gap separation between the sphere and cylindrical tube $\delta(\boldsymbol{x})$ is a function of vertical distance.

The solution to (2) for the problem we consider is well known (Matar et al. 2006; Udofia and Jin 2003) but the application to determining the thickness of the deposited layer of the fluid appears new. To solve (2), we first make use of the fact that the flux of fluid between the sphere and tube, across a horizontal plane, is independent of vertical position of the plane. Since the gap thickness can be considered small compared to the tube radius ($\delta_0 << a$), conservation of the vertical mass flux reduces

$$2\pi f + (\bar{u} - v)\pi a^2 = 0, \qquad (3)$$

Where the circumferential flux is

$$f = \int_{a-\delta}^{a} u_x \cdot dr = \frac{1}{2} \cdot v\delta - \frac{\delta^3}{12\mu} \cdot \frac{dp}{dx}. \qquad (4)$$

Note: All mathematical Theory was developed by Prof. Ian Eames, (Department of Mechanical Engineering, UCL) and Dr. Mark Landeryou (Department of Medical Physics, UCL).

Since the pressure gradient is largely controlled by the vertical pressure difference across the thin gap, the pressure difference between above and below the sphere is estimated to be

$$\Delta P = \int_{-\infty}^{\infty} \frac{dp}{dx} \cdot dx = 6\mu v I_2 - 12\mu f I_3 , \qquad (5)$$

Where I_2 and I_3 are defined by $I_n = \int_{-\infty}^{\infty} dx / \delta^n$. The shear induced force, per unit circumferential distance is

$$S = \int_{-\infty}^{\infty} \mu \left[\frac{\partial u_x}{\partial r} \right]_{r=a-\delta} \cdot dx = \mu\left(4vI_1 - 6fI_2\right). \qquad (6)$$

We are interested in the case when the sphere is neutrally buoyant, so that the total force on the sphere is zero, with the shear stress and pressure forces balancing, that is

$$F_x = 2\pi a S - \pi a^2 \Delta P = 0 . \qquad (7)$$

By substituting (5) and (6) into (7), the relative slip between the sphere and ambient flow is estimated to be:

$$\frac{v - \bar{u}}{v} = \frac{4I_1 - 3I_2 a}{3\left(I_2 - I_3 a\right)} . \qquad (9)$$

Within the vicinity of the narrowest point between the sphere and tube, the gap thickness, to second order, is approximately

$$\delta(x) = \delta_0 + \frac{x^2}{2r_0} , \qquad (10)$$

Note: All mathematical Theory was developed by Prof. Ian Eames, (Department of Mechanical Engineering, UCL) and Dr. Mark Landeryou (Department of Medical Physics, UCL).

Where the radius of curvature of the gap (or the sphere radius) is r_0. Evaluating

$$I_n = \int_{-\infty}^{\infty} \frac{dx}{(\delta_0 + x^2/2r_0)^n}, \qquad (11)$$

we obtain

$$I_1 = \frac{\pi r_0^{1/2}\sqrt{2}}{\delta^{1/2}},\ I_2 = \frac{\pi\sqrt{2}}{2\delta^{3/2} r_0^{1/2}},\ I_3 = \frac{3\pi\sqrt{2}}{8\delta^{5/2} r_0^{1/2}}. \qquad (12)$$

Thus from (9) the sphere slip velocity is

$$\frac{v-\bar{u}}{v} \approx \frac{4\delta_0}{3r_0}\left(\frac{1-8\delta_0/3r_0}{1-4\delta_0/3r_0}\right). \qquad (13)$$

Thus the sphere moves faster than the average fluid velocity. The physical picture that emerges is one where the flow up and downstream of the sphere is parabolic and described by $u_x = 2\bar{u}(1-r^2/a^2)$, but in the vicinity of the sphere and near the narrow gap, it is determined by the lubrication analysis. We attempt to confirm this solution numerically before proceeding to estimate the layer thickness.

B3 Numerical Calculation of the Flow Field

To test the asymptotic analysis, we calculated the viscous flow around a neutrally buoyant sphere translating along the axis of cylindrical tube using a scripted set of equations within FEMLAB 3.1. The output from FEMLAB was processed using MATLAB. Figure B1 shows a schematic of the computational domain, with a

---

Note: All mathematical Theory was developed by Prof. Ian Eames, (Department of Mechanical Engineering, UCL) and Dr. Mark Landeryou (Department of Medical Physics, UCL).

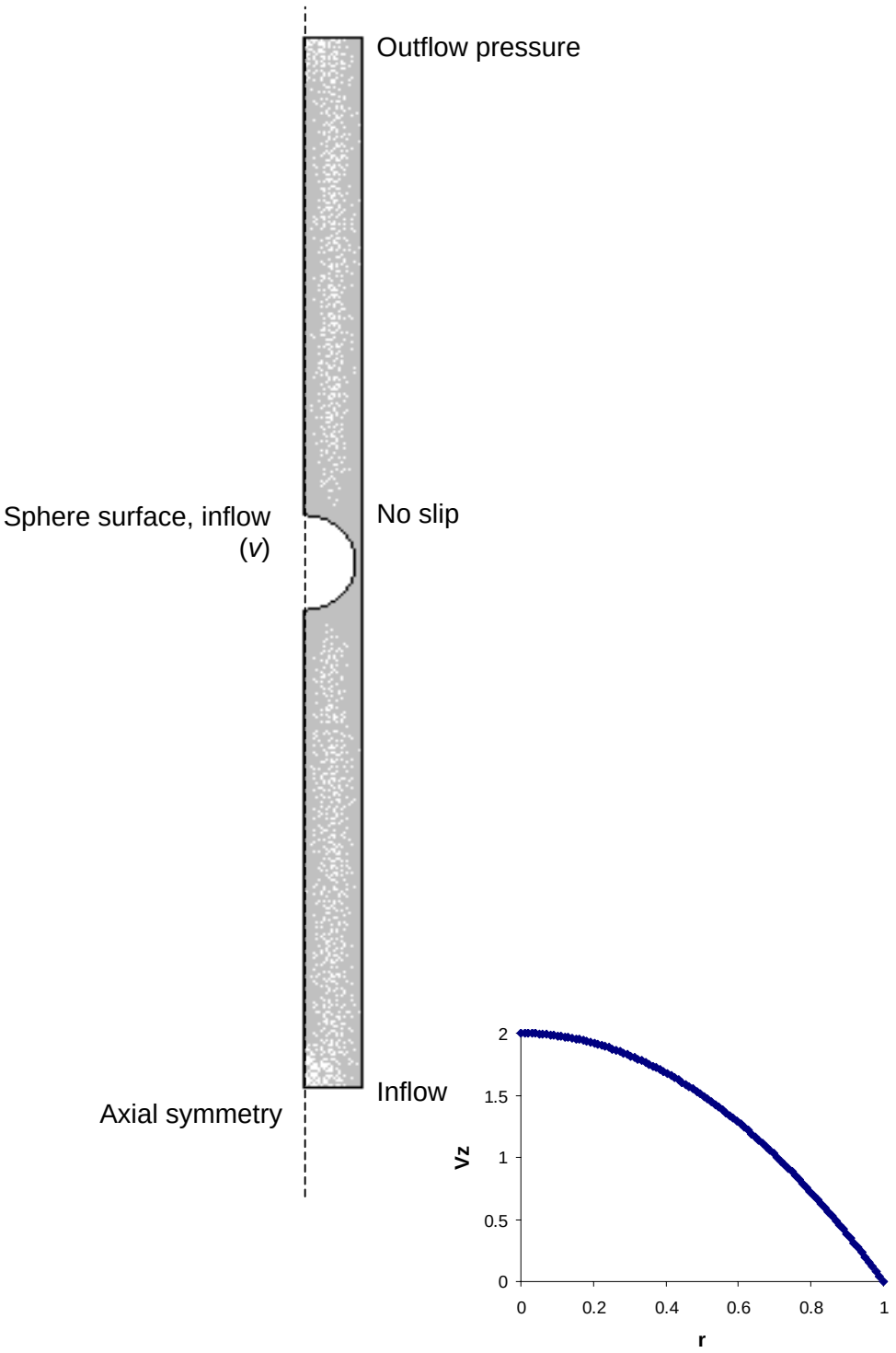

Figure B1 Schematic of the computational domain, with a parabolic velocity input velocity profile, a prescribed exit pressure and prescribed velocity of the sphere.

Note: All mathematical Theory was developed by Prof. Ian Eames, (Department of Mechanical Engineering, UCL) and Dr. Mark Landeryou (Department of Medical Physics, UCL).

parabolic velocity input velocity profile, a prescribed exit pressure and prescribed velocity of the sphere. For Stokes flows, the flow is determined by the instantaneous boundary conditions on the flow. The translation velocity of the sphere is unknown and is calculated iteratively by determining when the vertical force on the sphere was zero, consistent with the requirement from (7). The mesh in the small gap was refined and its influence on the resulting solution tested. Both three dimensional and axisymmetric formulations were considered and found to give the same results. Figure B2 shows a comparison between the calculated slip velocity of the sphere and the asymptotic expression (13), with excellent agreement for $\delta_0/a < 0.1$.

B4 Estimation of the Layer Thickness

As the sphere is propelled along the tube, fluid in front of the sphere is deposited on the inner wall of the cylindrical tube and forming a thin layer. The purpose is to estimate the thickness of the layer deposited. Two methods are used to estimate the thickness of a deposited layer: an approximation of the average layer thickness and calculation of the thickness by following the flow. We describe both approaches and show how they differ, but this difference can be reconciled by a more detailed analysis of the flow. We elaborate on the implications for interpreting the experimental results.

To estimate the deposited thickness we consider the experimental setup, where a cylinder is initially charged with a fluid of height λ. As the propelling fluid is injected into the cylinder (with an average velocity $\bar{u}$), the height of the matrix fluid is lifted by $\lambda + \bar{u}t$, while the sphere moves a distance vt. The sphere breaks through the surface of the liquid after time $t = \lambda/(v - \bar{u})$, producing a layer whose nominal thickness is

$$\frac{T_B}{a} = 1 - \sqrt{1 - \frac{(v - \bar{u})}{v}} \approx \frac{2\delta_0}{3r_0} - \frac{2{\delta_0}^2}{9{r_0}^2}. \qquad (14)$$

Note: All mathematical Theory was developed by Prof. Ian Eames, (Department of Mechanical Engineering, UCL) and Dr. Mark Landeryou (Department of Medical Physics, UCL).

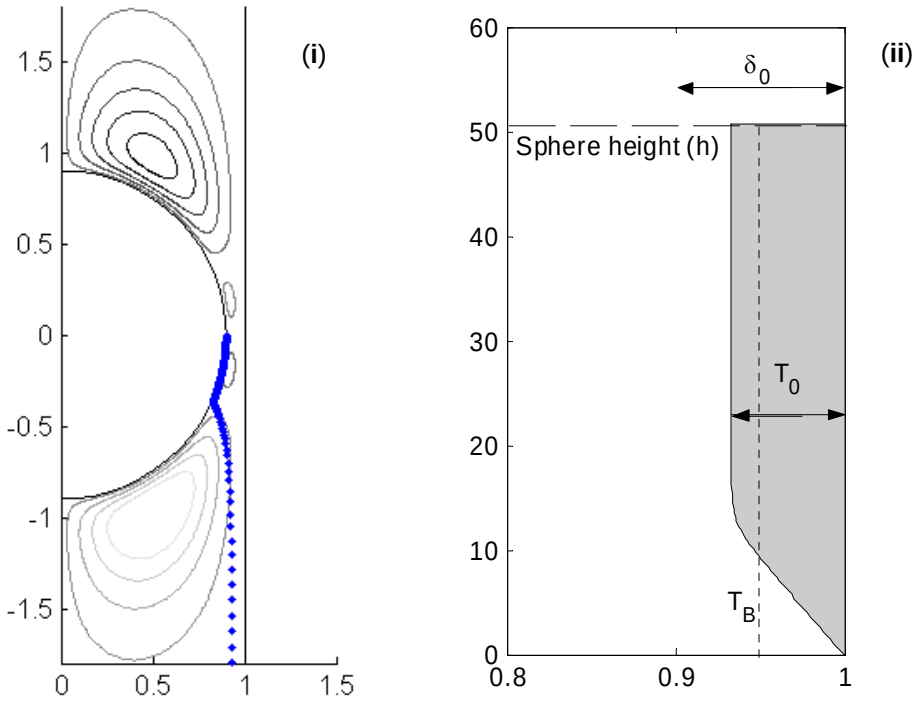

Figure B2 (**i**) Numerical results for the flow field for Re = 1 and δ_0/a = 0.1. The contours show values of the radial component of the velocity field (u_r). The dots denote the path of a fluid particle released adjacent to, and near the surface, of a rising sphere and are representative of the interface shape.
(**ii**) Calculated interface from tracking a number of particles distributed across the sphere-cylinder wall gap.

Note: All mathematical Theory was developed by Prof. Ian Eames, (Department of Mechanical Engineering, UCL) and Dr. Mark Landeryou (Department of Medical Physics, UCL).

The second method involves releasing tracer particles in the flow, which were swept past the sphere as it translated along the tube. Figure B2(*i)* shows a line of tracer particles released along the narrowest gap between the wall and sphere. Tracer particles in the vicinity of the sphere are carried forward as the sphere advances, while particles closest to the wall move much slower. As a consequence the sheet of tracer particles is deformed. The tube thickness T_0 may be found from the maximum thickness of the tracer layer far downstream of the sphere. Figure 3.4 shows numerical calculations of this thickness.

It is clear by comparing the results of (14) with those of the tracer particle study that the thicknesses are different, and this is caused by a subtlety in the problem. Once the tracer particles have been advected beyond the influence of the sphere, they do not come to rest, but continue to move in the presence of the viscous parabolic flow that propels the sphere. This flow induces the particles to move in the direction of the sphere. At this distance, x, from the sphere to where the tracer curve makes contact with the tube wall, the fluid interface is advected with speed $u_x(r_f)$ by the parabolic flow. For thin gap separations, the flow is approximately a linear shear in the vicinity of the wall, and the particles move according to $X_f(t) = X_f(t_0) + 4uT_f t/a$. This self-similar portion of the tracer layer is connected by a layer of uniform thickness, which increases in length, in proportion to the speed of the sphere. The total volume of fluid in the two layers is approximately constant with time. Figure B2*(ii)* shows the shape of the fluid interface downstream of the sphere where the interface is not changing in *r*. The end region forms a finite fraction of the tube length and causes the mean thickness of the layer estimated from volume conservation (14) to be slightly smaller than the true thickness.

Note: All mathematical Theory was developed by Prof. Ian Eames, (Department of Mechanical Engineering, UCL) and Dr. Mark Landeryou (Department of Medical Physics, UCL).

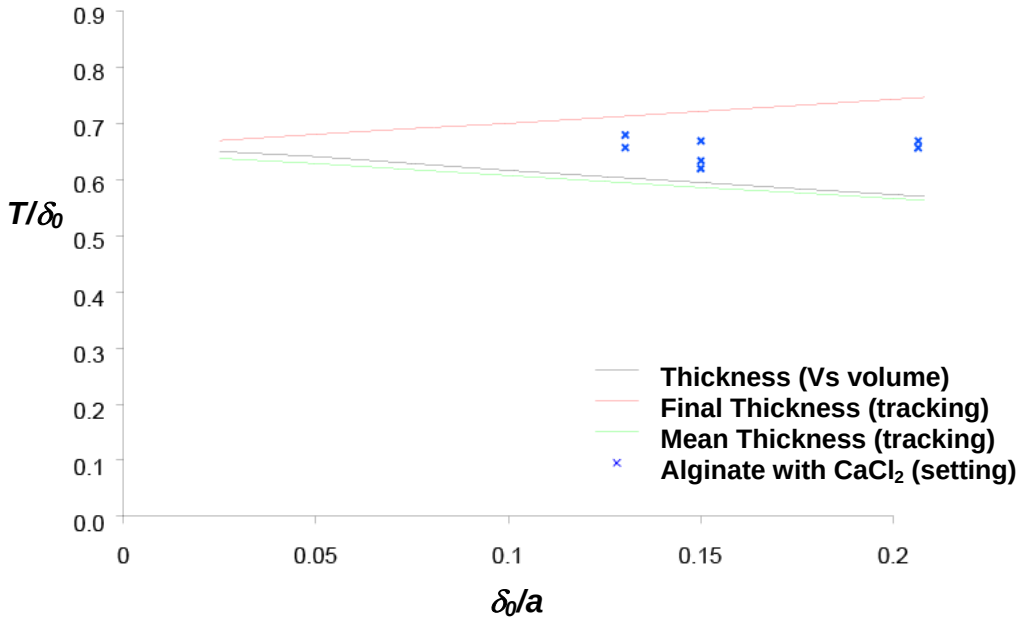

Figure 3.4 Tube wall thickness, 'T' as a fraction of gap width, 'δ_0' versus gap width as a fraction of cylinder radius 'a'. Alginate infused with $CaCl_2$ wall thickness data, T_0 is marked as (**X**). The predicted wall thickness (T_B) (14) is plotted as a green line.

Note: All mathematical Theory was developed by Prof. Ian Eames, (Department of Mechanical Engineering, UCL) and Dr. Mark Landeryou (Department of Medical Physics, UCL).

Appendix C: Statistical Analyses

All statistical tests were performed with the aid of http://faculty.vassar.edu statistical calculator.

Table C1 **Statistical results for ANOVA and TUKEY tests of the particle size data from figure 4.9*b*.**

Data Summary

	Samples					
	1	2	3	4	5	Total
N	32	32	32	32	32	160
∑X	1022642.3	1030349.4	710300.8	476084.6	80116.3	3319493.4
Mean	31957.5719	32198.4188	22196.9	14877.6438	2503.6344	20746.8337
$\sum X^2$	109255329396.87	89566031145.86	42161965141.2	22398434950.34	576694283.49	263958454917.7601
Variance	2470134341.684	1819045474.3822	851467397.2155	494045737.9574	12132656.8004	1226977844.1116
Std.Dev.	49700.4461	42650.2693	29179.9143	22227.1397	3483.1963	35028.2435
Std.Err.	8785.8806	7539.5737	5158.3288	3929.2403	615.7479	2769.2258

ANOVA Summary

Source	SS	df	MS	F	P
Treatment [between groups]	20037883364.5134	4	5009470841.1284	10.6816	<.0001
Error	58153866882.7667	124	468982797.4417		
Ss/Bl	116897726966.4577	31			
Total	195089477213.7378	159			

Tukey HSD Test

HSD[.05]=14993.28; HSD[.01]=18044.67
M1 vs M2 nonsignificant
M1 vs M3 nonsignificant
M1 vs M4 P<.05
M1 vs M5 P<.01
M2 vs M3 nonsignificant
M2 vs M4 P<.05
M2 vs M5 P<.01
M3 vs M4 nonsignificant
M3 vs M5 P<.01
M4 vs M5 nonsignificant

M1 = mean of Sample 1
M2 = mean of Sample 2
and so forth.

HSD = the absolute [unsigned] difference between any two sample means required for significance at the designated level. HSD[.05] for the .05 level; HSD[.01] for the .01 level.

Table C2 **Statistical results for ANOVA and TUKEY tests of the Leica QWin data from figure 4.10.**

Data Summary

	Samples					
	1	2	3	4	5	Total
N	12	12	12	12	12	60
∑X	273	311	191	131.5	17.5	924
Mean	22.75	25.9167	15.9167	10.9583	1.4583	15.4
$\sum X^2$	29508.875	24642.25	8563.875	3368.375	78.375	66161.75
Variance	2118.0114	1507.4697	502.1629	175.214	4.8049	880.2059
Std.Dev.	46.0219	38.8261	22.409	13.2368	2.192	29.6683
Std.Err.	13.2854	11.2081	6.4689	3.8211	0.6328	3.8302

ANOVA Summary

Source	SS	df	MS	F	P
Treatment [between groups]	4547.8583	4	1136.9646	3.319	0.018444
Error	15072.8917	44	342.5657		
Ss/Bl	32311.4	11			
Total	51932.15	59			

Ss/Bl = Subjects or Blocks depending on the design.
Applicable only to correlated-samples ANOVA.

Tukey HSD Test

HSD[.05]=21.56; HSD[.01]=26.22 M1 vs M2 nonsignificant M1 vs M3 nonsignificant M1 vs M4 nonsignificant M1 vs M5 nonsignificant M2 vs M3 nonsignificant M2 vs M4 nonsignificant M2 vs M5 P<.05 M3 vs M4 nonsignificant M3 vs M5 nonsignificant M4 vs M5 nonsignificant	M1 = mean of Sample 1 M2 = mean of Sample 2 and so forth. HSD = the absolute [unsigned] difference between any two sample means required for significance at the designated level. HSD[.05] for the .05 level; HSD[.01] for the .01 level.

Table C3 **Statistical results for ANOVA test on a correlated sample comparing data from the Leica QWin and Malvern Particle Sizer.**

Data Summary

	Samples					
	1	2	3	4	5	Total
N	5	5				10
∑X	299943.5	273				300216.5
Mean	59988.7	54.6				30021.65
$\sum X^2$	25599884478.47	29508.875				25599913987.345
Variance	1901665960.005	3650.7688				1842991033.3467
Std.Dev.	43608.0951	60.4216				42930.0714
Std.Err.	19502.133	27.0214				13575.6806

ANOVA Summary

Source	SS	df	MS	F	P
Treatment [between groups]	8980240857.025	1	8980240857.025	9.4263	0.037285
Error	3810732449.1975	4	952683112.2994		
Ss/Bl	3795945993.8975	4			
Total	16586919300.12	9			

Table C4 **Statistical results for ANOVA test on a correlated sample comparing data for the effect of passes using an auto-pipette, figure 4.15.**

Data Summary

	Samples					
	1	2	3	4	5	Total
N	32	32	32	32	32	160
ΣX	723465.1	783884.2	673594	1278669.4	990682.2	4450294.9
Mean	22608.2844	24496.3813	21049.8125	39958.4188	30958.8188	27814.3431
ΣX^2	63074395106.25	84416176020.4	77611909622.44	157092945749.16	176911458651.3	559106885149.55
Variance	1507035173.873	2103672574.2371	2046222007.1392	3419333497.4564	4717455096.2145	2737892174.802
Std.Dev.	38820.5509	45865.8105	45235.1855	58475.0673	68683.7324	52324.8715
Std.Err.	6862.5687	8108.0064	7996.5266	10337.0292	12141.6832	4136.6443

ANOVA Summary

Source	SS	df	MS	F	P
Treatment [between groups]	7719586976.9889	4	1929896744.2472	1.6264	0.171763
Error	147138315209.4711	124	1186599316.2054		
Ss/Bl	280466953607.0525	31			
Total	435324855793.5124	159			

Ss/Bl = Subjects or Blocks depending on the design.
Applicable only to correlated-samples ANOVA.

Table C5 **Statistical results for ANOVA and TUKEY HSD tests on a correlated sample comparing data for the effect of holding time (unfiltered), figure 4.16.**

Data Summary

	Samples				
	1	2	3	4	Total
N	32	32	32	32	128
ΣX	1093068.5	1241593.8	1673633	2027160.1	6035455.4
Mean	34158.3906	38799.8062	52301.0313	63348.7531	47151.9953
ΣX^2	169199909264.7501	177546485698.34	268251988739.56	494936158218.41	1109934541921.06
Variance	4253627369.7377	4173318929.5851	5829653448.5654	11823164306.4084	6498825017.2556
Std.Dev.	65219.8388	64601.2301	76352.1673	108734.375	80615.2902
Std.Err.	11529.3476	11419.992	13497.2838	19221.7035	7125.4523

ANOVA Summary

Source	SS	df	MS	F	P
Treatment [between groups]	16878091508.2629	3	5626030502.7543	3.1977	0.027011
Error	163626147795.5523	93	1759420944.0382		
Ss/Bl	644846537887.6422	31			
Total	825350777191.4574	127			

Ss/Bl = Subjects or Blocks depending on the design.
Applicable only to correlated-samples ANOVA.

Tukey HSD Test

HSD[.05]=27513.05; HSD[.01]=33543.21 M1 vs M2 nonsignificant M1 vs M3 nonsignificant M1 vs M4 P<.05 M2 vs M3 nonsignificant M2 vs M4 nonsignificant M3 vs M4 nonsignificant	M1 = mean of Sample 1 M2 = mean of Sample 2 and so forth. HSD = the absolute [unsigned] difference between any two sample means required for significance at the designated level. HSD[.05] for the .05 level; HSD[.01] for the .01 level.

Table C6 **Statistical results for ANOVA and TUKEY HSD tests on a correlated sample comparing data for the effect of holding time (filtered), figure 4.17.**

Data Summary

	Samples				
	1	**2**	**3**	**4**	**Total**
N	32	32	32	32	128
ΣX	1188034.1	1144142.1	1300742.5	1552208.5	5185127.2
Mean	37126.0656	35754.4406	40648.2031	48506.5156	40508.8063
ΣX^2	174520473018.77	189988297839.31	190837664383.89	273462535823.5901	828808971065.5602
Variance	4206885195.401	4809036679.2999	4450478033.2442	6392590644.0349	4872170534.954
Std.Dev.	64860.5057	69347.2183	66711.9032	79953.6781	69800.9351
Std.Err.	11465.8258	12258.9721	11793.1098	14133.947	6169.5893

ANOVA Summary

Source	SS	df	MS	F	P
Treatment [between groups]	3136950827.7738	3	1045650275.9246	1.1933	0.316705
Error	81489763819.2362	93	876234019.5617		
Ss/Bl	534138943292.145	31			
Total	618765657939.155	127			

Ss/Bl = Subjects or Blocks depending on the design.
Applicable only to correlated-samples ANOVA.

Table C7 **Statistical results for ANOVA test on a correlated sample comparing data for the effect of holding time at 3 hours (unfiltered vs. filtered), figures 4.16 & 4.17.**

Data Summary

	Samples					
	1	2	3	4	5	Total
N	32	32				64
∑X	2027160.1	1552208.5				3579368.6
Mean	63348.7531	48506.5156				55927.6344
$\sum X^2$	494936158218.41	273462535823.5901				768398694042
Variance	11823164306.4084	6392590644.0349				9019255169.6483
Std.Dev.	108734.375	79953.6781				94969.7592
Std.Err.	19221.7035	14133.947				11871.2199

ANOVA Summary

Source	SS	df	MS	F	P
Treatment [between groups]	3524672224.1024	1	3524672224.1024	1.7319	0.197817
Error	63089687623.2674	31	2035151213.6538		
Ss/Bl	501598715840.4744	31			
Total	568213075687.8442	63			

Table C8 **Statistical results for ANOVA test on a correlated sample comparing data for the effect of centrifugation, figure 4.18.**

Data Summary

	Samples					
	1	2	3	4	5	Total
N	32	32	32			96
∑X	1127765.7	1396068.2	1466707.7			3990541.6
Mean	35242.6781	43627.1313	45834.6156			41568.1417
$\sum X^2$	156729297548.47	200820624889.26	237573179437.0301			595123101874.76
Variance	3773671418.805	4513360461.0938	5495070831.3968			4518354771.7814
Std.Dev.	61430.2158	67181.5485	74128.745			67218.7085
Std.Err.	10859.4305	11876.1321	13104.2346			6860.4807

ANOVA Summary

Source	SS	df	MS	F	P
Treatment [between groups]	1998519269.0677	2	999259634.5339	2.5722	0.084496
Error	24085804057.0122	62	388480710.597		
Ss/Bl	403159379993.1535	31			
Total	429243703319.2334	95			

Table C9 **Statistical results for ANOVA test on a correlated sample comparing data for the cell distributions at passage number 19, 28, 14 and 13.**

Data Summary

	Samples				
	1	2	3	4	Total
N	32	32	32	32	128
ΣX	1022642.3	723464.8354	1093068.4445	1127765.7778	3966941.3576
Mean	31957.5719	22608.2761	34158.3889	35242.6806	30991.7294
ΣX^2	109255329396.87	63074390077.2616	169199901717.5395	156729308613.3255	498258929804.9966
Variance	2470134341.684	1507035397.5989	4253627248.6545	3773671598.9465	2955248479.3461
Std.Dev.	49700.4461	38820.5538	65219.8378	61430.2173	54362.1972
Std.Err.	8785.8806	6862.5692	11529.3474	10859.4308	4804.9848

ANOVA Summary

Source	SS	df	MS	F	P
Treatment [between groups]	3178030683.5598	3	1059343561.1866	0.7423	0.529508
Error	132716958589.6879	93	1427064070.8569		
Ss/Bl	239421567603.7122	31			
Total	375316556876.9599	127			

Table C10 **Statistical results for ANOVA and TUKEY HSD tests on a correlated sample comparing data for cell viability when exposed to N-Saline (Control), 0.5% and 1.0% alginate for 3 hours.**

Data Summary

	Samples					
	1	2	3	4	5	Total
N	7	7	7			21
ΣX	653.7	668.1	597.4			1919.2
Mean	93.3857	95.4429	85.3429			91.3905
ΣX^2	61268.37	63882.53	51812.42			176963.32
Variance	37.0214	19.5262	138.0995			78.3359
Std.Dev.	6.0845	4.4188	11.7516			8.8508
Std.Err.	2.2997	1.6702	4.4417			1.9314

ANOVA Summary

Source	SS	df	MS	F	P
Treatment [between groups]	398.8352	2	199.4176	6.8265	0.010478
Error	350.5448	12	29.2121		
Ss/Bl	817.3381	6			
Total	1566.7181	20			

Tukey HSD Test

HSD[.05]=7.71; HSD[.01]=10.31 M1 vs M2 nonsignificant M1 vs M3 P<.05 M2 vs M3 P<.05	M1 = mean of Sample 1 M2 = mean of Sample 2 and so forth. HSD = the absolute [unsigned] difference between any two sample means required for significance at the designated level. HSD[.05] for the .05 level; HSD[.01] for the .01 level.